

© Copyright by Mehmet Kurt 2014

All Rights Reserved

IDENTIFICATION, REDUCED ORDER MODELING AND MODEL UPDATING OF
NONLINEAR MECHANICAL SYSTEMS

BY

MEHMET KURT

DISSERTATION

Submitted in partial fulfillment of the requirements
for the degree of Doctor of Philosophy in Mechanical Engineering
in the Graduate College of the
University of Illinois at Urbana-Champaign, 2014

Urbana, Illinois

Doctoral Committee:

Professor Alexander F. Vakakis, Chair and Director of Research
Professor Lawrence A. Bergman, Co-Director of Research
Professor Andrew G. Alleyne
Research Associate Professor D. Michael McFarland

ABSTRACT

IDENTIFICATION, REDUCED ORDER MODELING AND MODEL UPDATING OF NONLINEAR MECHANICAL SYSTEMS

Mehmet Kurt, B.S., Bogazici University

Directed by: Professor Alexander F. Vakakis
Professor Lawrence A. Bergman

In this dissertation, we propose a new method for global/local nonlinear system identification, reduced order modeling and nonlinear model updating, applicable to a broad class of dynamical systems. The global aspect of the approach is based on analyzing the free and forced dynamics of the system in the frequency-energy domain through the construction of free decay or steady-state frequency-energy plots (FEPs). The local aspect of the approach considers specific damped transitions and leads to low-dimensional reduced order models that accurately reproduce these transitions. The nonlinear model updating strategy is based on analyzing the system in the frequency-energy domain by constructing Hamiltonian or forced and damped frequency-energy plots (FEPs). These plots depict the steady-state solutions of the systems based on their frequency-energy dependencies. The backbone branches, branches that correspond to 1:1 resonances, are calculated analytically (for fewer DOFs) or numerically (*e.g.*, shooting method). The system parameters are then characterized and updated by matching these backbone branches with the frequency-energy dependence of the given system by using

experimental/computational data. The main advantage of our approach is that we do not assume any type of nonlinearity model a priori, and the system model is updated solely based on numerical simulations and/or experimental results. As such, the approach is applicable to a broad class of nonlinear systems, including systems with strong nonlinearities and non-smooth effects, as will be shown in this dissertation. For larger scale systems, model reduction techniques (*e.g.*, Guyan reduction) are applied to construct reduced order models of the system to which the aforementioned methods are applied.

ACKNOWLEDGMENTS

It would not have been possible to write this dissertation without the help and support of the kind people around me, to only some of whom it is possible to give particular mention here.

First and foremost, I would like to express my deepest gratitude to my advisors Professors Alexander F. Vakakis and Lawrence A. Bergman. I have been amazingly fortunate to have advisors who gave me the freedom to explore on my own and at the same time the guidance to go in the right direction all the time. Their patience and support helped me overcome many obstacles in my research and finish this dissertation. I hope that one day; I will be as good an advisor to my students as they have been to me.

I would also like to extend my appreciation to my committee members: Prof. D.M. McFarland, Prof. Melih Eriten and Prof. Andrew G. Alleyne. I would like to thank Prof. McFarland for always guiding me towards the correct path in my research with his constructive criticism and invaluable suggestions, which made this dissertation possible. I was so fortunate to have Prof. Melih Eriten as a collaborator in my research and as a friend in my life; since without his help, motivation and support, it would not have been possible to complete and enjoy this research. I would also like to thank Prof. Young S. Lee for helping me kickstart my research and his insightful comments throughout my studies.

I would also like to acknowledge National Science Foundation (NSF) and Mechanical Science and Engineering Department (MechSE) of UIUC for their contributions in funding my research and PhD studies.

In no particular order, I would like to thank my friends Gizem Dilber for her continuous support and friendship, Thibaut Detroux for always being a brother, Ahmet Deniz Usta for understanding me better than anyone else, Enver Candan for always listening to me, Clémence Bacquet for always laughing with me, Itir Akgun for all the good times we shared, Oytun Babacan for his encouragement and Omer Ozgur Capraz for motivating me whenever I needed to. I would also like to acknowledge my colleagues Arif Hasan, Chaozhong Guo, Kevin Remick, Yijing Zhang, Randi Potekin, Bongwon Jeong and Ravi Kumar for their great advices and being the perfect officemates.

Most importantly, none of this would have been possible without the love and support of my family; my parents Mediha Esin Kurt and Necmiddin Kurt, and my sister Irem Tartici. This dissertation is dedicated to them.

TABLE OF CONTENTS

	Pages
LIST OF TABLES	x
LIST OF FIGURES	xi
CHAPTER 1 INTRODUCTION	1
1.1 Motivation.....	1
1.2 Literature Review of Nonlinear System Identification	3
1.3 Literature Review of Reduced Order Modeling and Model Updating	5
1.4 Proposed Methodology and Background Information.....	8
1.5 Organization.....	10
CHAPTER 2 BASIC ELEMENTS OF THE NONLINEAR SYSTEM IDENTIFICATION (NSI) AND MODEL UPDATING METHODOLOGY	12
2.1 Slow Flow Dynamics (Lee et al. 2010a; Vakakis et al. 2011; Lee, Tsakirtzis, et al. 2009; Lee, Tsakirtzis, et al. 2011).....	12
2.2 Empirical Mode Decomposition (EMD) (Lee, Tsakirtzis, et al. 2009; Lee, Tsakirtzis, et al. 2011).....	13
2.3 Correspondence Between Theoretical and Empirical Slow Flows (Lee, Tsakirtzis, et al. 2011).....	16
2.4 Reduced Order Models: Intrinsic Modal Oscillators – IMOs (Lee et al. 2010a; Vakakis et al. 2011; Lee, Tsakirtzis, et al. 2011).....	18
2.5 Spatio-Temporal IMOs	21
2.6 Frequency-Energy Plots.....	22
CHAPTER 3 LOCAL ASPECTS OF THE NSI METHODOLOGY	25
3.1 Introduction and Background Information	25
3.2 NSI of the Dynamics of a Vibro-Impact Beam (Kurt et al. 2012; H. Chen et al. 2014)	32
3.2.1 Introduction and System Description.....	32

3.2.2 Linear Beam.....	36
3.2.3 Vibro-impact (VI) Beam.....	41
3.2.4 Comparison with results of experimental data analysis.....	53
3.2.5. Concluding Remarks.....	56
3.3 NSI of Frictional Effects in a Beam with a Bolted Joint Connection (Eriten et al. 2013)	57
3.3.1 Introduction.....	57
3.3.2 Experimental Fixture and Process	58
3.3.3 Linear Modal Analysis.....	63
3.3.4 Nonlinear System Identification	66
3.3.5 Nonlinear Frictional Effects.....	70
3.3.6 Equivalent Damping Ratios	80
3.3.7 Concluding Remarks.....	83
3.4 Strongly Nonlinear Beats in the Response of a Beam with a Strongly Nonlinear Stiffness (Kurt, Eriten, et al. 2014a)	84
3.4.1 Introduction and System Description.....	84
3.4.2 Empirical Mode Decomposition.....	87
3.4.3 Intrinsic Modal Oscillators (IMOs)	90
3.4.4 Analysis of Nonlinear Beat Phenomena by Reduced Order Modeling.....	95
3.4.5 Slow Flow Modeling and NSI of Resonance-induced Beating Phenomena.....	104
3.4.5.1 Preliminaries: Analysis of Beating Signals.....	104
3.4.5.2 Nonlinear System Identification of Beating Signals.....	110
3.4.6 Concluding Remarks.....	114
CHAPTER 4 GLOBAL ASPECTS OF THE NSI METHODOLOGY	117
4.1 Introduction and Background Information	117

4.2 Frequency-Energy Plot Reconstructions.....	119
4.2.1 Analyzing the Frequency-Energy Plots of Different System Topologies	119
4.2.2 Experimental Results	123
4.3 Extending the Frequency-Energy Plots for Forced and Damped Systems	129
4.3.1 Forced and Damped Frequency-Energy Plots (FEPs) (Kurt, Eriten, et al. 2014b)	129
4.3.1.1 Introduction and System Description	129
4.3.1.2 Constructing the Forced and Damped Frequency- Energy Plots (FEPs).....	133
4.3.1.3 Application to Vibration Isolation By Means of Nonlinear Energy Transfer	146
4.3.1.4 Concluding Remarks	159
4.3.2 Application to 1:3 Resonance in a Two-Degree-of- Freedom Oscillator (Kurt, Slavkin, et al. 2014)	160
4.3.2.1 Introduction and System Description	160
4.3.2.2 Study of the Frequency-Energy Plots (FEPs) of the system	162
4.3.2.3 Time-Periodic Solutions of the Hamiltonian System	166
4.3.2.4 Steady-State Dynamics of the Forced and Undamped System.....	172
4.3.2.5 Effect of Varying the Magnitude of the Harmonic Excitation on the Steady-State Dynamics	177
4.3.2.6 Concluding Remarks	187
Chapter 5 NONLINEAR MODEL UPDATING	189
5.1 Introduction and Background Information	189
5.2 System with Hardening/Softening Behavior.....	191

5.2.1 Introduction and System Description.....	191
5.2.2 Numerical Simulations	194
5.2.2.1 Numerical Simulation with the FE model	194
5.2.2.2 Numerical Simulations of the Reduced Order Model.....	200
5.2.3 Frequency-Energy Plots of the System.....	204
5.2.4 Modeling the Nonlinear Connection.....	206
5.2.5 Comparisons between the Optimized and Original Models	214
5.3 Benchmark Problem	218
5.3.1 Introduction and System Description.....	218
5.3.2 Numerical Simulations of the Benchmark Model.....	220
5.3.3 Modeling the Nonlinear Properties of the Connection	223
5.4 Concluding Remarks.....	231
CHAPTER 6 CONCLUDING REMARKS AND FUTURE WORK	233
6.1 Summary.....	233
6.2 Future Work and Improvements	236
References.....	240

LIST OF TABLES

Table	Page
Table 3.1 Positions for the accelerometers, rigid stops and laser displacement sensors.....	34
Table 3.2 The leading 10 linear natural frequencies (in Hz) of the cantilever beam in Fig. 3.5 (<i>cf.</i> (Blevins 2001; Mane 2010))	35
Table 3.3 Experimental Linear Modal Analysis for the Monolithic and Bolted Beams.....	66
Table 3.4. Damping factors, fast frequencies and line slopes for each linear cantilever mode based on the beam tip response	92

LIST OF FIGURES









Figure	Page
Figure 2.1 Step-by-step description of the EMD method	15
Figure 2.2 (a) 2-DOF system consisting of two linear oscillators coupled with a nonlinear cubic spring (b) FEP of the 2-DOF system for parameters $m_1 = m_2 = 1$ kg, $k_1 = 2$ N/m, $k_2 = 1$ N/m, $k_{nl} = 1$ N/m ³	24
Figure 3.1 General outline of the local NSI approach	25
Figure 3.2 The two IMFs of the response $x_1(t)$	29
Figure 3.3 Comparison of $\ln \Lambda_1^{(i)}(t) $, $i = 1, 2$ with the analytical prediction (18) for the response $x_1(t)$	30
Figure 3.4 Exact and reconstructed (through IMOs) time series for the response $x_1(t)$	30
Figure 3.5 Experimental setup for the VI beam: $x_1 - x_{10}$, x_{LDS} , and x_{STP} respectively denote the spanwise locations of the accelerometers, of the laser displacement sensors, and of the rigid stops.	34
Figure 3.6 The normalized mode shape functions $\phi_n(x/L)$ of a cantilever beam: The first ten modes are depicted, and the vertical dashed lines denote the positions for accelerometers	35
Figure 3.7 Wavelet and Fourier transforms of the acceleration for the linear beam at position x_9	37
Figure 3.8 The 10 dominant IMFs extracted from the acceleration response in Fig. 3: (a) through (j) sequentially depict the 10th to 1 st IMFs, respectively	40
Figure 3.9 Comparison of the IMFs in Fig. 4 with their corresponding IMO solutions: (a) 10th IMF; (b) 5th IMF	41
Figure 3.10 Wavelet and Fourier transforms of the acceleration for the VI beam at $x = x_9$ (The Fourier transform in Fig. 3.7 is superimposed as a dashed line to illustrate the effects of vibro-impacts in frequency domain)	43

Figure 3.11 Depiction of the vibro-impacts: (a) the displacement response of the VI beam simulated at position x_{STP} and its corresponding impact loads on the beam from the rigid stops; (b) the nonsmooth component of the acceleration in Fig. 3.10 is decomposed via EMD analysis (Note that the <i>dashed lines</i> at $t = t_k$, $k = 1, \dots, 13$ imply the impact instants identified from the impact force, $p(t)$)	43
Figure 3.12 The 10 dominant IMFs extracted from the acceleration response in Fig. 3.10: a through j sequentially depict the 10th to 1 st IMFs, respectively (Note that the <i>dashed lines</i> imply the impact instants identified in Fig. 3.11)	45
Figure 3.13 Comparison of the IMFs in Fig. 3.12 with their corresponding IMO solutions: (a) 10th IMF; (b) 5th IMF	46
Figure 3.14 Comparison of the reconstructed acceleration from the 10 IMO solutions plus the nonsmooth IMF with the original response in Fig. 3.10.....	46
Figure 3.15 Comparison of the slowly-varying forcing functions $\Lambda_m(a_g, t)$: (a) $m = 10$ (<i>i.e.</i> , 10th IMO) and (b) $m = 4$ (<i>i.e.</i> , 4th IMO). Note that the dashed line simply the impact instants identified in Fig. 7.....	48
Figure 3.16 Linear correlation coefficient (%) between the slowly-varying forcing functions $\Lambda_m(a_k, t)$, $m, k = 1, \dots, 10$, where m and k denote the mode number and accelerometer position, respectively, of the linear and VI beams. We note that the thick solid (dashed) lines denote the boundary for 90% (80%) correlation.....	49
Figure 3.17 The spanwise magnitudes of nonlinear modal interaction for the VI beam: (a) through (j) sequentially depict the 10th to 1 st IMFs, respectively (Note that the logarithm with base 10 is taken for $ \Lambda_m(a_k, t) $ and that the sections at $t = t_n$, $n = 1, \dots, 9$, denote some of the impact instants identified in Fig. 3.10)	51
Figure 3.18 IMFs extracted from the experimentally measured acceleration at the sensing position x_9 : (a) 10th IMF (<i>cf.</i> Fig. 3.12a); (b) 5 th IMF (<i>cf.</i> Fig. 3.12f).....	54
Figure 3.19 Comparison of the reconstructed acceleration from the ten (smooth) IMO solutions with the original response measured at position x_9	55
Figure 3.20 The spatio-temporal variations of $\Lambda_m(a_g, t)$ the VI beam from experimental measurements (a) $m = 10$ (<i>i.e.</i> , 10th IMO) and (b) $m = 5$ (<i>i.e.</i> , 5th IMO).	55
Figure 3.21 The bolted beam used in the experimental tests (all dimensions given in mm).	59

Figure 3.22 Measurement grid for laser vibrometer measurements, positions of the two accelerometers and point of impulsive excitation for the bolted beam	60
Figure 3.23 Typical forcing and velocity spectra in the experimental tests for the monolithic and bolted beams: (a,b) Applied force in time and frequency domains, (c) velocity spectra.....	61
Figure 3.24 Velocity(m/s) measurements at 5 sensing positions on the monolithic.....	64
Figure 3.25 Measured and reconstructed mobility FRFs from sensing position 3 based on the RFP method with (a) SDOF and (b) 3-DOF curve-fitting algorithms.....	65
Figure 3.26 EMD analysis of the velocity time series at sensing position 1 on the monolithic beam.....	68
Figure 3.27 Measured and reconstructed velocity time series at sensing position 1 of (a) and (b) bolted beams; the reconstructed response was computed as the superposition of the IMO responses with the rigid body (pendulum) mode.	69
Figure 3.28 Logarithms of the magnitudes of the complex forcing amplitudes for the six IMOs of the velocity time series measured at sensing location 1 of the monolithic beam; both unfiltered and low-pass filtered data are shown and compared to theoretically predicted LMAs according to (21) (vertical line denotes the time instant where an IMO is nearly zero).....	72
Figure 3.29 Logarithms of the magnitudes of the complex forcing amplitudes for the six IMOs of the velocity time series measured at sensing location 1 of the bolted beam; both unfiltered and low-pass filtered results are shown and compared to theoretically predicted LMAs according to (21) (vertical line denotes the time instant where an IMO is nearly zero).....	74
Figure 3.30 Spatio-temporal variations of $\ln \Lambda_k^{(i)}(t) $ for the monolithic beam; the cross-line in each plot indicates the time instants of vanishing signals due to damping.....	75
Figure 3.31 Spatio-temporal variations of $\ln \Lambda_k^{(i)}(t) $ for the bolted beam; the cross-line in each plot indicates the time instants of vanishing signals due to damping.	76
Figure 3.32 Absolute value of the linear correlation coefficient (%) (interpolated along the half-span of the beam) for (a) $t = 0.10\text{sec}$, (b) $t = 0.15\text{sec}$, (c) $t = 0.20\text{sec}$, and (d) $t = 0.25\text{sec}$	79
Figure 3.33 The three different impulsive excitations applied to the bolted beam.....	81

Figure 3.34 Equivalent modal damping ratios extracted by the NSI methodology; each plot depicts the spatial dependence of this ratio on the applied modal energy.....	82
Figure 3.35. The system under consideration: (a) configuration, (b) applied impulsive force.....	85
Figure 3.36. Acceleration of the tip of the beam: (a) Linear case (no nonlinear spring attached), (b) case of weaker nonlinearity, $k_{nl} = 108 \text{ N/m}^3$, (c) case of stronger nonlinearity, $k_{nl} = 1010 \text{ N/m}^3$	86
Figure 3.37 The 1st and 6th intrinsic mode functions (IMFs) and their wavelet transforms: (a) Linear system, and (b) strongly nonlinear system.	88
Figure 3.38 Original reconstructed time series, the latter obtained by summing intrinsic mode functions (IMFs) and the responses of intrinsic modal oscillators, respectively, (IMOs) for (a) the linear system, and (b) the strongly nonlinear system; — original time series, — sum of IMF responses, - - - sum of IMO responses.....	90
Figure 3.39 Plots of $\ln \left \Lambda_{Tip}^{(m)}(t) \right $ for IMOs corresponding to the (a) 1st IMF, (b) 6th IMF of the linear and strongly nonlinear cantilever beams; — Linear, - - - strongly nonlinear, - . - . - predicted linear slope.	93
Figure 3.40 FEP of the RGM with end stiffness nonlinearity: (a) Backbone branches, (b) detail of the in-phase backbone branch indicating subharmonic tongues due to internal resonances; — Stable NNMs, — unstable NNMs.....	98
Figure 3.41 RGM (24): (a) Response of the first reduced DOF $x_1(t)$, (b) Response of the second reduced DOF $x_2(t)$; both in meters (wavelet transform spectra and Fourier transforms are also depicted).....	100
Figure 3.42 Wavelet transform spectrum of the second DOF of the RGM superimposed on the Hamiltonian FEP of Fig. 7; nonlinear beats in the neighborhood of subharmonic tongues S312 and S512 are evidenced by the corresponding broadband frequency components that emanate from these tongues.	100
Figure 3.43 Details of (a) the 1 st IMF, (b) the 2 nd IMF, (c) the transient response $x_2(t)$ in the region of nonlinear beats	103
Figure 3.44 Transient variation of $\ln \left \Lambda(t) \right $ (logarithm of the modulus of the complex forcing of the IMO) of a beating signal, and its comparison to the line with slope $-\zeta\omega$; — $\ln \left \Lambda(t) \right $, - - - predicted linear line, -o- nodal points.....	109

Figure 3.45 Application of the NSI technique to beating signals in the (a) 1st IMF, (b) 2nd IMF, (c) 3rd IMF, and (d) 4th IMF of the strongly nonlinear system; $c_{Tip}^{(m)}(t)$, $\ln \Lambda_{Tip}^{(m)}(t) $, predicted linear slope.	111
Figure 3.46 Application of the NSI technique to beating signals in the (a) 5 th IMF, and (b) 6 th IMF of the strongly nonlinear system; $c_{Tip}^{(m)}(t)$, $\ln \Lambda_{Tip}^{(m)}(t) $, predicted linear slope.	112
Figure 3.47 Application of the NSI technique to beating signals in the a) 7 th IMF, and (b) 8 th IMF of the strongly nonlinear system (<i>cf.</i> Fig. 7b); $c_{Tip}^{(m)}(t)$, $\ln \Lambda_{Tip}^{(m)}(t) $, predicted linear slope.	113
Figure 4.1 General outline of the global NSI approach	118
Figure 4.2 Possible system configurations for the examined system.....	120
Figure 4.3 FEP of the system studied in 4.2.1	121
Figure 4.4 FEP of the system studied in Section 3.4	123
Figure 4.5. (a) Picture of the experimental setup (b) Graphic representation of the experimental setup.....	124
Figure 4.6 (a) Impulse response of the LO (b) Impulse response of the NES for forcing depicted in (c).....	125
Figure 4.7 EMD results for the NES response in Figure 4.6b	127
Figure 4.8 Superposition of the WTs of IMFs (in Figure 4.7) on the FEP.	128
Figure 4.9 Superposition of the WTs from combined impulse tests (NES data).	128
Figure 4.10 Two-DOF weakly coupled and weakly damped system under weak harmonic forcing.	132
Figure 4.11 Normalized amplitude of the LO as function of frequency for the forced and undamped system: NNMs of the underlying Hamiltonian system, Forced fundamental resonance branches.	139

Figure 4.12 Normalized amplitude of the NES as function of frequency for the forced and undamped system:  NNMs of the underlying Hamiltonian system,  Forced fundamental resonance branches.	139
Figure 4.13 Frequency-energy plots (FEPs) for fundamental resonances of the forced and undamped system: (a) Global FEPs, (b) detail showing the bifurcations of fundamental resonances; gray solid lines depict the NNMs of the underlying Hamiltonian system.	140
Figure 4.14 Normalized amplitude of the LO as function of frequency for the forced and damped system:  NNMs of the underlying Hamiltonian system,  Forced fundamental resonance branches.	143
Figure 4.15 Normalized amplitude of the NES as a function of frequency for the forced and damped system:  NNMs of the underlying Hamiltonian system,  forced fundamental resonance branches.	143
Figure 4.16 Frequency-energy plots (FEPs) for fundamental resonances of the forced and damped system: (a) Global FEPs, (b) detail showing the bifurcations of fundamental resonances; gray solid lines depict the NNMs of the underlying Hamiltonian system.	144
Figure 4.17 Effect of the mass ratio m_1/m_2 on the steady-state amplitude of the LO for system parameters $\lambda_1 = 0.05, \lambda_2 = 0.1, \varepsilon = 0.05, k_c = 1, C = 1, P = 1$	148
Figure 4.18 Effect of the stiffness coefficient C_s on the steady-state amplitude of the LO for system parameters $\lambda_1 = 0.05, \lambda_2 = 0.1, \varepsilon = 0.05, k_c = 1, m_1 = 30, m_2 = 1, P = 1$	150
Figure 4.19 Effect of the damping coefficient λ_2 on the steady-state amplitude of the LO for system parameters $\lambda_1 = 0.05, \varepsilon = 0.05, k_c = 1, m_1 = 30, m_2 = 1, C = 1, P = 1$	151
Figure 4.20 Effect of the forcing amplitude P on the steady-state amplitude of the LO for system parameters. $\lambda_1 = 0.05, \lambda_2 = 0.1, C = 1, \varepsilon = 0.05, k_c = 1, m_1 = 30, m_2 = 1$	152
Figure 4.21. Steady state dynamics of the optimized solution: (a)  Response of LO without the attached NES and  of LO with the attached NES; (b) response of NES, (c) damped FEP where gray solid lines depict the NNMs of the underlying Hamiltonian system (the comparisons of the steady	

state responses with and without NES attached are shown to assess the effectiveness of vibration suppression).	153
Figure 4.22. Time simulations carried out for selected steady-state solutions of the plots of Figure 12 for the LO without attached NES, the LO with attached NES, and the NES; initial conditions are taken on the steady-state branch 2 at frequency (a) 1.4 rad/s, (b) 1.5 rad/s, (c) 1.6 rad/s.	154
Figure 4.23 Projection of the domains of attraction of the competing stable steady state solutions I and II of Figure 12: Gray dots (•) depict the initial conditions corresponding to solutions that converge to the optimized localized steady state I, whereas black crosses (x) depict the initial conditions corresponding to solutions converge to the competing stable solution II; points S1 and S2 denote the initial conditions of the stable steady states I and II, respectively, whereas U1 the initial conditions for the unstable solution III.....	157
Figure 4.24 Time simulations for initial conditions depicted in Figure 14: (a) Point A corresponding to $X_1=-0.36$, $X_2=2.06$, (b) point B corresponding to $X_1=-0.36$, $X_2=2.03$, (c) Point C corresponding to $X_1=0.48$, $X_2=-0.05$, (d) zero initial conditions.	158
Figure 4.25. Grounded nonlinear oscillator and light linear attachment under harmonic forcing.	161
Figure 4.26. Frequency-energy plot (FEP) of the unforced and undamped (Hamiltonian) system; the box indicates the branch produced by 1:3 resonance which is depicted in detail in Figure 4.27.....	168
Figure 4.27. $S_{13\pm}$ branches due to 1:3 resonance; — FEP of the Hamiltonian system, ▲ points for which the configuration plots are depicted.	169
Figure 4.28. Comparisons of $S_{13\pm}$ and S_{33-} branches for the underlying Hamiltonian system: — Analytical results obtained by solving equations (8), — results from direct numerical integrations of system (1) with no damping or forcing.	171
Figure 4.29. Perturbations of the Hamiltonian branches $S_{13\pm}$ and S_{33-} for applied harmonic forcing of constant magnitude $F = 5 N$ and no damping in system (1): — Branches of time-periodic steady state solutions; ■ selected points corresponding to the shown plots of the responses in the configuration plane; ◆ coalescence points between branches $S_{13\pm}$ and S_{33-}	173
Figure 4.30. FEP of the forced and undamped system computed by solving (7) for $F = 5 N$, and with both ω and 3ω harmonic components shown (—);	

underlying numerical Hamiltonian FEP for the undamped and unforced system (-----).....	175
Figure 4.31: Effect of varying the magnitude of the applied excitation on the branches $S_{13 \pm}$ of the forced and undamped system for: $F = 1 N$, $F = 3 N$, $F = 5 N$	177
Figure 4.32. Direct numerical simulation results showing the steady state responses of system (1) (with small damping $c_1 = c_2 = 0.001 Ns / m$) and their Fourier spectra with the excitation frequency $\omega = 1 rad / s$, and, (a) $F = 0.01 N$, (b) $F = 1 N$, (c) $F = 5 N$, (d) $F = 20 N$; for comparison we depict the analytical predictions (\bullet) for the harmonic content from the slow-flow equations (4.25).....	178
Figure 4.33. Stability analysis of the numerical branches $S_{13 \pm}$ for the underlying Hamiltonian system by studying Floquet multipliers of the steady state responses; unstable NNMs are denoted by (\times).....	182
Figure 4.34. Steady-state periodic solutions computed by system (4.25) for the forced and undamped system with $F = 5 N$, with points where the stability is investigated denoted by (\blacksquare); letters refer to the numerical simulations of Figure 4.35.	183
Figure 4.35. Direct numerical simulation results showing the steady state responses of system (1) and their Fourier spectra for $F = 5 N$ with initial conditions and the excitation frequency taken from (a) Point A, (b) Point B (c) Point C (d) Point D (e) Point E in the plot of Figure 4.34; weak damping values, $c_1 = c_2 = 0.001 Ns / m$, were used for the simulations.	184
Figure 5.1 Summary of the proposed nonlinear model updating approach.....	190
Figure 5.2 Overview of the examined system with the physical properties and dimensions. The two clamped beams are connected by a non-linear element whose force-displacement curve is given in Figure 5.3.	192
Figure 5.3 The force-displacement relationship of the nonlinear connection in Figure 5.2.	193
Figure 5.4 Impulse force used for the numerical simulations of the system depicted in Figure 5.2, which is applied to the tip point of the first beam.....	195







Figure 5.5 Impulse responses of the tip points of the two beams $w_1(x_{Tip,1},t)$ and $w_2(x_{Tip,2},t)$ for (a) $F_{max} =1$ N (b) $F_{max} =100$ N (c) $F_{max} =500$ N (d) $F_{max} =750$ N.....	196
Figure 5.6 Impulse responses of the tip points of the two beams $w_1(x_{Tip,1},t)$ and $w_2(x_{Tip,2},t)$ for (a) $F_{max} =1000$ N (b) $F_{max} =2500$ N (c) $F_{max} =5000$ N (d) $F_{max} =20000$ N.....	197
Figure 5.7 Wavelet and Fourier transforms of the tip point deflection for the first beam, $w_1(x_{Tip,1},t)$ for (a) $F_{max}=100$ N, (c) $F_{max}=2500$ N, (e) $F_{max}=10000$ N. (b),(d) and (f) are the close-up of the WTs of the time signals depicted in (a), (c) and (e) respectively.....	199
Figure 5.8 Reduced-order model of the system depicted in Figure 5.2 with parameters.....	200
Figure 5.9 Comparison of impulse responses of the tip points of the two beams $w_1(x_{Tip,1},t)$ and $w_2(x_{Tip,2},t)$ between  Reduced order model,  FEM model for (a) $F_{max} =1$ N (b) $F_{max} =100$ N (c) $F_{max} =500$ N (d) $F_{max} =750$ N.....	202
Figure 5.10. Comparison of Impulse responses of the tip points of the two beams $w_1(x_{Tip,1},t)$ and $w_2(x_{Tip,2},t)$ between  Reduced order model,  FEM model for for (a) $F_{max} =1000$ N (b) $F_{max} =2500$ N (c) $F_{max} =5000$ N (d) $F_{max} =20000$ N.....	203
Figure 5.11 Frequency-Energy Plot of the ROM depicted in Figure 5.8, with the nonlinear connection given in Figure 5.3.....	204
Figure 5.12 Superposition of WTs of the 2 nd DOF responses (Figures 5.9 and 5.10) of the ROM onto:  Adjusted frequency-energy transition of the 2 nd mode, obtained from the numerical simulations  Backbone branches computed by NNMcont (Peeters et al. 2009).....	205
Figure 5.13 The general form of the assumed nonlinearity, based on the findings of Figure 5.12.....	207
Figure 5.14 Optimization result of the smooth part of the 2 nd backbone branch to find the coefficient of the hardening nonlinearity a_1	210

Figure 5.15 (a) Iterations showing the optimization process of x_b for the nonlinearity model assumed in Figure 5.13, (b) Close-up of (a) within the rectangle region.....	212
Figure 5.16 Iterations showing the optimization process of k_b for the nonlinearity model assumed in Figure 5.13.....	213
Figure 5.17 The comparison between the optimized and original nonlinearity models	214
Figure 5.18 Comparison of the (a) 1 st (b) 2 nd backbone branches with the reference and numerical backbone branches.	215
Figure 5.19 Comparison of time series, wavelet and Fourier transforms for the tip point deflection of the first beam, $w_1(x_{Tip,1}, t)$ for (a) $F_{max}=1000$ N, (c) $F_{max}=2500$ N between the optimized ROM and original system.	216
Figure 5.20 Comparison of time series, wavelet and Fourier transforms for the tip point deflection of the first beam, $w_1(x_{Tip,1}, t)$ for $F_{max}=1000$ N.	218
Figure 5.21 Benchmark structure. The two clamped beams are connected by a non-identified element. A force in the positive direction on sensor D is indicated.....	219
Figure 5.22 Time series, wavelet and Fourier transforms for the tip point deflection of the first beam, $w_1(x_D, t)$ for $F_{max}=1$ N.	220
Figure 5.23 Time series, wavelet and Fourier transforms for the tip point deflections of the first and second beam, $w_1(x_D, t)$ and $w_2(x_E, t)$ for (a) $F_{max}=2500$ N (b) $F_{max}=5000$ N (c) $F_{max}=7500$ N.....	221
Figure 5.24 Superpositions of FFTs resulting from the impulse test with varying F_{max} values ,for the tip point deflection of the first beam , $w_1(x_D, t)$	222
Figure 5.25 Superposition of the WT spectra onto the frequency-energy domain. The transient data used is the impulse test results from the previous section for $w_1(x_D, t)$	223
Figure 5.26 Modeling of the nonlinear properties for the “non-identified” connection in Figure 5.2	224
Figure 5.27 Optimized backbone branches with $k_1=6\times 10^5$ N/m, $k_2 = 5\times 10^2$ N/m, $x_b = 0.02$ mm	226

Figure 5.28 Comparisons of the time series, wavelet and Fourier transforms for the tip point deflections of the first and second beam, $w_1(x_D, t)$ and $w_2(x_E, t)$ for (a) $F_{\max}=1$ N (b) $F_{\max}=5000$ N (c) $F_{\max}=10000$ N.	227
Figure 5.29 (a) Impulse response of the tip point of the first beam, $w_1(x_D, t)$ with $F_{\max}=20000$ N (b) Close-up to its WT.	228
Figure 5.30 The maximum displacement configurations of the two beams for $F_{\max}=17500, 20000, 21000, 22000, 23000, 24000$ N respectively in the increasing amplitude direction.	229
Figure 5.31 Comparison of the simulation result by using the 2-DOF system of Figure 5.8 with the explained configuration switching mechanism to the benchmark output for $F_{\max}=20000$ N at the tip of the first beam, $w_1(x_D, t)$	231

CHAPTER 1

INTRODUCTION

1.1 Motivation

For centuries, much of our understanding of science was built on the idea that a natural system subjected to well-defined external conditions will follow a unique course and that a slight change in these external conditions will likewise cause a slight change in the response. This led the scientific community to imagine a *linear* world, which is, in fact, *nonlinear*.

This line of thinking provides only a partial view of the natural world and cannot be used to accurately analyze complex systems. Consider the case of multi-physical systems. As these systems become more complex, potentially incorporating not only electrical and mechanical components but also biological and biomimetic elements, it is highly likely that their dynamics will be strongly nonlinear and nonstationary. Some examples include but are not limited to local buckling, plastic deformations, clearance and backlash, hysteresis, friction-induced oscillations, and vibro-impact motions, which cannot be accurately modelled by linearized techniques. Moreover, in many multi-physics problems such as interfacial effects, thermal-induced oscillations, fluid-structure interactions, plasma physics, ocean-atmosphere system or sensor-tissue interactions, a physically-based parametric model of the system will not be known *a priori*. However, given the placement of a sufficiently dense set of sensors, measured time series recorded throughout the system will contain all of the information reflecting both nonlinearity and nonstationarity. Hence, it is the analyst's responsibility to be able to extract information about the dynamics directly from the measured time series.

Clearly, linear methods such as the classical Fourier Transform (FT) are not able to properly isolate and extract this information, especially in strongly nonlinear applications (Vakakis 2008; Lee et al. 2008) where concepts such as "normal mode", "natural frequency", and "modal space" need to be carefully reconsidered, redefined and extended to nonlinear regimes.

This discussion motivates the need to develop nonlinear system identification (NSI), reduced order modeling and nonlinear model updating methodologies that ideally would be as practical as experimental linear modal analysis, and applicable to a broad class of nonlinear systems, including systems with weak or strong nonlinearities having smooth or non-smooth characteristics and time-invariant or time-variant properties. Based on our previous discussion, we can conclude that some of the basic properties the method should possess are as follows:

- It should be based on direct analysis of measured time series, since, as explained, they contain all necessary information about the underlying dynamics.
- It should be physics-based, relying on a solid theoretical foundation.
- It should be applicable to a broad class of dynamical systems, including those that are strongly nonlinear and nonstationary. For instance, it should be able to analyze complex nonlinear resonance interactions, providing interpretation and modeling of such interactions.
- It should address the dependence of the nonlinear dynamical response on the level and type of excitation, and its sensitivity to the initial conditions.

Therefore, the focus of this dissertation will be to discuss the efforts towards developing such an NSI, reduced order modeling and nonlinear model updating approach of broad applicability.

1.2 Literature Review of Nonlinear System Identification

Experimental modal analysis based on Fourier transforms (FTs) has been well established based on the assumption of linearity and stationarity of the measured signals (see, for example (Ewins 1984)) and system identification, modal analysis and reduced order modelling of linear dynamical systems have all been well documented (Ibrahim 1973; Ljung 1987; Soderstrom and Stoica 1989; Ewins; Allemang and Brown 1998; Allemang and Phillips 2004). In many practical situations, however, the measured data is likely to exhibit strong nonlinearity and nonstationarity, particularly when the tested systems involve nonlinearities due to complexity caused by multi-physical nonlinear interactions (Brandon 1998). In addition, FT-based methods are not able to properly isolate and extract nonlinearity and nonstationarity from the measured data, frequently misleading the less experienced analyst to wrong conclusions (for example, to misinterpret internal and combination resonances as natural frequencies). As a result, there is a need for an effective, straightforward, system identification and reduced-order modeling method for characterizing strongly nonlinear and nonstationary, complex, multi-component systems.

Reviews of nonlinear system identification (NSI) and reduced-order modeling (ROM) methods are provided in works by (Kerschen et al. 2005; Kerschen et al. 2006; Worden and Tomlinson 2010). Typical nonparametric NSI methods include proper orthogonal decomposition (POD, also known as Karhunen-Loève decomposition) (Feeny and Kappagantu 1998; Kerschen and Golinval 2002; Bellizzi and Sampaio 2006; Allison, Miller, and Inman 2008), smooth orthogonal decomposition (Chelidze and Zhou 2006), Volterra theory (Li and Billings 2011), Kalman filter (Mariani and Ghisi 2007), Bayesian approaches (Worden and Manson 2012; Tiboaca et al. 2014; Worden and Becker 2011; Worden and Hensman 2012) and so on. As for the methods of nonlinear parameter estimation, we mention

the restoring force surface method (Masri and Caughey 1979), NARMAX (Nonlinear Auto-Regressive Moving Average models with eXogenous inputs) methods (Leontaritis and Billings 1985), harmonic balance method (Thothadri et al. 2003), methods based on Hilbert transform (Feldman 1994; Feldman 2006), subspace identification (Noël and Kerschen 2013) and others. The neural network approach is another popular nonparametric methodology for system identification and damage-detection. Several noteworthy works related to this approach were performed by (Liang, Feng, and Cooper 2001; Masri et al. 2000).

POD has been employed to study system identification and nonlinear normal modes of a system of coupled beams (Ma, Azeez, and Vakakis 2000) and rods (Georgiou 2005), and in structural damage detection (Galvanetto, Surace, and Tassotti 2008). The method of POD has also been utilized to study chaotic vibrations of a 10-degree-of-freedom (DOF) impact oscillator and a flexible-beam impact oscillator, respectively, in (Cusumano and Bai 1993) and (Cusumano, Sharkady, and Kimble 1994). In these studies, the spatial structure of impacting responses under harmonic excitation of the boundary was demonstrated to be close to what can be obtained by averaging over many impulse-response tests on the linear system (even though the system is strongly nonlinear). Moreover, POD was applied to model reduction of a vibro-impact (VI) rod (Ritto, Buezas, and Sampaio 2011), and also to extracting dominant *coherent* structures of a VI beam from experimental time-series data (Azeez and Vakakis 2001) with the goal being to eventually derive low-dimensional ROMs through a Galerkin reconstruction process based on the extracted mode shape functions. (Clement et al. 2014) proposed a new method named Sliding Window Proper Orthogonal Decomposition (SWPOD) combining POD and Continuous Gabor Transform (CGT) to extract the linear and nonlinear normal modes of weakly damped MDOF mechanical systems.

We note, however, that these techniques are only applicable to specific classes of dynamical systems; in addition, some functional form is assumed for modeling the system nonlinearity. Recently, a nonlinear system identification (NSI) method with broad applicability based on empirical mode decomposition (EMD (Huang et al. 1998)) was proposed by (Lee et al. 2010a), which will be a focus of this dissertation. The key assumption of the methodology is that the measured time series can be decomposed in terms of a finite number of oscillating components that are in the form of fast monochromatic oscillations modulated by slow amplitudes. The empirical slow-flow model of the dynamics is obtained from EMD, and its correspondence with the analytical slow-flow model has been established (Lee, Tsakirtzis, et al. 2009) paving the way for constructing local nonlinear interaction models (NIMs (Lee, Tsakirtzis, et al. 2011)).

1.3 Literature Review of Reduced Order Modeling and Model Updating

Predictions from analytical and computational models are often called into question when they conflict with test results. *Model updating* concerns the correction of these models by processing and integrating dynamic response data from test structures (Mottershead and Friswell 1993).

More specifically, finite element model updating emerged in the 1990s as a topic thought to be very crucial for the design, construction and maintenance of mechanical systems and other engineering structures (Friswell and Mottershead 1995). Reviews of existing FE model updating techniques are given in (Friswell and Mottershead 1995; Mottershead and Friswell 1993; Hemez and Doebling 2001; Datta 2002). These give a clear overview of sensitivity-based updating methods. Sensitivity-based FE model updating methods have been embraced for damage assessment and structural health monitoring applications (*e.g.*, (Teughels, Maeck,

and De Roeck 2002; Brownjohn et al. 2001; Link, Rohrmann, and Pietrzko 1996), but have been limited in application to linear systems.

Data-driven modeling and updating is an increasingly important field in science and engineering. There have been recent attempts to utilize this “data-driven” approach in model updating (*e.g.*, (Jaishi and Ren 2005; Derkevorkian et al. 2014; Pokale and Gupta 2014)). Another model updating strategy, proposed by (Kerschen and Golinval 2004) for nonlinear vibrating structures, is based on proper orthogonal decomposition and its nonlinear generalizations based on auto-associative neural networks. (Derkevorkian et al. 2014) used data from relatively large-scale experimental soil-foundation-superstructure interaction (SFSI) systems to develop reduced-order computational models for response prediction by employing trained neural networks. (Pokale and Gupta 2014) applied a particle filtering algorithm on the experimentally measured tip accelerations using Bayesian principles to estimate the changes in damping and flexural rigidity of the beam. Another Bayesian approach is proposed by (Jensen et al. 2014), wherein a Bayesian finite element model updating strategy using dynamic response data is employed for structural response prediction.

Application of structural modification methods for data-driven modeling and updating are shown to be useful for large structures when the modifications remain local, *i.e.*, when the nonlinearities in the system do not affect the global dynamics significantly (Kalaycıoğlu and Özgüven 2014).

Techniques to construct reduced-order models (ROMs) have been developed primarily for linear models to reduce their size. Reviews of model reduction techniques exist in literature. However, these reviews mostly focus on methods from individual fields, *i.e.* on methods from structural dynamics (Roy Craig 2014; Klerk, Rixen, and Voormeeren 2008) , systems and control (Gugercin and Antoulas 2004; Bai 2002) or numerical mathematics (Freund 2003)

only. A review of reduced-order modeling (ROM) methods for nonlinear systems is provided in (Kerschen et al. 2006).

Component mode synthesis (CMS) (Benfield and Hruda 1971; Hurty 1965), originally developed for linear systems, has been extended to nonlinear systems by using a nonlinear normal modes approach (NNM) (Apiwattanalungarn, Shaw, and Pierre 2005) and also applied to systems with localized nonlinearities. (Kisa, Brandon, and Topcu 1998; Nataraj and Nelson 1989)

Proper orthogonal decomposition (POD) has been used extensively for constructing ROMs of nonlinear systems. (Kerschen et al. 2005). POD was applied for model reduction of a vibro-impact (VI) rod (Ritto, Buezas, and Sampaio 2011) and also to extracting dominant *coherent* structures of a VI beam from experimental time-series data (Azeez and Vakakis 2001) to derive low-dimensional ROMs through a Galerkin reconstruction process based on the extracted mode shape functions.

Other examples of approaches for ROM of nonlinear systems include the following: (Krysl, Lall, and Marsden 2001) proposed an approach to the dimensional reduction of nonlinear finite element models of solids and structures based on Ritz approximation. Another technique for ROM of nonlinear systems is bi-linear normal modes, which represent the spatial coherences in the system dynamics with two sets of normal modes with special boundary conditions (Saito and Epureanu 2011); these have also been used for model reduction. (Zucca and Epureanu 2014). (Segalman 2007) developed a methodology of reduced order models for systems with local nonlinearities which used the augmentation of conventional basis functions with others having appropriate discontinuities at the locations of nonlinearity. (Mohammadali and Ahmadian 2014) proposed an exact condensation technique based on the harmonic balance method (HBM) in conjunction with the modal expansion

technique to convert the motion equations of such structural dynamic systems to a set of nonlinear algebraic equations that are considerably small.

1.4 Proposed Methodology and Background Information

In this dissertation, a new methodology for nonlinear system identification, reduced order modeling, and nonlinear model updating of a wide array of dynamical systems is proposed. The methodology has global and local components and relies on direct processing of measured time series. The central assumption of the method is that the measured dynamics can be decomposed in terms of slowly modulated fast oscillations, which is a reasonable assumption for non-chaotic measured data. The basic elements of the method are outlined below, although a detailed discussion of each aspect will be given in the next chapters.

- (i) Measure time series simultaneously from a number of sensors throughout the system under transient excitation, and perform EMD of the measured time series. Extract the intrinsic mode functions (IMFs) at each sensing location. Hilbert-transform the computed IMFs to extract their instantaneous frequencies and compare them to wavelet transform (WT) spectra of the corresponding time series, thus determining the *dominant IMFs* and the corresponding *fast frequencies* in the dynamics at each sensing location. This will identify the basic time scales and the dimensionality of the dynamics. (*local aspect of NSI*).
- (ii) Based on the correspondence between the measured dominant IMFs and the underlying slow-flow dynamics of the system (see discussion in Section 2), relate the slow components of the dominant IMFs to the slow flow dynamics (*local aspect of NSI*).

- (iii) Using the dominant IMFs reconstruct the time series and depict it in a frequency – energy plot (FEP) by superimposing its WT spectra; under the assumption of weak dissipation, this will reconstruct a portion of the FEP of the dynamics of the system under investigation; no *a priori* model is assumed for this reconstruction. (*global aspect of NSI*).
- (iv) Characterize and update the system parameters by matching the backbone branches of the FEPs with the frequency-energy dependence of the given system by using experimental/computational data. (*nonlinear model updating*).

At this point, it will be useful to provide some definitions of certain of the strongly nonlinear dynamical phenomena that will be addressed in this work. Starting from the definition of *internal resonance*: This denotes a strongly nonlinear energy transfer phenomenon, whereby two structural modes (even widely spaced in the frequency domain) become coupled by the system nonlinearity and start exchanging energy between them giving rise to *nonlinear beat phenomena* (Manevich and Manevitch 2005). In linear systems nonlinear beating can occur only when two modes possess closely spaced natural frequencies, whereas in nonlinear systems this is not necessary. Due to internal resonances, *mode-mixing* or *nonlinear modal interactions* can occur, whereby, with varying energy, a certain structural mode starts interacting with another structural mode in the form of a beat phenomenon, until the former mode is completely “transformed” to the latter. It follows that, when nonlinear mode mixing occurs, the dynamic response is composed of two (or more) structural modes coupled by the nonlinearity; depending on the frequencies of the “mixed modes” the overall response can be either time-periodic (for rational frequency ratios between modes) or quasi-periodic (for irrational frequency ratios) (Kerschen et al. 2008).

1.5 Organization

The organization of this dissertation will be as follows: In Chapter 2, the basic elements of the global/local nonlinear system identification, reduced order modeling and nonlinear model updating methodology considered in this dissertation will be introduced and discussed. Understanding and correctly utilizing these tools will prove to be crucial in the applications to be discussed later.

In Chapter 3, the local aspects of the proposed NSI methodology will be discussed and three main applications of the methodology will be presented: The first application will explore the nonlinear and non-smooth dynamics of a vibro-impact beam (Section 3.2). Then, the local NSI methodology will be applied to studying the effects of frictional connections in the dynamics of a bolted beam assembly (Section 3.3). As a final application, nonlinear system identification of a cantilever beam with an essentially (non-linearizable) nonlinear stiffness will be studied and the local NSI methodology will be extended to study strongly nonlinear beating phenomena (Section 3.4).

In Chapter 4, the global aspects of the NSI methodology will be discussed and some improvements made to the global NSI procedure will be presented. Frequency-energy plots (FEPs) will be used to extract information about the nonlinear characteristics (*e.g.*, location of the nonlinearity, nonlinearity order and coefficient) and the topology of dynamical systems (Section 4.2.1). Tracking the backbone branches of a 2-DOF system by simply using the experimental data will be demonstrated (Section 4.2.2). In Section 4.3, FEPs will be extended to study forced and damped systems and then applied to study the performance of an NES as a vibration absorber within predefined frequency ranges (Section 4.3.1.3) as well as the interesting and complicated dynamics of a 2-DOF system consisting of a grounded nonlinear

oscillator under harmonic forcing coupled to a light linear attachment under condition of 1:3 resonance (Section 4.3.2).

In Chapter 5, a novel nonlinear model updating strategy, which relies on analyzing the system in the frequency-energy domain by constructing Hamiltonian or forced and damped frequency – energy plots (FEPs) will be proposed, and two applications of the proposed methodology will be investigated. The first application will involve a system consisting of two cantilever beams, connected through an element which possesses softening/hardening behavior. By using the nonlinear model updating approach, the system will be modeled as a simple 2-DOF system, and the nonlinear connection will be identified (Section 5.2). The second application, a benchmark problem, consists of two cantilever beams connected through an “unknown” nonlinear element, will be studied using a similar approach (Section 5.3). Finally, in Chapter 6, the main points of this dissertation will be summarized, and some suggestions for future work and applications will be discussed.

CHAPTER 2

BASIC ELEMENTS OF THE NONLINEAR SYSTEM IDENTIFICATION (NSI) AND MODEL UPDATING METHODOLOGY

2.1 Slow Flow Dynamics (Lee et al. 2010a; Vakakis et al. 2011; Lee, Tsakirtzis, et al. 2009; Lee, Tsakirtzis, et al. 2011)

The *slow-flow model* of the dynamics of an n degree-of-freedom (DOF) dynamical system (e.g., $\dot{\mathbf{X}} = \mathbf{f}(\mathbf{X}, t)$, $\mathbf{X} = \{\mathbf{x}, \dot{\mathbf{x}}\} \in \mathbb{R}^{2n}$, $t \in \mathbb{R}$) is constructed by assuming that the dynamics possesses N distinct components at frequencies $\omega_1, \dots, \omega_N$, respectively, and expressing the response of each DOF as a summation of independent components

$$x_k(t) = x_k^{(1)}(t) + \dots + x_k^{(N)}(t), \quad k = 1, \dots, n \quad (2.1)$$

where $x_k^{(m)}(t)$ denotes the response of the k^{th} coordinate of (2.1) associated with the basic frequency ω_m with the ordering $\omega_1 > \dots > \omega_N$. We will denote these as *fast frequencies* of the problem. For each component of (2.1) we assign a new complex variable

$$\psi_k^{(m)}(t) = \dot{x}_k^{(m)}(t) + j\omega_m x_k^{(m)}(t) = \underbrace{\varphi_k^{(m)}(t)}_{\text{Slow-Flow}} \underbrace{e^{j\omega_m t}}_{\text{Fast-Flow}}, \quad m = 1, \dots, N \quad (2.2)$$

with $j = (-1)^{1/2}$, where a slow/fast partition of the dynamics in terms of the “slow” (complex) amplitude $\varphi_k^{(m)}(t)$ and the ‘fast’ oscillation $e^{j\omega_m t}$ was assumed. That such a partition holds is a central assumption in our methodology. Obviously, such a slow/fast partition is by no means unique or universal; yet at this point we will restrict our analysis to

measured signals that can be decomposed as in (2.1-2.2). Substituting (2.1-2.2) into the equations of motion and performing N averaging operations with respect to each of the fast frequencies yields a set of n complex differential equations that provides the slow flow of the system

$$\dot{\varphi}_k = \mathbf{F}_k(\varphi_1, \dots, \varphi_n), \quad \varphi_k = \{\varphi_k^{(1)}, \dots, \varphi_k^{(N)}\} \in C^N, \quad k = 1, \dots, n \quad (2.3)$$

The slow-flow (2.3) captures the slow modulations of the N harmonic components of each coordinate of the response. The number of fast frequencies, N , determines the dimensionality of the slow-flow.

2.2 Empirical Mode Decomposition (EMD) (Lee, Tsakirtzis, et al. 2009; Lee, Tsakirtzis, et al. 2011)

The second element of the proposed methodology is empirical mode decomposition (EMD) combined with the Hilbert Transform, which has been used previously for analyzing nonstationary and nonlinear time series and for nonlinear system identification and damage detection of structures (Yang et al. 2003a; Yang et al. 2003b; Yang et al. 2004). This decomposition identifies the characteristic time scales of a measured oscillatory time series, is adaptive, highly efficient, and especially suitable for nonlinear and nonstationary processes. In particular, EMD decomposes a measured time series $x_k(t)$ (following the previous notation, this is the response of the k^{th} coordinate of the considered dynamical system) into a nearly orthogonal basis of oscillatory intrinsic mode functions (IMFs). These are nearly mono-component oscillatory modes embedded in a measured time series $x_k(t)$, each with its own characteristic time scale (or fast frequency ω_m), whose linear superposition reconstructs the measured time series. (Lee et al. 2010b) applied the EMD method for reduced-order modeling of aeroelastic systems, whereas (Tsakirtzis et al. 2010) applied it to nonlinear

system identification of a linear continuum (rod) with a local essential stiffness nonlinearity.

The EMD algorithm (denoted as the sifting algorithm) consists of the following steps:

- (i) Identify all extrema of $x_k(t)$
- (ii) Interpolate minima and maxima of $x_k(t)$ by spline approximations, forming two envelopes $e_{min}(t)$ and $e_{max}(t)$, respectively
- (iii) Compute the average curve $R(t) = (e_{min}(t) + e_{max}(t))/2$
- (iv) Extract the remainder $c(t) = x_k(t) - R(t)$
- (v) Apply steps (i)-(iv) repetitively until the residual $R(t)$ becomes smaller than a prescribed tolerance tol

Once this criterion (through the sifting process) is met, the remainder $c(t) \equiv c_k^{(1)}(t)$ is regarded as the first, or highest-frequency, IMF of the measured time series. By subtracting this IMF from the original time series and applying the algorithm iteratively; that is to say, substituting $x_k(t) - \sum_{l=1}^m c_k^{(l)}(t)$ instead of $x_k(t)$ in (i) above for each step m , we extract additional IMFs, so that the original signal $x_k(t)$ is decomposed sequentially from high- to low-frequency into components as

$$x_k(t) = \sum_{l=1}^K c_k^{(l)}(t) + R_k^{(l+1)}(t), \quad R_k^{(l+1)}(t) < tol \quad (2.4a)$$

Hence, the original time series can be reconstructed by superposition of the K leading IMFs; however, only a subset of these IMFs is physically meaningful. A comparison of wavelet transforms of the original time series and the computed nearly mono-component IMFs is necessary to identify the dominant (*i.e.*, physically-meaningful) IMFs. Given that EMD is

applied to a time series obtained from a physical coordinate of our dynamical system in Section 2.1, the decomposition in terms of dominant IMFs finally yields

$$x_k(t) = c_k^{(1)}(t) + c_k^{(2)}(t) + \dots + c_k^{(N)}(t) \quad (2.4b)$$

where $c_k^{(m)}(t)$ is the m^{th} dominant nearly mono-component IMF of the response $x_k(t)$ associated with the fast frequency ω_m .

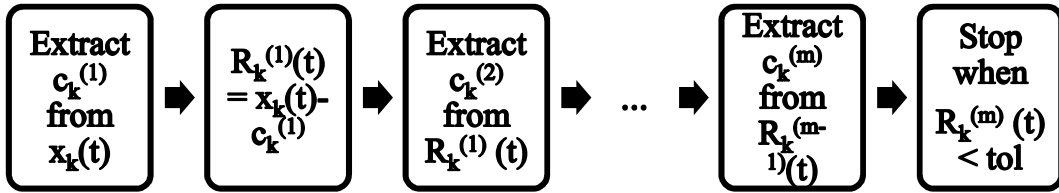


Figure 2.1 Step-by-step description of the EMD method

Given that EMD is applied in an *ad hoc* manner, it has certain deficiencies, related to issues such as uniqueness of the EMD results, and lack of orthogonality between the computed IMFs (Vakakis et al. 2011). These issues can be addressed through the use of masking and mirror-image signals (Lee, Tsakirtzis, et al. 2009; Lee, Tsakirtzis, et al. 2011) that lead to well-decomposed, nearly mono-chromatic and orthogonal sets of IMFs. The resulting “step-by-step” EMD method is summarized in Fig. 2.1. In short, instead of applying the EMD method all at once, we start by extracting the first IMF out of the given time signal, $x_k(t)$ and treat each remainder as our new time signal. This can be summarized as follows:

$$\begin{aligned}
 R_k^{(1)}(t) &= x_k(t) - c_k^{(1)}(t) \\
 &\vdots \\
 R_k^{(m)}(t) &= R_k^{(m-1)}(t) - c_k^{(m)}(t), R_k^{(m)}(t) < tol
 \end{aligned} \quad (2.5)$$

A final issue concerns the lack of a theoretical foundation for the derived near-orthogonal basis of the IMFs, so the next element of the proposed NSI methodology needs to address this by providing a link between the theoretical slow flow discussed in Section 2.1 and the numerically derived IMFs discussed herein.

2.3 Correspondence Between Theoretical and Empirical Slow Flows (Lee, Tsakirtzis, et al. 2011)

To formulate the correspondence between slow flows and IMFs derived by EMD we shift the analysis to the complex plane. For the slow flow this was performed through relation (2.2) for the response x_k of the k^{th} coordinate of the dynamical system. To perform a similar complexification of the dominant IMFs in (2.4b) we employ the Hilbert transform, complexifying the m^{th} IMF $c_k^{(m)}(t)$ of the measured signal $x_k(t)$ through the relation

$$\hat{\psi}_k^{(m)}(t) \equiv c_k^{(m)}(t) + j\mathcal{H}\left[c_k^{(m)}(t)\right] \quad (2.6)$$

where $\mathcal{H}[\bullet]$ represents the Hilbert transform. This leads to estimates of the instantaneous amplitude and phase of the m^{th} IMF

$$\hat{A}_k^{(m)}(t) = \left\{ c_k^{(m)^2}(t) + \mathcal{H}\left[c_k^{(m)}(t)\right]^2 \right\}^{1/2}, \quad \tan \hat{\theta}_k^{(m)}(t) = \mathcal{H}\left[c_k^{(m)}(t)\right] / c_k^{(m)}(t) \quad (2.7)$$

from which the *instantaneous frequency* of the IMF is computed as $\hat{\omega}_k^{(m)}(t) = \dot{\hat{\theta}}_k^{(m)}(t)$. This leads to the slow-fast representation of the complexified IMF (5)

$$\hat{\psi}_k^{(m)}(t) \equiv \underbrace{\hat{A}_k^{(m)}(t)}_{\text{'Slow' component}} e^{j\hat{\theta}_k^{(m)}(t)} = \underbrace{\hat{A}_k^{(m)}(t)}_{\text{'Slow' component}} e^{j[\hat{\theta}_k^{(m)}(t) - \omega_k^{(m)}t]} \underbrace{e^{j\omega_k^{(m)}t}}_{\text{'Fast' component}} \quad (2.8)$$

We note that this is in the same form as the complexification (2.2) introduced in the slow flow construction in Section 2.1. This provides a *direct* way to relate the IMFs to the slow flow dynamics and physically interpret the dominant IMFs in terms of the slow flow dynamics.

In summary, we relate the theoretical slow flow decomposition of Section 2.1 and the extracted IMFs by EMD of the response of the k^{th} coordinate by the two expansions

Slow flow:

$$x_k(t) = x_k^{(1)}(t) + \dots + x_k^{(N)}(t), \quad \psi_k^{(m)}(t) = \dot{x}_k^{(m)}(t) + j\omega_m x_k^{(m)}(t) \equiv \underbrace{\varphi_k^{(m)}(t)}_{\text{'Slow' component}} \underbrace{e^{j\omega_m t}}_{\text{'Fast' component}} \quad (2.9a)$$

EMD:

$$x_k(t) = c_k^{(1)}(t) + \dots + c_k^{(N)}(t), \quad \hat{\psi}_k^{(m)}(t) \equiv c_k^{(m)}(t) + j \mathcal{H}[c_k^{(m)}(t)] = \underbrace{\hat{A}_k^{(m)}(t)}_{\text{'Slow' component}} e^{j[\hat{\theta}_k^{(m)}(t) - \omega_k^{(m)}t]} \underbrace{e^{j\omega_k^{(m)}t}}_{\text{'Fast' component}} \quad (2.9b)$$

Given that (2.9a) and (2.9b) represent identical expansions of the same measured time series it holds that $\omega_k^{(m)} \approx \omega_m$ for $m = 1, \dots, N$, where N is the number of dominant harmonic components in the slow flow decomposition of the dynamics (*i.e.*, the dimensionality, or the number, of significant frequency-time scales in the dynamics). This implies the correspondence between the theory and measurement (Lee, Tsakirtzis, et al. 2011)

$$\underbrace{x_k^{(m)}(t)}_{\text{Theory}} \rightarrow \underbrace{c_k^{(m)}(t)}_{\text{Measurement}}, \quad k = 1, \dots, n, \quad m = 1, \dots, N \quad (2.10)$$

Noting that the complexification (2.6) is different than the corresponding complexification (2.2) for the slow flow analysis in Section 2.1, we introduce the alternative complexification

$$\hat{\psi}_k^{(m)}(t) = \dot{c}_k^{(m)}(t) + j\omega_m c_k^{(m)}(t) \equiv \underbrace{\hat{\varphi}_k^{(m)}(t)}_{\text{'Slow' part}} \underbrace{e^{j\omega_m t}}_{\text{'Fast' part}} = \underbrace{\hat{A}_k^{(m)}(t)}_{\text{'Slow' part}} e^{j[\hat{\theta}_k^{(m)}(t) - \omega_m t]} \underbrace{e^{j\omega_m t}}_{\text{'Fast' part}} \quad (2.11)$$

Where $\hat{\psi}_k^{(m)}(t) = \hat{A}_k^{(m)}(t) e^{j\hat{\theta}_k^{(m)}(t)}$. In terms of the complexification (2.8) it holds that $\hat{\psi}_k^{(m)}(t) = (j\omega_m)^{-1} \hat{\psi}_k^{(m)}(t)$. We conclude that the correspondence between the theoretical and measured complexifications can be shown to be

$$\psi_k^{(m)}(t) \rightarrow \hat{\psi}_k^{(m)}(t) = j\omega_m \hat{\psi}_k^{(m)}(t) \Rightarrow \underbrace{\phi_k^{(m)}(t) \rightarrow j\omega_m \hat{A}_k^{(m)}(t) e^{j[\hat{\theta}_k^{(m)}(t) - \omega_m t]}}_{\text{Equivalence of 'slow' complex amplitudes}} \quad (2.12)$$

This final relation provides a *physics-based theoretical foundation for EMD*, whereby the dominant IMFs represent the underlying slow flow of the dynamics and, hence, capture all the important (multi-scale) dynamics. This correspondence between analytical and measured slow flows will be the foundation of the reduced-order modeling of the local dynamics. The standard EMD often cannot separate distinct frequency components, especially when these components are closely spaced to each other (that is, when their ratios are between 0.5 and 2). However, the use of masking signals (Deering and Kaiser 2005), and heterodyning (Senroy and Suryanarayanan 2007) can greatly enhance EMD's capacity to separate distinct frequency components.

2.4 Reduced Order Models: Intrinsic Modal Oscillators – IMOs (Lee et al. 2010a; Vakakis et al. 2011; Lee, Tsakirtzis, et al. 2011)

Based on the previous formulation and results one can construct local reduced-order models that capture the transient dynamics of the dynamical system. To this end, intrinsic modal oscillators (IMOs) were introduced in the form of forced linear oscillators that reproduce a measured time series over different time scales. Since many structural dynamics problems involve slowly-modulated oscillatory responses, a linear, damped oscillator with a forcing function containing all modal interactions and nonlinearity is an obvious candidate for reproducing the m -th dominant IMF in the form

$$\ddot{x}_k^{(m)}(t) + 2\lambda_k^{(m)}\omega_m \dot{x}_k^{(m)}(t) + \omega_m^2 x_k^{(m)}(t) = F_k^{(m)}(t), \quad k = 1, \dots, n, \quad m = 1, \dots, N \quad (2.13)$$

We note that this model is based on the central assumption that the fast frequencies of the measured time series are well-separated. The time-dependent forcing term can be written in terms of slow/fast partitions of all dominant fast frequencies in the general form

$$F_k^{(m)}(t) = \text{Re} \left\{ \Lambda_k^{(1)}(t) e^{j\omega_1 t} + \Lambda_k^{(2)}(t) e^{j\omega_2 t} + \dots + \Lambda_k^{(m)}(t) e^{j\omega_m t} + \dots + \Lambda_k^{(N)}(t) e^{j\omega_N t} \right\} \quad (2.14)$$

where the forcing amplitudes $\Lambda_k^{(m)}$ are slowly varying complex modulations of the corresponding fast oscillations $e^{j\omega_m t}$. However, we note that since the IMOs constitute a set of linear oscillators with well-separated natural frequencies, only forcing terms with fast frequencies identical to the natural frequencies of the IMOs can cause significant responses to the IMOs. It follows that the IMO equations simplify to

$$\begin{aligned} \ddot{x}_k^{(m)}(t) + 2\lambda_k^{(m)}\omega_m \dot{x}_k^{(m)}(t) + \omega_m^2 x_k^{(m)}(t) &= F_k^{(m)}(t) \equiv \text{Re} \left\{ \Lambda_k^{(m)}(t) e^{j\omega_m t} \right\}, \\ k &= 1, \dots, n, \quad m = 1, \dots, N \end{aligned} \quad (2.15)$$

Using the complexification introduced in (2.2), we express

$$x_k^{(m)}(t) = \frac{\phi_k^{(m)}(t) e^{j\omega_m t} - \bar{\phi}_k^{(m)}(t) e^{-j\omega_m t}}{2j\omega_m} \quad (2.16)$$

and apply averaging with respect to the fast frequency ω_m to compute the slowly varying complex forcing amplitude

$$\Lambda_k^{(m)}(t) \approx 2 \left[\dot{\phi}_k^{(m)}(t) + \lambda_k^{(m)}\omega_m \phi_k^{(m)}(t) \right] \quad (2.17)$$

Finally, we use the equivalence of slowly-varying analytical and experimental slow modulations (2.12), to express the forcing amplitudes in terms of quantities that can be directly identified by post-processing the measured time series

$$\Lambda_k^{(m)}(t) \approx 2 \left[\frac{d}{dt} \left(j \omega_m A^{(m)}(t) e^{j[\theta^{(m)}(t) - \omega_m t]} \right) + j \lambda_k^{(m)} \omega_m^2 A^{(m)}(t) e^{j[\theta^{(m)}(t) - \omega_m t]} \right] \quad (2.18)$$

In this relation the instantaneous amplitude and phase can be computed directly from the measured data using the correspondence (2.12) as $A^{(m)}(t) = |\hat{\psi}^{(m)}(t)|$ and $\theta^{(m)}(t) = \angle \hat{\psi}^{(m)}(t)$. The damping ratio of the IMO is the only parameter that needs to be evaluated by minimizing the difference between the measured and reproduced time series based on (2.15).

The complex forcing amplitudes $\Lambda_k^{(i)}(t)$ of the IMOs contain essential information about the slow-flow dynamics of the modal coordinates and nonlinear interactions between the multi-scale dynamics. If we take the natural logarithm of the expression (2.17)'s amplitude, we obtain

$$\ln |\Lambda_k^{(i)}(t)| \approx C_k^{(i)}(\lambda_k^{(i)}, \omega_i, \zeta_i, F_i) - \zeta_i \omega_i t, \quad k=1, \dots, N, \quad i=1, \dots, M \quad (2.19)$$

In this notation ζ_i is the modal damping of the i -th mode, ω_i is the i -th modal (fast) frequency, F_i is the impulse amplitude acting at the i -th mode, and, $\lambda_k^{(i)}$ is the damping ratio of the i -th IMO of the response at the k -th sensing position. The real coefficient $C_k^{(i)}(\lambda_k^{(i)}, \omega_i, \zeta_i, F_i)$ can be assumed to be constant with respect to time (in actuality it is an oscillatory function due to fast oscillatory components, but a low pass filter can remove these oscillations). It follows that *linear temporal decay of the logarithm of the magnitude of the complex forcing amplitude of an IMO indicates linear dynamic behavior of that mode*, with the corresponding rate of decay being approximately equal to the viscous modal damping ratio. Moreover, based on this finding, we may state that *any deviation from linear decay of the temporal plot of the logarithm of the magnitude of the complex forcing of an IMO with respect to time is representative of nonlinear dynamical behavior of that mode*.

Examples and applications of the outlined NSI methodology were given in (Lee et al. 2010a; Vakakis et al. 2011; Lee, Nucera, et al. 2009; Lee, Tsakirtzis, et al. 2011; Lee et al. 2010b; Tsakirtzis et al. 2010; Kurt et al. 2012; Eriten et al. 2013), together with a discussion of an additional component of the method involving global identification of the dynamics in the frequency – energy domain. Starting from the next Section we consider the main problem addressed in this work; namely, the study and identification of strongly nonlinear beat phenomena in a linear flexible beam with a strong nonlinearity at its free end, and discuss how the previous NSI methodology can be extended to account for this type of strongly nonlinear dynamics.

2.5 Spatio-Temporal IMOs

Spatio-temporal IMOs are the extensions of the reduced order model IMOs, discussed in 2.4, to the continuous spatial domain. Let's consider the dynamical response of a system in the spatio-temporal domain and denote it as $\alpha(x, t)$. The response can be decomposed into its slowly varying amplitude and fast component as follows.

$$\alpha(x, t) \approx \sum_{m=1}^N W_m(x, t) e^{j\omega_m t} \quad (2.20)$$

where $W_m(x, t)$ is a slowly-varying amplitude satisfying the spatio-temporal IMO

$$\frac{\partial^2 W_m(x, t)}{\partial t^2} + 2\hat{\zeta}_m \omega_m \frac{\partial W_m(x, t)}{\partial t} + \omega_m^2 W_m(x, t) \approx \text{Re} \left[\Lambda_m(x, t) e^{j\omega_m t} \right] \quad (2.21)$$

The nonlinear modal interaction term can be obtained in terms of the corresponding spatio-temporal slow flow such that $\Lambda_m(x, t) \approx 2 \left[\dot{\phi}_m(x, t) + \hat{\zeta}_m \omega_m \phi_m(x, t) \right]$

where $\varphi_m(x, t) = \hat{A}_m(x, t) \exp\left[j\left(\hat{\theta}_m(x, t) - \omega_m t\right)\right]$, and $\hat{A}_m(x, t) = \sqrt{W_m(x, t)^2 + \mathcal{H}[W_m(x, t)]^2}$,
 $\hat{\theta}_m(x, t) = \tan^{-1}[\mathcal{H}[W_m(x, t)]/W_m(x, t)]$.

By using spatio-temporal IMOs, one can obtain substantial information regarding the effects of the nonlinearities on the particular mode shapes. Since they depict the evolution of the mode shapes in the time domain, one can observe how the underlying linear mode shape changes as the system response become nonlinear. These properties make them useful tools in both local and global nonlinear system identification since the study of spatio-temporal IMOs reveals the time/energy level at which the nonlinear effects start to dominate the system response.

2.6 Frequency-Energy Plots

NNMs were defined as vibrations-in-unison of dynamical systems starting from the seminal works of Rosenberg (Rosenberg 1960; Rosenberg 1962), and were proposed in (Kerschen et al. 2009; Peeters et al. 2009) as a way to extend experimental modal analysis to the nonlinear regime. The appropriate graphical depiction of NNMs is key to their exploitation. In this dissertation, extensive use will be made of frequency-energy plots (FEPs) where the amplitude of a NNM is plotted as function of its (conserved) energy.

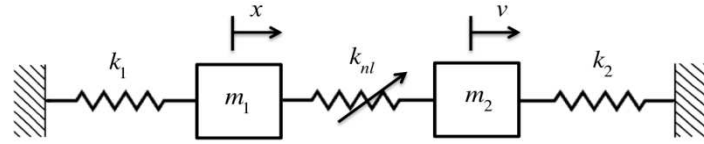
A very useful feature of the FEP for system identification purposes is its relation to the transient dynamics of the corresponding weakly damped system. This is due to the fact that *the effect on the dynamics of weak damping is parasitic*. Instead of introducing “new” dynamics, it just causes transitions of the dynamics between branches of normal modes leading to multi-frequency nonlinear dynamical transitions. It follows that *different initial or*

forcing conditions may lead to drastically different transitions in the FEP. To construct the FEP, we compute the periodic orbits of the Hamiltonian system for different initial conditions. This can be done analytically for systems with few degrees-of-freedom (Kurt, Eriten, et al. 2014b); however, due to the complexity of the equations, advanced computational tools have been developed (*e.g.*, shooting method (Peeters et al. 2009), harmonic balance method (Detroux et al. 2014)) to find NNMs.

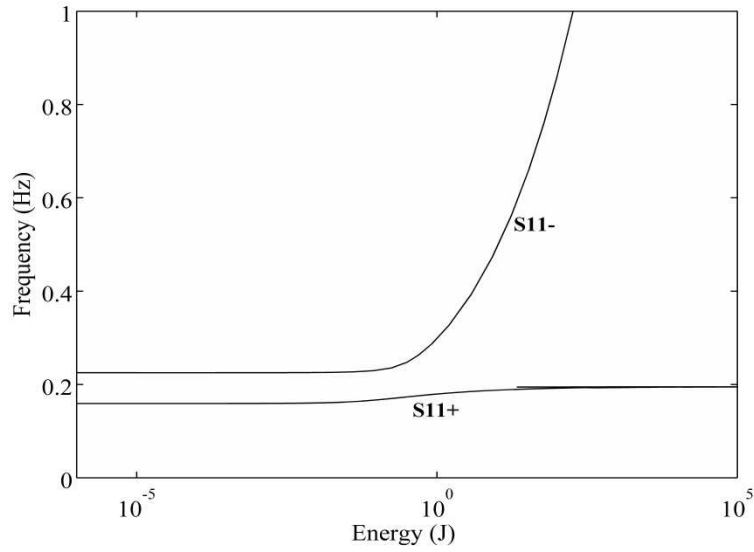
To have a basic understanding of the frequency-energy plots, we consider the 2-DOF system depicted in Figure 2.2a, which has the equations of motion

$$\begin{aligned} m_1 \ddot{x} + k_1 x + k_{nl} (x - v)^3 &= 0 \\ m_2 \ddot{v} + k_2 v + k_{nl} (v - x)^3 &= 0 \end{aligned} \tag{2.22}$$

where the system parameters are $m_1 = m_2 = 1$ kg, $k_1 = 2$ N/m, $k_2 = 1$ N/m, $k_{nl} = 1$ N/m³. In Figure 2.2b, we depict the FEP of the 2-DOF system, computed by NNMcont (Peeters et al. 2009). There are two branches of nonlinear normal modes for this system denoted as *backbone branches*. These branches are labeled $S11 \mp$ since they correspond to in-phase (+ sign) and out-of-phase (− sign) synchronous oscillations of the two masses of (2.22) with both degrees of freedom oscillating with identical frequencies; *i.e.*, they satisfy the condition of 1:1 internal resonance between the two degrees of freedom of the system (2.22). The notation $Smn \pm$ denotes a time-periodic motion of system (2.22) with n being the number of half-waves in x , m the number of half-waves in v , both in a half-period of the response, and (\pm) denotes the in-phase or out-of-phase character of the oscillations. Note that, for low energies, the frequencies of the in-phase and out-of phase modes are almost constant, which correspond to the linear regimes.



(a)



(b)

Figure 2.2 (a) 2-DOF system consisting of two linear oscillators coupled with a nonlinear cubic spring
 (b) FEP of the 2-DOF system for parameters $m_1 = m_2 = 1$ kg, $k_1 = 2$ N/m, $k_2 = 1$ N/m, $k_{nl} = 1$ N/m³.

CHAPTER 3

LOCAL ASPECTS OF THE NSI METHODOLOGY

3.1 Introduction and Background Information

In this chapter, the local aspects of the proposed NSI methodology will be discussed, and some applications of the methodology will be presented. Different techniques are combined to formulate the local aspects of the proposed methodology, and these are shown in the chart of Figure 3.1. The basic elements of the local aspect of the methodology are: (i) construction of slow flow models (analytical part); (ii) empirical mode decomposition combined with Hilbert transform (numerical part); (iii) correspondence between the analytical and numerical parts; (iv) construction of local reduced-order models (IMOs) that capture the transient dynamics of the dynamical system. Note that these concepts were discussed in great detail in Chapter 2.

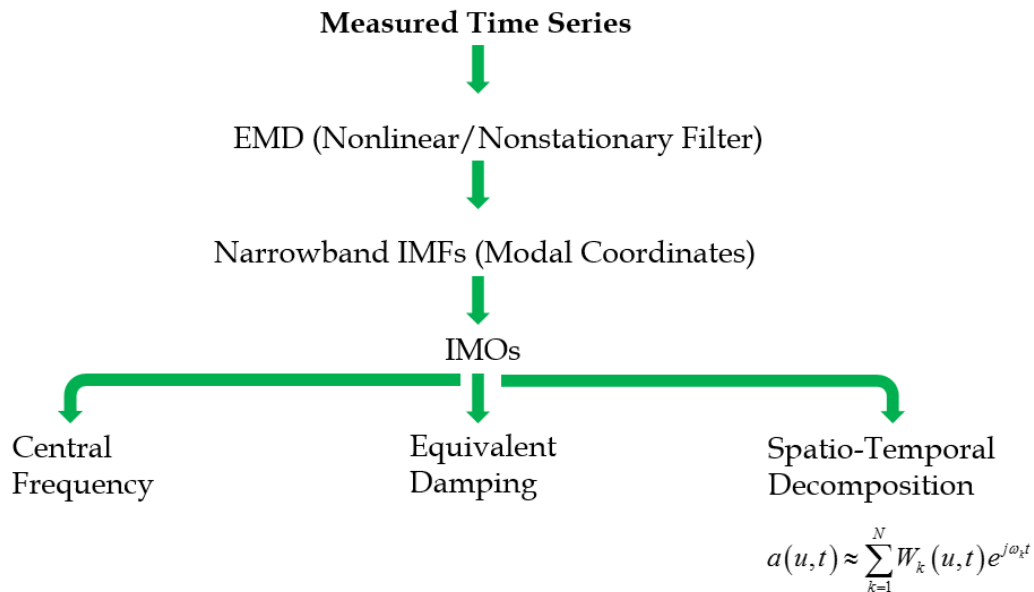


Figure 3.1 General outline of the local NSI approach

Figure 3.1, represents the main steps for the application of the local NSI methodology. Since the proposed methodology promises to be solely based on direct analysis of measured time series, the application of the local aspect starts there as well. Then, through EMD, the time series is decomposed into nearly orthogonal modes, IMFs. The next step is to construct intrinsic modal oscillators (IMOs), which were introduced in the form of forced linear oscillators that reproduce a measured time series over different time scales. By using the nonlinear modal interaction terms (see Section 2.4), one can obtain important information regarding the local dynamics of the system, such as central frequencies, equivalent damping values and mode shapes (by using spatio-temporal IMOs).

As an example of a local NSI application of this methodology, we consider a two-DOF linear system of coupled oscillators, which provides us with the added advantage of comparing the methodology to linear modal analysis. The governing equations of motion are given by

$$\mathbf{M}\ddot{\mathbf{X}}(t) + \mathbf{C}\dot{\mathbf{X}}(t) + \mathbf{K}\mathbf{X}(t) = \mathbf{F}(t), \quad \mathbf{X}(t) = [x_1(t) \ x_2(t)]^T \quad (3.1)$$

where, $\mathbf{M} = \begin{bmatrix} m_1 & 0 \\ 0 & m_2 \end{bmatrix}$, $\mathbf{K} = \begin{bmatrix} k_1 + k_c & -k_c \\ -k_c & k_2 + k_c \end{bmatrix}$, and $\mathbf{C} = \alpha \mathbf{M} + \beta \mathbf{K}$. Note that we assume proportional damping so that we can construct the real modal equations that will better illustrate the main motivation behind our technique. Indeed, transforming (3.1) to modal equations, we express this system as

$$\ddot{r}_i + 2\zeta_i \omega_i \dot{r}_i + \omega_i^2 r_i = f_i(t), \quad i = 1, 2 \quad (3.2)$$

where $\zeta_i = \frac{\alpha}{2\omega_i} + \frac{\beta\omega_i}{2}$. Further, we assume that the natural frequencies of the system are nonzero and well separated. The modal responses are found to be

$$r_i(t) = A_i e^{-\zeta_i \omega_i t} \sin(\omega_{di} t + \phi_i) + \omega_{di}^{-1} e^{-\zeta_i \omega_i t} \int_0^t f_i(\tau) e^{\zeta_i \omega_i \tau} \sin(\omega_{di}(t-\tau)) d\tau, \quad \omega_{di} = \omega_i (1 - \zeta_i^2)^{1/2}, \quad i = 1, 2 \quad (3.3)$$

Therefore, the responses of the system can be computed as the superposition of the two modal responses, so each response is the summation of the two distinct modes at different time scales (frequencies) of the dynamics; thus, application of EMD yields two IMFs, each corresponding to a modal response. For example, considering the response $x_1(t)$, we may decomposed it as

$$x_1(t) = x_1^{(1)}(t) + x_1^{(2)}(t) \approx c_1^{(1)}(t) + c_1^{(2)}(t) \quad (3.4)$$

where $x_1^{(i)}(t)$ and $c_1^{(i)}(t)$, $i = 1, 2$ are the i -th harmonic component and corresponding IMF, respectively, of the response $x_1(t)$ [with similar decomposition for $x_2(t)$] with

$$\begin{aligned} c_1^{(1)}(t) \approx x_1^{(1)}(t) &= \frac{u_{11}}{\sqrt{m_1}} \left[A_1 e^{-\zeta_1 \omega_1 t} \sin(\omega_{d1} t + \phi_1) + \frac{1}{\omega_{d1}} \int_0^t f_1(t-\tau) e^{-\zeta_1 \omega_1 \tau} \sin(\omega_{d1} \tau) d\tau \right] \\ c_1^{(2)}(t) \approx x_1^{(2)}(t) &= \frac{u_{21}}{\sqrt{m_1}} \left[A_2 e^{-\zeta_2 \omega_2 t} \sin(\omega_{d2} t + \phi_2) + \frac{1}{\omega_{d2}} \int_0^t f_2(t-\tau) e^{-\zeta_2 \omega_2 \tau} \sin(\omega_{d2} \tau) d\tau \right] \end{aligned} \quad (3.5)$$

and u_{ij} are appropriately defined modal constants. At this point, we assume that system (3.1) is excited by impulses, $\mathbf{F}(t) = [F_1 \delta(t) \quad F_2 \delta(t)]^T$, and express the response $x_1(t)$ through the complexification-averaging approach discussed in section 2.1. To this end, we introduce the complex variables

$$\begin{aligned} \varphi_1^{(1)}(t) e^{j\omega_1 t} &\equiv \dot{x}_1^{(1)}(t) + j\omega_1 x_1^{(1)}(t) \\ \varphi_1^{(2)}(t) e^{j\omega_2 t} &\equiv \dot{x}_1^{(2)}(t) + j\omega_2 x_1^{(2)}(t) \end{aligned} \quad (3.6)$$

with ω_i , $i = 1, 2$ the two ‘fast frequencies’ and $\varphi_1^{(i)}(t)$, $i = 1, 2$ the two slow amplitude modulations of the harmonic components. Substituting (3.6) into (3.1) and performing

averaging separately with respect to each of the two fast frequencies, we obtain the complex forcing amplitudes $\Lambda_1^{(i)}(t)$, $i=1,2$ of the two corresponding IMOs, as explained in Section 2.4. As in the majority of applications in structural dynamics, we assume that modal damping is small, giving that $\omega_{di} \approx \omega_i$. With the added assumption that the damping coefficients in the IMOs are much larger than the modal dampings, $\lambda_1^{(i)} \gg \zeta_i$ (this assumption is required in order to match the IMO responses with the extracted IMFs), we can approximate the forcing amplitudes $\Lambda_1^{(i)}(t)$, $i=1,2$ as

$$\begin{aligned}\Lambda_1^{(i)}(t) &\approx 2\left[\dot{\phi}_1^{(i)}(t) + \lambda_1^{(i)}\phi_1^{(i)}(t)\right], \quad i=1,2 \Rightarrow \\ \ln|\Lambda_1^{(1)}(t)| &\approx C_1^{(1)}(\lambda_1^{(1)}, \omega_1, \zeta_1, F_1) - \zeta_1\omega_1 t \\ \ln|\Lambda_1^{(2)}(t)| &\approx C_1^{(2)}(\lambda_1^{(2)}, \omega_2, \zeta_2, F_2) - \zeta_2\omega_2 t\end{aligned}\tag{3.7}$$

In these expressions the (real) coefficients $C_1^{(1)}$ and $C_1^{(2)}$ are functions that do not depend on time, which means that the slopes of the quantities $\ln|\Lambda_1^{(i)}(t)|$ are computed simply by the negative of the product of the modal damping and fast frequency of each mode. Note, however, that this result is based on the previous assumptions and under impulsive excitation of system (3.1).

As a numerical example, we consider the parameters

$$\begin{aligned}k_1 = k_2 = k = 1, \quad k_c = 4k = 4, \quad m_1 = m_2 = m = 1, \\ \alpha = 0.006, \quad \beta = 0.002, \quad F(t) = [5\delta(t) \quad 0]^T\end{aligned}\tag{3.8}$$

The two harmonic components of the response $x_1(t)$ are computed as

$$\begin{aligned}c_1^{(1)}(t) \approx x_1^{(1)}(t) &= \frac{1}{\sqrt{2m}} \left[e^{-\zeta_1\omega t} \sin(\omega_d t) + \frac{F}{\omega_d} e^{-\zeta_1\omega t} \sin(\omega_d t) \right] \\ c_1^{(2)}(t) \approx x_1^{(2)}(t) &= \frac{1}{\sqrt{2m}} \left[e^{-\zeta_2 3\omega t} \sin(3\omega_d t) \right]\end{aligned}\tag{3.9}$$

In Figure 3.2, we depict the above monochromatic components together with their wavelet transforms. These can be regarded as the identified IMFs of the signal $x_1(t)$ which, due to the simplicity of the linear system under consideration, are evaluated in closed form. Based on these IMFs we construct a set of IMO in the form (2.15) with their forcing terms $\Lambda_1^{(i)}(t)$, $i=1,2$ evaluated in terms of the IMFs through relations (2.18).

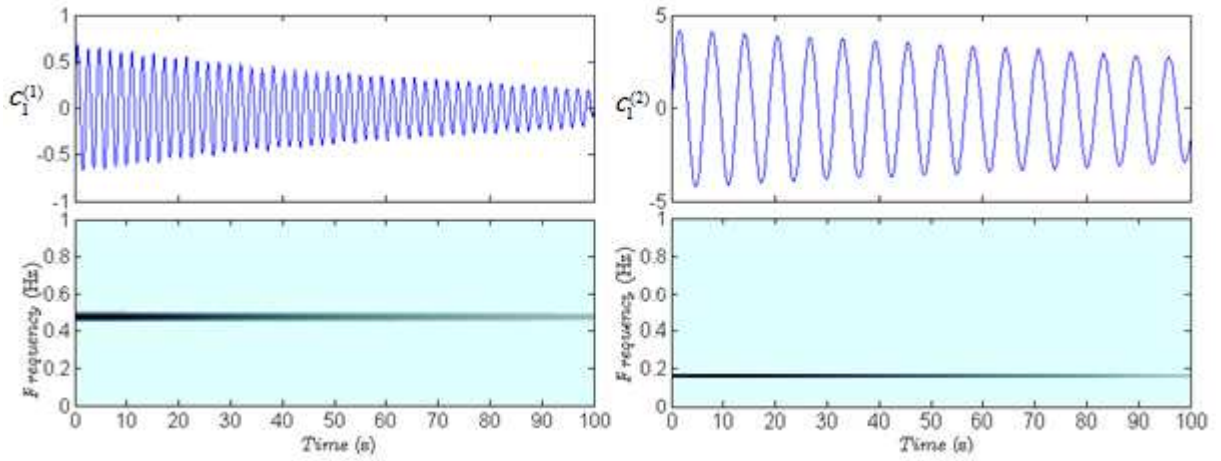


Figure 3.2 The two IMFs of the response $x_1(t)$.

Focusing on the complex amplitudes of the forcing terms of the IMO in Figure 3.3, we compare the logarithms of their moduli $\ln|\Lambda_1^{(i)}(t)|$, $i=1,2$ to the analytical result (3.7), with the coefficients $C_1^{(1)}$ and $C_1^{(2)}$ selected to match the two results. We note that the slopes predicted by our analysis are in agreement with the actual plots of $\ln|\Lambda_1^{(i)}(t)|$, exhibiting linearly decaying behavior with superimposed small-amplitude oscillations; however, after these higher-frequency oscillations are averaged out, there is agreement between the two sets of results. Hence, *the linearly decaying responses of $\ln|\Lambda_1^{(i)}(t)|$ provide clear signatures of the*

linear dynamics of the system, so deviations from this behavior indicates the presence of nonlinear dynamical effects.

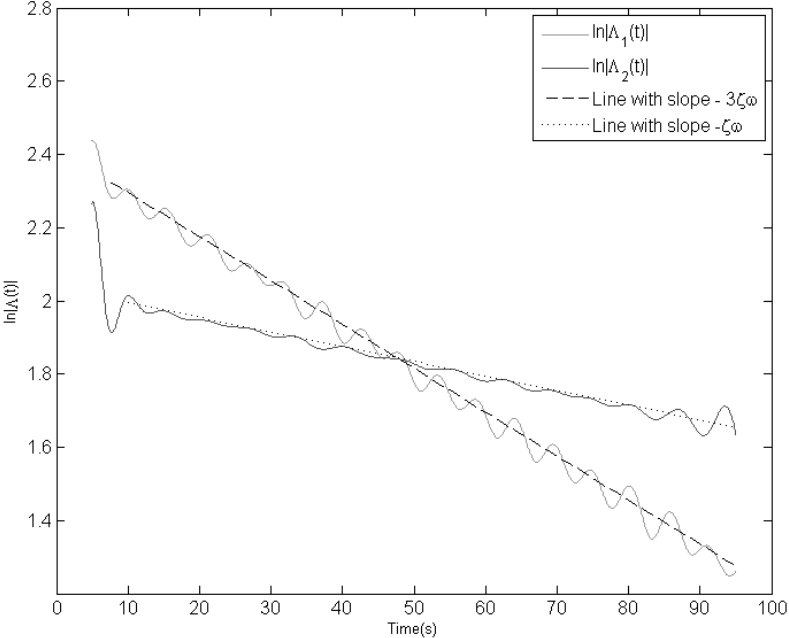


Figure 3.3 Comparison of $\ln|\Lambda_i^{(i)}(t)|$, $i = 1, 2$ with the analytical prediction (18) for the response $x_1(t)$.

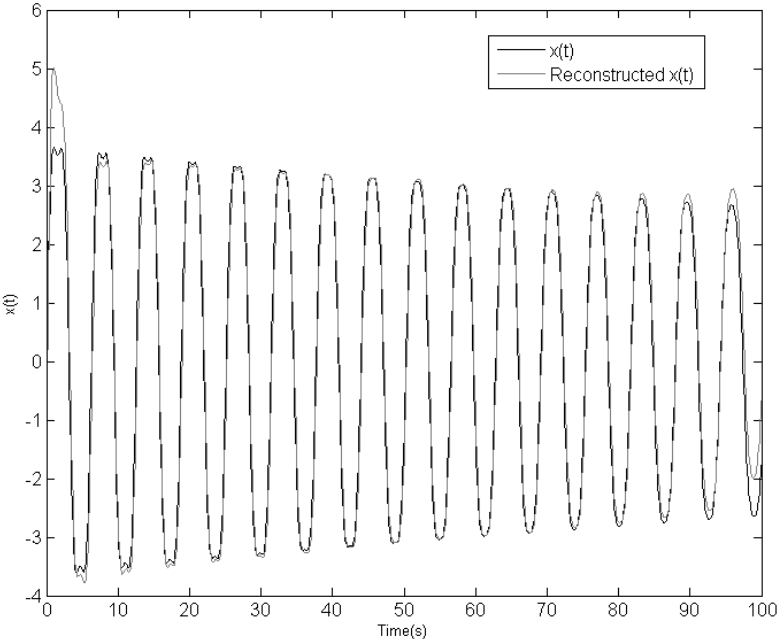


Figure 3.4 Exact and reconstructed (through IMOs) time series for the response $x_1(t)$.

In Figure 3.4, we depict the exact signal $x_1(t)$ and the reconstructed time series by superposition of the two IMO responses, indicating the capability of the method to reconstruct the given time series with no *a priori* assumptions about the system itself. Note that there is a slight mismatch between the reconstructed and exact time series at the beginning of the signal, but this discrepancy is dissipated quickly by the damping of the IMO when optimized properly.

In Section 3.2, we will study the application of our NSI methodology to non-smooth dynamics of a vibro-impact beam. We study the dynamics of a cantilever beam with two rigid stops of certain clearances by performing nonlinear system identification (NSI) based on the correspondence between analytical and empirical slow-flow dynamics. In Section 3.3, we move to study damping nonlinearities as we investigate the effects of frictional connections in the dynamics of a bolted beam assembly. Finally, in Section 3.4, we consider a linear cantilever beam attached to ground through a strongly nonlinear stiffness at its free boundary and identify the type of strongly nonlinear modal interactions in the dynamics of the system.

3.2 NSI of the Dynamics of a Vibro-Impact Beam (Kurt et al. 2012; H. Chen et al. 2014)

3.2.1 Introduction and System Description

In this section, we explore the nonlinear dynamics of a VI beam (whose setup is similar to that used in (Azeez and Vakakis 2001)) using this NSI method (Lee et al. 2010a) to reveal *coherent* structures (e.g., (Dawes 2010)) in terms of IMO of strongly nonlinear dynamics due to vibro-impacts. Study of such systems will provide essential dynamical features of structures with defects in applications to structural health monitoring and damage detection (e.g., (Chati, Rand, and Mukherjee 1997; H. G. Chen, Yan, and Jiang 2007)). The dynamics of a cantilever beam with two rigid stops of certain clearances will be investigated by performing nonlinear system identification (NSI) based on the correspondence between analytical and empirical slow-flow dynamics. The NSI method in this work can proceed in two directions: One for the numerical data obtained from a reduced-order model by means of the assumed-modes method, and the other for experimental data measured at the same positions as indicated in the numerical simulations. This work focuses on the analysis of the numerical data, providing qualitative comparison with some experimental results. First, we perform empirical mode decomposition (EMD) on the acceleration responses at ten, almost evenly-spaced, spanwise positions along the beam leading to sets of intrinsic modal oscillators governing the vibro-impact dynamics at different time scales. In particular, the EMD analysis can separate nonsmooth effects caused by vibro-impacts between the beam and the rigid stops from the smooth (elastodynamic) response so that nonlinear modal interactions caused by vibro-impacts can be explored only with the remaining smooth components. Then, we establish nonlinear interaction models (NIMs) for the respective intrinsic modal oscillators, where the NIMs invoke slowly-varying forcing amplitudes that can be computed from empirical slow-flows. By comparing the spatio-temporal variations of nonlinear modal

interactions for the vibro-impact beam and the underlying linear model (*i.e.*, the beam with no rigid constraints), we demonstrate that vibro-impacts significantly influence the lower frequency modes introducing spatial modal distortions, whereas the higher frequency modes tend to retain their linear dynamics between impacts. We compute the linear correlation coefficient as a measure of linear dependence between the slowly-varying complex forcing amplitudes for the linear and vibro-impact beams, and demonstrate that only the several lower-frequency modes are strongly influenced by vibro-impacts, capturing most of the essential nonlinear dynamics. These results demonstrate the efficacy of the proposed approach to analyze strongly nonlinear measured time-series.

We consider the uniform, homogeneous cantilever beam (made of steel with density $\rho = 7850 \text{ kg/m}^3$ and Young's modulus $E = 200 \text{ GPa}$) depicted in Fig. 3.5, with dimensions $L \times h \times t = 1.311 \text{ m} \times 0.0446 \text{ m} \times 0.008 \text{ m}$, so that the cross-sectional area and the second moment of area with respect to the z axis are $A = 3.57 \times 10^{-4} \text{ m}^2$ and $I_{zz} = 1.9 \times 10^{-9} \text{ m}^4$, respectively (we refer to Fig. 3.5 for a definition of the system of axes). Table 3.1 summarizes the positions of the accelerometers $x_1 - x_{10}$ along the beam span, the position of the laser displacement sensor x_{LDS} , and the placement of the two symmetric rigid stop x_{STP} causing vibro-impacts. The leading ten natural frequencies (theoretical and experimental) $\omega_n / 2\pi$ in Hz are listed in Table 3.2, with the corresponding normalized mode shape functions $\phi_n(x/L), n = 1, \dots, 10$, presented in Fig. 3.6 (Blevins 2001; Mane 2010).

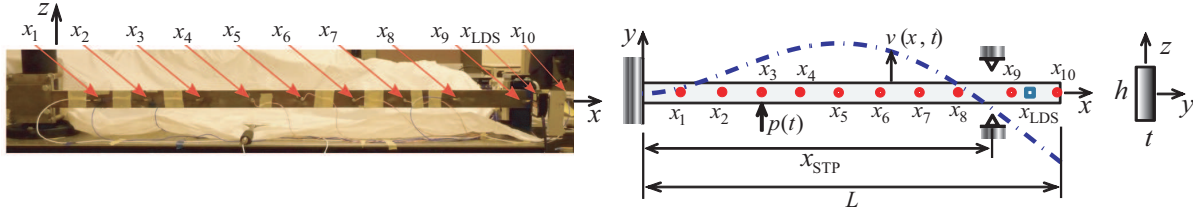


Figure 3.5 Experimental setup for the VI beam: $x_1 - x_{10}$, x_{LDS} , and x_{STP} respectively denote the spanwise locations of the accelerometers, of the laser displacement sensors, and of the rigid stops.

Table 3.1 Positions for the accelerometers, rigid stops and laser displacement sensors

Positions (mm)	x_1	x_2	x_3	x_4	x_5	x_6	x_7	x_8	x_9	x_{10}	x_{STP}	x_{LDS}
	131	263	395	527	657	787	917	1052	1215	1311	1185	1230

Two clearance levels between the cantilever beam and the rigid stops are considered: namely, infinite clearance corresponding to the case of the linear cantilever beam, and 4mm clearance corresponding to the strongly nonlinear VI beam. Experimental procedures for measuring time series data involve (i) applying impulsive excitation $p(t)$ of various magnitudes at position x_3 by means of an impact hammer, selecting an excitation frequency band by using several types of tips on the impact hammer (*e.g.*, plastic, rubber and metal), and (ii) measuring the accelerations at x_1 through x_{10} and the displacement at x_{LDS} .

In this work we utilize numerically generated acceleration signals from a reduced-order model based on the assumed-modes method, and such numerical solutions are updated and validated by the experimental measurement. That is, the beam was excited at each node with an impact hammer, and averages of four measurements were taken at each node; from the resulting 100 transfer functions, the leading 10 mode shapes, modal damping factors, and natural frequencies were obtained and used to update the assumed-modes model. In the assumed-modes method the analytical natural frequencies were replaced with the measured ones, and

numerically simulated time series were obtained by solving the reduced system of differential equations. Details of this computation can be found in (Mane 2010).

Table 3.2 The leading 10 linear natural frequencies (in Hz) of the cantilever beam in Fig. 3.5 (*cf.* (Blevins 2001; Mane 2010))

ω_n	1st	2nd	3rd	4th	5th	6th	7th	8th	9th	10th
Theoretical	3.8	23.8	66.6	130.5	215.7	322.2	450.0	599.1	769.5	961.2
Experimental	3.7	23.2	64.9	126.9	209.4	314.7	433.9	580.7	751.3	926.7

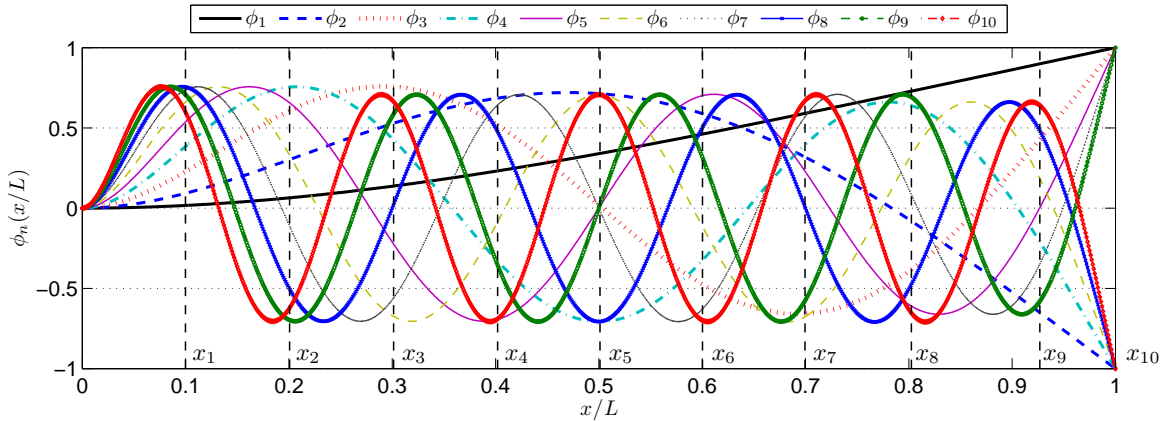


Figure 3.6 The normalized mode shape functions $\phi_n(x/L)$ of a cantilever beam: The first ten modes are depicted, and the vertical dashed lines denote the positions for accelerometers.

We remark that the 5th mode, with linearized natural frequency of 209 Hz, has a node at x_9 , which is very close to the point of vibro-impact x_{STP} . Furthermore, the impulsive excitation is applied at location x_3 , which is close to another node of the 5th mode. As shown below, this will affect the EMD analysis used for reconstructing the 5th mode at those particular points (*i.e.*, the issues of observability) in the sense that the flexible dynamics of the beam at these locations is small and consequently is dominated by the vibro-impacts (non-smooth effects).

Similar observations apply for the 8th mode, which possesses a node near the excitation point (x_3).

3.2.2 Linear Beam

By linear beam, we mean the cantilever beam in Fig. 3.5 without rigid stops (or with impacting boundaries at infinite clearance). Then, since the beam is homogeneous and uniform, we can assume that its transverse vibrations can be approximately governed by the Bernoulli-Euler beam model with the equation of motion

$$\rho A \ddot{v}(x, t) + EI_{zz} v''''(x, t) = p(t) \delta(x - x_3) \quad (3.10)$$

where $v(x, t)$ denotes the displacement field for the beam in the transverse (y) direction at (x, t) (cf. Fig. 3.5); $p(t) = P_0 \delta(t)$ is the impulsive excitation at $t = 0$, where $\delta(t)$ and $\delta(x)$ denote Dirac delta functions; and primes and overdots indicate partial differentiation with respect to x and t , respectively. Then, the general solution for Eq. (3.10) can be written as

$$v(x, t) = \sum_{m=1}^{\infty} A_m \phi_m(x) e^{-\zeta_m \omega_m t} \cos(\omega_{md} t - \theta_m) \quad (3.11)$$

where $\omega_{md} = \omega_m \sqrt{1 - \zeta_m^2}$; ω_m is the natural frequency of the m th linear bending mode; ζ_m is the modal damping factor (when viscous damping is assumed in the system); and $\phi_m(x)$ is the normalized mode shape function for the m th mode (cf. Fig. 3.6). The corresponding acceleration can be written as

$$a(x, t) \triangleq \ddot{v}(x, t) = \sum_{m=1}^{\infty} \bar{A}_m \phi_m(x) e^{-\zeta_m \omega_m t} \cos(\omega_{md} t - \bar{\theta}_m) \quad (3.12)$$

where $\bar{A}_m = A_m \omega_m^2$ and $\bar{\theta}_m = \theta_m + 2 \tan^{-1}[\sqrt{1 - \zeta_m^2} / \zeta_m]$.

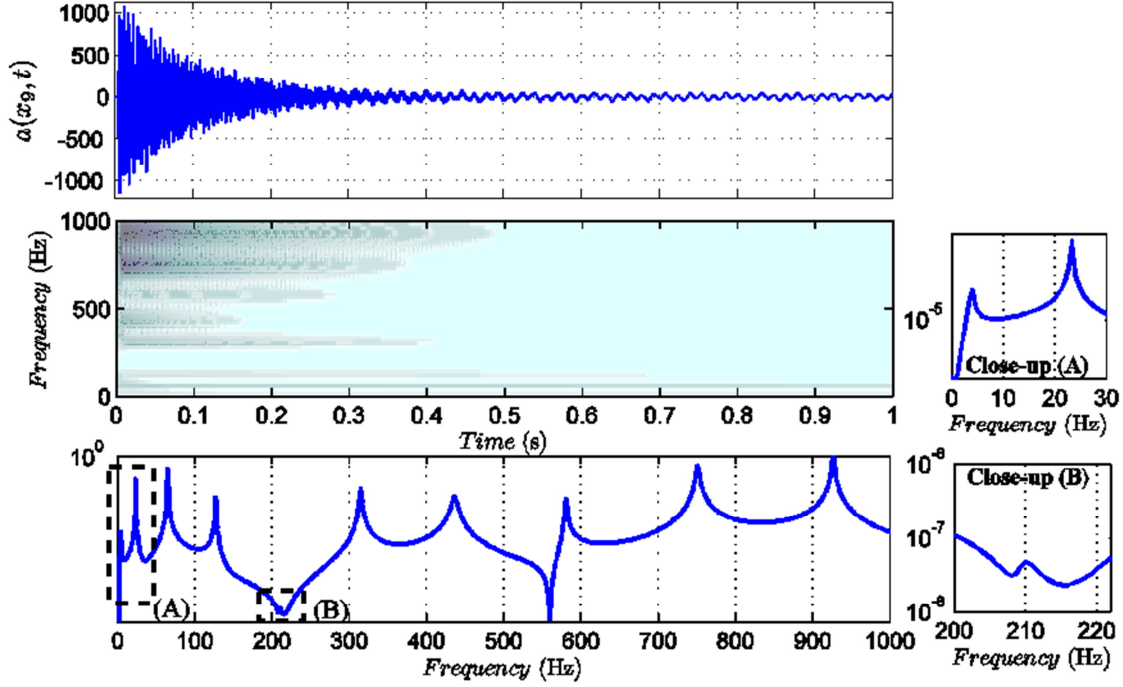


Figure 3.7 Wavelet and Fourier transforms of the acceleration for the linear beam at position x_9 .

Now we consider the acceleration response of the linear beam at x_9 depicted in Fig. 3.7. The wavelet and Fourier transforms clearly depict the ten dominant fast frequencies identified from experimental modal analysis in Table 3.2. As discussed before, the harmonic at 209 Hz appears negligible because the position x_9 is close to one of the nodes for the 5th mode. That is, we write

$$a_9(t) \equiv a(x_9, t) \approx \sum_{m=1}^{10} \bar{A}_m \phi_m(x_9) e^{-\zeta_m \omega_m t} \cos(\omega_m t - \bar{\theta}_m) \quad (3.13)$$

for small damping ζ_m . Therefore, by means of EMD analysis, we wish to obtain the relation between the acceleration time series and the intrinsic mode functions (IMFs) such that

$$a_9(t) \approx \sum_{m=1}^{10} c_m(a_9, t) \approx \sum_{m=1}^{10} \bar{A}_m \phi_m(x_9) e^{-\zeta_m \omega_m t} \cos(\omega_m t - \bar{\theta}_m) \quad (3.14)$$

where $c_m(a_9, t)$ denotes the m -th IMF of the acceleration at position x_9 (and is usually associated with the m -th normal mode vibration that can be observed at the same position of the beam). Figure 3.7 depicts the ten dominant IMFs from the advanced EMD analysis algorithm introduced in (Lochak, Meunier, and Dumas 2013), demonstrating that the relation (3.14) is valid except for the 5th mode of the beam due to observability issues. For this kind of a linear response, one might get similar or even better decomposition with a typical bandwidth filter; however, we note that the results in Fig. 3.7 were obtained through an *ad hoc* method (*i.e.*, EMD) without any artificial treatment.

We establish the reduced-order model (ROM) for the acceleration in Fig. 3.7 for the linear beam dynamics at x_9 in terms of intrinsic modal oscillators (IMOs). That is, we write the IMO corresponding to each IMF, where $m = 1, \dots, 10$, and the instantaneous slowly-varying envelope and phase of the m -th IMF are computed as $\hat{A}_m(t) = \sqrt{c_m(a_9, t)^2 + H[c_m(a_9, t)]^2}$ and $\hat{\theta}_m(t) = \tan^{-1}[H[c_m(a_9, t)]/c_m(a_9, t)] - \omega_m t$, respectively. Since the slowly-varying complex forcing amplitude $\Lambda_m(t)$ is computed from the time series (or IMF) in an effort to match the solution $x_m(t)$ of the IMO with the corresponding IMF, we write $x_m(t) \approx c_m(a_9, t)$ after validating the IMO. During this process the damping factor $0 < \hat{\zeta}_m < 1$ is chosen such as to minimize the error between $x_m(t)$ and $c_m(a_9, t)$. Then, the original response can be reconstructed as the sum of all IMO solutions; that is, via the expression

$$a_9(t) \approx \sum_{m=1}^{10} x_m(t) \approx \sum_{m=1}^{10} c_m(a_9, t) \quad (3.15)$$

Figure 3.9 compares the 10th / 5th IMFs with the corresponding IMO solutions, which exhibit good agreement.

Finally, we consider the physical meaning of the complex-valued forcing function $\Lambda_m(t)$ for the m th IMO of the linear problem, whereas it is known to be associated with nonlinear modal interactions in nonlinear dynamical systems. In our linear beam problem, the slowly-varying envelope $\hat{A}_m(t)$ and phase $\hat{\theta}_m(t)$ in Eq. (3.11) can be identified from Eq. (3.14) as

$$\hat{A}_m(t) = \bar{A}_m \phi_m(x_9) e^{-\zeta_m \omega_m t}, \hat{\theta}_m(t) = -\bar{\theta}_m = \text{constant} \quad (3.16)$$

Then, the slow-flow variable can be expressed as

$$\varphi_m(t) \approx j \omega_m \bar{A}_m \phi_m(x_9) e^{-j \bar{\theta}_m} e^{-\zeta_m \omega_m t} \Rightarrow \dot{\varphi}_m(t) \approx -j \zeta_m \omega_m^2 \bar{A}_m \phi_m(x_9) e^{-j \bar{\theta}_m} e^{-\zeta_m \omega_m t} \quad (3.17)$$

If $\hat{\zeta}_m = \zeta_m$ (*i.e.*, the damping factor in the IMO is the same as the modal damping factor identified from experimental modal analysis and carries a direct physical meaning), then we can easily show that $\Lambda_m(t) \approx 0$. This approach is feasible and reasonable, because the resulting reduced-order model will be the same as that obtained from standard linear modal analysis with $x_m, m = 1, \dots, 10$, being the modal coordinates. Furthermore, the solution for the IMO will appear as a free damped response, which may naturally retrieve the relation in Eq. (3.14). However, as is the case for many other nonlinear system identification methods where it is of more interest to check whether the proposed parametric model is able to reproduce the measured (or simulated) dynamics, the damping factor in the IMO is not necessarily the same as the physical one (*i.e.*, $\hat{\zeta}_m \neq \zeta_m$, in general). In this case, the complex forcing amplitude $\Lambda_m(t)$ can be expressed as

$$\Lambda_m(t) \approx j(\hat{\zeta}_m - \zeta_m) \omega_m^2 \bar{A}_m \phi_m(x_9) e^{-j \bar{\theta}_m} e^{-\zeta_m \omega_m t} \quad (3.18)$$

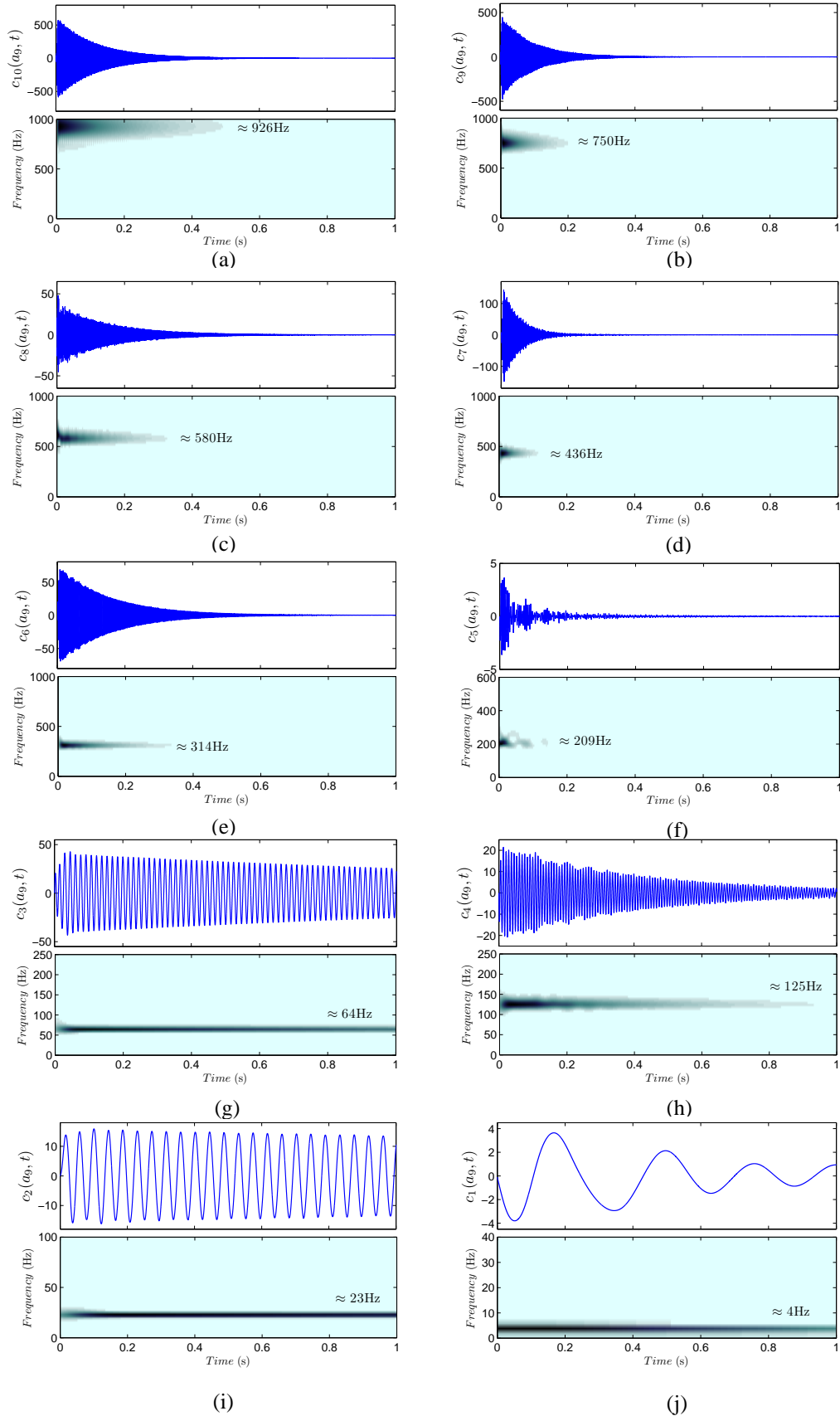


Figure 3.8 The 10 dominant IMFs extracted from the acceleration response in Fig. 3: (a) through (j) sequentially depict the 10th to 1st IMFs, respectively.

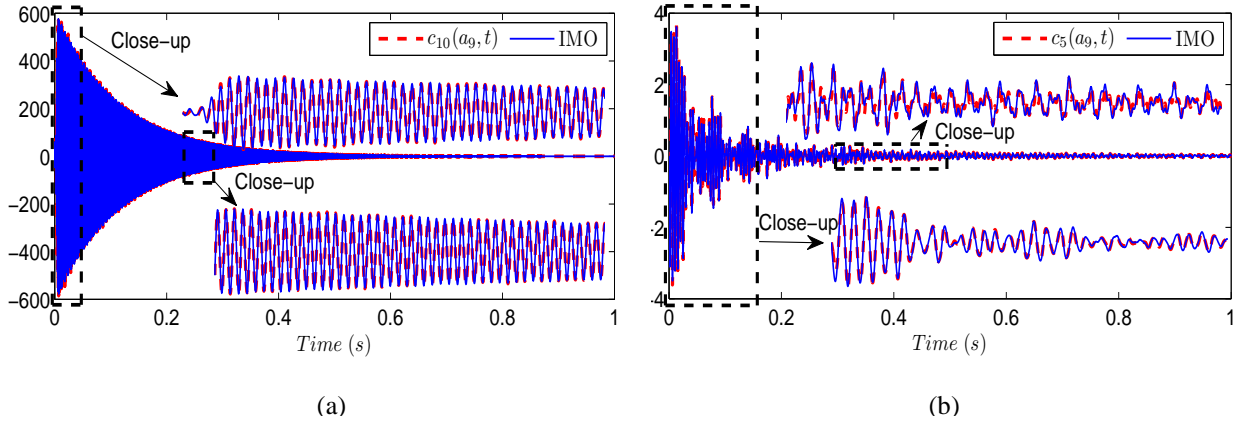


Figure 3.9 Comparison of the IMFs in Fig. 4 with their corresponding IMO solutions: (a) 10th IMF; (b) 5th IMF

The absolute value of Eq. (3.18) is a *monotonically* and exponentially decaying function; and yet, such a forcing function will not generate any modal interactions (consistent with a linear system). Nonetheless, the solution for the IMO, which is strongly driven by the forcing $\Lambda_m(t)e^{j\omega_m t}$ because $\hat{\zeta}_m \gg \zeta_m$, can be approximated by the IMF in Eq. (3.14). Similar discussions can be made not only for the response at position x_s , but also for those at all other positions along the linear beam.

3.2.3 Vibro-impact (VI) Beam

In this section we consider the cantilever beam in Fig. 3.5 but with the two symmetric rigid stops of 4mm clearance at position x_{STP} . If the displacement $|v(x_{STP}, t)| < 4\text{mm}$, then the dynamics of the beam is linear. Whenever the beam displacement $|v(x_{STP}, t)| = 4\text{mm}$, then a vibro-impact occurs applying a new impact load equal to $\bar{p}(t)\delta(x - x_{STP})$ as well as causing energy dissipation due to impact. Mathematically speaking, the nonsmoothness due to the vibro-impacts means that the displacement response is of class C^0 (*i.e.*, continuous but not continuously differentiable).

For this strongly nonlinear, nonsmooth dynamical system, there is no closed-form solution available in general. Furthermore, such a VI dynamical system may possess a very complicated topological structure of periodic orbits even in the simplest model with two degrees of freedom (*e.g.*, see (Lee, Nucera, et al. 2009)). This is mainly because nonsmooth dynamical systems may involve certain behaviors such as grazing bifurcations (Nordmark 2001) and even chaotic dynamics (Cusumano, Sharkady, and Kimble 1994). We wish to characterize such complicated nonlinear dynamics of the VI beam by applying the proposed NSI method.

As in the linear beam problem, we consider the acceleration signal at x_9 , depicted in Fig. 3.10, where the effects of vibro-impacts generate multiple broadband perturbations in the wavelet transforms. In particular, comparing the Fourier transforms of the linear beam response (dashed line) with that of the VI beam, this broadband excitation of the beam due to vibro-impacts is observed. Figure 3.11a depicts the numerically computed displacement and the corresponding impact load on the beam at x_{STP} , to identify the instants of impact (*i.e.*, the time instants when the beam displacement at x_{STP} reaches the thresholds $\pm 4\text{mm}$).

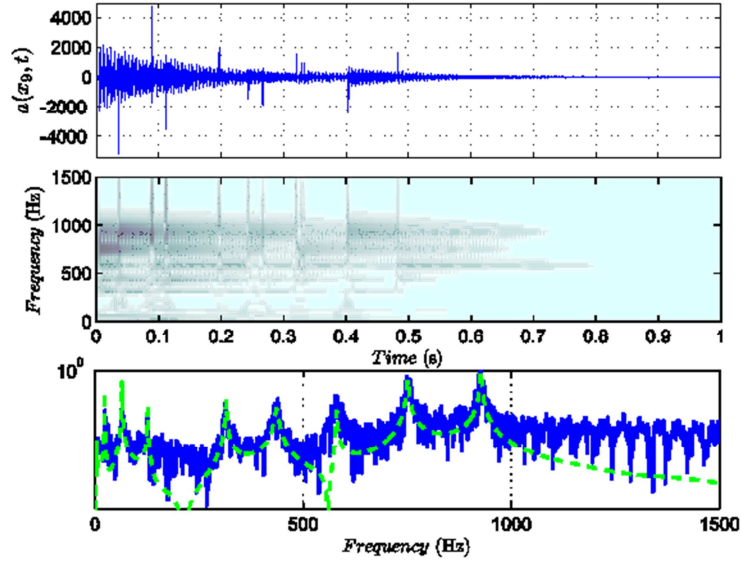


Figure 3.10 Wavelet and Fourier transforms of the acceleration for the VI beam at $x = x_0$ (The Fourier transform in Fig. 3.7 is superimposed as a dashed line to illustrate the effects of vibro-impacts in frequency domain).

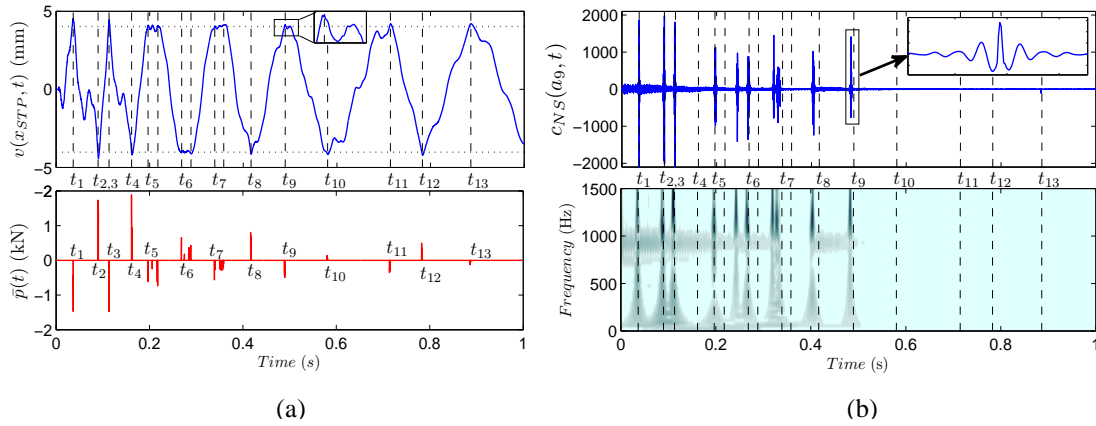


Figure 3.11 Depiction of the vibro-impacts: (a) the displacement response of the VI beam simulated at position x_{STP} and its corresponding impact loads on the beam from the rigid stops; (b) the nonsmooth component of the acceleration in Fig. 3.10 is decomposed via EMD analysis (Note that the *dashed lines* at $t = t_k$, $k = 1, \dots, 13$ imply the impact instants identified from the impact force, $p(t)$)

It was shown in (Lee, Nucera, et al. 2009) that the nonlinear modal interactions due to vibro-impacts are purely due to the smooth parts of the VI dynamics, whereas the non-smooth parts tend to create frequency-energy relations involving numerical artifacts. Such numerical artifacts can lead to wrong conclusions regarding the nonlinear resonances involved in the nonlinear modal interactions between the measured IMFs. Furthermore, it was demonstrated

that the smooth parts of the VI dynamics can be obtained by separating out the nonsmoothness by means of EMD analysis (Lee, Nucera, et al. 2009) . Typically, the nonsmooth part is computed as the first IMF with the help of masking and mirror-image signals (Deering and Kaiser 2005). The characteristics of the nonsmooth IMF were explored in previous works by relating them to Fourier series expansions of saw-tooth wave signals (Lee, Chen, et al. 2011) , and also by a partial-differential-equation-based sifting process (Deléchelle, Lemoine, and Niang 2005) noting that EMD acts, in essence, as a dyadic filter bank.

Figure 3.11b depicts such a nonsmooth IMF for the acceleration signal in Fig. 3.10. Superposition of the impact instants identified from Fig. 3.11a illustrates that the isolated nonsmoothness agrees reasonably well with the time instants of the vibro-impacts. We note that the numerical displacement was calculated from the reduced-order model through the assumed-modes method, which means that some other modes higher than 10th may need to be included to get a better match between the numerical simulations and experimental measurements. Some quantitative discrepancies prevail after 0.2 seconds with the current reduced-order model.

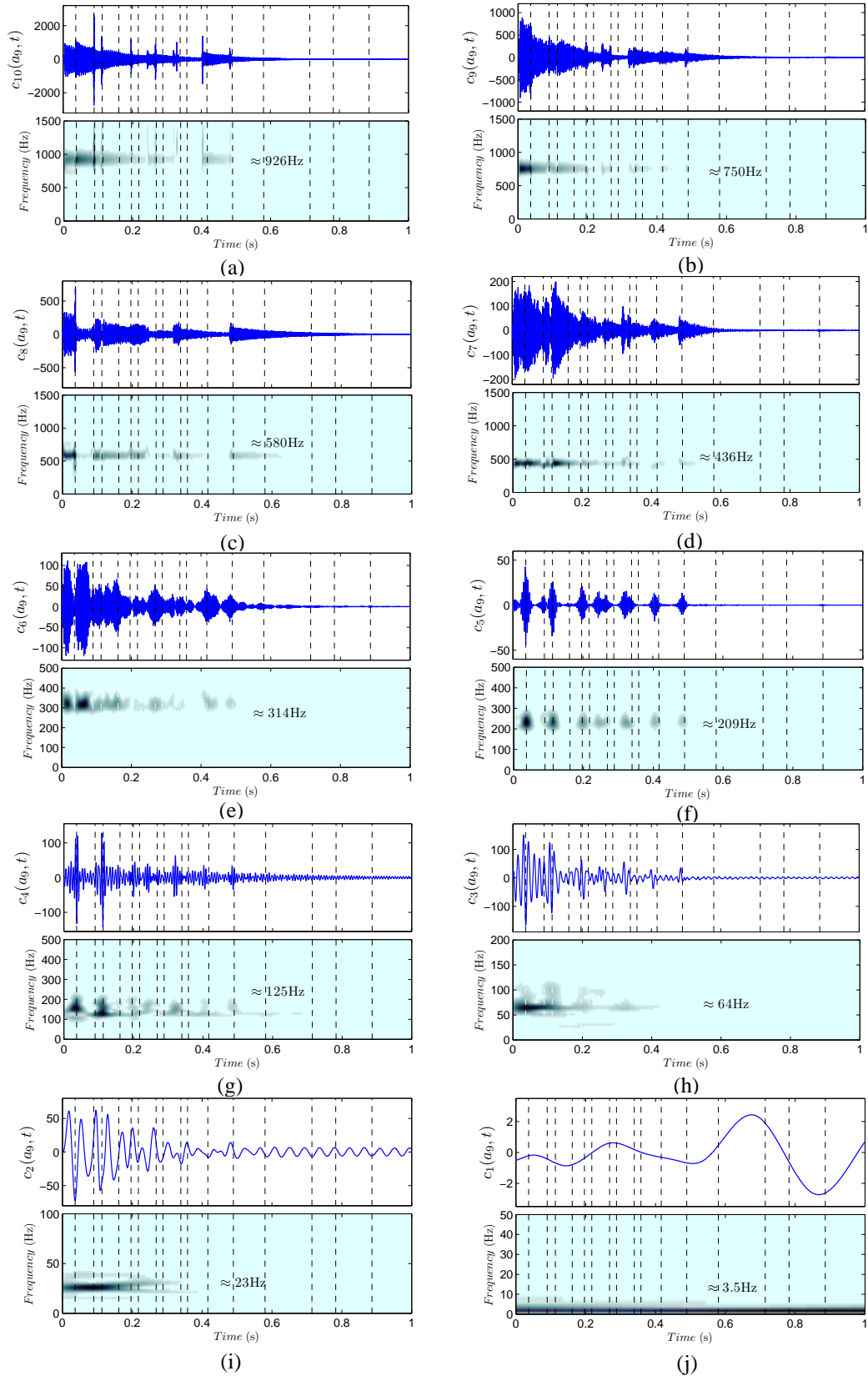


Figure 3.12 The 10 dominant IMFs extracted from the acceleration response in Fig. 3.10: **a** through **j** sequentially depict the 10th to 1st IMFs, respectively (Note that the *dashed lines* imply the impact instants identified in Fig. 3.11)

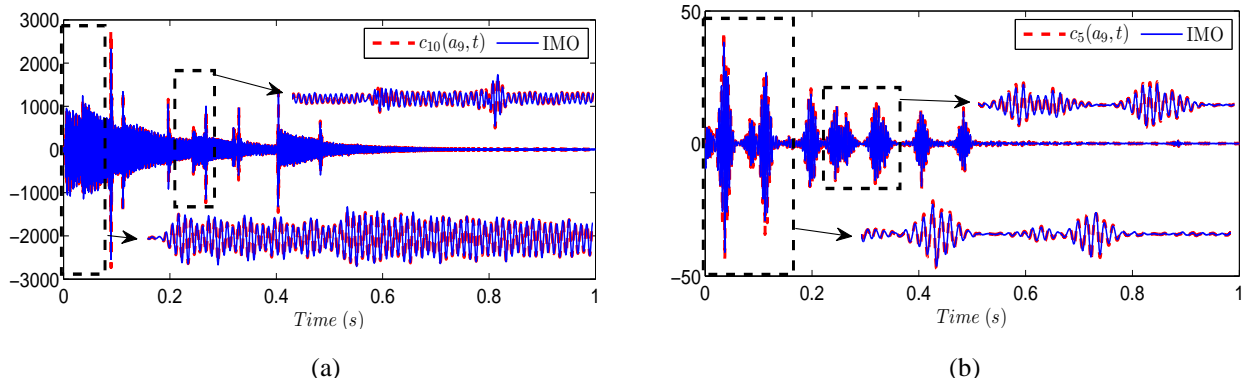


Figure 3.13 Comparison of the IMFs in Fig. 3.12 with their corresponding IMO solutions: (a) 10th IMF; (b) 5th IMF

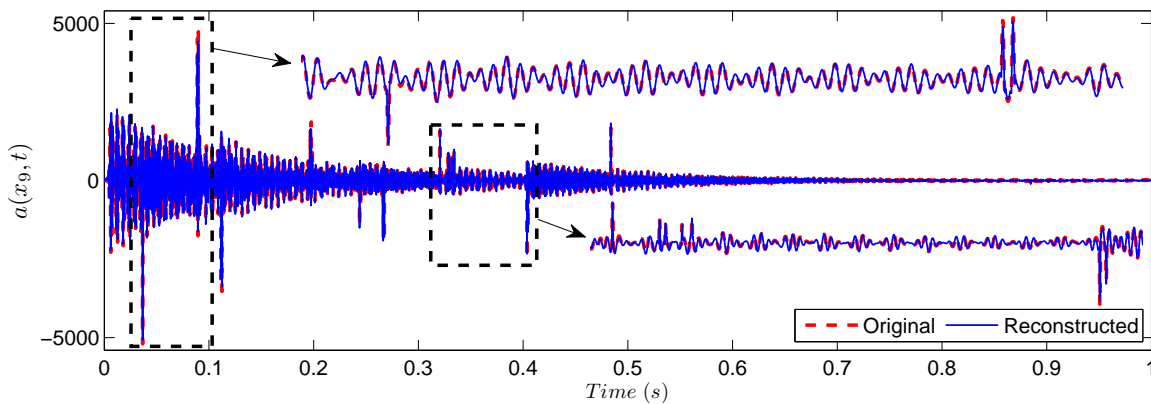


Figure 3.14 Comparison of the reconstructed acceleration from the 10 IMO solutions plus the nonsmooth IMF with the original response in Fig. 3.10

EMD is then applied to the remaining *smooth* part of the acceleration signal after subtracting the nonsmooth IMF in Fig. 3.11b from the original acceleration in Fig. 3.10. The ten dominant IMFs are depicted in Fig. 3.12. By superimposing the vertical dashed line at each impact instant identified from Fig. 3.11a, one can at least qualitatively observe the effects of vibro-impacts on each IMF at position x_9 . For example, vibro-impacts seem to directly influence higher IMFs (above the 5th). Indeed, considering these higher frequency IMFs, we note linear dynamical behavior between consecutive vibro-impacts, in the form of

exponentially decaying damped responses. On the other hand, lower IMFs do not seem to exhibit such straightforward patterns implying that these IMFs may undergo more strongly nonlinear modal interactions. These aspects will be explored further in the context of the nonlinear modal interaction terms of the corresponding IMOs.

As in the linear beam, we can also establish a nonlinear interaction model (NIM) for the IMFs obtained in Fig. 3.12 in terms of a set of IMOs. Computing the nonlinear modal interaction forcing $\Lambda_m(t)$ from each IMF by means of the slow-flow correspondence, we solve for the ten IMOs, respectively. Figure 3.13 compares the IMFs with the corresponding IMO solutions for 10th and 5th IMFs, and shows good agreement. We sum all IMO solutions to reconstruct the original signal, and these exhibit a nearly perfect match as depicted in Fig. 3.14. That is, the NIM we established has been validated so that it can be used to study the nonlinear dynamics of the VI beam (at position x_9) as an alternative reduced-order model.

Understanding the physical meaning of the slowly-varying complex forcing amplitude $\Lambda_m(t)$ in the ROM (or NIM for the VI beam) is essential, because the response obtained from the IMO in the ROM is strongly dictated by this nonhomogeneous forcing term whereas the influence from the homogeneous part of the ROM is minimal. In other words, the ROM will predict linear (nonlinear) responses if the slowly-varying forcing term $\Lambda_m(t)$ exhibits linear (nonlinear) behaviors.

Now the physical meaning of $\Lambda_m(a_k, t), m, k = 1, \dots, 10$, in the nonlinear dynamics of the VI beam can be explored by being compared with that for the linear beam. We first note that the magnitude of $\Lambda_m(a_9, t)$ for all m for the linear beam appears as almost a straight line in a logarithmic scale (*cf.* Fig. 3.15), which would make sense due to the analytical consideration in Eq. (3.14).

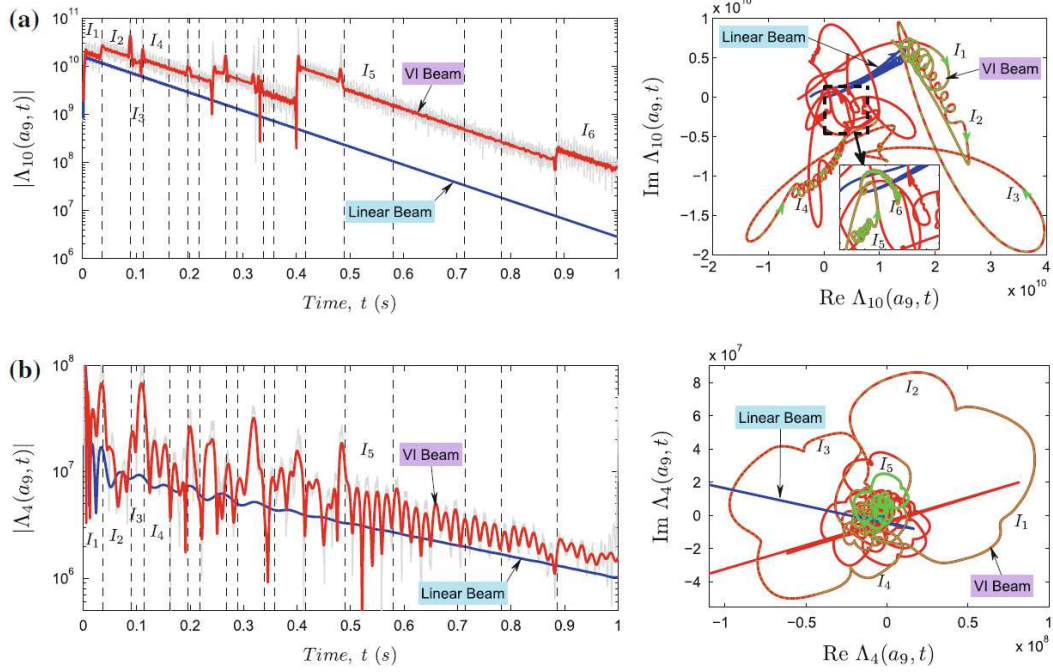


Figure 3.15 Comparison of the slowly-varying forcing functions $\Lambda_m(a_9, t)$: (a) $m=10$ (*i.e.*, 10th IMO) and (b) $m=4$ (*i.e.*, 4th IMO). Note that the dashed line simply the impact instants identified in Fig. 7

Similarly, $|\Lambda_m(a_9, t)|$ for the VI beam can also exhibit the linearity with the same slope on average in a logarithmic scale as in the case of the linear beam, but such linear pattern appears only in between impact instants and, in particular, when $m \geq 6$ (*cf.* Fig. 3.13a for the 10th IMO). The trajectory of $\Lambda_{10}(a_9, t)$ in the complex plane for the linear beam appears as a single, monotonic, decaying pattern (*i.e.*, time-like behavior in a logarithmic scale), which implies no modal coupling or interactions in the ROM. The trajectory of $\Lambda_{10}(a_9, t)$ for the VI beam also exhibit such monotonic behaviors but only in between vibro-impacts denoted by the intervals $I_n, n=1, 2, \dots$, and the role of impacts is to cause phase shifts of slowly-varying forcing $\Lambda_{10}(a_9, t)$ at the impact instants. On the other hand, the slowly-varying complex forcing function $\Lambda_{10}(a_9, t)$ for the 4th IMO of the VI beam does not exhibit any linearity but only

slowly-varying wavy envelope regardless of vibro-impacts (*cf.* Fig. 3.11b). Such wavy patterns in the plot of $|\Lambda_4(a_9, t)|$ indicate that certain modal interactions occur through nonlinear resonant conditions such as internal resonance or resonance capture (Dawes 2010). Also, nonlinear modal interactions can be evidenced by the spiral (or non-time-like) patterns of the trajectory in the complex plane.

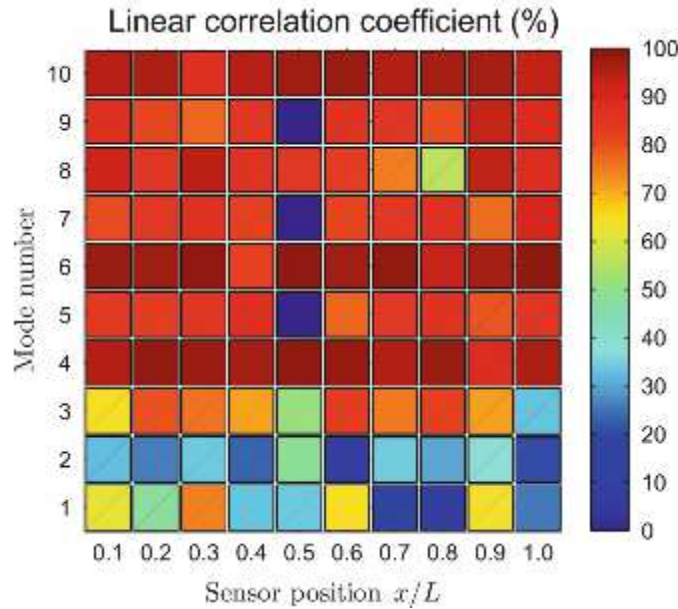


Figure 3.16 Linear correlation coefficient (%) between the slowly-varying forcing functions $\Lambda_m(a_k, t), m, k = 1, \dots, 10$, where m and k denote the mode number and accelerometer position, respectively, of the linear and VI beams. We note that the thick solid (dashed) lines denote the boundary for 90% (80%) correlation.

From these two typical examples, we may conjecture the following: Whereas the higher IMOs (*i.e.*, the IMOs associated with higher frequency components) tend to maintain their linear dynamics in between impacts (although the overall dynamics is strongly nonlinear), the lower IMOs exhibit strongly nonlinear modal interactions independent of vibro-impact patterns. The role of vibro-impacts is just to exert broadband impulsive excitations on the linear beam causing instantaneous phase shifts for the higher IMOs. In addition, since the overall response should be damped out due to the viscous damping, vibro-impacts feed some amount of energy

to certain IMOs, while extracting some from the other ones; or they simply dissipate energy from all IMOs.

To verify this conjecture we first compute the Pearson's linear correlation coefficient for the slowly-varying complex forcing amplitudes $\Lambda_m(a_k, t), m, k = 1, \dots, 10$, of all IMOs for the linear and VI beams at all the positions along the beam. This correlation coefficient is widely utilized in statistics as a measure of the linear dependence between two variables, and a MATLAB command 'corn' was used in this work. Figure 3.16 depicts the interpolated contour map of the absolute value of the linear correlation coefficient for each mode number along the beam span. Note that by 'mode number' m in Fig. 3.16 we mean the IMO which is associated with the m th linear mode; and hence there is no such continuous distribution with respect to the vertical axis. From these simple calculations, we find that the IMOs higher than the 4th possess strong linear dependence (linear correlation coefficient higher above 90%) between the linear and VI responses of the beam, regardless of the position along the beam. Again, it is noted that the low correlation for the 3rd, 5th, 7th and 9th IMOs at the midspan of the beam is due to the fact that the position is very close to one of the nodes for the respective linear modes. Similar things can be addressed for those for the 5th and 7th IMOs at position x_9 , and for the 8th IMO at position x_8 . Therefore, the aforementioned conjecture is confirmed by means of the linear correlation coefficients between $|\Lambda_m(a_k, t)|$ (and hence the corresponding IMO responses) for the linear and VI beams confirms. That is, vibro-impacts do not alter much the linear dynamics for the higher modes (typically, higher than 4th), but rather significantly affect the lower modes creating strongly nonlinear modal interactions. This result agrees with Cusumano's previous work (Cusumano, Sharkady, and Kimble 1994), where the topological characterization of the spatial structure of the VI beam vibrations was studied by means of the two-point spatial correlation (*i.e.*, correlation dimension)

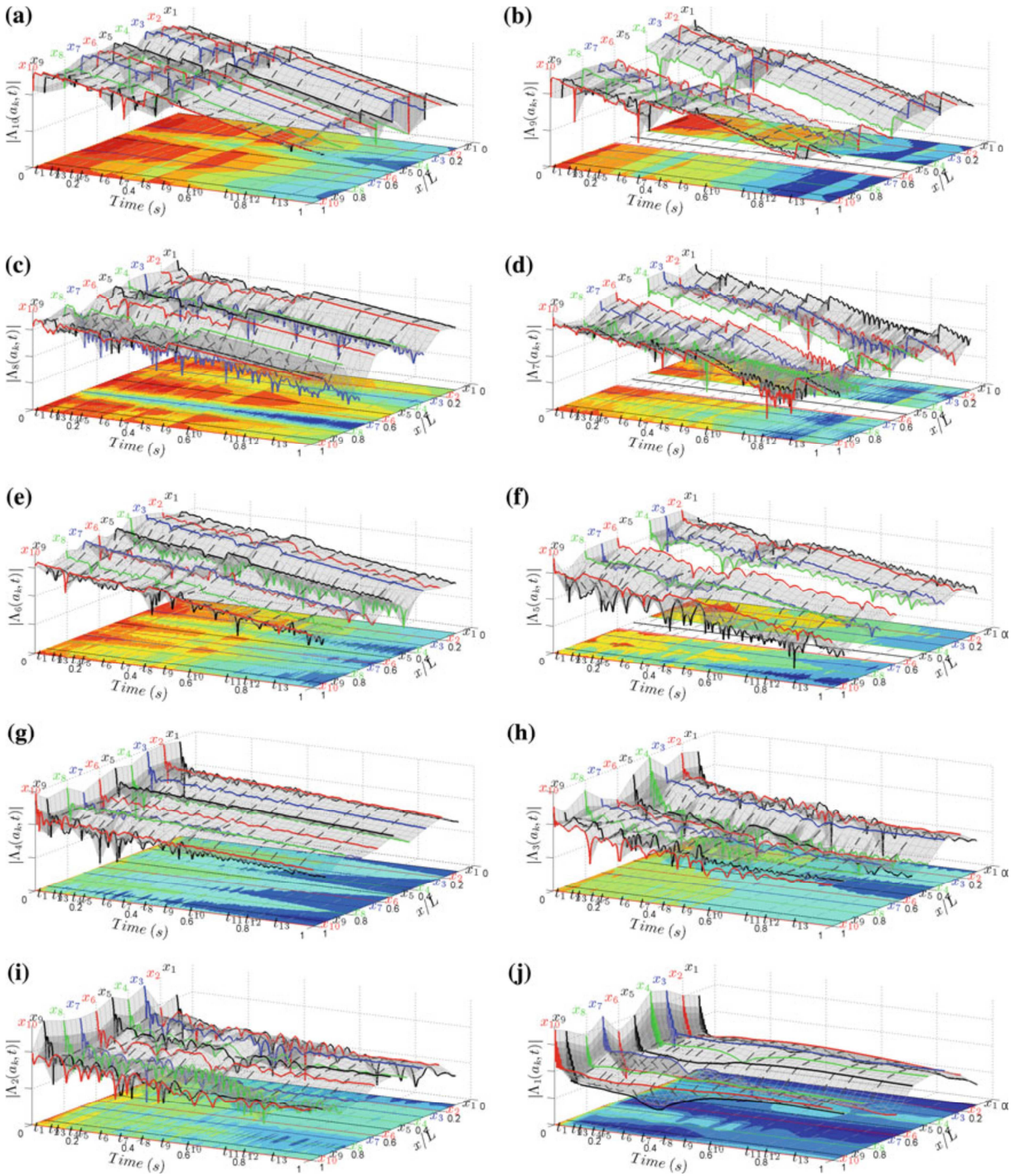


Figure 3.17 The spanwise magnitudes of nonlinear modal interaction for the VI beam: (a) through (j) sequentially depict the 10th to 1st IMFs, respectively (Note that the logarithm with base 10 is taken for $|\Lambda_m(a_k, t)|$ and that the sections at $t = t_n$, $n = 1, \dots, 9$, denote some of the impact instants identified in Fig. 3.10)

and the POD. In particular, the estimate for the correlation dimension of the VI dynamics was obtained lower than but near 4, which dictates that the low-dimensional model can capture the overall complicated, chaotic-like VI beam dynamics. Furthermore, if such complicated dynamics can be captured by low-dimensional model with several lower IMOs, then energy transfers (or cascades) from the higher to the lower modes through certain nonlinear modal interactions such as internal resonances can be responsible.

While the linear correlation coefficient provides excellent physical insights to the VI beam dynamics, we note that it should be a static, global measure; that is, it does not contain any possible temporal variations (or propagations, or localization) of the vibro-impacts. Moreover, it cannot suggest useful information, particularly when the IMF for the linear beam corresponds to the linear mode which possesses a node near the measurement position. Hence, we construct different types of map for the spatio-temporal variations of $|\Lambda_m(a_k, t)|, m, k = 1, \dots, 10$, which are depicted in Fig. 3.17 for all the IMOs. We note that, since the position x_5 is very close to one of the nodes for the 5th, 7th and 9th linear modes, the meaningful IMFs were not obtained creating discontinuous surface plots in Figs. 3.17 (b), (d) and (f), respectively. Linear logarithmic decrements of $|\Lambda_m(a_k, t)|$ in time in between vibro-impacts evidences that linear dynamics of the VI beam prevails for the higher IMOs than the 3rd (*cf.* Figs. 3.17(a)–(g)). On the other hand, we can still confirm that the lower modes than the 4th are significantly influenced by vibro-impacts (*cf.* Figs. 3.17(h)–(j)). That is, strong wavy, wrinkling spatio-temporal distributions of $|\Lambda_m(a_k, t)|$ can be observed from the 3-dimensional surface plot, as compared to the almost flat distributions of $|\Lambda_m(a_k, t)|$ with simultaneous occurrences of spikes due to vibro-impacts for the higher IMOs. The lower IMOs also appear as high-frequency, smudged images of recurrent nested contours in the 2-

dimension projection, and accordingly, the impact patterns associated with vibro-impacts are hard to read and no longer simultaneous.

Finally, we remark that not all the higher IMO's behave completely linear in between vibro-impacts. Whereas the spatio-temporal variations of $|\Lambda_m(a_k, t)|$ for the 9th and 10th IMO's are almost globally linear (evidenced by the formation of nearly rectangular strips of the contour plot on the (x, t) plane, neglecting changes of their absolute magnitude), those for the 4th–8th IMO's manifest spatially-localized nonlinear behavior, in particular, at position x_9 where vibro-impacts from the rigid stops can strongly affect the beam dynamics. The slowly-varying complex forcing at positions x_3 and x_8 for the 8th IMO, and at position x_4 for the 5th IMO also demonstrate spatially-localized nonlinear effects on the VI beam. Furthermore, the 7th IMO exhibits even temporal localization of nonlinear dynamics in between the impact instants t_{11} and t_{13} in Fig. 3.17(d).

3.2.4 Comparison with results of experimental data analysis

In this section, we compare the NSI results of the numerical data in the previous section with experimental measurements for the VI beam. Note that comparisons in this section will remain qualitative, because the impulsive excitation by an impact hammer for the experiments was different from that for the numerical data. That is, a plastic cap was put on the impact hammer for experiments, whereas an aluminum tip was considered in the numerical simulations. Use of such plastic cap on the impact hammer will limit the frequency band for excitation (typically with a cut-off frequency around 1,000Hz), whereas an aluminum tip will broaden the excitation bandwidth (typically with a cut-off frequency around 1,200Hz). A more complete NSI analysis on the experimental data is discussed in a companion paper (H.

Chen et al. 2014), so here we provide only a qualitative comparison between computational and experimental results.

The procedures for NSI of the experimental VI beam responses are the same as those for the numerical data. We perform EMD analysis on the ten acceleration measurements respectively at the ten positions (x_1 through x_{10}) along the beam span. For the purpose of comparison, NSI of the acceleration at x_9 is our first interest in this section. The 10th and 5th IMFs of this experimental acceleration response are depicted in Figs. 3.18 (a) and (b), respectively. Comparing them with those depicted in Fig. 3.12, we find qualitative similarity. That is, the 10th IMF exhibits multiple exponential decays initiated at every vibro-impact, whereas the 5th IMF seems to exhibit strong nonlinear modal interactions. Indeed, this observation is qualitatively consistent with that for the numerical data.

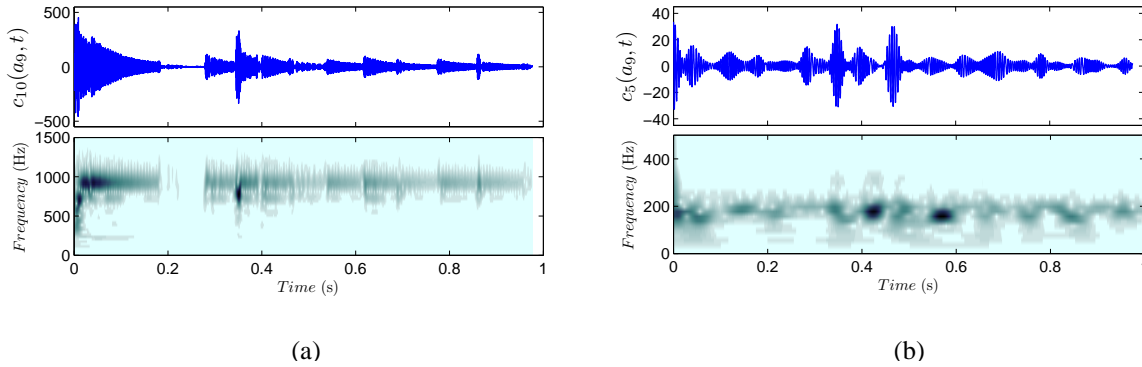


Figure 3.18 IMFs extracted from the experimentally measured acceleration at the sensing position x_9 : (a) 10th IMF (*cf.* Fig. 3.12a); (b) 5th IMF (*cf.* Fig. 3.12f)

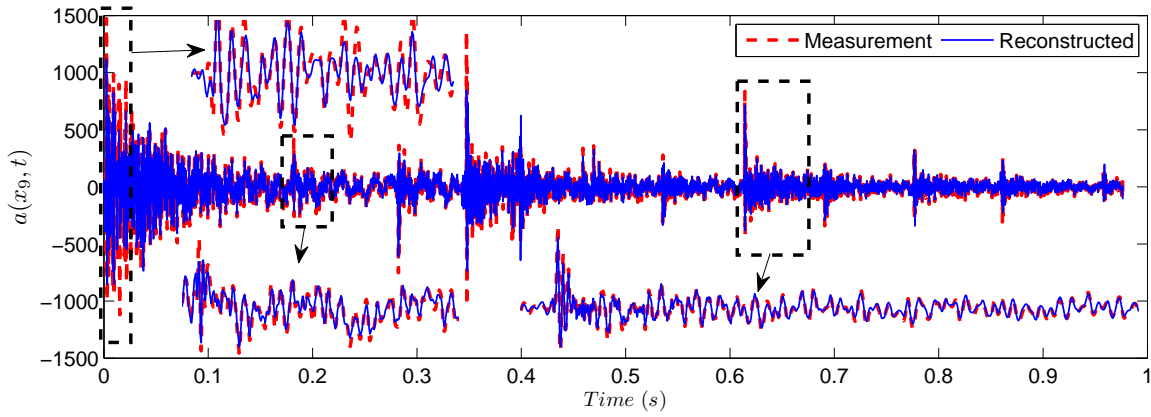


Figure 3.19 Comparison of the reconstructed acceleration from the ten (smooth) IMO solutions with the original response measured at position x_9 .

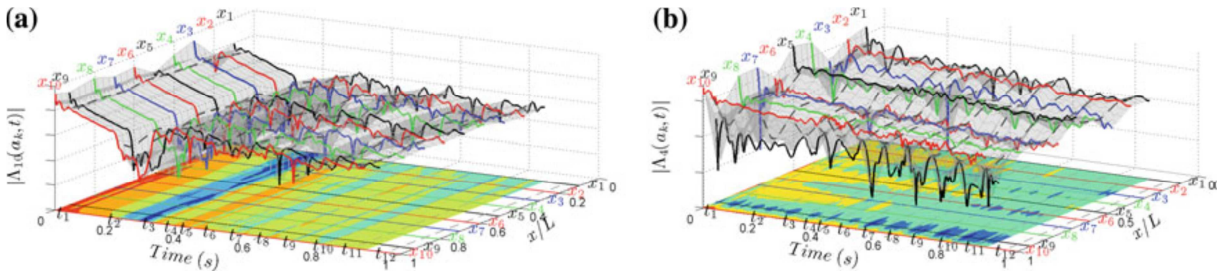


Figure 3.20 The spatio-temporal variations of $\Lambda_m(a_n, t)$ the VI beam from experimental measurements (a) $m=10$ (i.e., 10th IMO) and (b) $m=5$ (i.e., 5th IMO).

Then, we establish a nonlinear interaction model (NIM) as a set of IMOs, whose solutions are verified and validated to match the respective IMFs. Furthermore, we confirm completeness of the IMO solutions as a basis with which the given measurement can be expanded. This is demonstrated in Fig. 3.19. Note that the apparent discrepancies between the measured and reconstructed acceleration signals are due to the fact that the nonsmooth IMF was not included when reconstructing the original signal.

Finally, Figs. 3.20 (a) and (b) depict the spatio-temporal variations of $|\Lambda_m(a_k, t)|, k = 1, \dots, 10$, respectively, for the 10th ($m=10$) and 4th ($m=4$) IMFs from experimental measurements at the 10 positions along the beam. As was discussed from the NSI of the numerical data, the 10th (4th) IMO manifests globally (locally) linear dynamics in between vibro-impacts (*cf.* Figs. 3.17(a) and(g)). For the 10th (or higher) IMO, formation of the flat strips is more evident, compared to that of the numerical data; and moreover, vibro-impacts occur simultaneously along the whole beam. On the other hand, the 4th (or lower) IMO retains linear dynamics, except for the position at x_9 where direct effects due to vibro-impacts from the rigid stops can be made on the beam dynamics; also, the positions as x_1 and x_3 exhibit localized nonlinear modal interactions evidenced by the wavy, wrinkled surface plot. Overall, NSI of the experimental results demonstrates dynamical behaviors qualitatively similar to that of the numerical results.

3.2.5. Concluding Remarks

We studied the dynamics of a cantilever beam with two symmetric rigid stops with prescribed clearances by performing nonlinear system identification (NSI) based on the correspondence between analytical and empirical slow-flow dynamics. Performing empirical mode decomposition (EMD) analysis on the numerically-computed acceleration responses at ten, almost evenly-spaced, spanwise positions along the beam, we constructed sets of the intrinsic modal oscillators at different time scales of the dynamics. In particular, the EMD analysis can separate nonsmooth effects due to vibro-impacts between the beam and the rigid stops from the underlying smooth dynamics governed by the flexible beam dynamics, so that nonlinear modal interactions can be explored only with the remaining smooth components. Then, we established nonlinear interaction models (NIMs) for the respective intrinsic mode oscillations,

where the NIMs invoke slowly-varying forcing amplitudes (or nonlinear modal interaction terms) that can be computed from empirical slow-flows and directly dictate nonlinear modal interactions between different-scale dynamics. By comparing the spatio-temporal variations of the nonlinear modal interactions for the vibro-impact beam and the underlying linear beam model, we demonstrated that vibro-impacts significantly influence the lower intrinsic mode functions involving strongly nonlinear modal interactions, whereas the higher modes tend to retain their linear dynamics in between impacts. Also, computation of the linear correlation coefficients as a measure for linear dependency between the dynamics of the linear and VI beams manifested the same results but only with spatial information. A preliminary comparison of the numerical NSI results with those resulting from analyzing experimental measurements provided the same qualitative results.

3.3 NSI of Frictional Effects in a Beam with a Bolted Joint Connection (Eriten et al. 2013)

3.3.1 Introduction

Frictional connections are common in assembled structures whether bolted, welded or riveted. These joints introduce additional flexibility and damping to the overall structural dynamics. Identification of joint parameters is a challenging task due to the nonlinear nature of the joint mechanics spanning multiple spatial and temporal scales. Various experimental and theoretical identification and modeling approaches for simple jointed structures have been proposed in the literature. Experimental studies focus on replacing the jointed interfaces with equivalent external forces and/or moments applied to the jointed members. Force-state mapping (Jalali, Ahmadian, and Mottershead 2007; Crawley and Aubert 1986) and multi-harmonic balance methods (Y. Ren 1998) are two examples of these approaches. A systematic identification through experiments is conducted by (Ma, Bergman, and Vakakis

2001) for two cantilever beams connected by a lap joint; they compare the responses of the bolted assembly with a monolithic solid piece with identical geometry in order to isolate the joint effects. In (Ma, Bergman, and Vakakis 2001) it is found that the joints introduce non-proportional damping and nonlinear softening effects in the structure due to micro-impacts at the connections.

In this section, we perform nonlinear system identification (NSI) of the effects of frictional connections in the dynamics of a bolted beam assembly. The methodology utilized in this work combines experimental measurements with slow-flow dynamic analysis and empirical mode decomposition, and reconstructs the dynamics through reduced-order models. These are in the form of single-degree-of-freedom linear oscillators (termed intrinsic modal oscillators – IMOs, see 2.4) with forcing terms derived directly from the experimental measurements through slow-flow analysis. The derived reduced order models are capable of reproducing the measured dynamics, whereas the forcing terms provide important information about nonlinear damping effects. The NSI methodology is applied to model nonlinear friction effects in a bolted beam assembly. A ‘monolithic’ beam with identical geometric and material properties is also tested for comparison. Three different forcing (energy) levels were considered in the tests in order to study the energy-dependencies of the damping nonlinearities induced in the beam from the bolted joint. In all cases, the NSI methodology employed was successful in identifying the damping nonlinearities, their spatial distributions and their effects of the vibration modes of the structural component.

3.3.2 Experimental Fixture and Process

We consider two simple beams of identical geometries and composed of low-carbon steel, one made from a solid piece (labeled the ‘monolithic beam’) and the other composed of two half-beams connected by a bolted lap-joint (labeled the ‘bolted beam’). By comparing the

dynamics of the two beams, we wish to isolate and identify the frictional effects of the lap joint on the structural dynamics. Each of the two half-beams of the bolted beam are of length 254mm; they are joined by two lap plates of the same thickness and width but with shorter length of 81.3mm. Two 6.4 mm hex head stainless steel bolts, four 6.4 mm stamped steel washers and two 6.4 mm stainless steel hex nuts are used for bolting (*cf.* Fig. 3.21).

The monolithic beam is machined from a single piece of steel, with bolt holes in the middle and identical bolting in order to achieve identical geometric properties and mass distribution as the bolted beam. Hence, the monolithic beam requires no assembly except for bolts and washers. Bolts are first carefully centered in the holes and are hand-tightened in order not to touch the sides of the holes. This step is required to prevent any complication due to micro-impacts between the bolts and the edges of the holes. Once fixed in position, the bolts are tightened to 6214 N-mm. by a dial type torque wrench with a memory needle (Precision Instruments, D2F300H). The assembly of the bolted beam requires more attention for joining the two half beams and the lap plates.

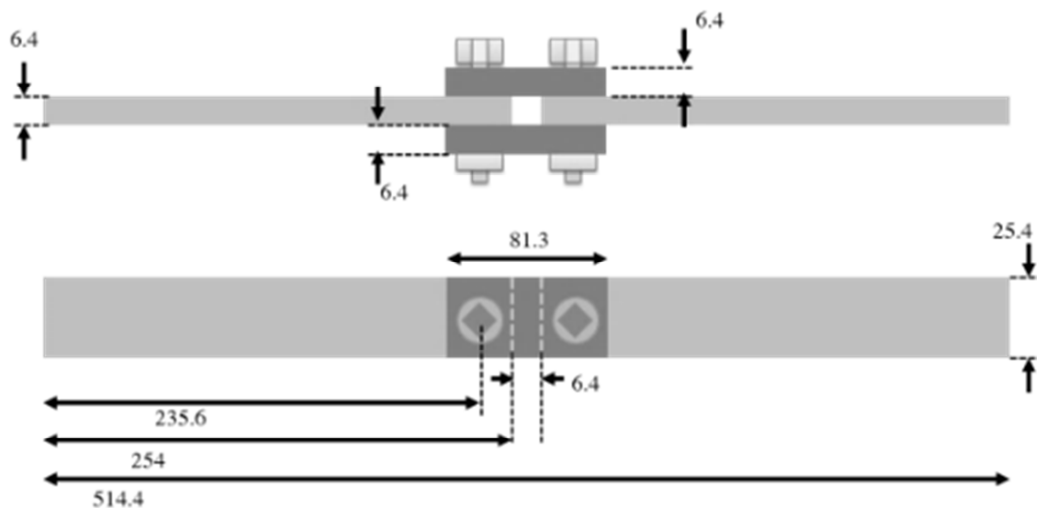


Figure 3.21 The bolted beam used in the experimental tests (all dimensions given in mm).

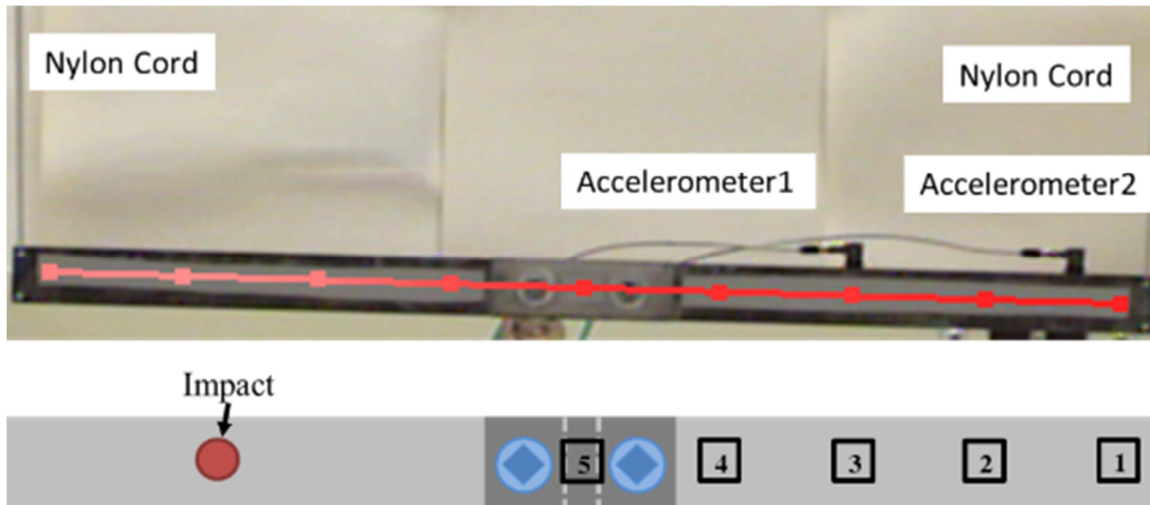


Figure 3.22 Measurement grid for laser vibrometer measurements, positions of the two accelerometers and point of impulsive excitation for the bolted beam

After the beams were suspended at each end by 1.6m long nylon cords (*cf.* Fig. 3.22). Impulsive excitations were then applied at points on the longitudinal axis of symmetry of the beams by an impact hammer with a metal tip (Model PCB 086C04) in order to excite the bending modes and avoid the excitation of any torsional modes. Vibration measurements from different sensing locations on each beam were recorded by means of two shear accelerometers (Models PCB 353B15) and a scanning laser vibrometer system (Polytec Model PSV-400). The accelerometers were attached through mounting adhesives and used to check the speckle effect (which can decrease the quality of the velocity measurements taken by the laser vibrometer). Each accelerometer weighted 2 grams (which amounted to 0.15% of the total mass of each beam), so it did not affect the mass distribution of each beam. Moreover, each beam was covered with reflective tape to improve the laser vibrometer signal quality. To perform the vibrometer measurements a total of 9 grid points were utilized as sensing locations along the longitudinal symmetry axis of each beam in order to identify the lower-frequency lateral bending modes of the beams. The placement and labeling of the measurement grid are presented in in Fig. 3.22. Only one half of the beam is labeled due to the symmetry of the problem. A junction box (PSV-E-400-H4) and an acquisition board (NI

PCI-4452) are used for data acquisition with a sampling frequency of 6.4 kHz (the total duration of each time signal is limited to 2.56s). After averaging three successful hits per grid point, the measurements for all nine points are recorded and the average spectra of the force, velocity and acceleration signals were checked; the Fast Fourier Transform (FFT) settings were set to a 2.5 kHz bandwidth with 0.39 Hz resolution, and rectangular windows were applied to all measured signals.

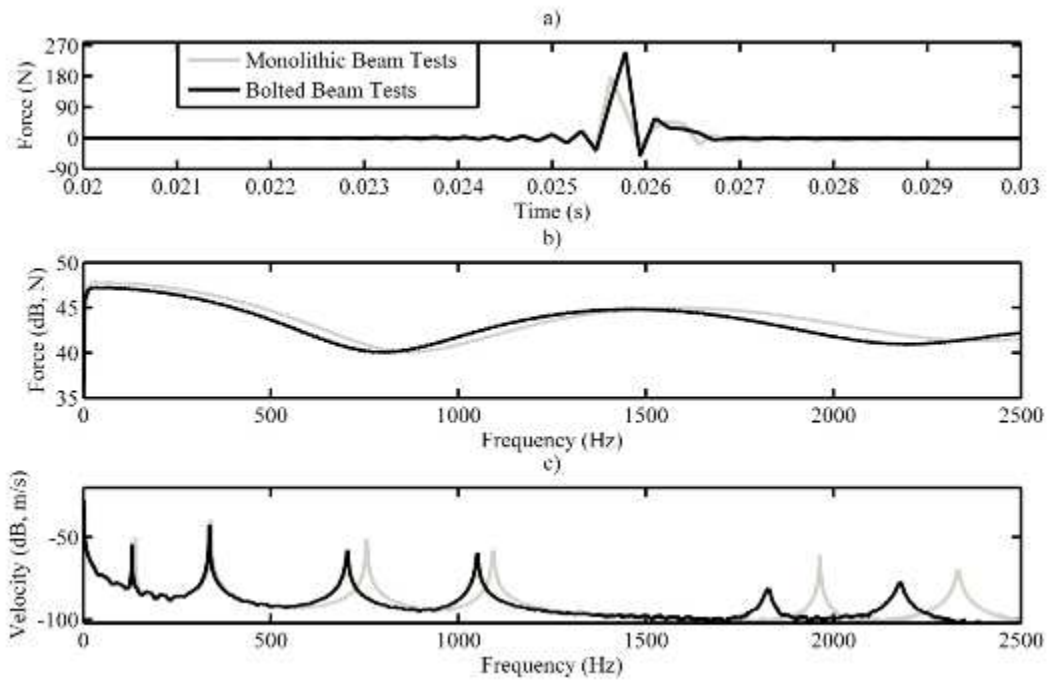


Figure 3.23 Typical forcing and velocity spectra in the experimental tests for the monolithic and bolted beams: (a,b) Applied force in time and frequency domains, (c) velocity spectra

An example of force input and velocity measurements (in time and frequency domains) are presented in Fig 3.23 for the monolithic and bolted beams. The force inputs resemble perfect impulses within the bandwidth of interest; *i.e.*, there is a 5-6 dB drop in the power spectrum over the frequency range of interest from 0 and 2,500 Hz. Considering the velocity spectra for both beams, six clear peaks corresponding to the first six bending modes of the free-free fixtures can be identified, whereas no torsional modes appear [the low frequency mode with nearly zero frequency correspond to rigid body (pendulum) modes,

since the beams tested were suspended by nylon cords in order to impose free boundary conditions]. Even though the force inputs seem to be nearly identical for both beams, the corresponding velocity response spectra differ significantly, especially considering the higher bending modes; indeed, the spectrum of the bolted beam indicates increased compliance and damping compared to the monolithic beam. Clearly, this difference is attributed solely to the frictional interface in the bolted beam assembly, as the lap joint inevitably softens the overall stiffness of the beam, and introduces friction forces over the contact patch leading to energy dissipation and increased damping. Note, however, that the softening and energy dissipation effects are not affecting uniformly all modes within the frequency range of interest, but rather a subset of them. One of the main objectives of this work is to identify and model the effects of the lap joints on the individual modes of the bolted beam.

As mentioned above, measurements from 5 different positions along one half of each beam are recorded for a time window of 2.56 s. Typical time series measured from the five sensing positions on the monolithic beam are presented in Fig. 3.24. FFTs and wavelet spectra for each time series are also provided and, except for sensing position 5, contain a sufficient amount of modal data for all six bending modes of interest. Sensing point 5 coincides with the mid-point of the beam and, hence, corresponds to the nodal point for the 2nd, 4th and 6th modes; this can be inferred from the wavelet spectra that show the frequency contents of the time series, as well as the relative contribution of each mode to the response. Moreover, the rigid body (pendulum) mode of the beam can be observed directly in the frequency content of the time series (as pointed out in the previous section, the suspending nylon cords are 1.6 m long, leading to a pendulum mode of approximately 0.4 Hz). The corresponding signals obtained from the bolted beam resemble their monolithic equivalents with softening and added dissipative effects mentioned above. In the next subsection we perform linear modal

analysis of the experimental measurements in order to use the results as a basis for comparison with the NSI methodology.

3.3.3 Linear Modal Analysis

As a first step, experimental modal analysis is used to extract the modal parameters of the leading six bending modes of the two beams. These are identified by analyzing mobility functions from sensing location 1 by the rational fraction polynomial (RFP) method (Richardson and Formenti 1982), as if the dynamics were linear; whereas this assumption holds for the monolithic beam, it does not hold for the bolted beam due to the frictional interface at the lap joint.

Indeed, the RFP method using a single degree of freedom (SDOF) approximation yields very successful results for the monolithic beam, since it is a linear structure with limited modal interactions. In contrast, the bolted beam measurements cannot be matched adequately using a SDOF approximation in the RFP method; instead, the multi-DOF variant of RFP is employed. The RFP curve-fits with SDOF and 3-DOF approximations for the mobility plots measured at sensing position 3 are presented in Fig 3.25. Although the peaks are matched satisfactorily with the 3-DOF RFP method, there are additional resonances or anti-resonances created by the RFP algorithm that are computational artifacts resulting in modal damping values that are either unrealistically high or even negative (unstable modes). Clearly, these modes have no physical meaning and arise due to the fact that a *linear* modal analysis technique is used to curve-fit *nonlinear* data. Hence, the existence of these artificial resonances and anti-resonances in a best-fit condition is an automatic indication of the presence structural nonlinearity in the frequency domain of the measurements of the bolted beam (Ewins 1984).

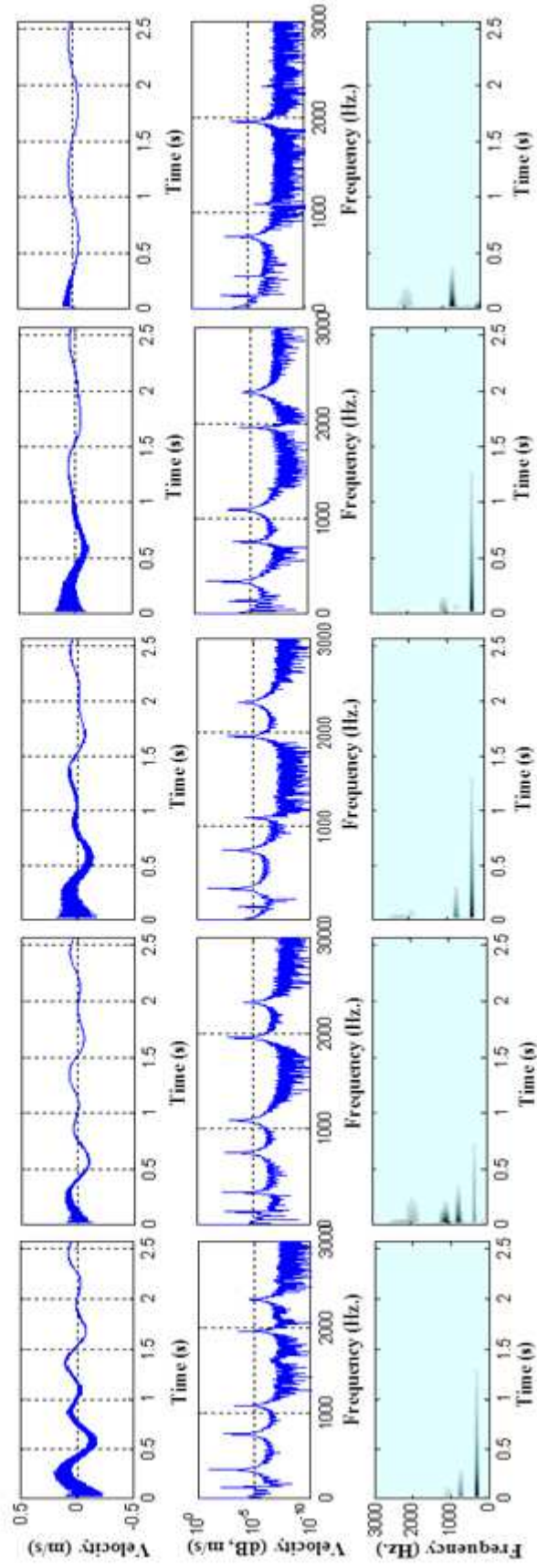
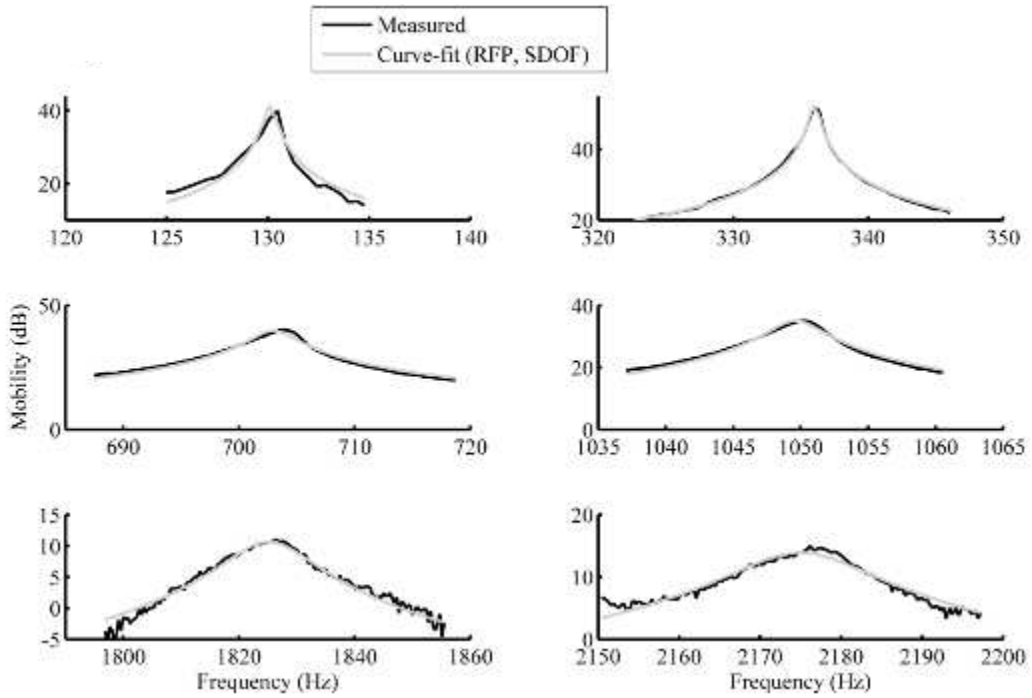
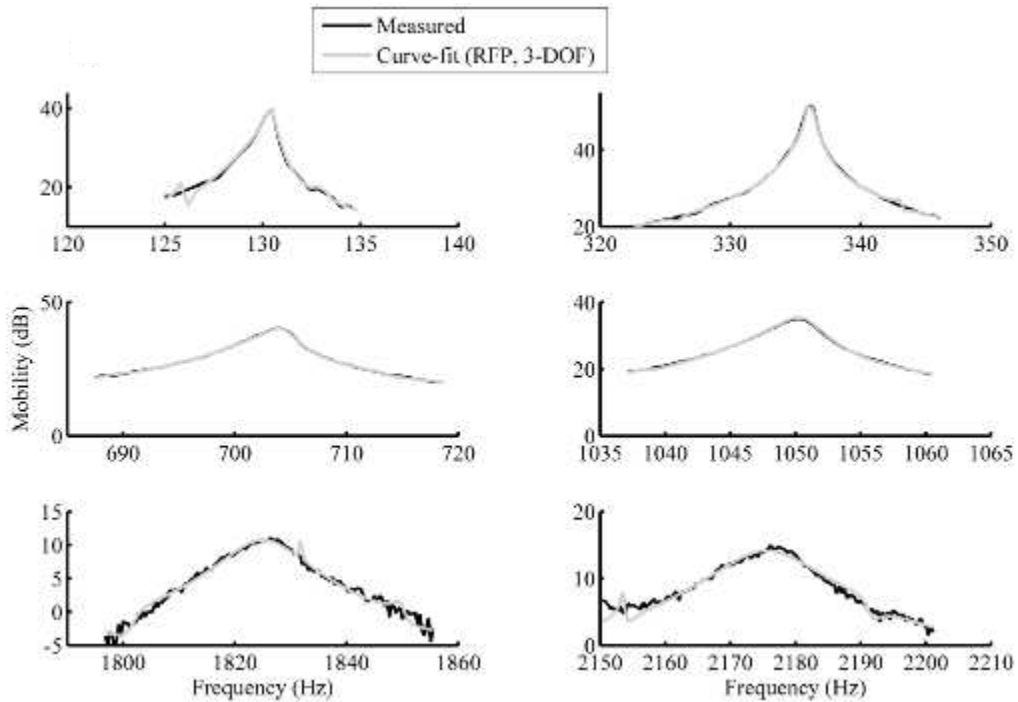


Figure 3.24 Velocity(m/s) measurements at 5 sensing positions on the monolithic beam showing time series, FFTs and wavelet transforms.



(a)


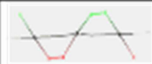






(b)

Figure 3.25 Measured and reconstructed mobility FRFs from sensing position 3 based on the RFP method with (a) SDOF and (b) 3-DOF curve-fitting algorithms.

In Table 3.3, we summarize the experimental modal frequencies (Hz) and viscous damping ratios (%) extracted from the mobility frequency response functions (FRFs). The parameters are fairly consistent for the mobility FRFs derived from all sensing positions. Bolted beam measurements yield significantly lower modal frequencies and higher modal damping ratios compared to the monolithic beam, especially for the higher modes; as mentioned previously these effects are due to the frictional interface. The mode shapes presented in Table 3.3 are obtained using laser vibrometry (Polytec PSV-400 with PSV-S-UNI-HM software and PSV-S-ImpGeo geometry import option) considering only the leading six bending modes and using 9 grid points along the beam.

Table 3.3 Experimental Linear Modal Analysis for the Monolithic and Bolted Beams

Modal Shapes	Monolithic Beam w. Bolts 55 lb-in.		Bolted Beam w. Bolts 55 lb-in. (SDOF)		Bolted Beam w. Bolts 55 lb-in. (3-DOF)	
	Frequency (Hz) f_{avg}	Damping Ratio ζ_{avg} (%)	Frequency (Hz) f_{avg}	Damping Ratio ζ_{avg} (%)	Frequency (Hz) f_{avg}	Damping Ratio ζ_{avg} (%)
	138	0.15	130	0.2	130	0.18
	340	0.08	336	0.1	336	0.09
	755	0.10	703	0.23	704	0.18
	1093	0.13	1050	0.16	1050	0.17
	1963	0.05	1825	0.34	1825	0.32
	2333	0.2	2177	0.35	2177	0.34

3.3.4 Nonlinear System Identification

As mentioned in subsection 2.2, the EMD technique is a time-domain method used to decompose a time series into a set of nearly monochromatic time series. The measured time series that will be analyzed are the transverse velocity measurements at each of the sensing positions 1-5 depicted in Fig 3.24. As shown in Fig 3.24, each velocity signal is composed of

several harmonics corresponding to the excitation of the bending modes. EMD decomposes a given measured velocity signal in terms of IMFs which provide information about the modal content of the signal. Hence, the participation of each mode – that is, the corresponding IMF – can be studied in isolation from the other modes. It follows that the first step of the NSI methodology is to analyze the measured time series by EMD.

A demonstration of application of the EMD procedure is presented Fig 3.26, where the velocity signal measured from sensing point 1 of the monolithic beam and resulting IMFs are depicted. We note that in our analysis EMD was enhanced with application of masking signals and heterodyning (Deering and Kaiser 2005; Senroy and Suryanarayanan 2007; Lee, Tsakirtzis, et al. 2011), in order to accurately decompose the signal in terms of IMFs. The wavelet spectrum of the measured time series response shows the existence of three separate frequency bands, mainly corresponding to the 2nd, 3rd and 4th bending modes, and a very weak band for the 1st mode. The same trend can be observed when considering the time series of the corresponding IMFs and their wavelet spectra. Since the IMFs are nearly monochromatic, they contain additional frequency components of lesser magnitudes. This is because it is not possible to compute a fully-orthogonal set of IMFs (Lee, Tsakirtzis, et al. 2009; Lee, Tsakirtzis, et al. 2011); for example, random noise and speckle effects introduced in the velocity measurements by the vibrometer can contaminate the signals over broad frequency ranges. In addition, for weakly excited modes (such as the 1st mode in the measurement of Figure 3.26), frequency contamination from neighboring modes may be inevitable due to the very nature of the EMD technique. Finally, we note that the rigid body mode was subtracted from the response so that it does not appear as an IMF in the results of Figure 3.26.

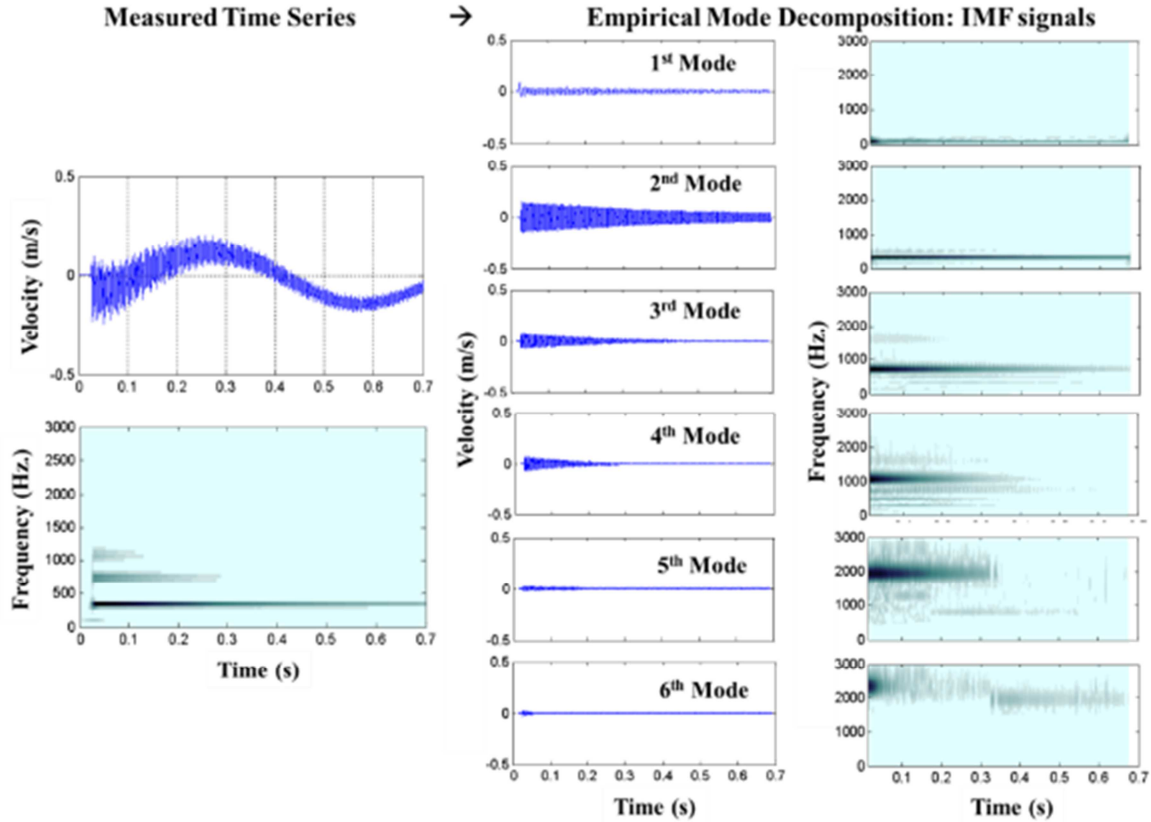


Figure 3.26 EMD analysis of the velocity time series at sensing position 1 on the monolithic beam.

The next step in the nonlinear system identification methodology is to model and reproduce the dominant IMFs in terms of a set of IMOs, as discussed in Chapter 2. The IMO forcing amplitudes are calculated directly from the IMF signals using relation (12) for viscous damping ratios equal to $\lambda_i = 0.1$. As discussed previously this damping ratio yields a satisfactory match between each IMF and the corresponding IMO because of the light structural damping. As demonstrated in the example in Section 3.1, an IMO damping ratio sufficiently larger than the physical damping of the system (*i.e.*, $\lambda_k \gg \zeta_k$) generally guarantees satisfactory reproduction of the corresponding IMF. The corresponding IMO responses match well with the measured IMFs for all the modes in the frequency range of interest. For example, the four highest frequency modes possess higher energies than the two lower frequency modes for measurements taken from sensing location 1; this can be explained

by studying the deformations of the modal at this sensing location. Moreover, the rigid body mode (pendulum swing motion) is extracted directly from the measured time series by the EMD procedure, and summed with the six IMO responses to reconstruct the measured velocity signals at each of the sensing positions. In Figure 3.27, we provide a typical comparison of the experimental and reconstructed velocity time series for sensing position 1 of the monolithic and bolted beams. We note good agreement between these responses. Such comparisons validate the NSI methodology and demonstrate that the leading six bending modes are sufficient for reproducing the experimental measurements. Finally we note that in both monolithic and bolted beam cases, the fast frequencies of the IMOs are found to coincide with the corresponding damped modal frequencies; in essence, each of the IMOs corresponds to a structural mode. Hence, in the following discussion, ‘IMO’ and ‘Mode’ will be interchanged in the discussion of the NSI results.

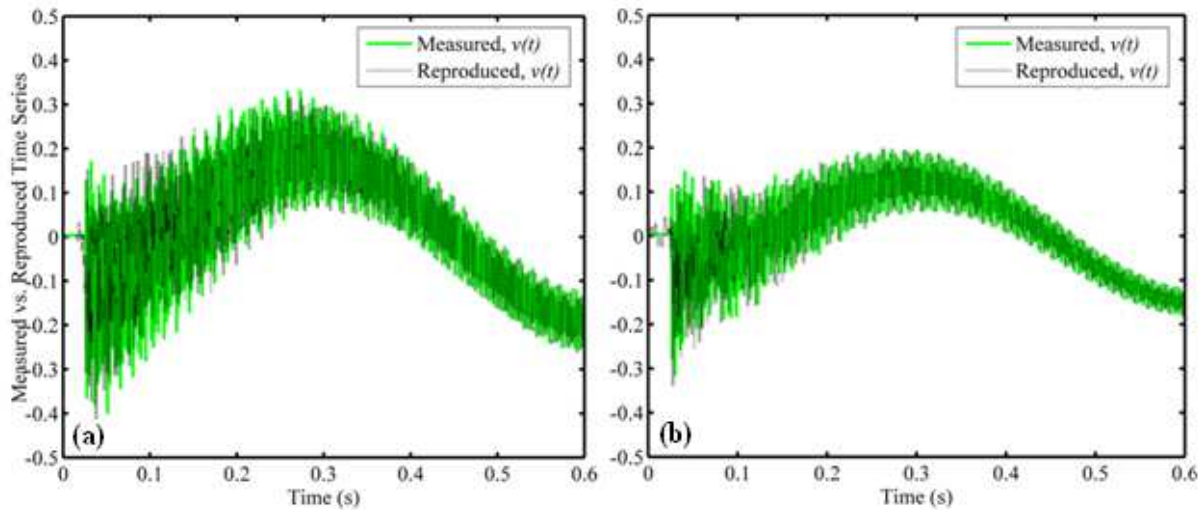


Figure 3.27 Measured and reconstructed velocity time series at sensing position 1 of (a) and (b) bolted beams; the reconstructed response was computed as the superposition of the IMO responses with the rigid body (pendulum) mode.

3.3.5 Nonlinear Frictional Effects

The complex forcing amplitudes $\Lambda_k^{(i)}(t)$ of the IMOs contain essential information about the slow-flow dynamics of the modal coordinates and nonlinear interactions between the multi-scale dynamics. The linear modal analyses provided in subsection 3.3.3 were performed under the assumption that the structural responses were composed of nearly decoupled modes, so that individual modal responses could be approximated by linear oscillators. From that example we recall that for a good match between the measured IMFs and the corresponding IMOs it was necessary that the damping ratios of the IMOs be much greater than the modal dampings, and under that condition the logarithms of the magnitudes of the complex forcing amplitudes of the IMOs could be approximated as linear functions of time; then for the i -th harmonic component of the measurement at the k -th sensing position it holds that

$$\ln \left| \Lambda_k^{(i)}(t) \right| \approx C_k^{(i)}(\lambda_k^{(i)}, \omega_i, \zeta_i, F_i) - \zeta_i \omega_i t, \quad k = 1, \dots, 5, \quad i = 1, \dots, 6 \quad (3.19)$$

In this notation ζ_i is the modal damping of the i -th mode, ω_i is the i -th modal (fast) frequency, F_i is the impulse amplitude acting at the i -th mode, and, $\lambda_k^{(i)}$ is the damping ratio of the i -th IMO of the response at the k -th sensing position. The real coefficient $C_k^{(i)}(\lambda_k^{(i)}, \omega_i, \zeta_i, F_i)$ can be assumed to be constant with respect to time (in actuality it is an oscillatory function due to fast oscillatory components, but a low pass filter can remove these oscillations). It follows that *linear temporal decay of the logarithm of the magnitude of the complex forcing amplitude of an IMO indicates linear dynamic behavior of that mode*, with the corresponding rate of decay being approximately equal to the viscous modal damping ratio. Moreover, based on this finding, we may state that *any deviation from linear decay of*

the temporal plot of the logarithm of the magnitude of the complex forcing of an IMO with respect to time is representative of nonlinear dynamical behavior of that mode.

In Figure 3.28, we depict the temporal evolutions of the magnitudes of the forcing amplitudes of the six IMOs of the velocity response at sensing position 1 of the monolithic beam. In the absence of a mechanical joint in this structure we expect the dynamics to be linear, and this is confirmed by the results of this Figure. In addition to the actual forcing amplitudes, low-pass filtered versions (with cut-off at 60 Hz) and the theoretically predicted linear modal approximations (LMAs) [based on multi-DOF RPF modal analysis of the measured time series and relation (21)] are plotted in Figure 11. We note that the plots decay approximately linearly with time as long as the signal-to-noise ratios are above a certain threshold, whereas deviations occur only after the signals decay to nearly zero values. In particular, the three leading IMOs are nearly zero after approximately 0.69 sec; however, the 4th, 5th and 6th IMOs nearly vanish after 0.4, 0.56 and 0.2 sec, respectively. These times are exactly the instants when the linear decays of the plots break down, and highly-oscillatory behaviors occur for larger times, which should be regarded as computational artifacts.

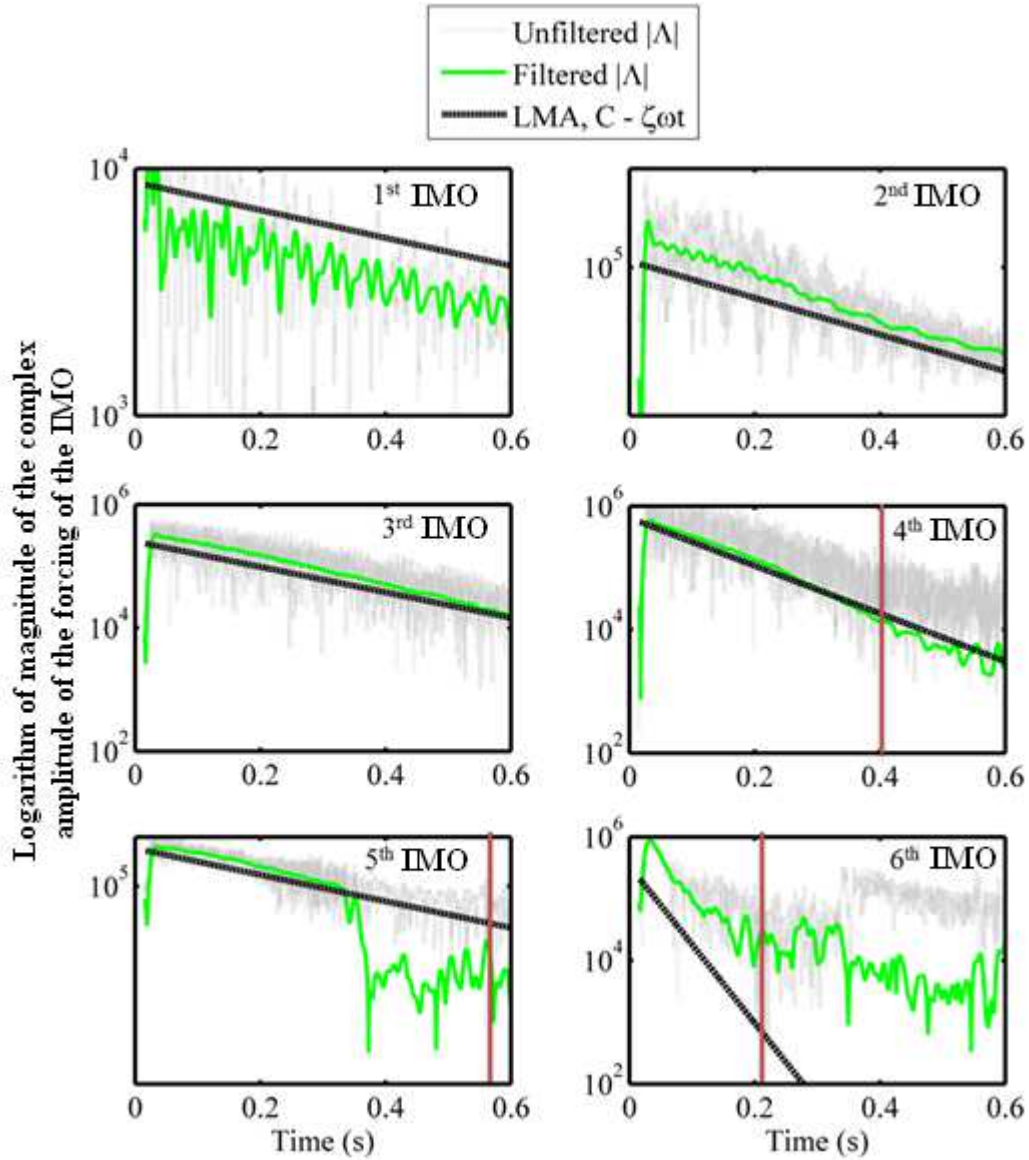


Figure 3.28 Logarithms of the magnitudes of the complex forcing amplitudes for the six IMOs of the velocity time series measured at sensing location 1 of the monolithic beam; both unfiltered and low-pass filtered data are shown and compared to theoretically predicted LMAs according to (21) (vertical line denotes the time instant where an IMO is nearly zero).

In Figure 3.29, we depict the results of a similar study for the forcing amplitudes of the IMOs of the experimental velocity time series at sensing position 1 of the bolted beam. As in Figure 3.28, the experimental results are compared to the theoretical prediction based on multi-DOF RFP modal analysis of the measured time series (the corresponding modal parameters are listed in Table 1). We note that the linear prediction correlates reasonably well

with the experimental results for the even-order modes (in the time period where the signal to noise ratio is sufficiently large), but deviates considerably for the odd-ordered modes. This clearly suggests that only a subset of structural modes is affected by the frictional nonlinearity at the joint (the modes of odd order), whereas there is a subset of modes of even order that is not affected by the nonlinearity. This is reasonable, since the frictional interface located in the middle of the bolted beam introduces additional damping to the structural response; however, even-order modes are influenced very little by the joint since they have a node at the position (and source) of the frictional nonlinearity. As in the monolithic case, a vanishing IMO signal causes artificial oscillatory behavior in the computed forcing amplitudes, especially for the 5th and 6th IMOs. Nevertheless, the other IMOs as well as the initial parts of the 5th and 6th IMOs clearly demonstrate the effect of friction and mismatch compared to the linear theoretical predictions. Moreover, by computing the variations of the slopes of the filtered results in Figure 3.29 we can derive estimates for the variations of equivalent viscous damping ratios due to the frictional nonlinearity, and obtain quantitative estimates of the nonlinear effects on each IMO (mode) of the structural response. This result will be used in the next subsection to study the spatial distribution of the nonlinear effects across the length of the bolted beam at different levels of impulsive excitation.

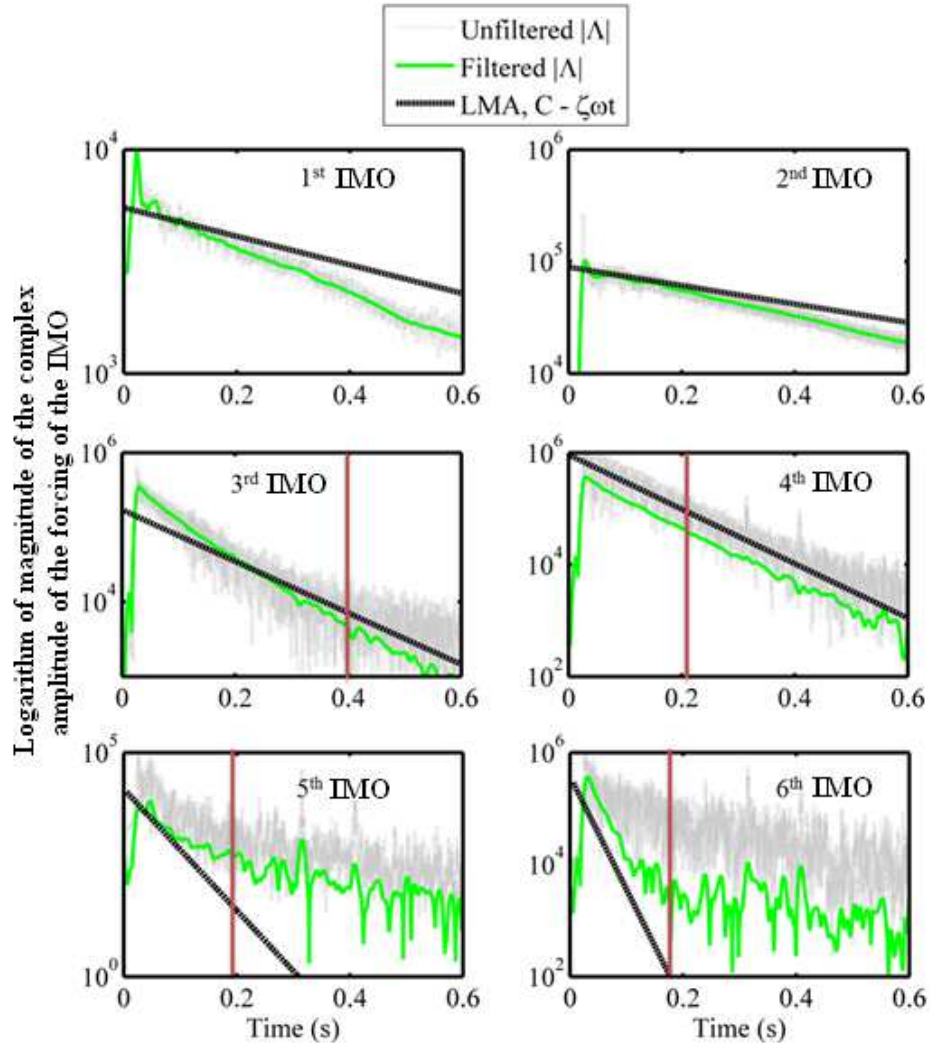


Figure 3.29 Logarithms of the magnitudes of the complex forcing amplitudes for the six IMOs of the velocity time series measured at sensing location 1 of the bolted beam; both unfiltered and low-pass filtered results are shown and compared to theoretically predicted LMAs according to (21) (vertical line denotes the time instant where an IMO is nearly zero).

Note that the analyses above are conducted using the forcing amplitudes of the IMOs corresponding to the velocity time series measured at a single point (sensing position 1) on the bolted beam. By analyzing velocity time series measured at the other sensing positions we can study the spatial distribution of the nonlinear frictional effects along the span of the bolted beam. In Figures 3.30 and 31, we depict the spatio-temporal variations of the logarithms of the moduli

of the forcing amplitudes of the IMOs, $\ln|\Lambda_k^{(i)}(t)|$ [where $k = 1, \dots, 5$ denotes the sensing position and $i = 1, \dots, 6$ the dominant harmonic (mode)], for the monolithic and bolted beams, respectively. All plots are expected to decrease linearly in time for the monolithic beam, and indeed this is confirmed until the time instants where the measured signals nearly vanish.

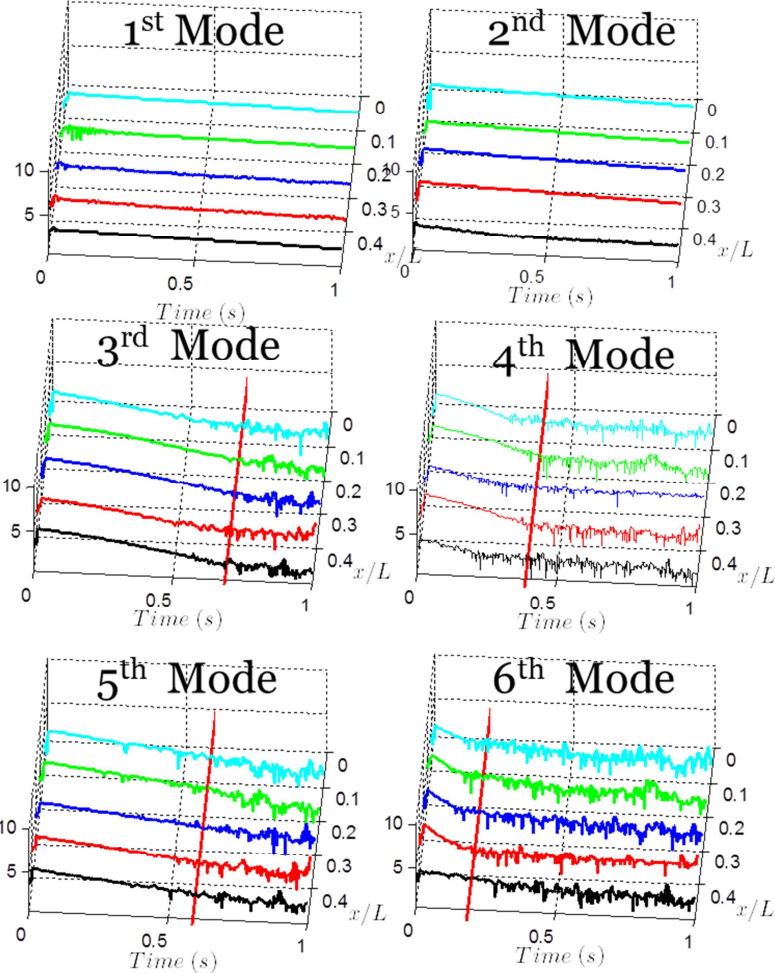


Figure 3.30 Spatio-temporal variations of $\ln|\Lambda_k^{(i)}(t)|$ for the monolithic beam; the cross-line in each plot indicates the time instants of vanishing signals due to damping.

For the bolted case shown in Figure 3.31, nonlinear deviations due to the frictional contact are noted in the spatio-temporal patterns especially for the 4th and 5th IMOs. In this case, we can

study the spatial distribution of the nonlinear frictional effects along the span of the bolted beam by studying the local slopes of the graphs of Figure 3.31 as they involve in time and space. In addition, we note that the mode shapes of the bolted beam are nearly identical to the corresponding mode shapes of the monolithic beam, so frictional effects do not influence the mode shapes (these are influenced predominantly by nonlinear stiffness effects, which are absent in the present case).

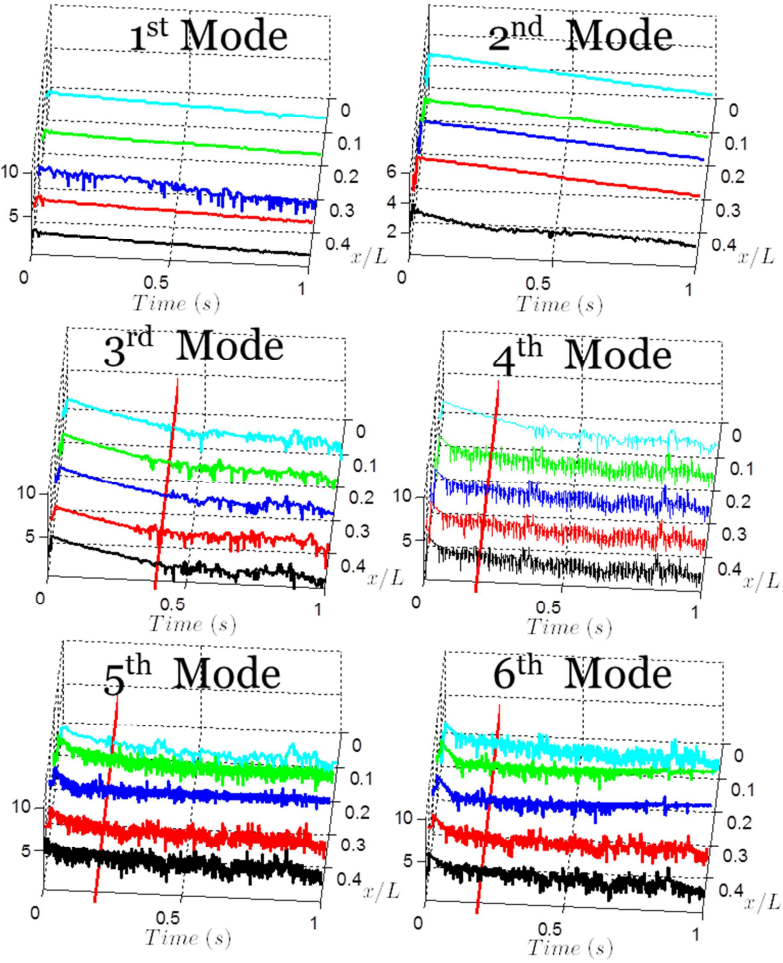


Figure 3.31 Spatio-temporal variations of $\ln|\Lambda_k^{(i)}(t)|$ for the bolted beam; the cross-line in each plot indicates the time instants of vanishing signals due to damping.

Up to this point, the analysis of the nonlinear effects was purely qualitative, except for the comparison of the dynamics of the monolithic and bolted beams with experimental modal analysis of subsection 3.2; therefore, we need to define quantitative or statistical measures to study in detail the nonlinear frictional effects. For this purpose, we compute Pearson's linear correlation coefficient (Kurt et al. 2012) for the moduli of the slowly varying complex forcing amplitudes $\Lambda_k^{(i)}(t)$ for all IMO of the monolithic and bolted beam cases (*i.e.*, for $i = 1, \dots, 6$), and at all positions along the beam (*i.e.*, for $k = 1, \dots, 5$). This linear correlation coefficient – LCC is widely utilized in statistics as a measure of the linear dependence between two variables and in this work was implemented through MATLAB. The expression used to compute LCC is

$$\text{LCC} = \left| \text{corr} \left(\ln(|\Lambda_{k,monolithic}^{(i)}|), \ln(|\Lambda_{k,bolted}^{(i)}|) \right) \right| = \frac{100}{N} \times \left| \sum_{n=1}^N Z_{\ln(|\Lambda_{k,monolithic}^{(i)}|)} Z_{\ln(|\Lambda_{k,bolted}^{(i)}|)} \right| \quad (22)$$

where N is the data array dimension, and variables $Z_{\ln(|\Lambda_{k,monolithic}^{(i)}|)}$ and $Z_{\ln(|\Lambda_{k,bolted}^{(i)}|)}$ denote the scores (distance between the raw data and the mean of this data in units of standard deviation) of the variables $\ln(|\Lambda_{k,monolithic}^{(i)}|)$ and $\ln(|\Lambda_{k,bolted}^{(i)}|)$.

In Figure 3.32, we depict the interpolated strips along the beam of the absolute value of the linear correlation coefficient for the first 6 modes for durations of 0.1, 0.15, 0.2 and 0.25 seconds. These four snapshots are selected in order to study how the correlation of the forcing amplitudes of the IMO of the monolithic and bolted beams evolves in time for each of the six bending modes in the frequency range of interest. It is clear from the results of Figure 3.32 that the strongest linear correlation between the dynamics of the monolithic and bolted beams is realized for the 2nd and the 4th modes (IMOs), with corresponding correlation values on the order

of 95%. Since the source of frictional nonlinearity in the bolted beam is local and located exactly at the middle of the beam, the even-order modes are expected to be influenced less by the nonlinearity (since each of these modes possesses a node at the bolted joint); the high values of the correlation coefficient noted for the 2nd and 4th modes confirm this fact.

Focusing now on the 3rd mode of the bolted beam, we note that in the initial snapshot strong linear correlation with the corresponding mode of the monolithic beam is observed. However, in later snapshots this correlation gradually deteriorates; a similar behavior is noted for the correlation of the 6th mode. In general, the odd-ordered modes of the bolted beam show weak correlation with the corresponding modes of the monolithic beam, indicating that the nonlinear frictional effects affect mainly these modes. In addition, examining the odd-ordered modes, we note a slight decrease of the linear correlation coefficient as the mid-span of the beam is approached; this is expected due to the location of the bolted joint at this position. The correlation values at each modal strip and spatial coordinate can be used as a quantitative measure of the effects of the frictional nonlinearity. In the bolted beam experiments, the frictional interface does not affect the modal frequencies much (this can be confirmed by the experimental modal analysis results of Table 3.3), but frictional dissipative effects introduce additional damping in each mode.

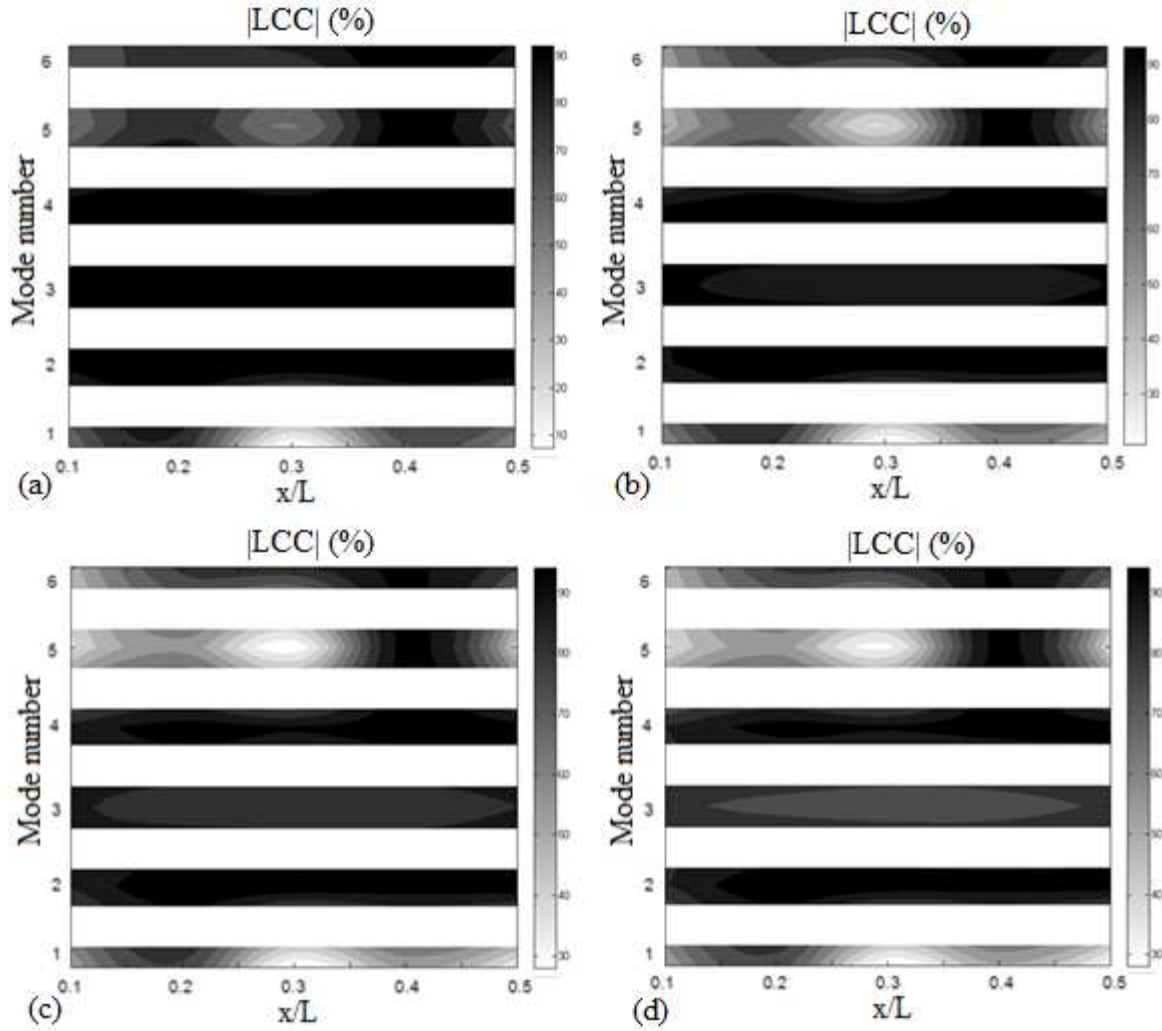


Figure 3.32 Absolute value of the linear correlation coefficient (%) (interpolated along the half-span of the beam) for (a) $t = 0.10\text{sec}$, (b) $t = 0.15\text{sec}$, (c) $t = 0.20\text{sec}$, and (d) $t = 0.25\text{sec}$.

While a study based on the linear correlation coefficient provides physical insight into the spatial distribution of the frictional effects on the dynamics, it does not provide any information regarding the temporal variation of the nonlinear effects along the half-span of the bolted beam. Such effects can be studied by defining equivalent damping coefficients based on computations of local slopes of the graphs of $\ln|\Lambda_k^{(i)}(t)|$ versus time for each IMO and at each sensing position along the bolted beam.

3.3.6 Equivalent Damping Ratios

Considering the results of Figure 3.29 in the previous subsection, we mentioned that the deviations of the graphs of $\ln|\Lambda_k^{(i)}(t)|$ from the linear decaying behavior predicted by LMA provide a clear indication of the presence of nonlinear damping effects in the IMO responses. Given the fact that the dynamics of the bolted beam is expected to reach a linearized limit for sufficiently small impulsive excitation, we anticipate that the nonlinear effects should decrease with decreasing applied excitation. To verify this, we performed three independent hammer tests of the bolted beam by applying strong, moderate and light impulsive excitations at the same forcing position on the beam indicated in Figure 3.22. The case of strong excitation corresponds to the results reported in the previous subsection. In Figure 3.33, we present the time histories of the three different impulsive excitations realized in the experiments, and focus on the velocity time series measured at each sensing position of the bolted beam. In particular, after decomposing the experimental time series into their dominant IMFs by means of EMD, we construct sets of IMOs that reconstruct the extracted IMFs. Based on these reconstructions we compute the quantities $\ln|\Lambda_k^{(i)}(t)|$, $k = 1, \dots, 5$, $i = 1, \dots, 6$ for each experimental test based on the forcing terms of the IMOs. Lastly, we compute the average slopes of graphs of $\ln|\Lambda_k^{(i)}(t)|$ in order to estimate equivalent modal damping ratios ζ_i for each mode, at each sensing position, and for each of the three experimental tests.

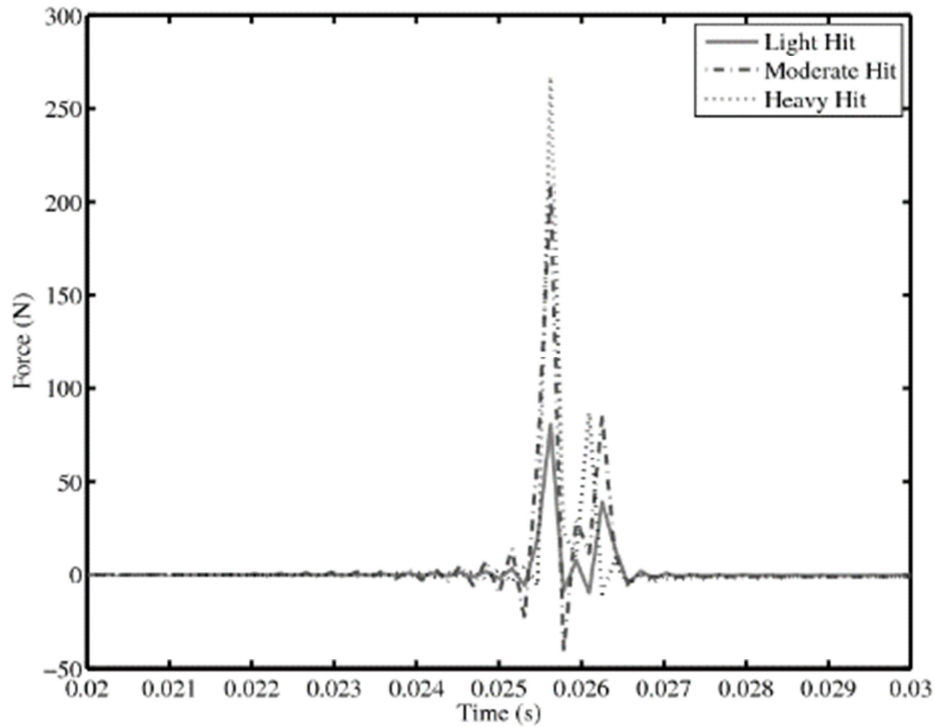


Figure 3.33 The three different impulsive excitations applied to the bolted beam.

The energy applied to each mode (IMO) is estimated at the time instant immediately after the application of the hammer excitation by assuming that this energy scales with the square of the measured initial velocity of the mode at the point of impact. Hence, heavy, moderate and light hit experiments give three different energy levels and corresponding damping ratios for each mode and at each sensing position along the half-span of the bolted beam. For each mode (IMO) the results are interpolated in the spatial direction and in the applied energy. The results of this analysis are depicted in Figure 3.34. It is clear that the equivalent damping ratios for the odd-order modes exhibit a significant increase with increasing energy, indicating an increase in the friction-induced damping nonlinearity as the magnitude of the applied impulse increases; on the contrary, even-order modes are not influenced much by the increase in applied impulse,

confirming the small influence of frictional effects on the dynamics of these modes. Moreover, the results of Figure 3.34 not only yield quantitative measures of the frictional damping effects, but also provide the spatial distribution of these effects along the half-span of the bolted beam and their dependence on energy. We note, however, that the appearance of nodes may lead to deterioration of the results (this can be seen, for example, by the results of the first mode at $x/L \approx 0.3$).

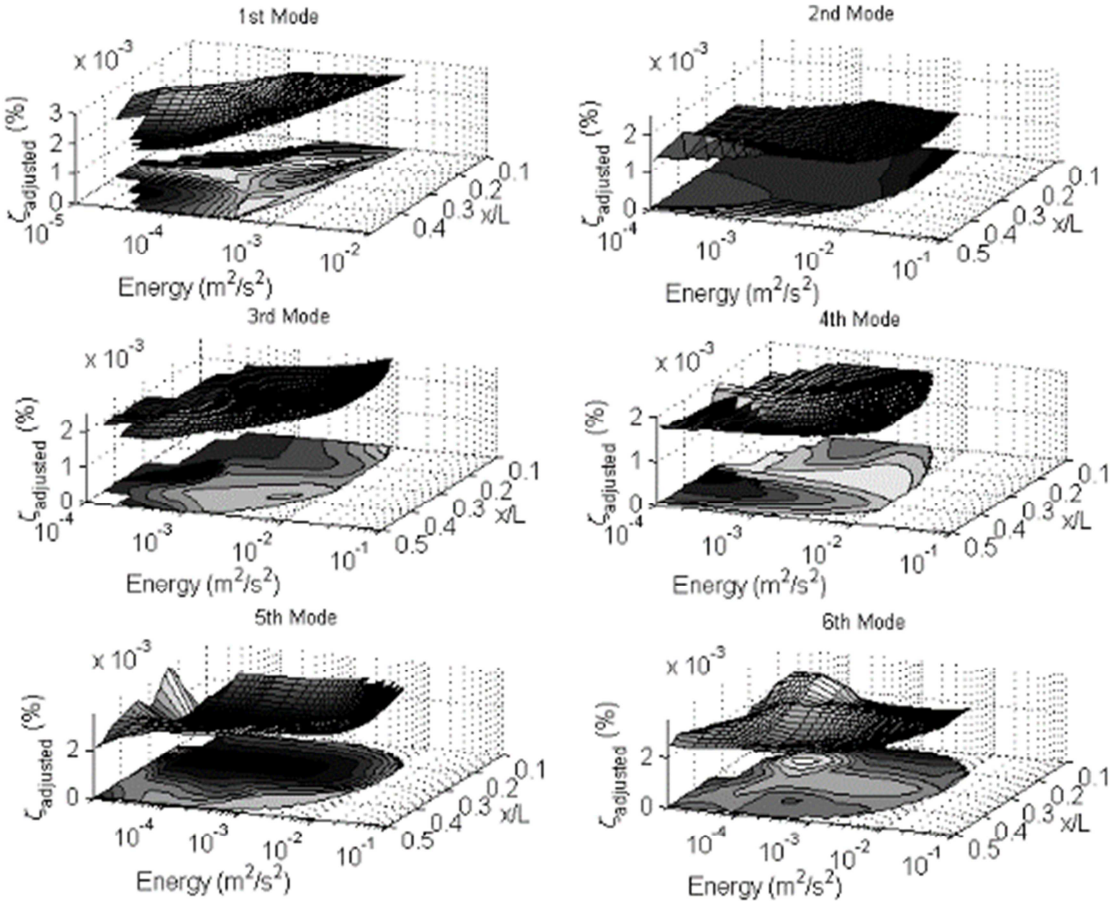


Figure 3.34 Equivalent modal damping ratios extracted by the NSI methodology; each plot depicts the spatial dependence of this ratio on the applied modal energy.

3.3.7 Concluding Remarks

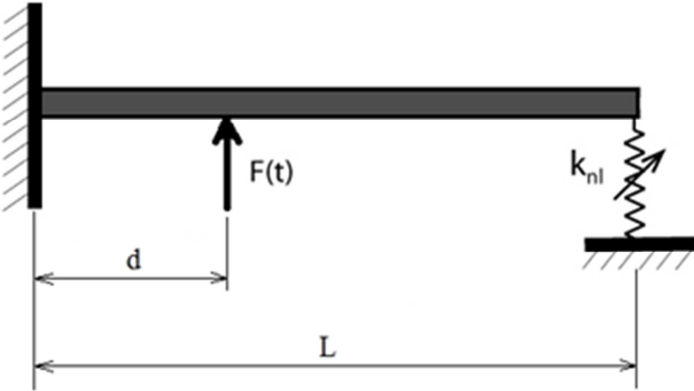
We applied a new nonlinear system identification methodology to the analysis and modeling of the nonlinear damping effects induced by a frictional interface on the dynamics of a beam with a bolted joint connection. The analysis was performed by decomposing measured time series using empirical mode decomposition (EMD), and modeling the resulting dominant intrinsic modal functions (IMFs) in terms of sets of intrinsic modal oscillators (IMOs) that capture the multi-scale dynamics in the measured time series. In particular, we showed that by studying the temporal decays of the logarithms of the moduli of the complex amplitudes of the forcing functions of the IMOs we can deduce the nonlinear damping effects in the dynamics. This is due to the fact that linear modes correspond to linear decays of these quantities, so deviations from this linear decay law provide clear indications of the presence of nonlinear damping effects in the measured data. Based on this finding we were able to provide estimates for the nonlinear damping effects of the frictional interface on the beam dynamics, study how these damping effects are distributed along the span of the beam, and analyze the dependencies of these nonlinear effects on the level of energy (or applied level of external applied excitation). The outlined methodology can be employed to study nonlinear damping effects in structural assemblies with more complex mechanical joints, and nonlinear stiffness effects in structural components with local or distributed nonlinearities of a different source (*e.g.*, geometric, kinematic or material nonlinearities). Moreover, it is possible to study the effects of non-proportional (linear or nonlinear) damping distribution on the modal responses, and conceive methods for modeling such effects and for examining how these effects perturb the results of classical experimental modal analysis.

3.4 Strongly Nonlinear Beats in the Response of a Beam with a Strongly Nonlinear Stiffness (Kurt, Eriten, et al. 2014a)

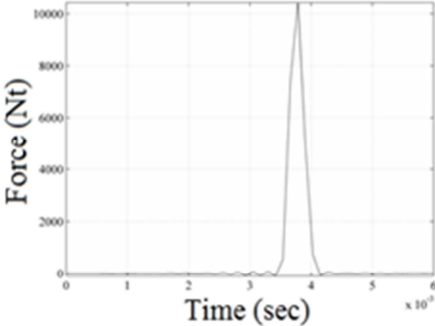
3.4.1 Introduction and System Description

In this work, we consider nonlinear system identification of a cantilever beam with an essentially (non-linearizable) nonlinear stiffness at its free end. Our aim is two-fold: First, we aim to show that this system can exhibit an unexpected nonlinear beat phenomenon resulting from internal resonances between beam modes that are coupled through the strong nonlinearity; second we will develop a nonlinear system identification methodology capable of identifying the parameters of the system and the participating modes for which nonlinear beats occur. In general, our motivation is to study and identify the strongly nonlinear dynamics that arise in flexible structures with local stiffness nonlinearities. Unexpected nonlinear beat phenomena involving low-frequency modes are observed in this system caused by strongly nonlinear modal interactions induced by the local essential stiffness nonlinearity. We provide an explanation of these nonlinear phenomena and then proceed to extend the NSI methodology reviewed in (Lee, Tsakirtzis, et al. 2011; Vakakis et al. 2011) in order to account for this type of complex multi-scale dynamics. We will do this by considering the nonlinear normal modes (NNMs) of the system in the frequency-energy domain. NNMs were defined as vibrations-in-unison of dynamical systems starting from the seminal works of (Rosenberg 1960; Rosenberg 1962) and were proposed in (Kerschen et al. 2009; Peeters et al. 2009) as a way to extend experimental modal analysis to the nonlinear regime. In the next section, we perform an NSI study of the nonlinear dynamics of the cantilever beam considering the linearized, weakly nonlinear and strongly nonlinear response regimes. The source of the strongly nonlinear beat phenomena in the dynamics of this system is investigated using a reduced order model based on Guyan reduction, showing the generation of multi-scale nonlinear

modal interactions due to the presence of a local, strong stiffness nonlinearity. Finally, in the last part, we extend the NSI technique to account for nonlinear beats in the measured time series, and then apply it to the NSI of the low-frequency nonlinear dynamics of the cantilever beam. We end the section with concluding remarks.



(a)



(b)

Figure 3.35. The system under consideration: (a) configuration, (b) applied impulsive force.

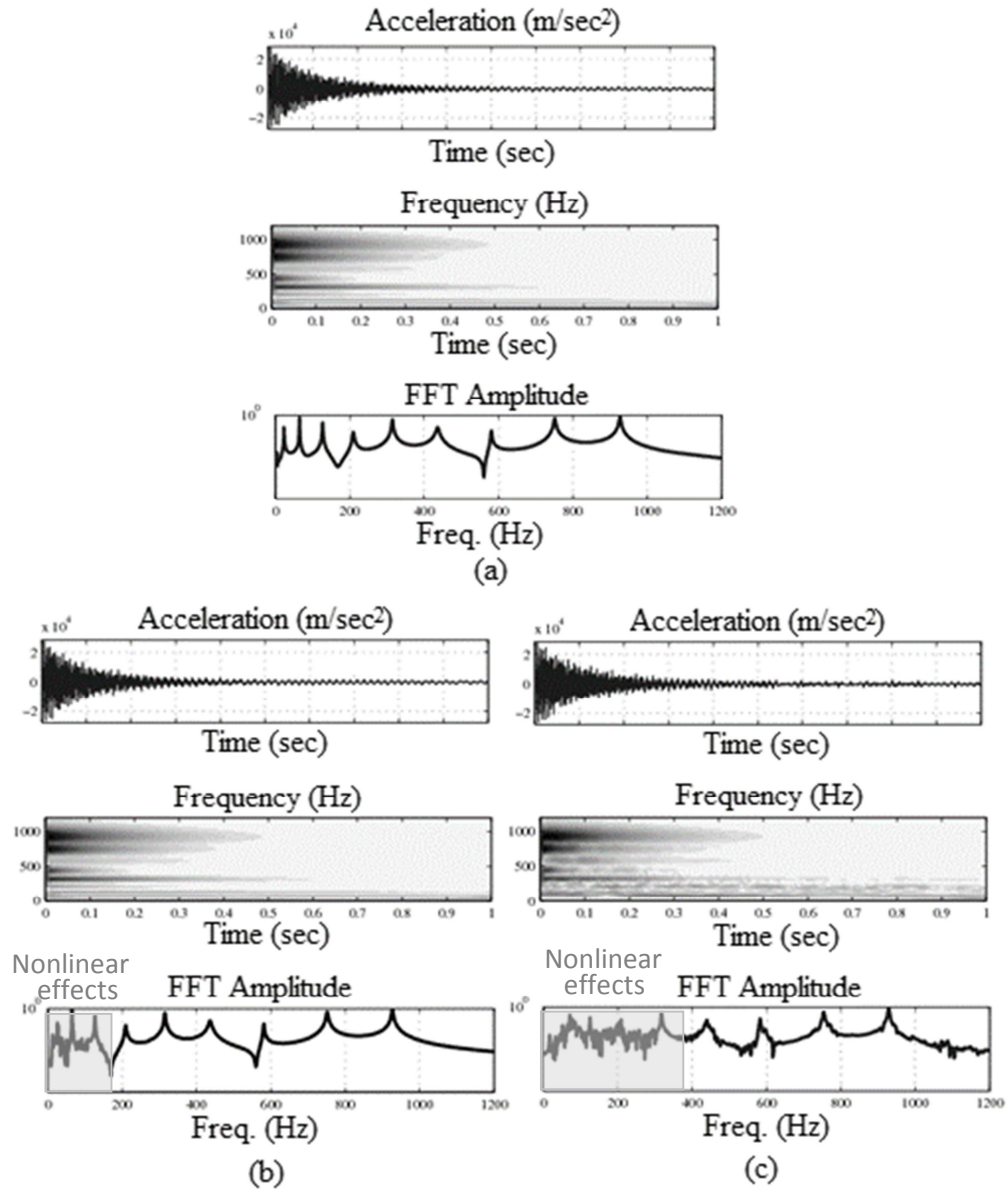


Figure 3.36. Acceleration of the tip of the beam: (a) Linear case (no nonlinear spring attached), (b) case of weaker nonlinearity, $k_{nl} = 10^8 \text{ N/m}^3$, (c) case of stronger nonlinearity, $k_{nl} = 10^{10} \text{ N/m}^3$.

In a series of simulations the dynamics of the system of Fig. 3.35 is studied for two different values of the nonlinear cubic stiffness (specifically, $k_{nl} = 10^8 \text{ N/m}^3$, and $k_{nl} = 10^{10} \text{ N/m}^3$), and for the case when the nonlinear spring is detached (*i.e.*, the linear beam). The results of the simulations are depicted in Fig. 3. For each simulated case we depict the transient acceleration of

the tip of the beam, together with its Morlet wavelet transform and Fourier spectrum. The wavelet transform provides information regarding the temporal evolutions of the dominant frequency components of the measured signals, and, hence, it can be regarded as a ‘dynamic analog’ of the classical Fourier transform that provides averaged information regarding the frequency content of a signal under the assumption of stationarity and linearity. The wavelet transform (WT) is especially useful for post-processing the nonstationary and nonlinear time series considered in this work.

From the examination of the linear (Fig. 3.36a) and nonlinear (Figs. 3.36b and 3.36c) we can readily deduce the effects of the strong nonlinearity on the dynamics. As evidenced by the WT plots and the Fourier spectra, the local nonlinearity considerably affects the frequency content of the response. Moreover, whereas the weak nonlinear stiffness case mainly affects the lower structural modes, the stronger nonlinear stiffness seems to affect the entire frequency range of the response.

3.4.2 Empirical Mode Decomposition

In this section, we post-process the previous nonlinear time series of the tip response of the beam by EMD. Although the EMD of the linear response of Fig. 3.36a is somewhat straightforward, this is not the case for the nonlinear time series of Figs. 3.36b and 3.36c, for which the analysis will pose some distinct challenges. First, due to the realization of nonlinear internal resonances between distinct nonlinear normal modes of the beam, we will encounter difficulties in extracting nearly monofrequency IMFs. Second, we need to determine a certain frequency value around which to extract a narrowband IMF, which is not generally trivial for the strongly nonlinear case.

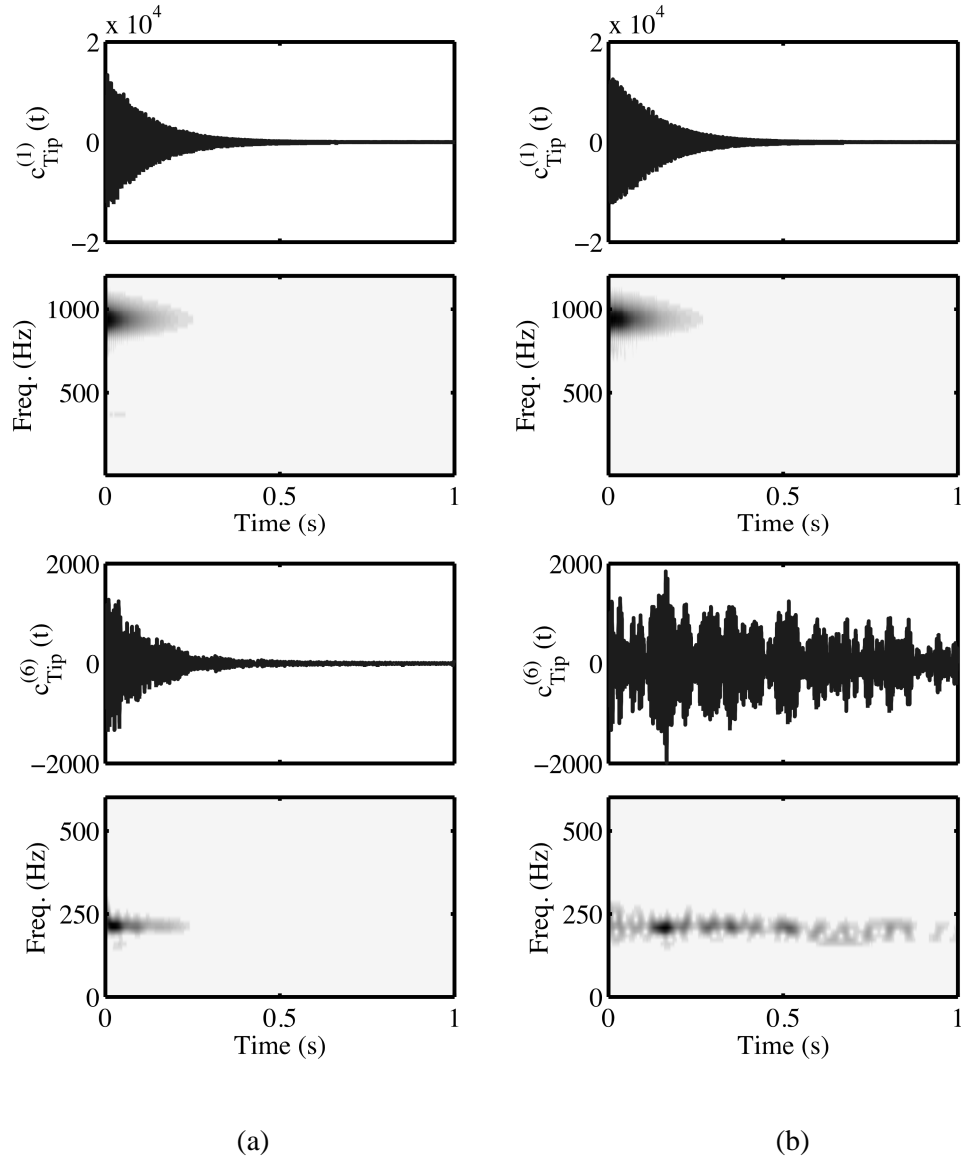


Figure 3.37 The 1st and 6th intrinsic mode functions (IMFs) and their wavelet transforms: (a) Linear system, and (b) strongly nonlinear system.

We now proceed with the results of the empirical mode decomposition of the acceleration time series of the linear (*cf.* Fig. 3.36a – no nonlinear spring attached) and strongly nonlinear (*cf.* Fig. 3.36c – case of the nonlinear spring with stiffness constant $k_{nl} = 10^{10} \text{ N/m}^3$) beams discussed in subsection 3.4.1. Although as many as 10 IMFs were extracted for both systems, in Figure 3.37, we only present the 1st and 6th IMFs for both linear and strongly nonlinear systems,

since those IMFs are good representatives of linear and strongly nonlinear behaviors, respectively. For each IMF we also depict its corresponding wavelet spectrum depicting the temporal variation of its frequency content. We note that, whereas in the linear case the harmonic components of the IMFs are expected to be at fixed frequencies (identical to the damped natural frequencies of the linear beam), this is not so for the strongly nonlinear case, where temporal variation of the harmonic content of the IMFs is expected (especially for the lowest frequency IMFs).

From the results of EMD and the comparison between the linear and nonlinear IMFs, we note that the nonlinear effects are more pronounced in the 6th IMF; *i.e.*, the nonlinear effects seem to predominantly affect this beam mode. In addition, in the nonlinear case for the 6th IMF, we observe beating phenomena which dominate the entire IMF response. This indicates a continuous exchange of energy between nonlinearly interacting modes for the entire duration of the dynamical response. This type of nonlinear beating is generated by strongly nonlinear modal interactions induced in the dynamics by the local strong stiffness nonlinearity.

In Fig. 3.38 we show the transient response reconstruction of both linear and nonlinear time series using the superposition of all the IMFs extracted for both systems. The IMFs do not form an orthogonal basis of functions (although they are nearly orthogonal); however, their superposition reconstructs the measured time series. Therein lies the usefulness of EMD, as it provides a multi-scale decomposition of the oscillatory time series in terms of embedded oscillatory components (the IMFs) at the dominant time scales of the dynamics.

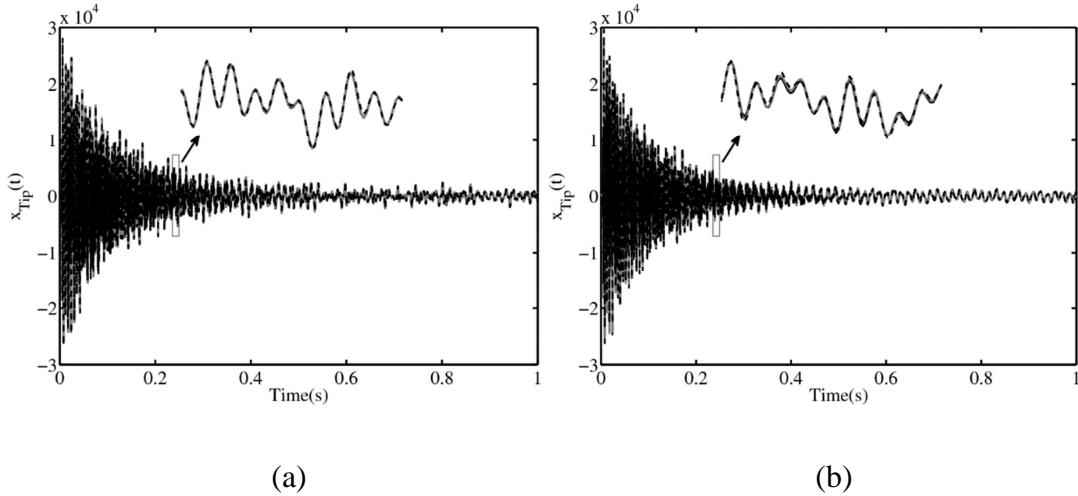


Figure 3.38 Original reconstructed time series, the latter obtained by summing intrinsic mode functions (IMFs) and the responses of intrinsic modal oscillators, respectively, (IMOs) for (a) the linear system, and (b) the strongly nonlinear system; — original time series, - - - sum of IMF responses, . . . sum of IMO responses.

3.4.3 Intrinsic Modal Oscillators (IMOs)

Based on the EMD results of subsection 3.4.2, we construct sets of intrinsic modal oscillators – IMOs that reproduce the nonlinear transient dynamics (as described in Section 2). In Fig. 3.38, it is demonstrated that the original time series can be reconstructed by summing the IMFs identified in the previous section, and by summing the responses of the corresponding intrinsic modal oscillators (IMOs – see Section 2.4) that will be computed below.

As discussed in Section 2.4, the forcing amplitudes of the IMOs contain essential information about the slow-flow dynamics of the system and the nonlinear interactions that occur between the nonlinear modes of the beam. In linear modal analysis the structural response is composed of nearly decoupled modes, which are the corresponding IMOs in our methodology. Hence, in a digression we consider a linear system with a forcing for the m^{th} IMO (mode)

obtained from a physical response linked to the k^{th} degree of freedom given by $F_k^{(m)}\delta(t)$. Then the corresponding IMO (mode) has the simple solution

$$c_k^{(m)}(t) = \frac{F_k^{(m)}}{\omega_{d,m}} e^{-\zeta_k^{(m)}\omega_m t} \sin \omega_{d,m} t \quad (3.20)$$

where $\omega_{d,m} = \omega_m [1 - \zeta_k^{(m)2}]^{1/2}$ is the damped frequency of the m^{th} dominant frequency (natural frequency) and $\zeta_k^{(m)}$ the damping ratio associated with the m^{th} IMO of the k^{th} degree of freedom. Using the equivalence between the analytical and measured slow-flows (see discussion in Section 2.3), and substituting this solution into (2.2) yields the corresponding slow complex amplitude $\varphi_k^{(m)}(t)$ which, in turn, provides the forcing amplitude for the m^{th} IMF of the k^{th} degree of freedom

$$\Lambda_k^{(m)}(t) = 2F_k^{(m)} e^{-t(j+\zeta_k^{(m)})\omega_m} \left\{ \left(-2\zeta_k^{(m)} + \lambda_k^{(m)} \right) \omega_m \cos \omega_{d,m} t + \left[-\omega_{d,m} + \left(1 + \zeta_k^{(m)2} + j\lambda_k^{(m)} - \zeta_k^{(m)}\lambda_k^{(m)} \right) \omega_m^2 / \omega_{d,m} \right] \sin \omega_{d,m} t \right\} \quad (3.21)$$

As shown in (Eriten et al. 2013), the natural logarithm of the forcing amplitude (3.21) yields an expression of the form

$$\ln \left| \Lambda_k^{(m)}(t) \right| \approx C(\lambda_k^{(m)}, \omega_m, \zeta_k^{(m)}, F_k^{(m)}) - \zeta_k^{(m)} \omega_m t \quad (3.22)$$

where $\lambda_k^{(m)}$ is the damping ratio for the corresponding IMO equation and $C(\lambda_k^{(m)}, \omega_m, \zeta_k^{(m)}, F_k^{(m)})$ is a coefficient that is constant with respect to time. Hence, when the proposed NSI technique is applied to a linear structure and an IMO is forced properly to reproduce the measured modal coordinate response (IMF), the corresponding forcing amplitude $\left| \Lambda_k^{(m)}(t) \right|$ is expected to scale linearly with the modal damping in a log-linear plot with a slope value equal to $-\zeta_k^{(m)}\omega_m$.

Table 3.4. Damping factors, fast frequencies and line slopes for each linear cantilever mode based on the beam tip response

Mode No. (m)	$\zeta_{Tip}^{(m)}$	ω_m (rad/s)	$-\zeta_{Tip}^{(m)} \omega_m$ (rad/s)
1	0.0071	23	-0.17
2	0.0011	146	-0.16
3	0.0012	409	-0.49
4	0.0029	798	-2.3
5	0.0068	1319	-9.0
6	0.0034	1979	-6.7
7	0.0074	2758	-20
8	0.0018	3657	-6.6
9	0.0023	4719	-11
10	0.0015	5818	-8.7

In Table 3.4, we provide the expected slopes for the modes of the linear beam under consideration (*i.e.*, with nonlinear spring detached), along with the corresponding modal damping factors and natural frequencies (fast frequencies in EMD notation). These estimates are computed by analyzing the 10 IMFs (IMOs), some of which are shown in Fig. 3.37, which are extracted by EMD of the cantilever tip response.

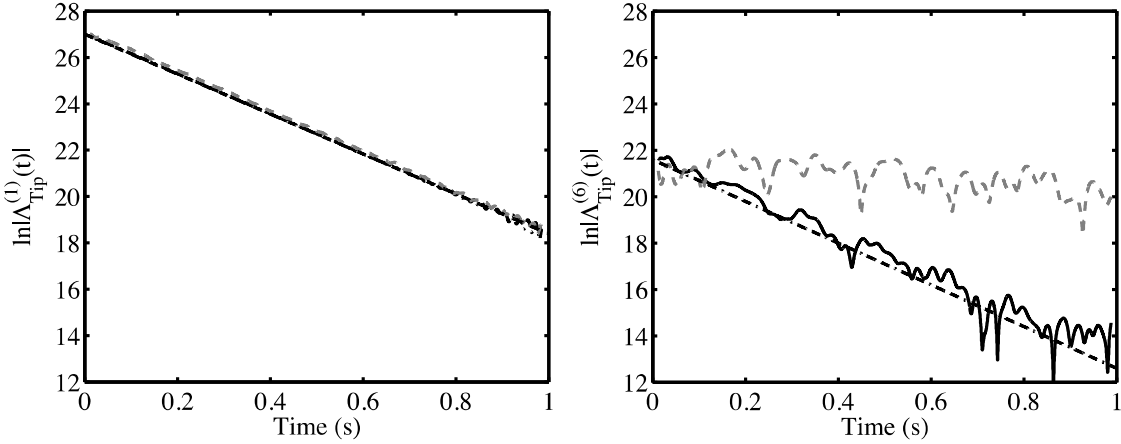


Figure 3.39 Plots of $\ln|\Lambda_{Tip}^{(m)}(t)|$ for IMOs corresponding to the (a) 1st IMF, (b) 6th IMF of the linear and strongly nonlinear cantilever beams; _____ Linear, - - - - strongly nonlinear, - . - . predicted linear slope.

From these results and the previous discussion it should be clear that linearity in an identified IMO is demonstrated by a *linear plot of the logarithm of the magnitude of its forcing function*. Hence, any nonlinear deviation from linearity in this plot provides a clear indication of nonlinear effects in the measured IMOs. We show this by computing the logarithms $\ln|\Lambda_{Tip}^{(m)}(t)|$ for the IMFs of the linear and nonlinear beams. The corresponding results for the IMFs depicted in Figure 3.37 are depicted in Figure 3.39, from which we deduce that not all cantilever modes are affected to the same extent by the strongly nonlinear local stiffness attached to the boundary of the beam. Specifically, and referring to the plot of Figure 3.39a, we observe that for the first (highest-frequency) IMO the logarithms of the forcing amplitudes are on almost perfect match with the predicted slope lines for both the linear and nonlinear beams, indicating that this highest frequency mode is nearly unaffected by the local stiffness nonlinearity.

However, considering the lower frequency IMO depicted in Fig. 3.39, we note a different trend. Focusing on Fig. 39b we observe a strong nonlinear effect in this IMO. Recalling the result depicted in Figure 37, we observed that due to the high modal damping and the mode shape effect, the 6th IMF (corresponding to the 5th beam mode) exhibited strongly nonlinear effects at various time instants; that is, new nonlinear modes appeared near the fast frequency of this mode caused by mode mixing due to internal resonances. Similarly, in Figure 6b, we observe that the logarithm of the forcing amplitude of the 6th IMO of the linear beam lines up well with the predicted slope line until 0.2 s after which noise effects introduce perturbations. For the strongly nonlinear beam, however, the corresponding logarithm of the forcing amplitude exhibits a completely different behavior and deviates significantly from the predicted linear trend. This is

caused by the nonlinear effects generated by internal resonances, and shows that this particular mode is strongly affected by the local stiffness nonlinearity of the beam.

Thus, by examining the temporal dependence of the magnitude of the forcing function of each IMO, one is able to detect the presence of nonlinear effects in its respective IMO. It follows that by employing the outlined methodology it is possible to identify which of the modes (IMOs) of the cantilever beam with the local stiffness nonlinearity at its end are significantly affected by nonlinear effects. We conclude from the analysis of these IMOs that whereas lower frequency modes are affected by the nonlinear effects, higher frequency modes are less affected by the nonlinearity appearing to be nearly linear. In the following Section we construct a reduced-order model of the system of Fig. 3.35a in order to investigate (and explain) the origin of the nonlinear beat phenomena detected in the IMFs in Fig. 3.37. Based on this understanding, in a later Section we will develop a method for system identification of these strongly nonlinear dynamics.

3.4.4 Analysis of Nonlinear Beat Phenomena by Reduced Order Modeling

To analyze nonlinear beat phenomena in the system of Fig. 3.35a it is necessary to consider a reduced-order model of this flexible system. To this end we apply Guyan reduction, a *static* model reduction method (Guyan 1965). Ignoring the damping effects for the moment, a linear discrete dynamical system with mass matrix $[m]$ and stiffness matrix $[k]$ can be partitioned in terms of *driven* ($\{z_b\}$) and *driver* ($\{z_a\}$) coordinates as

$$[k]\{z\} = \begin{bmatrix} k_{aa} & k_{ab} \\ k_{ba} & k_{bb} \end{bmatrix} \begin{Bmatrix} z_a \\ z_b \end{Bmatrix} = \begin{Bmatrix} F_a \\ 0 \end{Bmatrix} \equiv \{F\} \quad (3.23)$$

where we assume that degrees of freedom $\{z_a\}$ are excited by the external forces $\{F_a\}$, and we ignore forces (external and inertial) associated with the degrees of freedom $\{z_b\}$. This yields the coordinate transformation

$$[k_{ba}]\{z_a\} + [k_{bb}]\{z_b\} = 0 \Rightarrow \{z_b\} = \underbrace{-[k_{bb}]^{-1}[k_{ba}]}_{[T_{ba}]} \{z_a\} \Rightarrow \{z\} = \begin{Bmatrix} z_a \\ z_b \end{Bmatrix} = \underbrace{\begin{bmatrix} I \\ T_{ba} \end{bmatrix}}_{[T]} \{z_a\} \equiv [T]\{z_a\} \quad (3.24)$$

Returning to the original linear dynamical system (with inertia, damping and all forcing terms included) we apply the static transformation (3.24) to reduce the system to a form that involves only the driver coordinates $\{z_a\}$

$$\underbrace{[T]^T [m] [T]}_{[\tilde{M}_R]} \{\ddot{z}_a\} + \underbrace{[T]^T [c] [T]}_{[\tilde{C}_R]} \{\dot{z}_a\} + \underbrace{[T]^T [k] [T]}_{[\tilde{K}_R]} \{z_a\} = [T]^T \begin{Bmatrix} F_a \\ F_b \end{Bmatrix} = \underbrace{\{F_a\} + [T_{ba}]\{F_b\}}_{\{\tilde{F}_R\}} \quad (3.25)$$

where $\{F_b\}$ represents the vector of forces applied to the driven coordinates, and $\{\tilde{F}_R\}$ the vector of forces applied to the reduced model.

We now consider the nonlinear cantilever system of Fig. 3.35a. We apply Guyan reduction to the global mass and stiffness matrices assembled through finite element (FE) discretization of the cantilever beam. In the application considered in this Section the FE model consists of two planar beam elements leading to a four-DOF full model (two translations and two rotations), which reduces to a two-DOF reduced Guyan model (RGM) involving only the two translations. The mass, damping and stiffness matrices of the RGM are given by

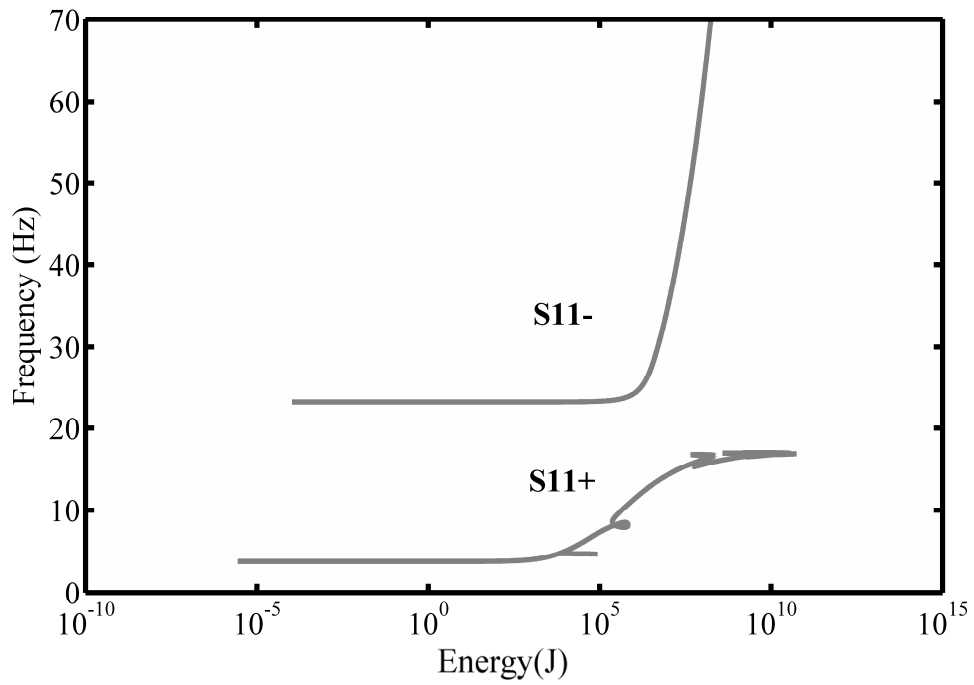
$$\left[\tilde{M}_R \right] = \begin{bmatrix} 1.66 & 0.33 \\ 0.33 & 0.51 \end{bmatrix}, \quad \left[\tilde{C}_R \right] = \begin{bmatrix} 0.5329 & 0.1140 \\ 0.1140 & 0.1675 \end{bmatrix}, \quad \left[\tilde{K}_R \right] = \begin{bmatrix} 17709 & -5534 \\ -5534 & 2214 \end{bmatrix} \quad (3.26)$$

reproducing the two lowest modes of the cantilever beam with natural frequencies equaling 23 and 146 rad/s (3.7 Hz and 23.3 Hz). Moreover, in correspondence with the original beam we assume proportional damping in the RGM, selecting the damping coefficients to match those of the two lowest modes of the cantilever beam, as given in Table 3.4. In summary, the RGM of the system of Fig. 3.35 is given in the form

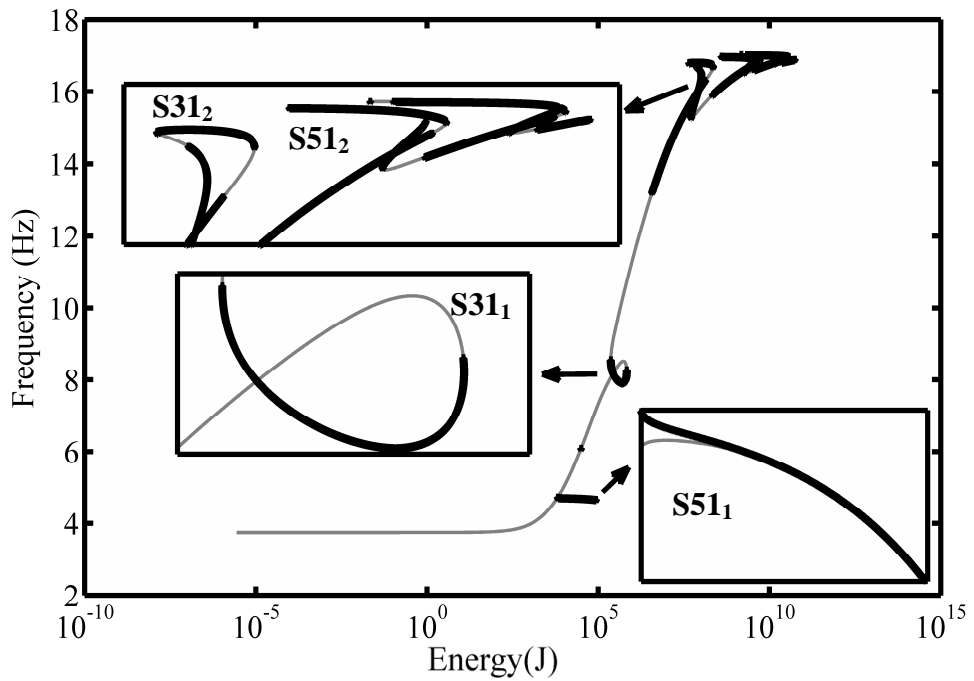
$$\left[\tilde{M}_R \right] \{ \ddot{z}_a \} + \left[\tilde{C}_R \right] \{ \dot{z}_a \} + \left[\tilde{K}_R \right] \{ z_a \} = \{ \tilde{F}_R \} = \{ F_{nl} \} + [F_e(t) \quad 0]^T \quad (3.27)$$

where $\{z_a\} = [x_1 \quad x_2]^T$, $\{F_{nl}\} = [0 \quad -k_{nl}x_2^3]^T$ represents the force due to the strong nonlinearity connected to the second DOF of the RGM (with coefficient $k_{nl} = 10^{10} \text{ N/m}^3$, representing the strongly nonlinear case studied in Section 3.4.1), and $F_e(t)$ the external shock excitation (given in Fig. 3.35b) applied to the first DOF. In the previous notation x_1 and x_2 represent the amplitudes of the two translations that represent the two-DOF of the RGM.

Next, we consider the nonlinear normal modes (NNMs) (Vakakis 2002) of the RGM (3.27) by considering the Hamiltonian system resulting when we omit the damping and set the external excitation equal to zero. The nonlinear modes of the reduced system are depicted in a frequency-energy plot (FEP) as discussed in (Vakakis 2008). This plot depicts the periodic orbits of the RGM in the frequency-energy plane. Of special interest will be strongly nonlinear modal interactions generated by internal resonances since, as shown below, they are responsible for nonlinear beat phenomena of the type identified in the transient responses of the full flexible system.



(a)

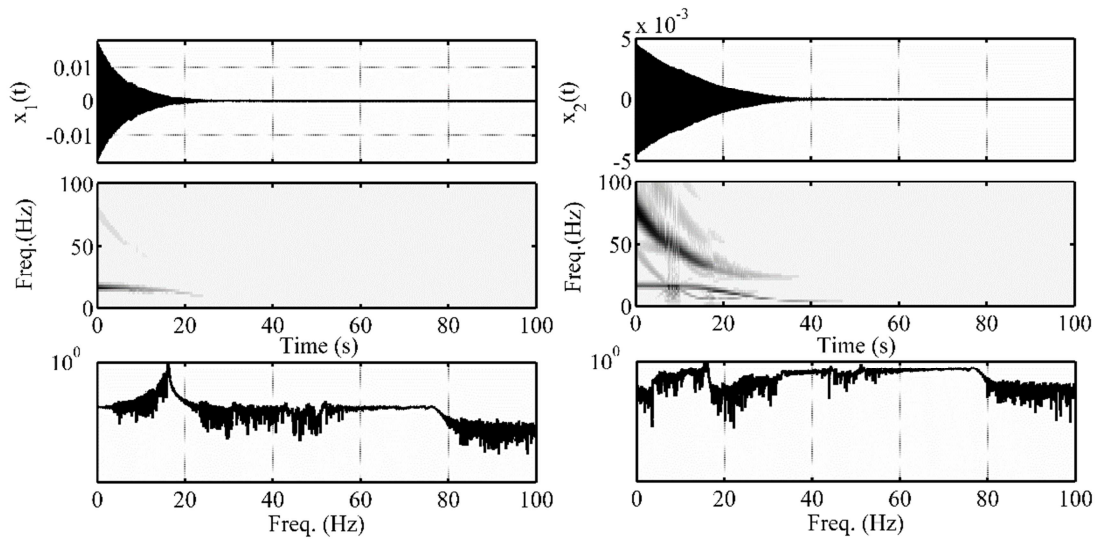


(b)

Figure 3.40 FEP of the RGM with end stiffness nonlinearity: (a) Backbone branches, (b) detail of the in-phase backbone branch indicating subharmonic tongues due to internal resonances; — Stable NNMs, ——— unstable NNMs.

In Fig. 3.40a we depict the FEP of the RGM; this plot was computed using the numerical continuation code developed by (Peeters et al. 2009). There are two branches of nonlinear normal modes for this system denoted as *backbone branches*. These branches are labeled $S_{11} \mp$ since they correspond to in-phase (+ sign) and out-of-phase (– sign) synchronous oscillations of the two masses of the RGM with both degrees of freedom oscillating with identical frequencies; *i.e.*, they satisfy the condition of 1:1 internal resonance between the two degrees of freedom of the RGM. Due to the stiffening effect of the cubic nonlinearity, the frequency of the in-phase NNM converges to a certain asymptotic limit with increasing energy, as the cubic stiffness becomes approximately rigid and the system approaches a beam with pinned right end. The out-of-phase NNM ‘decouples’ from the in-phase mode during this limiting process, becoming a purely nonlinearity-governed NNM.

Apart from the backbone branches, of particular interest for our discussion are the *subharmonic tongues* appearing as bifurcating branches out of the lower frequency in-phase backbone branch $S_{11} +$, generated by 1: n internal resonances between the in-phase and out-of-phase NNMs of the RGM. In Fig. 3.40b we depict the subharmonic tongues S_{31} and S_{51} corresponding to 3:1 and 5:1 internal resonances, respectively, between the two backbone modes. The reason that we find two of each of these subharmonic tongues (labeled as $S_{31_{1,2}}$ and $S_{51_{1,2}}$ in Fig. 7b) is that the ratio between the frequencies of the in-phase and out-of-phase backbone branches reaches 3 and 5, respectively, at two different energy levels. We mention that, if the ratio of the linearized frequencies of these two NNMs were smaller than 3, it would be impossible to obtain these tongues. The stability of the NNMs on the backbone curves and the subharmonic tongues was studied by means of Floquet theory (Peeters et al. 2009), and the results are depicted in Fig. 3.40.



(a)

(b)

Figure 3.41 RGM (24): (a) Response of the first reduced DOF $x_1(t)$, (b) Response of the second reduced DOF $x_2(t)$; both in meters (wavelet transform spectra and Fourier transforms are also depicted).

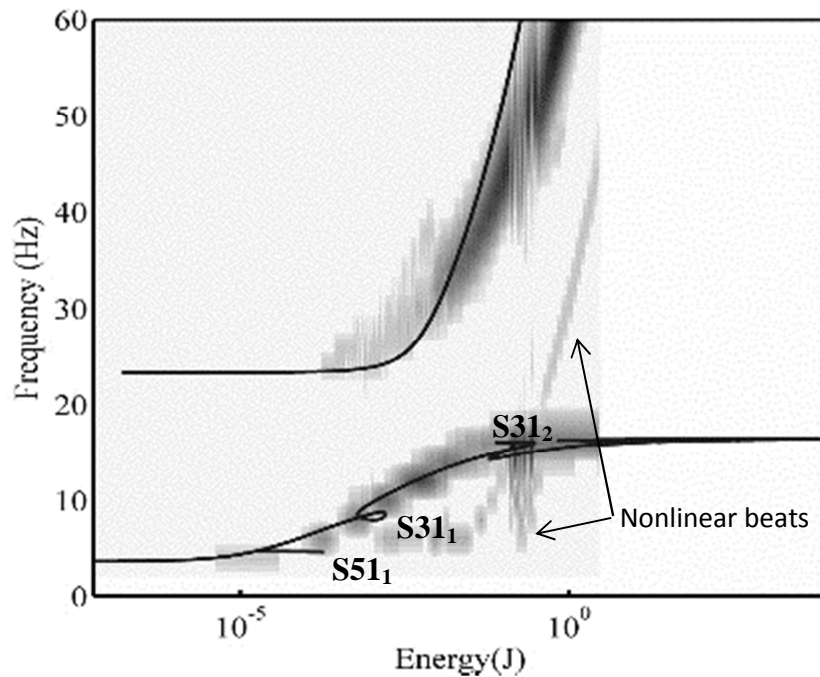


Figure 3.42 Wavelet transform spectrum of the second DOF of the RGM superimposed on the Hamiltonian FEP of Fig. 7; nonlinear beats in the neighborhood of subharmonic tongues $S31_2$ and $S51_2$ are evidenced by the corresponding broadband frequency components that emanate from these tongues.

As discussed in (Vakakis 2008), on subharmonic tongues there occurs mode conversion from the in-phase to the out-of-phase NNM, since the orbit of each subharmonic tongue corresponding to maximum energy correspond to a point of bifurcation with the out-of-phase NNM (S_{33} – for the branches $S31_{1,2}$, and S_{55} – for the branches $S51_{1,2}$). Hence, on each subharmonic tongue mode mixing occurs and the corresponding periodic orbits are in the form of nonlinear beats (Peeters et al. 2009). It turns out that it is the excitation of such subharmonic tongues due to nonlinear internal resonance that gives rise to the nonlinear beat phenomena observed in the numerical simulations of subsection 3.4.1 for the beam with the nonlinear stiffness at its end.

To demonstrate the effect of these internal resonances on the transient response we now consider the full RGM (3.27) and perform numerical simulations of its dynamics for the transient force used in the Section 3 and depicted in Fig. 3.35b. In Fig. 3.41 we depict the responses of the two degrees of freedom (DOFs) of the RGM, together with their wavelet spectra and Fourier transforms. In Fig. 3.41b we clearly observe that at $t \approx 9$ s the response of the second DOF approaches the neighborhood of the $S31_2$ subharmonic tongue, as can be deduced by considering the frequency ratios of the two modes of the response in the wavelet transforms around this particular time instant. It is evident from the WTs that the dynamics in the second DOF is richer, due to the fact that the second mass of the RGM is directly attached to the strongly nonlinear end spring. Therefore, in the remaining part of this section, we will focus our analysis on the transient response $x_2(t)$.

In Fig. 3.42 we depict the WT spectrum of $x_2(t)$ superimposed onto the Hamiltonian FEP of Fig. 3.40. This WT spectrum was computed from the corresponding spectrum of Fig. 3.41b by

replacing time with the instantaneous energy of the forced and damped system at every time instant. The comparison of the Hamiltonian FEP to the WT spectrum of the damped and forced response of the RGM is purely phenomenological; however, it shows how the underlying Hamiltonian dynamics (periodic orbits and nonlinear internal resonances) affect the response of the same RGM when damping and forcing are added. Indeed, at high energies (that is, in the initial highly energetic phase of the dynamics) the WT spectrum approximately follows the Hamiltonian S_{11} – branch, indicating that initially the dynamics is dominated by 1:1 resonance between the two DOFs. However, complex modal interactions are found in the vicinity of the subharmonic tongues S_{31_2} and S_{51_2} ; these lead to complex nonlinear beat phenomena, as evidenced by multiple higher and lower harmonic components emanating from the neighborhood of these tongues. Hence, the study of the dynamics of the RGM reveals that internal resonances due to the strong local stiffness nonlinearity lead to nonlinear beat phenomena.

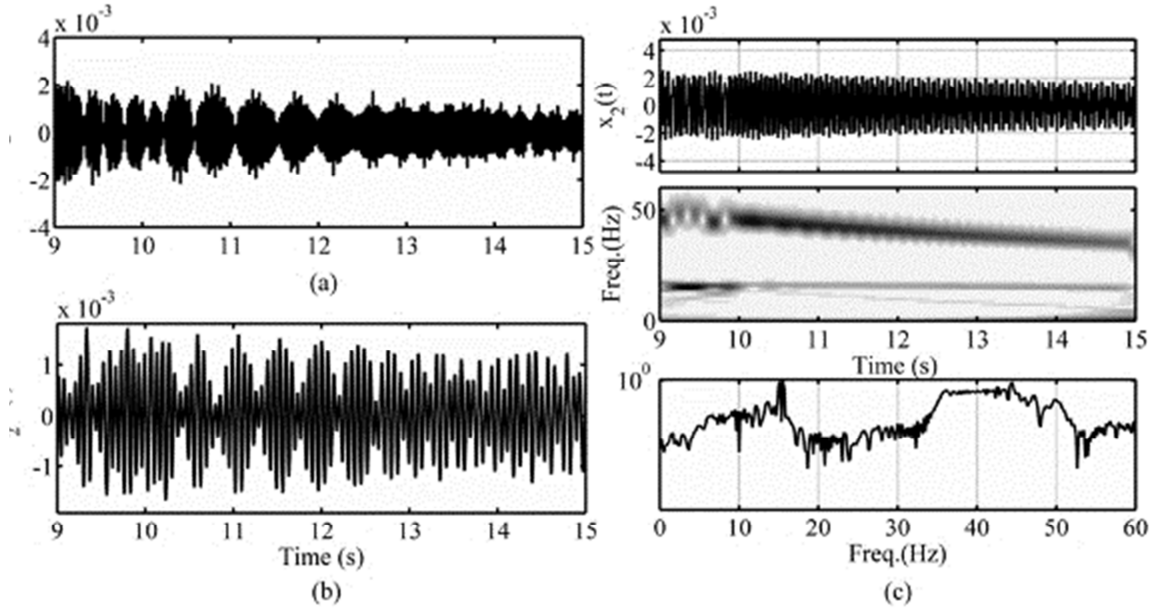


Figure 3.43 Details of (a) the 1st IMF, (b) the 2nd IMF, (c) the transient response $x_2(t)$ in the region of nonlinear beats

We investigate the two dominant modes separately by carrying out empirical mode decomposition (EMD), through which we separate the in-phase and out-of-phase dynamics. Note that, although a computed IMF is expected to possess a narrow frequency bandwidth (see discussion in Section 2), it makes more sense to separate the damped physical modes as ‘single’ IMFs, rather than partitioning them into smaller narrow-band components. We extract the two IMFs of the response of the second DOF, $x_2(t)$, corresponding to the out-of-phase and in-phase modes of the RGM, respectively. The realization of complex nonlinear modal interactions in these IMFs is evident. To study these modal interactions in more detail and highlight the resulting nonlinear beat phenomena, in Fig. 3.43 we depict the regions of nonlinear beats in the 1st and 2nd IMFs, and in the transient response $x_2(t)$. In the time interval 9-15 s, we clearly observe the realization of strong nonlinear beats in both IMFs. This particular time interval was examined since this region corresponds to the $S31_2$ suharmonic tongue, as discussed above. Note that the

beats tend to vanish as soon as the transient dynamics leaves the $S31_2$ region as the total energy of the motion decreases due to damping dissipation. It is clear from the WT spectrum of Fig.10c that in this time interval there exist strong nonlinear interactions (mode mixing) between the out-of-phase and in-phase modes, which cause the nonlinear beats observed in the corresponding IMFs.

The results of this Section based on the RGM demonstrated that the source of the nonlinear beats in the transient dynamics of the cantilever system of Fig. 3.35a is the nonlinear internal resonances realized due to the local strong stiffness nonlinearity, leading to complex modal interactions between cantilever modes. It follows that this type of nonlinear ‘mode coupling’ is rather generic in linear flexible systems with local strong stiffness nonlinearities, so complex nonlinear beat phenomena are expected to be present in the dynamics of this type of structures. We note that these nonlinear beating phenomena signal energy exchanges between different modes, which we attempted to model by using RGMs. This calls for the extension of the nonlinear system identification (NSI) methodology discussed in Section 2 to account for such nonlinear beat phenomena or nonlinear modal interactions. This is performed in the next Section.

3.4.5 Slow Flow Modeling and NSI of Resonance-induced Beating Phenomena

3.4.5.1 Preliminaries: Analysis of Beating Signals

We start the analysis and modeling of beating signals by considering a preliminary example. As discussed in Section 2, since the general ‘nearly monochromatic’ IMO (2.16) models a nearly monochromatic IMF (*i.e.*, possessing a single dominant frequency), any analysis based on IMOs of the form (2.15) fails to be valid for a beating signal which contains at least two different

closely spaced frequency components. The simplest model that can reproduce beating signals is the following linear damped oscillator with a harmonic forcing

$$\ddot{y} + 2\zeta\omega\dot{y} + \omega^2 y = \cos[\omega(1 + \varepsilon)t] \equiv \cos\Omega t \quad (3.28)$$

where $\Omega = \omega(1 + \varepsilon) = \omega + \varepsilon\omega \equiv \omega + \omega_d$. The response of oscillator (3.28) is expressed as the superposition of a homogeneous and particular solution, $y_h(t)$ and $y_p(t)$, respectively

$$y(t) = y_h(t) + y_p(t) = \underbrace{C e^{-\zeta\omega t} \cos(\omega_d t + \phi)}_{y_h(t)} + \underbrace{\frac{1}{\sqrt{(\Omega^2 - \omega^2)^2 + (2\zeta\omega\Omega)^2}} \cos(\Omega t - \psi)}_{y_p(t)} \quad (3.29)$$

which can be expressed as

$$y(t) = C e^{-\zeta\omega t} \cos\left[\left(\frac{\Omega - \omega_d}{2}\right)t - \left(\frac{\phi + \beta}{2}\right)\right] \cos\left[\left(\frac{\Omega + \omega_d}{2}\right)t - \left(\frac{\phi - \beta}{2}\right)\right] + \left[\frac{1}{\sqrt{(\Omega^2 - \omega^2)^2 + (2\zeta\omega\Omega)^2}} - C e^{-\zeta\omega t} \right] \cos(\Omega t - \beta) \quad (3.30)$$

where $\beta = \tan^{-1}\left(\frac{2\zeta\omega\Omega}{\Omega^2 - \omega^2}\right)$. Viewed in the context of the previous Sections the response $y(t)$ can be regarded as the only IMF of system (3.28). The amplitude C and the phase difference ϕ are obtained by imposing the initial conditions of the problem, but this is not critical for our further analysis in this Section.

At this point, we apply a slow flow analysis by introducing the complexification

$$\dot{y}(t) + j\omega y(t) = \psi(t) = \varphi(t) e^{j\omega t}, \quad \varphi(t) = j\omega A(t) e^{j\theta(t)} \quad (3.31)$$

Note the different definition of the complex amplitude $\varphi(t)$ compared to the corresponding definition in Section 2 for the nearly monochromatic signal. Upon matching (3.30) and (3.31), we evaluate the slow envelope and the slow phase of the beating signal

$$A(t) = Ce^{-\zeta\omega t} \cos \left[\left(\frac{\Omega - \omega_d}{2} \right) t - \left(\frac{\phi + \beta}{2} \right) \right] + \left[\frac{1}{\sqrt{(\Omega^2 - \omega^2)^2 + (2\zeta\omega\Omega)^2}} - Ce^{-\zeta\omega t} \right] = \quad (3.32)$$

$$Ce^{-\zeta\omega t} \left\{ \cos \left[\left(\frac{\Omega - \omega_d}{2} \right) t - \left(\frac{\phi + \beta}{2} \right) \right] - 1 \right\} + \frac{1}{\sqrt{(\Omega^2 - \omega^2)^2 + (2\zeta\omega\Omega)^2}} \theta(t) \approx \left(\frac{\phi - \beta}{2} \right) \quad (3.33)$$

Combining these results we evaluate the complex amplitude of the beating signal as

$$\varphi(t) = j\omega \left[Ce^{-\zeta\omega t} \left\{ \cos \left[\left(\frac{\Omega - \omega_d}{2} \right) t - \left(\frac{\phi + \beta}{2} \right) \right] - 1 \right\} + \frac{1}{\sqrt{(\Omega^2 - \omega^2)^2 + (2\zeta\omega\Omega)^2}} \right] e^{j\left(\frac{\phi - \beta}{2}\right)} \quad (3.34)$$

As discussed in Section 2, based on relation (2.16) we can express the slowly varying complex forcing amplitude of the IMO modeling the IMF (3.30) as

$$\Lambda(t) \approx 2[\dot{\varphi}(t) + \lambda\varphi\omega(t)] \quad (3.35)$$

where λ is the damping factor of the IMO equation (following the notation of relation (2.15)).

Neglecting the first term in (3.35) since it quickly decays to zero, the above complex amplitude can be approximated as

$$\Lambda(t) \approx \lambda\omega \left[\underbrace{C e^{-\zeta\omega t} \left\{ \cos \left[\left(\frac{\Omega - \omega_d}{2} \right) t - \left(\frac{\phi + \beta}{2} \right) \right] - 1 \right\}}_{\text{Homogeneous solution component}} + \underbrace{\left[(\Omega^2 - \omega^2)^2 + (2\zeta\omega\Omega)^2 \right]^{-1/2}}_{\text{Particular solution component}} \right] \quad (3.36)$$

At this point we denote the ratio, $R(t)$, of the amplitudes of the homogeneous and particular components in (3.29) as

$$R(t) = C e^{-\zeta\omega t} \sqrt{(\Omega^2 - \omega^2)^2 + (2\zeta\omega\Omega)^2} \quad (3.37)$$

It turns out that when damping is weak this ratio is very slowly varying, so it can be regarded as being approximately constant, $R(t) \approx R$. Taking the natural logarithm of the expression (3.36) and accounting for the approximation (3.37), we obtain the relation

$$\ln |\Lambda(t)| \approx \ln \left[\lambda\omega \left[C e^{-\zeta\omega t} \left\{ \cos \left[\left(\frac{\Omega - \omega_d}{2} \right) t - \left(\frac{\phi + \beta}{2} \right) \right] - 1 \right\} + R C e^{-\zeta\omega t} \right] \right] \quad (3.38)$$

At this point (and without loss of generality) we assume a zero phase difference for the sake of simplicity, $\phi = 0$. Finally, taking the derivative with respect of time of both sides of relation (36), we obtain

$$\frac{d}{dt} \ln |\Lambda(t)| \approx \frac{-e^{-t\zeta\omega} \zeta \omega + e^{-t\zeta\omega} R \zeta \omega - e^{-t\zeta\omega} R \zeta \lambda \omega^2 \cos(t\epsilon\omega/2) - (1/2) e^{-t\zeta\omega} R \zeta \lambda \omega^2 \sin(t\epsilon\omega/2)}{e^{-t\zeta\omega} (1-R) + e^{-t\zeta\omega} R \lambda \omega \cos(t\epsilon\omega/2)} \quad (3.39)$$

We will be mainly interested in two specific features of the approximate analytical expression (3.39). The first feature concerns the behavior of the slope of $\ln|\Lambda(t)|$ when t approaches the time instant t_{node} corresponding to a nodal point of the beating signal

$$\lim_{t \rightarrow t_{node}} \left\{ \frac{d}{dt} \ln |\Lambda(t)| \right\} \approx \frac{\omega [2(1-R)\zeta + R\varepsilon\lambda\omega]}{2(R-1)} = -\zeta\omega + \frac{R\varepsilon\lambda\omega^2}{2(R-1)} \quad (3.40)$$

Note that expression (3.40) is dependent on the ratio R . Indeed, when $R = 1$ the above limit reaches $-\infty$, whereas when $R = 0$ (which means that there is no beating) the limit equals $-\zeta\omega$ which is in agreement with the previous analysis based on relation (20). In between these limiting values of R the derivative of the slope is dependent on R, ε, λ and ω . In general, we should expect very steep slopes between the aforementioned limiting cases since R will usually be close to unity for a beating signal.

The second feature of interest in (3.39) is the behavior of the slope of $\ln|\Lambda(t)|$ at the maximum values of the beating signal. Assuming that at $t = t_{max}$ a maximum of the beating phenomenon is reached, we obtain the limiting expression

$$\lim_{t \rightarrow t_{max}} \left\{ \frac{d}{dt} \ln |\Lambda(t)| \right\} = \frac{-\zeta\omega + R\zeta\omega - R\zeta\lambda\omega^2}{1 - R + R\lambda\omega} = -\zeta\omega \quad (3.41)$$

Hence, in the vicinity of the maxima in the beating signal, the slope of $\ln|\Lambda(t)|$ approaches the value $-\zeta\omega$, which is identical to the corresponding slope of $\ln|\Lambda(t)|$ in the case of the nearly monochromatic signal examined in the previous section. [see expression (3.22)].

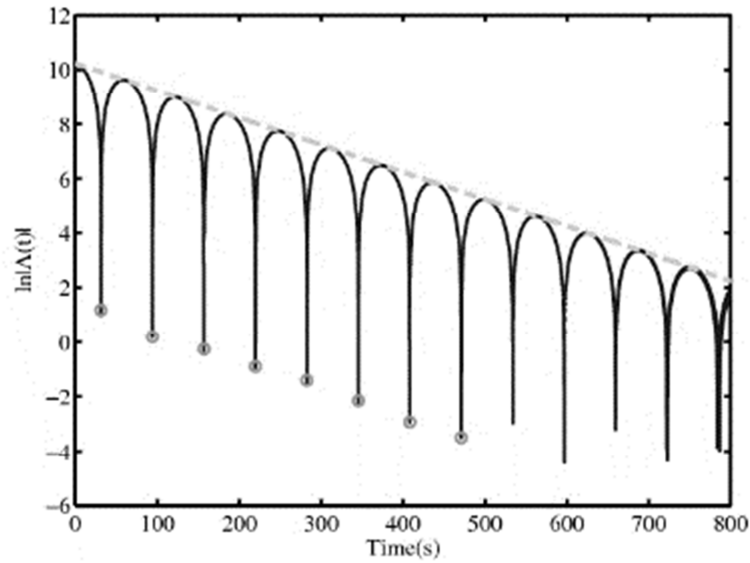


Figure 3.44 Transient variation of $\ln|\Lambda(t)|$ (logarithm of the modulus of the complex forcing of the IMO) of a beating signal, and its comparison to the line with slope $-\zeta\omega$; — $\ln|\Lambda(t)|$, - - - predicted linear line, -o- nodal points.

The limiting expressions (38) and (39) provide the necessary framework for extending the nonlinear system identification methodology outlined in Section 3 to the case of time series with beats. Before we proceed to formulate this extension, we provide a numerical example that highlights the previous findings.

In the following example we consider the beating signal composed of two harmonics with closely spaced frequencies given by $y(t) = e^{-\zeta\omega t} [\cos \omega t + \cos \omega(1 + \varepsilon)t]$ with $\omega = 100 \text{ rad/s}$, $\zeta = 0.01$ and $\varepsilon = 0.01$. In Fig. 11 we plot $\ln|\Lambda(t)|$ derived from this signal, and the predicted line with slope $-\zeta\omega$. We see that, in accordance with the previous analytical findings, the slope of $\ln|\Lambda(t)|$ tends to $-\infty$ at nodal points of the beat (since $R = 1$ in this

particular example). In addition, the slope of $\ln|\Lambda(t)|$ in the neighborhoods of the maxima of the beating approximates $-\zeta\omega$, again in accordance to the previous analysis.

3.4.5.2 Nonlinear System Identification of Beating Signals

Here, the analysis of the previous subsection for the SDOF oscillator (2.28) will be applied to the IMFs computed in Section 3 for the strongly nonlinear case. It was observed that, due to strong stiffness nonlinearity at the end of the cantilever, the lower frequency modes (*i.e.*, the higher order IMFs) exhibit nonlinear beating phenomena. As discussed before, these nonlinear beats are generated by internal nonlinear resonances which lead to nonlinear mode mixing and strongly nonlinear modal interactions.

In Fig. 3.45 we consider the first four IMFs of the beam with strongly nonlinear stiffness employing the NSI methodology for nonlinear beats discussed in the previous Section. As indicated, these IMFs correspond to the highest frequency oscillatory modes that are embedded in the measured time series. From Figs. 12a,b we deduce that IMFs $c_{Tip}^{(1)}(t)$ and $c_{Tip}^{(2)}(t)$ exhibit nearly linear behavior and do not appear to be significantly affected by the presence of the strong stiffness nonlinearity. This should be clear from the fact that the corresponding plots of $\ln|\Lambda_{Tip}^{(1)}(t)|$ and $\ln|\Lambda_{Tip}^{(2)}(t)|$ almost perfectly match the straight lines with slopes equaling $-\zeta_{Tip}^{(1)}\omega_1$ and $-\zeta_{Tip}^{(2)}\omega_2$, respectively, which is the prediction for linear behavior [as given in (3.22)]. Discrepancies from linear behavior are observed only when the amplitudes of the IMFs decrease below the noise level. Moreover, we note absence of nonlinear beats in these two IMFs.

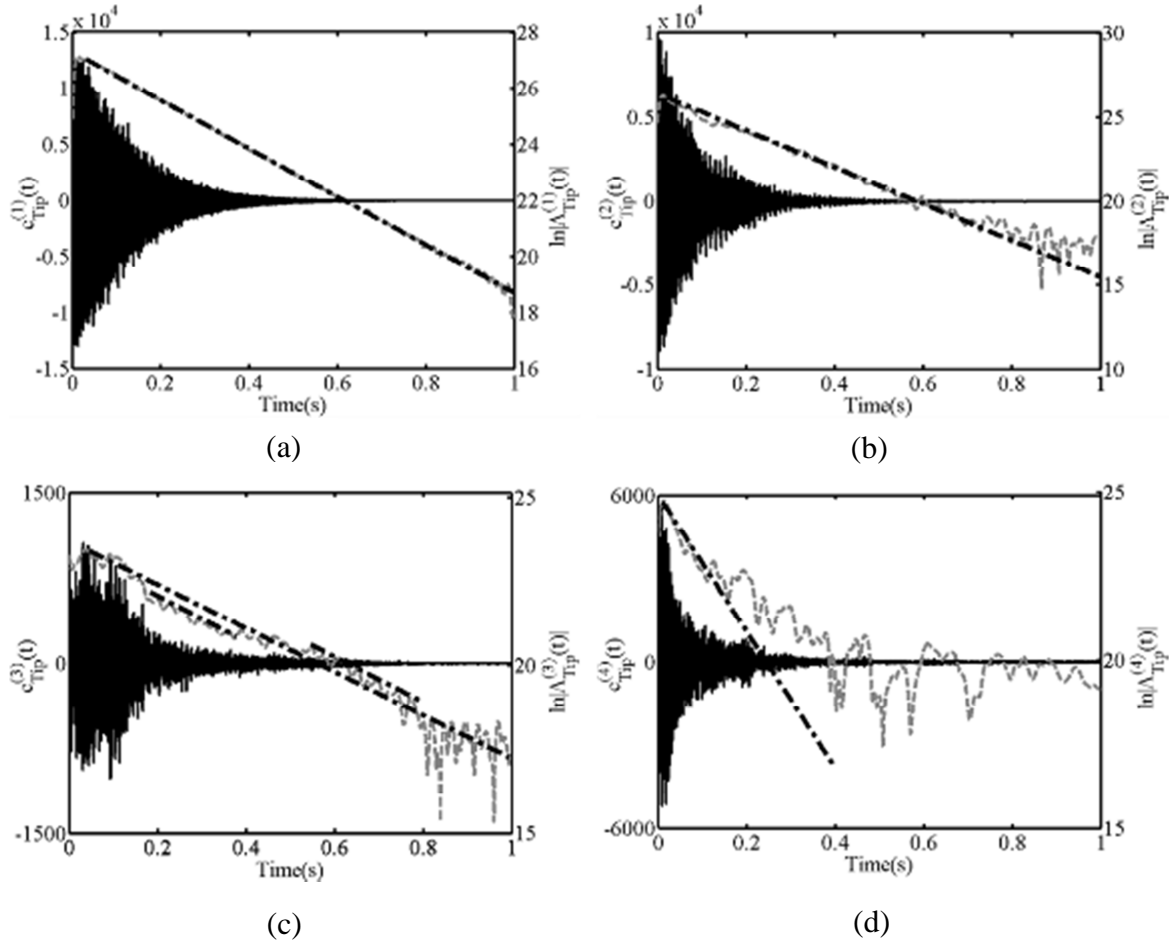


Figure 3.45 Application of the NSI technique to beating signals in the (a) 1st IMF, (b) 2nd IMF, (c) 3rd IMF, and (d) 4th IMF of the strongly nonlinear system; — $c_{Tip}^{(m)}(t)$, - - - $\ln|\Lambda_{Tip}^{(m)}(t)|$, - . - . - predicted linear slope.

Considering now the 3rd IMF depicted in Fig. 3.41c, we note the occurrence of nonlinear beats, as evidenced by the deviation of the plot of $\ln|\Lambda_{Tip}^{(3)}(t)|$ from the line with the slope $-\zeta_{Tip}^{(3)}\omega_3$. In addition, we observe that the line with slope $-\zeta_{Tip}^{(3)}\omega_3$ crosses the maxima of the plot of $\ln|\Lambda_{Tip}^{(3)}(t)|$ corresponding to nonlinear beats between 0.2 and 0.4 seconds, as predicted by relation (3.41). The reason for drawing multiple lines with the predicted slope comes from the fact that

there occur multiple nonlinear beats with different beating frequency; indeed, recalling the methodology derived in Section 5.1 we note that relation (39) was derived under the assumption that the nonlinear beats possess the same beating frequency. The occurrence of multiple beating phenomena will be further analyzed below when IMF $c_{Tip}^{(8)}(t)$ is considered. For the 4th IMF $c_{Tip}^{(4)}(t)$, we note that this mode has the highest modal damping (*cf.* Table 1) and the line with slope $-\zeta_{Tip}^{(4)}\omega_4$ crosses the maxima of the plot of $\ln|\Lambda_{Tip}^{(4)}(t)|$ only in the beginning of the time span.

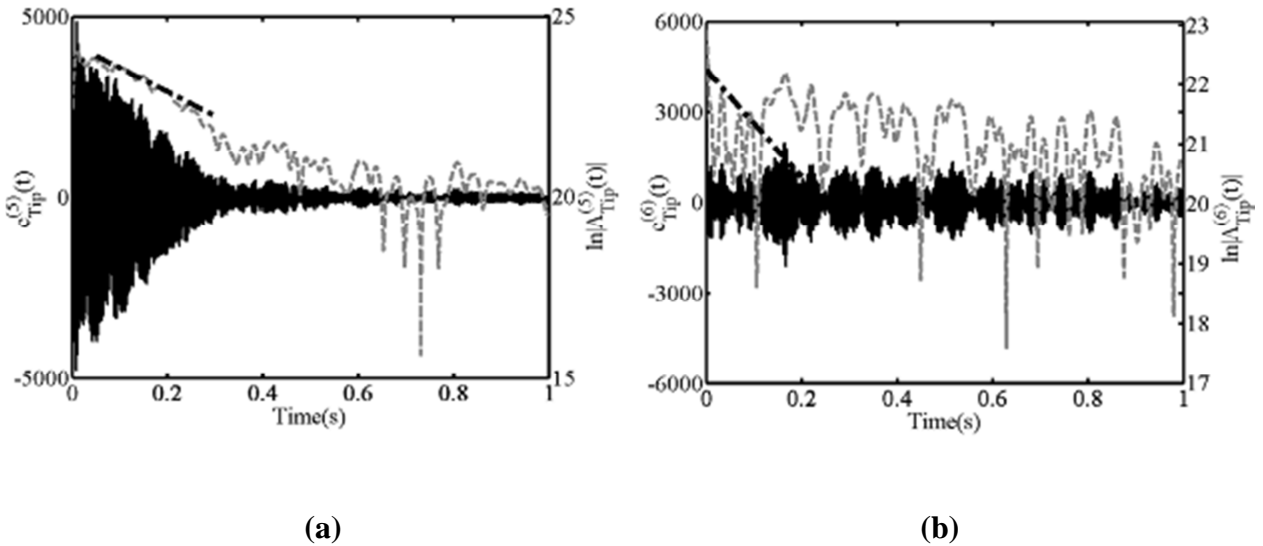


Figure 3.46 Application of the NSI technique to beating signals in the (a) 5th IMF, and (b) 6th IMF of the strongly nonlinear system; — $c_{Tip}^{(m)}(t)$, - - - $\ln|\Lambda_{Tip}^{(m)}(t)|$, - . - . - predicted linear slope.

In Fig. 3.46 we analyze the 5th and 6th IMFs of the strongly nonlinear system. From the plot of Fig. 13a the nonlinear beating in the early phase of the 5th IMF is evident, so relation (3.40) can be applied in this case. Indeed, we note that in accordance with the theoretical

prediction the maxima of the plot of $\ln|\Lambda_{Tip}^{(5)}(t)|$ that correspond to the maxima of the nonlinear beats, are approximately bounded by the predicted linear line with slope equal to $-\zeta_{Tip}^{(5)}\omega_5$.

Also, considering the 6th IMF depicted in Fig. 3.46b, it is clearly observed that this mode is dominated by nonlinear beats caused by the strong nonlinearity. The line with predicted slope $-\zeta_{Tip}^{(6)}\omega_6$ crosses the maxima of the nonlinear beats in the beginning of the time span; however, after approximately 0.1 s, this mode becomes dominated by nonlinear effects and traces of the linear mode disappear, which can be deduced by looking at the completely different damping behavior of that mode.

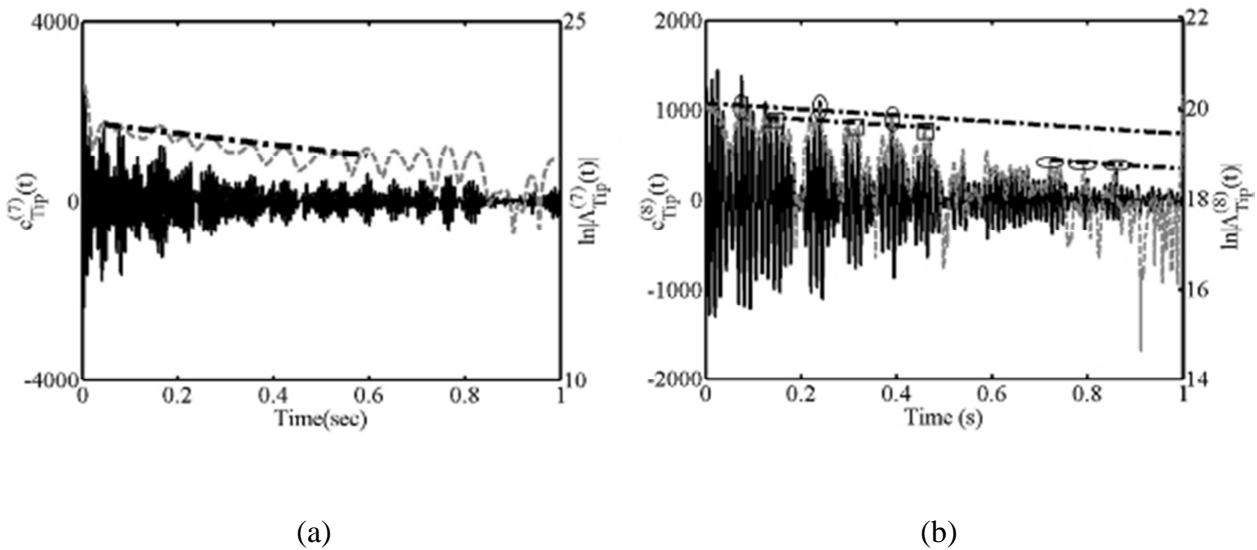


Figure 3.47 Application of the NSI technique to beating signals in the a) 7th IMF, and (b) 8th IMF of the strongly nonlinear system (cf. Fig. 7b); ——— $c_{Tip}^{(m)}(t)$, - - - - $\ln|\Lambda_{Tip}^{(m)}(t)|$, - . - . - predicted linear slope.

In Fig. 3.47 we consider the beating signals in the 7th and 8th IMFs. For the 7th IMF (at ~ 798 rad/s or 127 Hz) the line with slope $-\zeta_{Tip}^{(7)}\omega_7$ crosses the maxima of $\ln|\Lambda_{Tip}^{(7)}(t)|$ as predicted by

(38) until 0.6 s, where a different type of beating occurs. Moving on to the 8th IMF depicted in Fig. 3.47b, we noted previously that for the linear case this IMF has a fast frequency equaling 409 rad/s (or 65 Hz), whereas for the strongly nonlinear case that frequency is nearly 534 rad/s (or 85 Hz). Until around 0.5 s, strong nonlinearity governs this mode, whereas linear behavior is recovered afterwards. It is observed that the 8th IMF possesses multiple beating frequencies, so application of (39) requires the detection of the maxima of the beats corresponding to the same beating frequency. In Fig. 3.47b the maxima of $\ln|\Lambda_{Tip}^{(8)}(t)|$, denoted by horizontal ellipses, vertical ellipses and rectangles correspond to maxima of beats with identical beating frequencies. We note at this point that, since this represents a completely new mode that is generated by the strong stiffness nonlinearity (as it has no analogue in the linear case – that is, the fast frequency of this mode is different from that of the corresponding linear mode), we draw separate parallel lines with the predicted slope $-\zeta_{Tip}^{(8)}\omega_8$, where the damping and frequency values no longer correspond to those of the linear mode. We observe that each of these lines crosses the maxima of the plot of $\ln|\Lambda_{Tip}^{(8)}(t)|$ separately, as predicted in (3.41).

3.4.6 Concluding Remarks

In this section, we study a linear cantilever beam with a strongly nonlinear grounding stiffness at its free boundary. The nonlinear stiffness has no linear component, so it can be characterized as essentially nonlinear (since it is non-linearizable). Due to this strong local nonlinearity and the fact that no cantilever modes have nodes at the free end of the beam, we anticipate that all modes will be affected to a certain extent by the nonlinearity, although as this work shows, it is the lower-frequency cantilever modes that are most affected by the strong stiffness nonlinearity. In

addition, we observed strongly nonlinear beat phenomena, which upon further analysis we attributed to nonlinear modal interactions arising by internal resonances between cantilever modes. It is interesting to note that these internal resonances involve cantilever modes whose linearized natural frequencies are not necessarily close or even related by rational ratios; rather conditions of internal resonances in the present system are realized due to the strong energy-dependencies of the frequencies of the participating cantilever modes as they are affected by the strong local stiffness nonlinearity. These essentially nonlinear beat phenomena generate ‘nonlinear mode mixing,’ through which a cantilever modes is ‘mixed’ with another mode, ultimately being transformed to the lateral mode as energy varies. This is in marked contrast to the linear case (*i.e.*, in the system with either no spring or with a linear spring attached), where beat phenomena can only be generated by modal interactions of closely spaced modes. We note that this type of nonlinear mode mixing is generic in nonlinear systems, and its realization in the frequency-energy domain depends on the specific system configuration and the specific system parameters.

We demonstrate the relation between nonlinear beat phenomena and internal resonances by constructing a reduced order model of the full finite-element dynamic model using Guyan reduction and studying the dynamics of the reduced-order system in the frequency-energy plane. By superimposing the wavelet transform spectra of damped transitions onto the Hamiltonian frequency-energy plot of the periodic orbits of the reduced system, we show that nonlinear beats are caused by excitation of certain subharmonic tongues that are generated by nonlinear internal resonances involving well-separated beam modes. This provides an explanation of the nonlinear beat phenomena that are observed in the transient responses of the full system (beam with attached nonlinear stiffness).

Based on our understanding of the nonlinear dynamics of this system, we develop a nonlinear system identification method capable of identifying strongly nonlinear modal interactions and their effects on the cantilever modes participating in these interactions. The system identification method is based on an adaptive step-by-step application of empirical mode decomposition (EMD) to the measured time series, as explained in Section 2.2, which is extended to multi-frequency beating signals. In particular, our work extends an earlier nonlinear system identification approach developed for nearly mono-frequency (mono-chromatic) signals, and applies it to the identification of the complex nonlinear dynamics of the cantilever beam with the strong end nonlinearity. Important features of the beating nonlinear dynamics are recovered using the proposed approach, including the nodal positions, the positions of the maxima, the modal damping factors and the beating frequencies for each participating modal response. The methodologies and results presented in this work pave the way for identifying unexpected strongly nonlinear dynamical phenomena (such as the nonlinear beats considered herein) and the properties of the modes participating in these phenomena in flexible structures with local stiffness nonlinearities.

CHAPTER 4

GLOBAL ASPECTS OF THE NSI METHODOLOGY

4.1 Introduction and Background Information

In this chapter, the global aspects of the NSI methodology will be discussed and the improvements made to the global NSI tools will be presented. The global aspect of our NSI method can be applied to both discrete and continuous nonlinear dynamical systems, irrespective of their dimensionalities. The main feature we use in our global NSI methodology is the frequency-energy dependence of the nonlinear systems, therefore, as explained in Section 2.6, FEPs are key components in our understanding of the global dynamical characteristics of nonlinear systems. By constructing FEPs, we can identify global features of the dynamics, *e.g.*, ranges of frequencies and energies where the system possesses linearized responses (corresponding to nearly horizontal branches of solutions in the FEP), coexisting branches of strongly nonlinear solutions, bifurcation points signifying the limits of response branches, *etc.* In addition, it is well established that forced resonances of nonlinear systems occur in neighborhoods of free periodic solutions (NNMs); hence, by identifying the FEPs we gain understanding of the structure of nonlinear (fundamental or subharmonic) resonances in the forced dynamics. Since we are interested in the global frequency-energy dependence of the dynamical systems, we point out the benefit of considering transient instead of steady state responses in our proposed NSI. Indeed, analyzing transient responses is an efficient way of ‘probing’ the dynamics and obtaining a broader understanding of the frequency transitions. Performing transient tests allows us to

effectively probe the dynamics of a system and to depict these results in compact form in a FEP, as will be shown in this chapter.

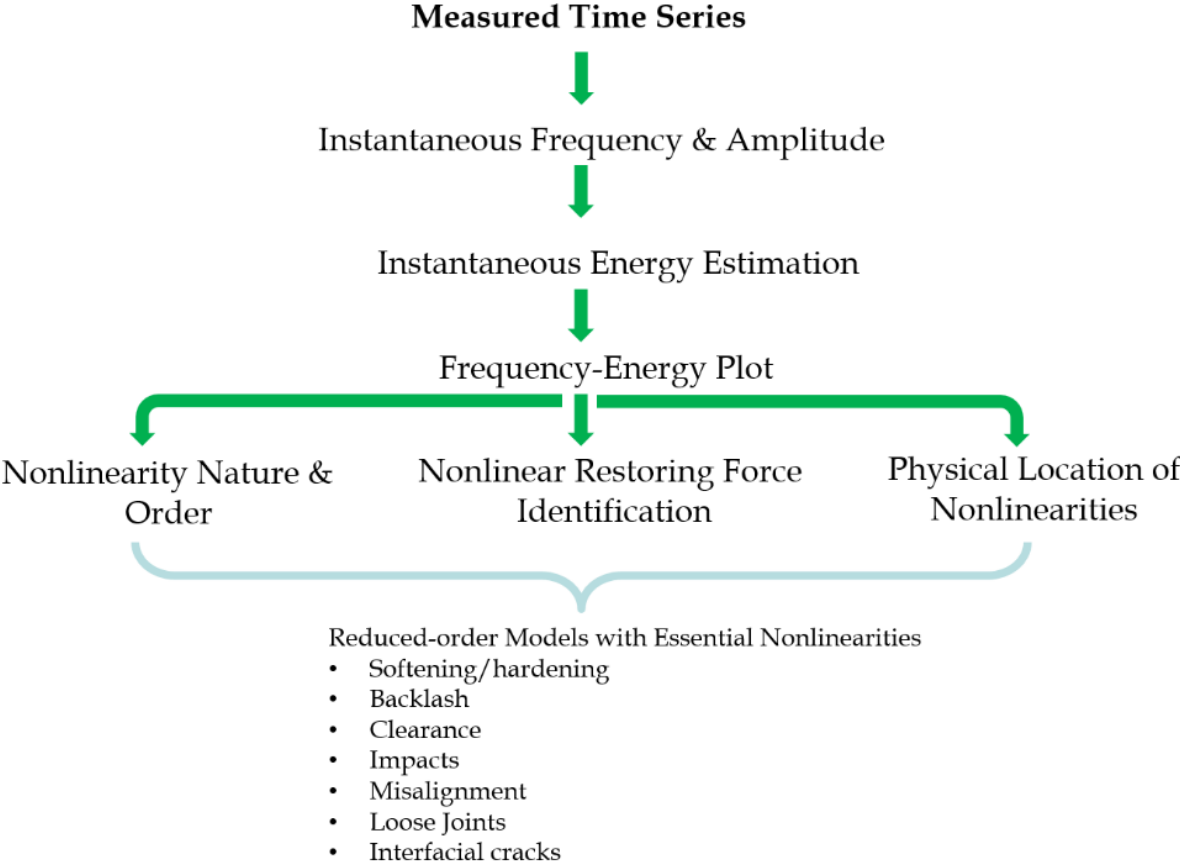


Figure 4.1 General outline of the global NSI approach

In Figure 4.1, the general outline of the global NSI methodology is depicted. As done for the local aspect, we start with the measured time series and extract the instantaneous frequency, amplitude and energy estimations. Then we construct FEPs (either numerically or analytically) and compare the empirical frequency-energy dependence with these reference FEPs. In doing so, one can extract many essential information about the system such as the nature, order and physical location of the nonlinearities. Then, we construct reduced-order models based on the

findings we obtain from the FEP analysis and try to reproduce the original time series, which will be further discussed in Chapter 5.

In Section 4.2, we will discuss the type and amount of information that can be extracted from frequency-energy plot reconstructions and give an insight regarding the necessary steps to analyze and interpret the FEPs. In Section 4.3, we extend the Hamiltonian FEPs to forced and damped systems as well, which make them a practical tool for analyzing strongly nonlinear systems. Finally, we study two applications of forced and damped FEPs, namely a vibration isolation problem through nonlinear targeted energy transfer and a study of 1:3 resonance in a 2-DOF oscillator.

4.2 Frequency-Energy Plot Reconstructions

4.2.1 Analyzing the Frequency-Energy Plots of Different System Topologies

In studying the FEPs to retrieve the nonlinear characteristics of the underlying system, the main assumption we make is that we can reconstruct/track the backbone branches of the system by simply using the empirical (experimental or numerical) data. In addition to the nonlinear characteristics, a great deal of information regarding the topology of a system can be deduced from FEPs. As described in Section 2.6, FEPs provide a synoptic global description of the frequency and energy dependencies of periodic orbits of Hamiltonian n -degree of freedom (DOF) dynamical systems. Therefore, by definition, FEPs also provide information about the underlying linear dynamics of the dynamical system under consideration since for very low energies, nonlinear normal modes (NNMs) will approximate to linear normal modes (LNMs), provided that they exist. Another type of information that can be extracted from FEPs is the asymptotic

behavior of each mode as the energy levels go to infinity. For very large energy levels, the system configuration might effectively change into a completely new one, since the effects of the nonlinearity

Due to the stiffening effect of the cubic nonlinearity, the frequency of the in-phase NNM converges to a certain asymptotic limit with increasing energy, as the cubic stiffness becomes approximately rigid and the system approaches a beam with pinned right end. The out-of-phase NNM ‘decouples’ from the in-phase mode during this limiting process, becoming a purely nonlinearity-governed NNM.

To give an example, let’s consider the system whose FEP is given in Figure 4.3. We assume that we know the mass distribution of this 2-DOF system, such that $m_1 = 1.45$, $m_2 = 0.27$. In order to find the system configuration, we study the asymptotic behaviors of the two backbone branches, namely the in-phase and out-of-phase modes, for lower and higher energy extremes. We note that, due to the 0 in phase frequency at low energies, we do know that only 1 linear spring exists in the system. So, we can deduce that, we are looking for one of the configurations below:

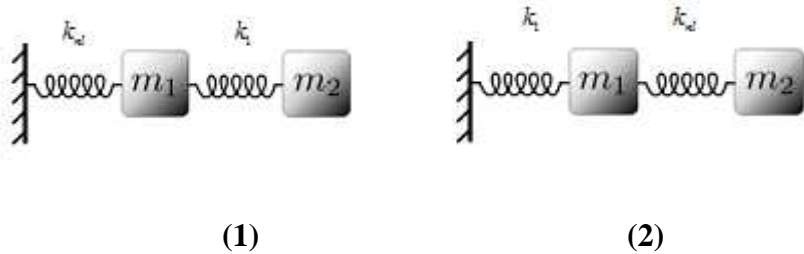


Figure 4.2 Possible system configurations for the examined system

We can also use the information available for the asymptotic region of the first backbone branch. For the first system in Figure 4.2, we see that the in phase frequency limit should be

$\lim_{E \rightarrow \infty} \omega_{in} \rightarrow \sqrt{k_1/m_2}$, and for the second system as $\lim_{E \rightarrow \infty} \omega_{in} \rightarrow \sqrt{k_1/(m_1 + m_2)}$. We immediately rule out first system, since this would yield a higher frequency value than the linear out-of-phase frequency, which is not possible. So we find that our system configuration is (2). A basic calculation based on the linear out-of-phase yields the linear spring value as $k_1 = 414$.

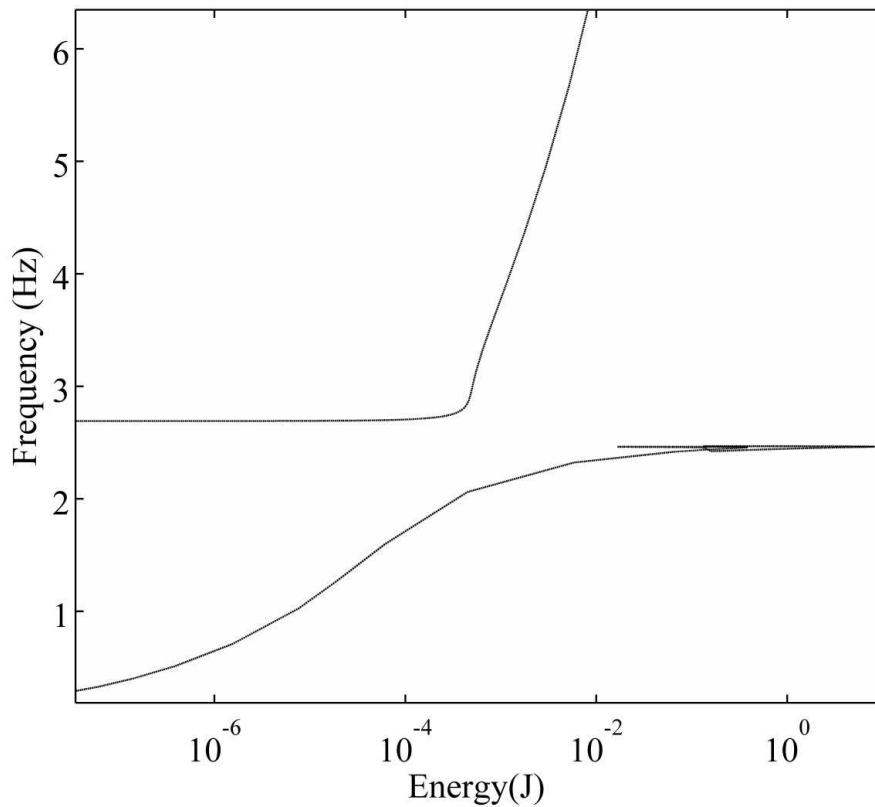


Figure 4.3 FEP of the system studied in 4.2.1

Another important information that can be extracted by using FEPs is the leading nonlinearity order. By using slow-flow analysis, one can show that, the energy of a SDOF nonlinear oscillator,

which possesses an integer order of nonlinearity, has the relationship with frequency as

$$E \approx \omega^{2\left(\frac{n+1}{n-1}\right)}. \text{ For example, for a Duffing oscillator, we have: } n = 3 \Rightarrow 2\left(\frac{n+1}{n-1}\right) = 4.$$

So, if we apply a power-type fit to the “highest mode of a nonlinear system” at high energies, we should be able to find the order of nonlinearity, since we would expect this highest mode to behave like a SDOF nonlinear oscillator at the high energy extremes.

As an application, we consider the frequency-energy plot of the cantilever beam with attached cubic nonlinear spring at its tip, which is studied in great detail in Section 3.4. Recalling that an assumed-modes approach consisting of 10 modes was applied to study the system, below in Fig. 15, 10 backbone branches for the corresponding modes are plotted. As seen in Figure 4.4, the highest mode approaches to the frequency-energy behavior of a Duffing oscillator, thus, by using the energy limit of the highest backbone branch, we can deduce the dominant nonlinearity order in the system.

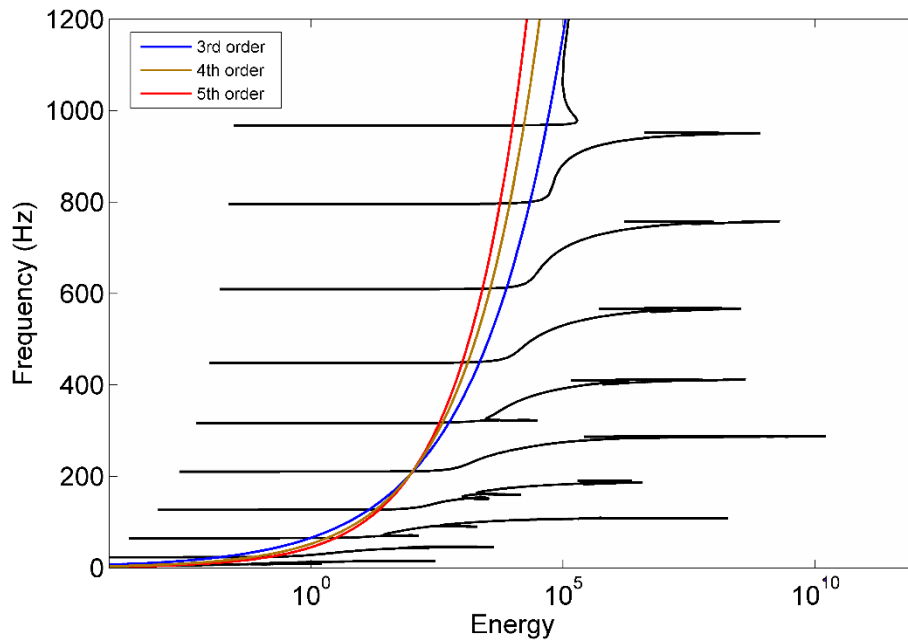
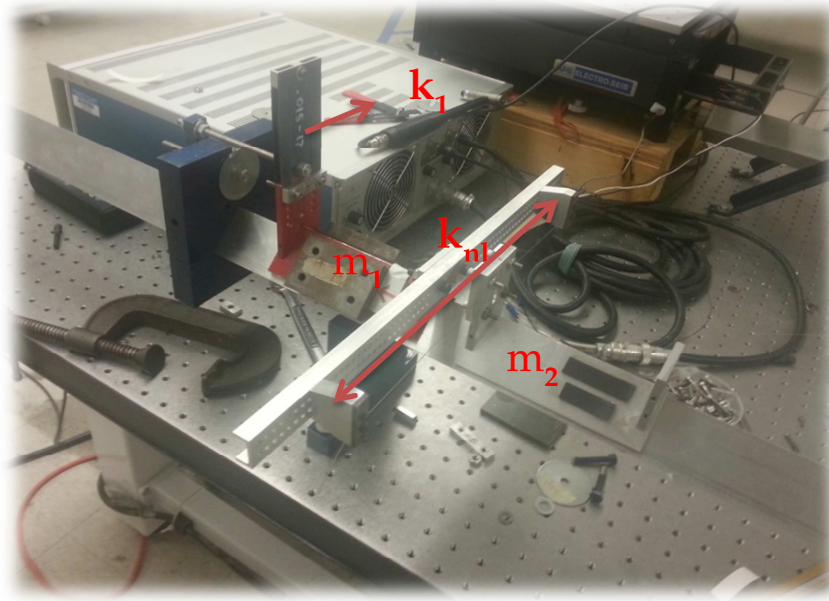


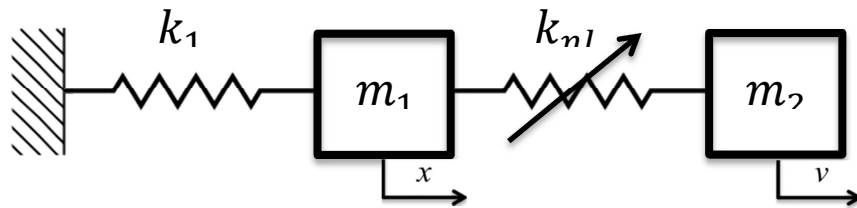
Figure 4.4 FEP of the system studied in Section 3.4

4.2.2 Experimental Results

In this section, a 2-DOF system consisting of a linear oscillator (LO) attached with a nonlinear energy sink (NES) is considered. As stated in Section 4.1, it is crucial to be able to reconstruct/track the backbone branches of the system from the experimental data, in order to identify the underlying global dynamics of a system. Therefore, the purpose of this experimental study is to show that we can predict the frequency-energy dependence of this nonlinear system by constructing and comparing with numerical and analytical FEPs.



(a)



(b)

Figure 4.5. (a) Picture of the experimental setup (b) Graphic representation of the experimental setup.

The experimental setup is shown in Figure 4.5. The linear oscillator (LO) consists of a leaf spring, connected to the ground and a cart upon which the masses are placed symmetrically. LO is connected to the nonlinear energy sink (NES) via a piano wire (.5 mm), which provides an almost cubic-order nonlinearity in between due to geometric nonlinearities. The whole setup is placed on an air-track, which provides very low damping values (damping ratios are on the order of 10^{-4}). Note that this is desired since the computation of Hamiltonian FEPs are much simpler than their

forced & damped counterparts, which makes them more practical for model updating and global system identification purposes.

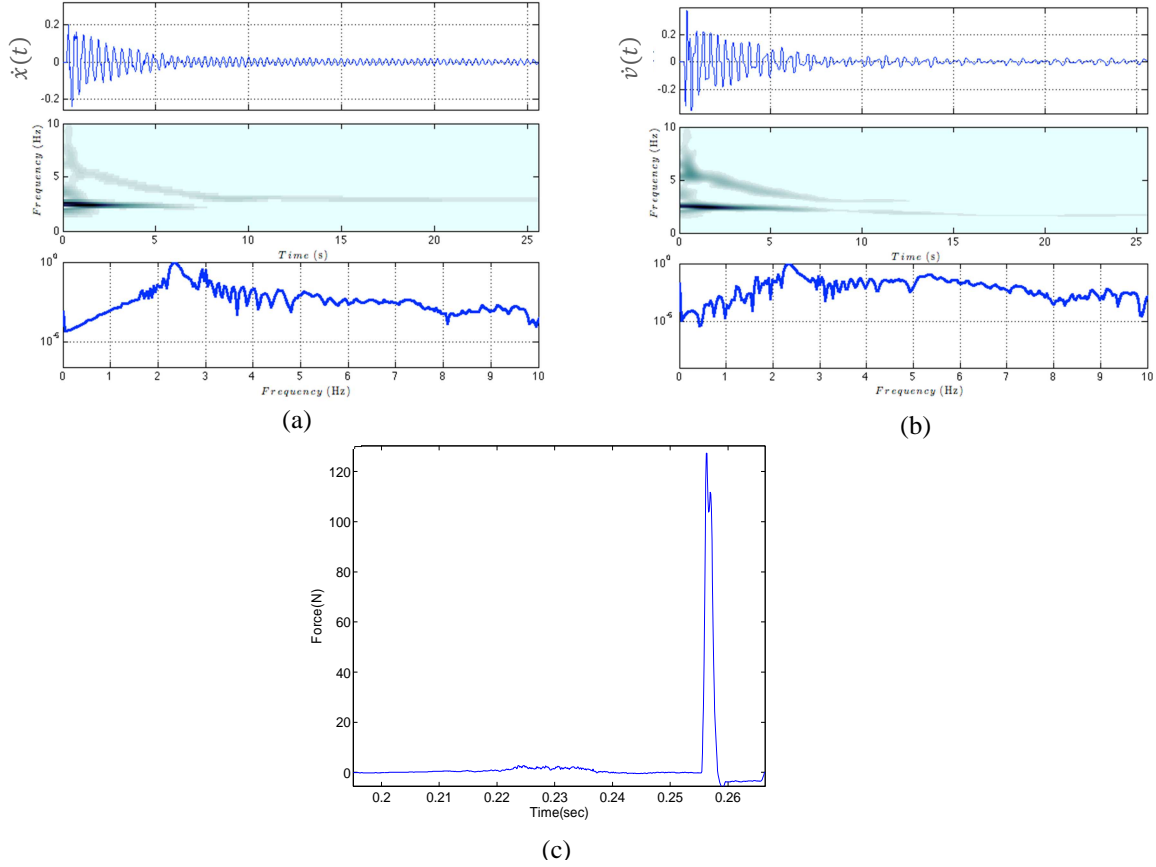


Figure 4.6 (a) Impulse response of the LO (b) Impulse response of the NES for forcing depicted in (c).

The parameters for LO are found by using logarithmic decrement method. In order to find NES parameters, we locked the LO and excited the NES with an impact hammer. NES parameters are then found by using restoring force method. The system parameters we found are $m_1 = 1.45$ kg, $m_2 = 0.27$ kg, $k_1 = 414.13$ N/m, $k_{nl} = 4.3 \times 10^6$ N/mⁿ, $n(\text{nonlinearity order}) = 2.89$.

In order to track the frequency-energy dependence of the system, we do multiple impulse tests and record the transient behaviors of the LO and the NES. One example data is given in Figure

4.6a,b. Looking at the raw velocity data for the LO and the NES, we can immediately observe the energy dependence of the in-phase and out-of-phase modes. Note also that, WTs of the experimental data reveal much more information regarding the dynamics of the system than the FTs, which is why we adhere to using WTs for such strongly nonlinear systems for identification and reduced-order modeling.

Before we move to studying the frequency-energy dependence of the system, we apply empirical mode decomposition (EMD) to the NES velocity data, depicted in Figure 4.6b. Note that, as noted in section 2.2, an intrinsic mode function (IMF) is generally extracted as a “narrow-band” component. As observed in Figure , $c_1(t)$ and $c_2(t)$, IMFs of the NES velocity data depicted in Figure , are not narrow-band components, but rather depict the damped frequency transitions of the in-phase and out-of phase modes. This is a (meaningful) extension of the definition of IMFs, since for our system identification purposes, it is more important to use “physically-meaningful” IMFs rather than narrow-banded signals. Therefore, one can think of $c_1(t)$ and $c_2(t)$ as the summation of many narrow-banded IMFs, and as a result depict the particular mode transitions of the NES response.

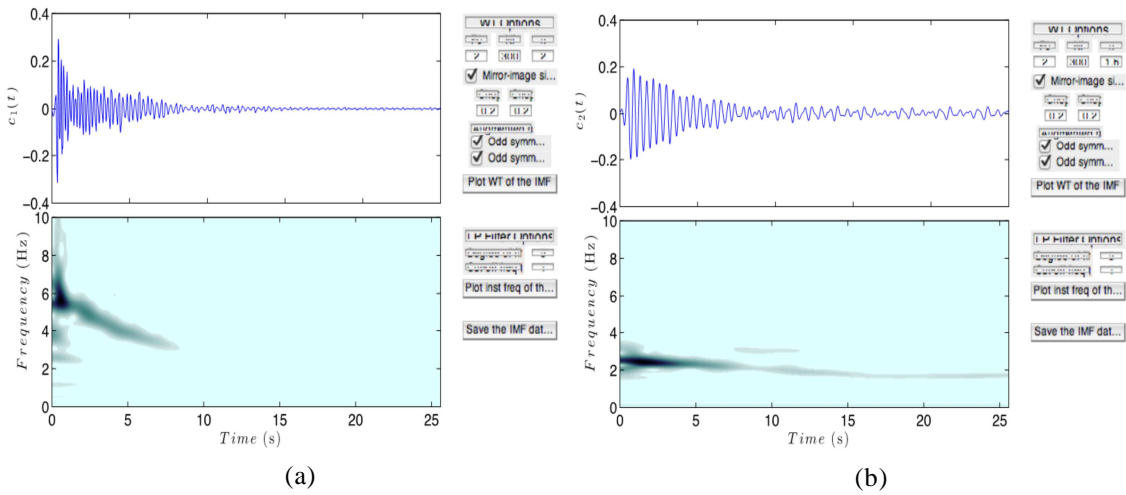


Figure 4.7 EMD results for the NES response in Figure 4.6b

Since the damped-transition of both in-phase and out-of-phase modes are very clear in Figure , it is a good idea to superimpose these onto the FEP of the original system. The FEP of the original system, depicted by dashed lines in Figure 4.8 and 4.9 are computed by using NNMcont (Peeters et al. 2009). In Figure 4.8, we superimpose the WTs of $c_1(t)$ and $c_2(t)$ onto the FEP of the original system. As predicted, the individual IMFs $c_1(t)$ and $c_2(t)$, which are extracted in an intentional way so that they would represent the damped frequency transitions of each mode, track the Hamiltonian backbone branches.

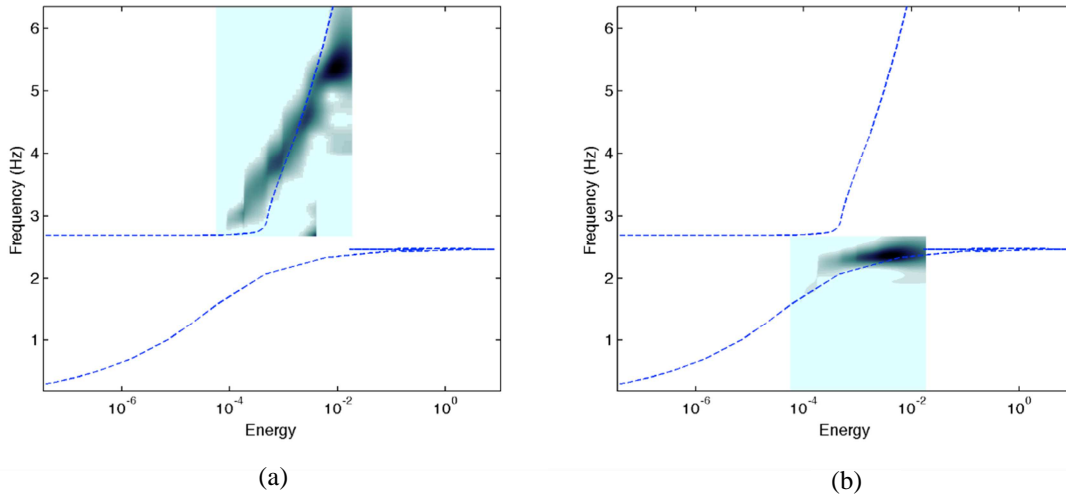


Figure 4.8 Superposition of the WTs of IMFs (in Figure 4.7) on the FEP.

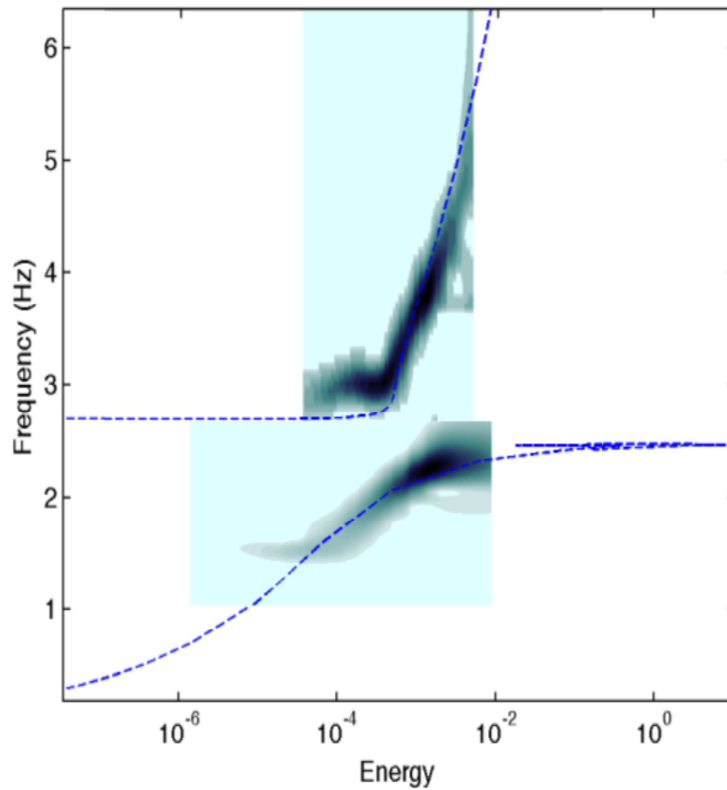


Figure 4.9 Superposition of the WTs from combined impulse tests (NES data).

As a final step, we combine the NES data from multiple impact tests with varying forcing amplitudes so that we would be able to span a greater energy range. We then superimpose the WTs of the whole data onto the computational FEP of the original system. This result is depicted in Figure 4.9. As one can observe, the damped frequency transitions seem to be agreeing with the Hamiltonian backbone branches with a good accuracy. Note that one of the crucial properties for this was to use low damping, which we ensured in our experiments, since we compare the experimental data with the Hamiltonian backbone branches. The superimposed WTs of the NES data is normalized with respect to the maximum amplitude of the energy range for each mode for visualization purposes.

4.3 Extending the Frequency-Energy Plots for Forced and Damped Systems

4.3.1 Forced and Damped Frequency-Energy Plots (FEPs) (Kurt, Eriten, et al. 2014b)

4.3.1.1 Introduction and System Description

In recent studies the free and forced dynamics of strongly nonlinear oscillators have been considered; *i.e.*, of dynamical systems with essential stiffness nonlinearities possessing negligible or very small linear components (Gendelman et al. 2001; Vakakis and Gendelman 2001; Gourdon et al. 2007; Gourdon, Lamarque, and Pernot 2007; Vakakis 2008). The high degeneracy that this class of strongly nonlinear systems possesses gives rise to interesting nonlinear dynamical phenomena, such as cascades of transient resonance captures (Arnold 1988; Vakakis et al. 2004), broadband vibration energy transfers between subcomponents (targeted energy transfers) (Vakakis 2008), and nonlinear localization phenomena (Gendelman et al. 2001). Tools for analyzing the strongly nonlinear dynamics of these systems have been developed, such as wavelet

spectra superposition on frequency-energy plots – FEPs of Hamiltonian dynamics and complexification/averaging analysis (Vakakis 2008). As shown in previous works two-dimensional FEPs provide a synoptic global description of the frequency and energy dependencies of periodic orbits of Hamiltonian n -degree of freedom (DOF) dynamical systems, and can be used to interpret complex dynamical transitions of weakly damped systems possessing even strong, non-smooth nonlinearities (Lee, Nucera, et al. 2009). This is achieved by superimposing wavelet spectra of the damped responses onto the Hamiltonian FEPs, thus identifying the underlying Hamiltonian dynamics that influence the damped transitions (Vakakis 2008).

The principal aim of the present work is to study the perturbations of the Hamiltonian FEPs in the presence of weak damping and small-amplitude harmonic excitation. This topic has not been addressed in the literature and, hence, the results reported here are new. Considering a specific two-DOF oscillator with strong nonlinearity, our analysis is carried out under conditions of 1:1 resonance; *i.e.*, when the two degrees of freedom oscillate in synchronicity with identical dominant frequencies. Moreover, the applied harmonic excitation is assumed to also possess a frequency close to the frequency of oscillation of the system, so an additional condition of fundamental resonance is assumed. Our analysis is based on complexification-averaging (CX-A) of the equations of motion, and the results are applied to the problem of optimizing vibration isolation of a harmonically forced linear system by means of transferring steady-state energy to a weakly coupled strongly nonlinear attachment (termed the nonlinear energy sink – NES).

Whereas interesting recent contributions to the problem of optimal vibration isolation through nonlinear targeted energy transfer have appeared (Gendelman and Starosvetsky 2006; Starosvetsky and Gendelman 2008a; Starosvetsky and Gendelman 2008b) our approach to the

optimization is different since it is based on the forced and damped FEP of the system. We note that a two-DOF system similar to the one considered in this work was first considered in (Jiang et al. 2003), where the feasibility of steady-state energy transfer from the directly excited linear oscillator to the nonlinear attachment was addressed without performing, however, any optimization related to vibration isolation. In fact, as pointed out in (Malatkar and Nayfeh 2007) where this system was re-examined, a Hopf bifurcation in the steady-state dynamics of the weakly coupled system leading to weakly modulated responses was missed in (Jiang et al. 2003). However, what we show in the present work is that optimization of the steady-state dynamics of the weakly coupled and weakly damped two-DOF system of (Jiang et al. 2003) can lead to effective vibration isolation by means of steady-state nonlinear targeted energy transfer and localization.

We consider in this report a two-DOF system, consisting of a weakly damped linear oscillator – LO weakly coupled with an essentially nonlinear, weakly damped attachment (which will act as a nonlinear energy sink – NES) through a weak linear stiffness of constant εk_c , where $|\varepsilon| \ll 1$ is a small quantity that will be designated as the *perturbation parameter* of our study. The stiffness nonlinearity is characterized as *essential* since its characteristic is purely cubic (with coefficient k_{nl}) and lacking a linear part; hence, the nonlinearity is completely *nonlinearizable*. The LO is excited by a small-amplitude harmonic force with amplitude equaling εP and frequency ω . The configuration of the system is depicted in Figure 1. We are mainly interested in the amplitude-frequency dependence of the steady-state responses of the LO and the NES.

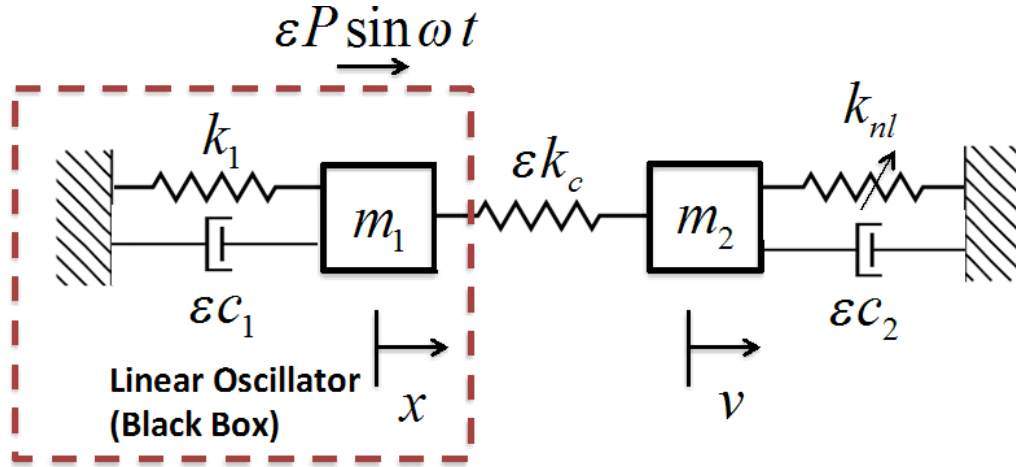


Figure 4.10 Two-DOF weakly coupled and weakly damped system under weak harmonic forcing.

We will study the steady-state dynamics of this system both analytically and numerically. First, under the assumption of fundamental resonance and 1:1 resonance between the LO and the NES, we apply the CX-A method and slow/fast partition of the steady-state dynamics and construct damped and forced perturbations of the FEP of the underlying Hamiltonian system (corresponding to no damping or forcing). We note that our analytical approach applies even in this strongly nonlinear case, when traditional asymptotic methods of nonlinear dynamics based on the assumption of weak nonlinearity and linear generating solutions are not valid (since the current problem is non-linearizable). Then, we will verify the analytical results by direct numerical simulation of the equations of motion, to highlight some interesting phenomena of practical interest.

The equations of motion of the system of Figure 4.10 are expressed as

$$\begin{aligned}
 \ddot{x}(t) + \varepsilon\lambda_1 \dot{x}(t) + \omega_0^2 x(t) + \varepsilon\alpha_1 [x(t) - v(t)] &= \varepsilon P \sin \omega t \\
 \ddot{v}(t) + \varepsilon\lambda_2 \dot{v}(t) + C_s v^3(t) - \varepsilon\alpha_1 [x(t) - v(t)] &= 0
 \end{aligned}
 \tag{4.1}$$

where the normalized coefficients are given by $\lambda_1 = c_1/m_1$, $\lambda_2 = c_1/m_2$, $\alpha_1 = k_c/m_1$, $\alpha_2 = k_c/m_2$, $C = k_{nl}/m_2$ and $\omega_0^2 = k_1/m_1$. For simplicity, we make the assumption of equal masses $m_1 = m_2$, so that $\alpha_1 = \alpha_2$, since this assumption will help us reduce the complexity of the resulting analytical derivations. Furthermore, again without loss of generality we set the natural frequency of the LO equal to unity, $\omega_0^2 = 1$ (this can always be achieved by appropriate rescaling of the time variable in (4.1)).

4.3.1.2 Constructing the Forced and Damped Frequency-Energy Plots (FEPs)

We now apply the complexification-averaging method (CX-A) to study the dynamics of *fundamental resonance* of system (4.1). The method was first developed by (Manevitch 1999) and then applied extensively in studies of nonlinear targeted energy transfer (Vakakis et al., 2008). To this end, we complexify the normalized equations of motion (3.43) by introducing new complex variables in the form

$$\psi_1(t) = \dot{x}(t) + j\omega x(t) \equiv \underbrace{\varphi_1(t)}_{\text{'Slow' part}} \underbrace{e^{j\alpha t}}_{\text{'Fast' part}}, \quad \psi_2(t) = \dot{v}(t) + j\omega v(t) \equiv \underbrace{\varphi_2(t)}_{\text{'Slow' part}} \underbrace{e^{j\alpha t}}_{\text{'Fast' part}}, \quad j = (-1)^{1/2} \quad (4.2)$$

In (3.44) a slow/fast decomposition was additionally imposed, whereby the new complex variables $\psi_i(t)$ were expressed in terms of slowly varying envelopes $\varphi_i(t)$ that modulate fast harmonic oscillations at frequency ω . Moreover, (4.2) indicates that the desired solutions possess dominant harmonic components at the frequency of the harmonic excitation, so only *fundamental resonances* of system (4.1) will be examined (as mentioned above, we will also refer to these motions as 1:1 resonances since the two oscillators are assumed to oscillate with identical frequencies). This means that other types of nonlinear resonance (*e.g.*, subharmonic and

superharmonic resonances) cannot be examined by the ansatz (4.2); see (Vakakis 2008; Andersen et al. 2012) for extension of the CX-A method to such cases. Then, we express the original variable x in terms of the new complex variables as

$$x = \frac{\varphi_1 e^{j\alpha x} - \varphi_1^* e^{-j\alpha x}}{2j\omega}, \quad \dot{x} = \frac{\varphi_1 e^{j\alpha x} + \varphi_1^* e^{-j\alpha x}}{2}, \quad \ddot{x} = \dot{\varphi}_1 e^{j\alpha x} + j\omega \frac{\varphi_1 e^{j\alpha x} - \varphi_1^* e^{-j\alpha x}}{2} \quad (4.3)$$

with similar expressions holding for the other variable v . Substituting these expressions into the original equations of motion (4.3) and averaging over the fast frequency ω we obtain the *approximate set of modulation equations*

$$\begin{aligned} \dot{\varphi}_1 - \frac{j\varphi_1}{2\omega} + \frac{1}{2}j\omega\varphi_1 + \frac{\varepsilon\alpha_1(\varphi_1 - \varphi_2)}{2j\omega} + \frac{1}{2}\varepsilon\lambda_1\varphi_1 &= \frac{\varepsilon P}{2j} \\ \dot{\varphi}_2 + \frac{1}{2}j\omega\varphi_2 + \frac{j\alpha_1\varepsilon(\varphi_2 - \varphi_1)}{2j\omega} + \frac{1}{2}\varepsilon\lambda_2\varphi_2 - \frac{3jC_s|\varphi_2|^2\varphi_2}{8\omega^3} &= 0 \end{aligned} \quad (4.4)$$

also referred to as the *slow flow system*. This system of slowly varying complex equations governs the essential (important) dynamics of fundamental resonance of system (4.2) after the unessential fast dynamics at frequency ω has been averaged out. We note that the approximation in (4.4) is caused by the fact that higher harmonics (e.g., at frequency 3ω) are neglected; it follows that our analytical study is only valid in regimes where the system responds primarily at the frequency of the applied harmonic excitation and is expected to be inaccurate for responses where higher harmonic components cannot be neglected.

As a first step we need to transform the modulation equations (4.4) back to the real domain in order to study the steady-state dynamics. To this end, we express the complex variables

in (4.4) in polar form, $\varphi_i = \phi_i e^{i\theta_i}$, where ϕ_i and θ_i are real amplitudes and phases. Separating real and imaginary parts yields the slow flow system in terms of real variables

$$\begin{aligned}
\dot{\phi}_1 + \frac{\varepsilon\lambda_1}{2}\phi_1 + \frac{\varepsilon P}{2}\sin\theta_1 + \frac{\alpha_1\varepsilon}{2\omega}\phi_2\sin(\theta_1 - \theta_2) &= 0 \\
\varepsilon(P\omega\cos\theta_1 + \alpha_1\phi_2\cos(\theta_1 - \theta_2)) + \phi_1(-1 + \omega^2 - \varepsilon\alpha_1 + 2\omega\dot{\theta}_1) &= 0 \\
\dot{\phi}_2 + \frac{\varepsilon\lambda_2}{2}\phi_2 - \frac{\varepsilon\alpha_1}{2\omega}\phi_2\sin(\theta_1 - \theta_2) &= 0 \\
\varepsilon\alpha_1\phi_1\cos(\theta_1 - \theta_2) + \phi_2(\omega^2 - \varepsilon\alpha_1 + 2\omega\dot{\theta}_2) - \frac{3C_s}{4\omega^2}\phi_2^3 &= 0
\end{aligned} \tag{4.5}$$

The stationary points of system (4.5) yield the periodic steady-state solutions for fundamental resonance. Setting $\dot{\phi}_k = 0$, $\dot{\theta}_k = 0$ we derive the system of nonlinear algebraic equations

$$\begin{aligned}
\frac{\varepsilon\lambda_1}{2}\phi_1 + \frac{\varepsilon P}{2}\sin\theta_1 + \frac{\varepsilon\alpha_1}{2\omega}\phi_2\sin(\theta_1 - \theta_2) &= 0 \\
\varepsilon(P\omega\cos\theta_1 + \alpha_1\phi_2\cos(\theta_1 - \theta_2)) + \phi_1(-1 + \omega^2 - \varepsilon\alpha_1) &= 0 \\
\frac{\varepsilon\lambda_2}{2}\phi_2 - \frac{\varepsilon\alpha_1}{2\omega}\phi_1\sin(\theta_1 - \theta_2) &= 0 \\
\varepsilon\alpha_1\phi_1\cos(\theta_1 - \theta_2) + \phi_2(\omega^2 - \varepsilon\alpha_1) - \frac{3C_s}{4\omega^2}\phi_2^3 &= 0
\end{aligned} \tag{4.6}$$

Solving these equations for the amplitudes ϕ_i and phases θ_i provides the approximate steady-state periodic responses of the two oscillators in (4.1), and allows us to obtain frequency-amplitude (energy) dependencies of these solutions.

First, we study the periodic orbits of the underlying Hamiltonian system by setting $\lambda_1 = \lambda_2 = P = 0$ in (4.6), which now take the simpler form

$$\begin{aligned}
\frac{\varepsilon\alpha_1}{2\omega}\phi_2 \sin(\theta_1 - \theta_2) &= 0 \\
\varepsilon\alpha_1\phi_2 \cos(\theta_1 - \theta_2) + \phi_1(-1 + \omega^2 - \varepsilon\alpha_1) &= 0 \\
\frac{\varepsilon\alpha_1}{2\omega}\phi_1 \sin(\theta_1 - \theta_2) &= 0 \\
\varepsilon\alpha_1\phi_1 \cos(\theta_1 - \theta_2) + \phi_2(\omega^2 - \varepsilon\alpha_1) - \frac{3C_s}{4\omega^2}\phi_2^3 &= 0
\end{aligned} \tag{4.7}$$

where $\gamma = \theta_1 - \theta_2$ is the phase difference. From (4.7) we conclude that the Hamiltonian system admits in-phase 1:1 periodic orbits corresponding to $\gamma = 0 \pmod{2\pi}$ when $\omega^2 < 1 + \varepsilon\alpha_1$, and out-of-phase periodic orbits for $\gamma = \pi \pmod{2\pi}$ when $\omega^2 > 1 + \varepsilon\alpha_1$. In Figures 4.11 and 4.12 we use solid gray lines to depict the frequency-amplitude plots (or approximate frequency response plots) for the linear (LO) and nonlinear (NES) oscillators, respectively, for parameters $\alpha_1 = 10$, $C_s = 1$ and $\varepsilon = 0.05$. These 1:1 steady-state periodic solutions of the Hamiltonian system are also referred to as nonlinear normal modes (Rosenberg 1966). In Figure 4.13 these two plots are combined into a single frequency-energy plot (FEP), where, again, solid gray lines are used to depict the Hamiltonian periodic motions. The lower branch of the FEP corresponds to the in-phase mode for $\gamma = 0$ (which for low energy approaches the natural frequency of the LO), whereas the upper branch corresponds to the out-of-phase mode for $\gamma = \pi$. We construct these plots analytically by solving the slow flow equations (4.7) for the normalized steady-state amplitudes $X = \phi_1 / \omega$, $V = \phi_2 / \omega$ and the phase difference $\gamma = \theta_1 - \theta_2$, giving

$$X = 2\varepsilon\alpha_1 \sqrt{\frac{\omega^4 + \varepsilon\alpha_1 - \omega^2(1 + 2\varepsilon\alpha_1)}{3C_s(-1 + \omega^2 - \varepsilon\alpha_1)^3}}, \quad V = 2 \sqrt{\frac{\omega^2(1 - 2\varepsilon\alpha_1) - \omega^4 - \varepsilon\alpha_1}{3C_s(1 - \omega^2 + \varepsilon\alpha_1)}}, \quad \gamma = 0, \pi \tag{4.8}$$

and then find the conserved energy of the Hamiltonian system E by calculating the maximum potential energy stored in the stiffness elements

$$E = \frac{X^2}{2} + \varepsilon\alpha_1 \frac{(X-Y)^2}{2} + C_s \frac{Y^4}{4} \quad (4.9)$$

When harmonic forcing is introduced to the undamped system (*i.e.*, when $P \neq 0$), the equations (4.6) governing the fundamental resonances take the form

$$\begin{aligned} \frac{\varepsilon P}{2} \sin \theta_1 + \frac{\varepsilon\alpha_1}{2\omega} \phi_2 \sin \gamma &= 0 \\ \varepsilon P \omega \cos \theta_1 + \varepsilon\alpha_1 \phi_2 \cos \gamma + \phi_1 (-1 + \omega^2 - \varepsilon\alpha_1) &= 0 \\ \frac{\varepsilon\alpha_1}{2\omega} \phi_1 \sin \gamma &= 0 \\ \varepsilon\alpha_1 \phi_1 \cos \gamma + \phi_2 (\omega^2 - \varepsilon\alpha_1) - \frac{3C_s}{4\omega^2} \phi_2^3 &= 0 \end{aligned} \quad (4.10)$$

Nontrivial solutions necessitate that the phase difference takes the form $\gamma = m\pi$, $m = 0, 1$; thus,

(4.10) simplifies to

$$\begin{aligned} \frac{\varepsilon P}{2} \sin \theta_1 &= 0 \\ \varepsilon P \omega \cos \theta_1 + (-1)^m \varepsilon\alpha_1 \phi_2 + \phi_1 (-1 + \omega^2 - \varepsilon\alpha_1) &= 0 \\ (-1)^m \varepsilon\alpha_1 \phi_1 + \phi_2 (\omega^2 - \varepsilon\alpha_1) - \frac{3C_s}{4\omega^2} \phi_2^3 &= 0 \end{aligned} \quad (4.11)$$

Note that since the first of equations (4.11) yields $\theta_1 = \pi n$, $n = 0, 1$, (4.11) can be further reduced to

$$\begin{aligned}
(-1)^n \varepsilon P \omega + \varepsilon \alpha_1 \left[(-1)^m \phi_2 - \phi_1 \right] + \phi_1 (-1 + \omega^2) &= 0 \\
\varepsilon \alpha_1 \left[(-1)^m \phi_1 - \phi_2 \right] + \omega^2 \phi_2 - \frac{3C_s}{4\omega^2} \phi_2^3 &= 0
\end{aligned} \tag{4.12}$$

In Figures 4.11 and 4.12 we depict the frequency-amplitude plots of the LO and NES oscillators, respectively, for the forced undamped system with parameters $\alpha_1 = 10$, $C_s = 5$, $\varepsilon = 0.05$, $P = 100$. As in the Hamiltonian case these two plots are combined in a single frequency-energy plot (FEP) in Figure 4.13. We partition each plot into four main branches, labeled branches 1-4. A first observation is that all branches can be regarded as forced perturbations of corresponding branches of the Hamiltonian system. Indeed, branch 1 is the forced perturbation of the in-phase NNM, below the linearized natural frequency of the LO at 6 rad/sec; these are predominantly linear, in-phase fundamental resonance oscillations, localized to the LO and exhibiting only weakly nonlinear effects. Branch 2 undergoes a very interesting dynamical transition with increasing frequency. In particular, at lower frequencies in the neighborhood of the linearized natural frequency of the LO, the fundamental resonance oscillations are predominantly linear, in-phase and localized to the LO, whereas at higher frequencies they become nonlinear, out-of-phase and strongly localized to the NES. This is due to the fact that branch 2 is a forced perturbation of two branches of NNMs of the Hamiltonian system; that is, for lower frequencies branch 2 is a forced perturbation of the in-phase (predominantly linear) NNM, whereas at higher frequencies it represents a perturbation of the strongly nonlinear, high-frequency and out-of-phase NNM which is strongly localized to the NES. The transition between these two qualitatively different dynamical behaviors is signified by the folding point on branch 2 in the FEP.

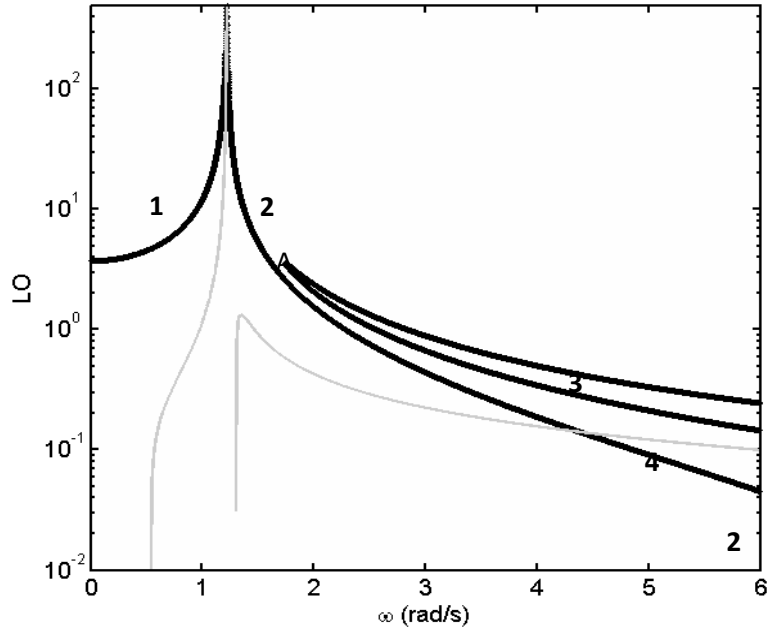


Figure 4.11 Normalized amplitude of the LO as function of frequency for the forced and undamped system: **—** NNMs of the underlying Hamiltonian system, **—** Forced fundamental resonance branches.

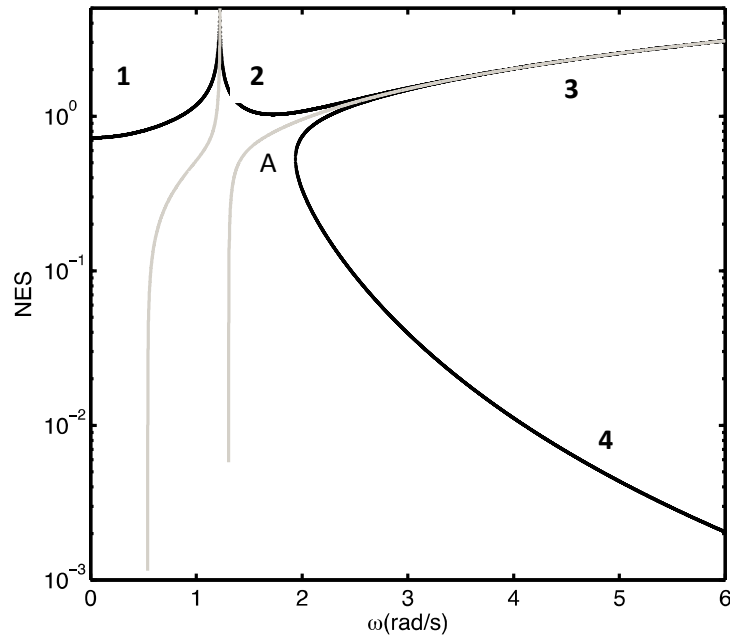


Figure 4.12 Normalized amplitude of the NES as function of frequency for the forced and undamped system: **—** NNMs of the underlying Hamiltonian system, **—** Forced fundamental resonance branches.

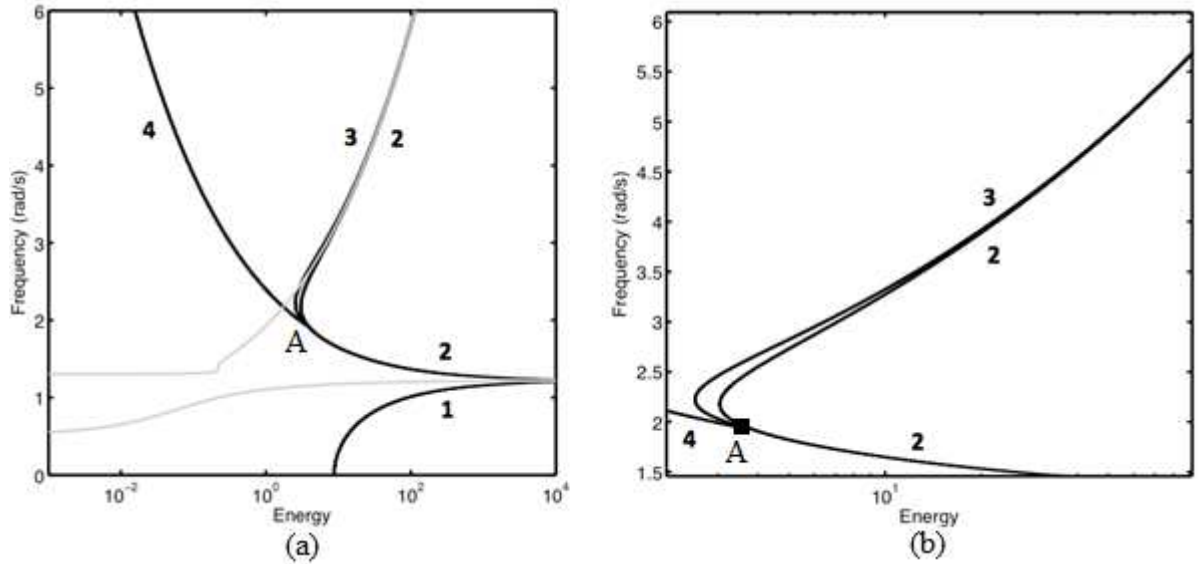


Figure 4.13 Frequency-energy plots (FEPs) for fundamental resonances of the forced and undamped system: (a) Global FEPs, (b) detail showing the bifurcations of fundamental resonances; gray solid lines depict the NNMs of the underlying Hamiltonian system.

Branch 3 represents a forced perturbation of the high-frequency out-of-phase strongly nonlinear NNM, so it consists of strongly nonlinear out-of-phase resonances localized to the NES. This branch meets the weakly nonlinear out-of-phase branch 4 at the bifurcation point A in the FEP. Branch 4 can be regarded as the forced perturbation of a trivial dynamical state (zero response) of the Hamiltonian system at frequencies above the linearized natural frequency of the LO. We note that there is an additional folding point for branch 3 with varying frequency in the FEP (*cf.* Figure 4.13).

The stability of the computed steady-state solutions was examined by linearizing the modulation equations (4) in the neighborhood of each stationary point and computing the eigenvalues of the matrix of coefficients of the resulting variational system. When the results of this numerical stability analysis were inconclusive we resorted to direct numerical integrations of the equations of motion with the theoretically predicted initial conditions for the fundamental resonances. We found that branches 1,2 and 4 are stable, whereas branch 3 is unstable.

By comparing the Hamiltonian and forced responses (especially the FEPs) it is possible to deduce the effect of the NNMs of the Hamiltonian dynamics on the fundamental resonances of the harmonically forced system. Indeed, the underlying topological structure of the NNMs of the Hamiltonian system affects the topological structure of the forced fundamental resonances, and the localization characteristics of the underlying NNMs get transferred to corresponding localization characteristics of the forced resonances. It is this later observation that will help us in designing the system for optimal energy transfer and localization to the NES and vibration isolation of the LO, as discussed in the next Section.

In a third step we consider the full slow flow (4.5) and the equations governing the fundamental resonances (4.6), by taking into account both weak harmonic excitation and weak damping. Solving the third equation in (4.6) for the phase difference yields

$$\sin(\theta_1 - \theta_2) = \frac{\omega \lambda_2}{\alpha_1} \phi_2 / \phi_1 \quad \text{which, when substituted into the first equation, gives}$$

$$\lambda_1 \phi_1^2 + \lambda_2 \phi_2^2 + P \phi_1 \sin \theta_1 = 0 \quad (4.13)$$

This equation provides the balance between the energy input by the external force and the energy dissipated by the damping elements, and basically states that, in order for a fundamental

resonance to be realized in the forced and damped system, the energy dissipated in each cycle should be balanced by the energy input provided by the harmonic excitation. The remaining two equations in the set (4.6) then simplify, (when the trigonometric identity $\cos\theta = \pm\sqrt{1-\sin^2\theta}$ is employed) to

$$\begin{aligned} \varepsilon \left[\pm P \omega \sqrt{1-\sin^2\theta_1} \pm \alpha_1 \phi_2 \sqrt{1-\left(\frac{\omega\lambda_2}{\alpha_1} \phi_2 / \phi_1\right)^2} \right] + \phi_1 (-1 + \omega^2 - \varepsilon\alpha_1) &= 0 \\ \pm \varepsilon\alpha_1 \phi_1 \sqrt{1-\left(\frac{\omega\lambda_2}{\alpha_1} \phi_2 / \phi_1\right)^2} + \phi_2 (\omega^2 - \varepsilon\alpha_1) - \frac{3C_s}{4\omega^2} \phi_2^3 &= 0 \end{aligned} \quad (4.14)$$

This set of equations relates the amplitudes of the steady-state responses of the LO and the NES during fundamental resonance and the frequency of the applied excitation ω . Hence, solving equations (4.13) and (4.14) provides the desired frequency-amplitude (energy) relations. The corresponding steady-state phases are then computed by the previous relationships.

In Figures 4.14 and 15 we depict the frequency-amplitude plots for the LO and NES, respectively, of the harmonically forced and damped system with parameters $\alpha_1 = 10$, $C_s = 5$, $\varepsilon = 0.05$, $P = 100$, $\lambda_1 = 0.2$ and $\lambda_2 = 0.2$. These results are combined in the FEP of Figure 7. One can regard these plots as damped perturbations of the corresponding plots of the harmonically forced and undamped system of Figures 4.11-13.

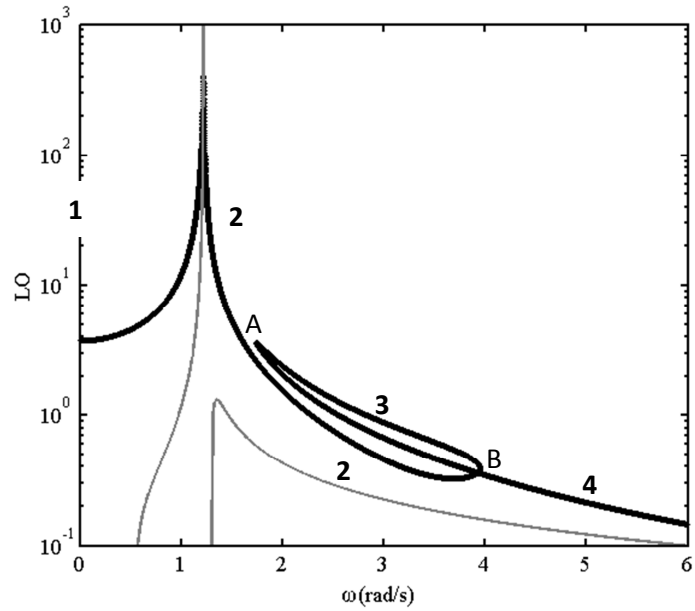


Figure 4.14 Normalized amplitude of the LO as function of frequency for the forced and damped system:
 — NNMs of the underlying Hamiltonian system, **—** Forced fundamental resonance branches.

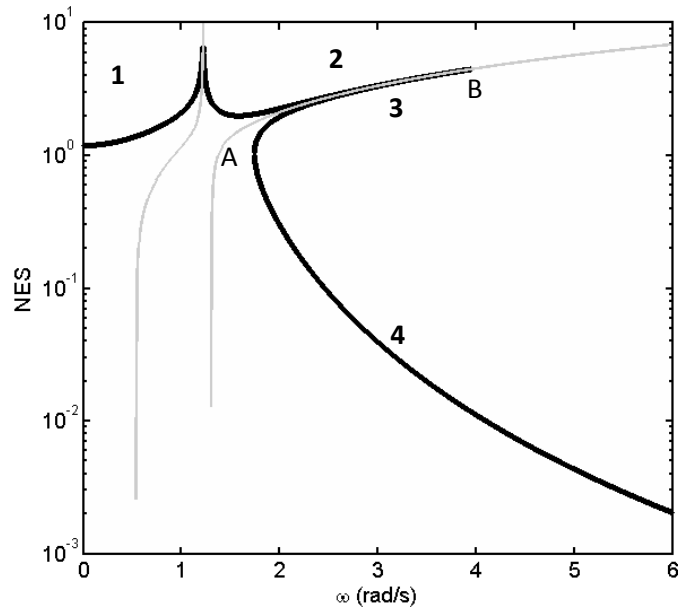


Figure 4.15 Normalized amplitude of the NES as a function of frequency for the forced and damped system:
 — NNMs of the underlying Hamiltonian system, **—** forced fundamental resonance branches.

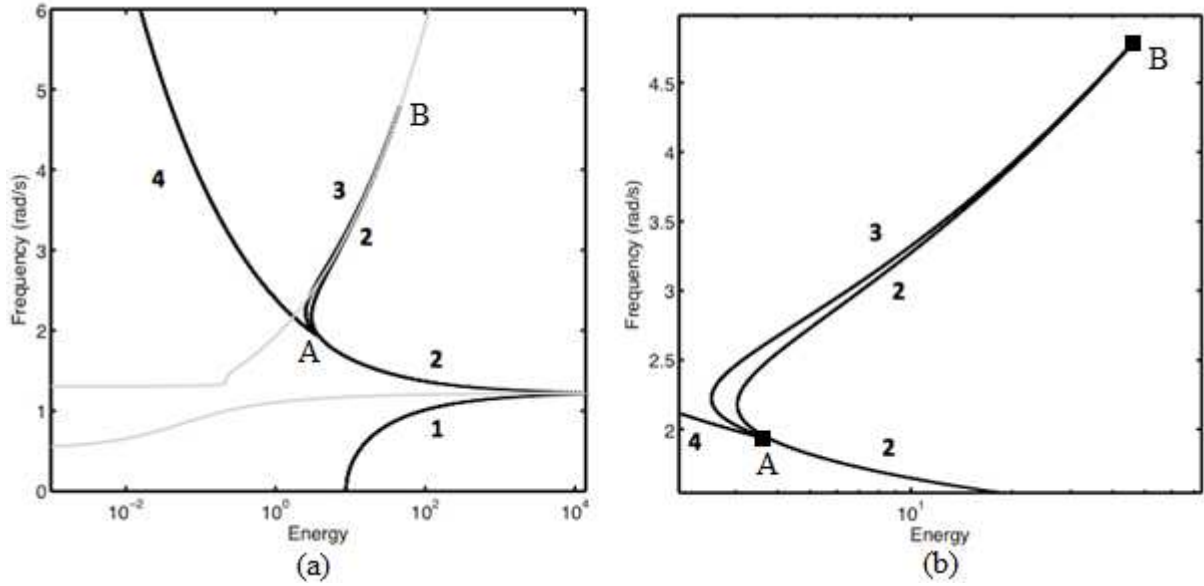


Figure 4.16 Frequency-energy plots (FEPs) for fundamental resonances of the forced and damped system: (a) Global FEPs, (b) detail showing the bifurcations of fundamental resonances; gray solid lines depict the NNMs of the underlying Hamiltonian system.

As before, we can partition each plot into four main branches. Keeping the same notation, we see that in the present case branch 2 extends over a finite frequency range as it coalesces with branches 3 and 4 at a frequency close to 4 rad/s. The same holds for branch 3 which now extends over a finite frequency range until it coalesces with branches 2 and 4. In summary, the basic topological features of the 1:1 fundamental resonance branches are preserved when weak damping is added, and the main damping effects are observed in branches 2 and 3, which now possess a cut-off frequency as discussed previously.

In the present case there exist two bifurcation points: A is the point of coalescence of branches 3 and 4 (as in the previous forced undamped case), and B is the point of coalescence of branches 2 and 3, which is exclusively due to the presence of damping. As discussed previously, branches 1 and 4 represent weakly nonlinear fundamental resonances localized to the LO which

can be considered perturbations of the corresponding linear resonance curves of the forced uncoupled LO; branches 2 and 3 are realized due to the strong (essential) stiffness nonlinearity of the NES and represent strongly nonlinear motions localized to the NES.

To study the stability of the computed fundamental resonances we reconsider the complex slow flow (4.4), but instead of a polar representation we introduce a Cartesian complex representation $\varphi_i(t) = y_i(t) + j z_i(t)$ to express the slow flow in terms of the real variables y_i and z_i . Further, we let $y_i(t) = y_{i0} + \varepsilon y_{i1}(t)$, $z_i(t) = z_{i0} + \varepsilon z_{i1}(t)$, $i=1,2$; *i.e.*, we introduce small time-dependent perturbations $y_{i1}(t)$, $z_{i1}(t)$ of the computed fundamental resonance solutions y_{i0} , z_{i0} , and substitute into the slow flow equations. The resulting linear variational system of equations derived when $O(\varepsilon)$ terms are considered takes the form

$$\underline{A} \begin{bmatrix} y_{11}(t) & y_{21}(t) & z_{11}(t) & z_{21}(t) \end{bmatrix}^T = \begin{bmatrix} 0 & 0 & 0 & 0 \end{bmatrix}^T \quad (4.15)$$

where the constant matrix \underline{A} depends on the computed steady-state solutions. Examination of the eigenvalues of the matrix \underline{A} reveals the linearized stability of the steady-state solutions. Theoretically speaking, all eigenvalues of \underline{A} should have negative real parts in order for a steady-state solution to be stable. Note, however, that the computed steady-state solutions are approximate since they are based on the averaging approximation discussed previously. As a result, for some steady-state branches the linearized stability results proved to be inconclusive as the real parts of the eigenvalues tended toward zero. Here we resorted to direct numerical simulation of the original equations of motion (4.1) with initial conditions determined by our previous analysis. This led to conclusive results since unstable steady-state solutions led to

strongly modulated responses and transitions to coexisting stable solutions. Our results indicate that branches 1, 2 and 4 are stable, whereas branch 3 is unstable.

4.3.1.3 Application to Vibration Isolation By Means of Nonlinear Energy Transfer

In this section we use the ideas developed in the prior Section to show that it is possible to design the system depicted in Figure 1 for vibration isolation of the directly excited LO through steady-state energy transfer to the strongly nonlinear attachment. We previously developed approximate analytical solutions for the fundamental resonances of the system of Figure 4.10, based on the simplifying assumption that the LO and NES have equal masses. Relaxing this assumption, the slow-flow modulation equations are expressed in physical coordinates as

$$\begin{aligned} \dot{\varphi}_1 - \frac{j\varphi_1}{2\omega} + \frac{1}{2}j\omega\varphi_1 + \frac{\varepsilon k_c(\varphi_1 - \varphi_2)}{2jm_1\omega} + \frac{1}{2}\varepsilon\lambda_1\varphi_1 &= \frac{\varepsilon P}{2j} \\ \dot{\varphi}_2 + \frac{1}{2}j\omega\varphi_2 + \frac{jk_c\varepsilon(\varphi_2 - \varphi_1)}{2j\omega m_2} + \frac{1}{2}\varepsilon\lambda_2\varphi_2 - \frac{3jC_s|\varphi_2|^2\varphi_2}{8\omega^3} &= 0 \end{aligned} \quad (4.16)$$

and the energy-amplitude relationship becomes (where the notation of the previous section holds)

$$E = \frac{X^2}{2} + \frac{\varepsilon k_c}{2m_1}(X - V)^2 + \frac{m_2}{4m_1}C(X - V)^4 \quad (4.17)$$

Following the earlier methodology, we numerically solve a set of nonlinear algebraic equations within a predefined frequency range to study the amplitude-frequency relationships and the corresponding FEP.

We note at this point that for practical applications where vibration isolation of the directly forced LO is sought, a smaller NES mass might be preferable. In the following we will study the fundamental resonances of the system numerically for varying parameters and investigate the reduction of the steady amplitude of the LO response through vibration energy

transfer to a lightweight NES. Although we will not perform a global optimization study by simultaneously varying all system parameters, we seek an understanding of how individual system parameters affect the steady-state responses of the LO. Our aim is to select a set of parameters that provide effective vibration reduction of the amplitude of the steady response of the LO over a significantly broad frequency range, so that the vibration isolation is robust to change in the frequency of the excitation. Thus, we will examine separately the effect of each of the important system parameters on the amplitude of steady-state vibration of the LO and compare it to the corresponding amplitude of the LO with no NES attached.

First we consider the effect of the mass ratio m_1/m_2 on the amplitude-frequency relation of the LO by fixing the system parameters $\lambda_1 = 0.05, \lambda_2 = 0.1, \varepsilon = 0.05, k_c = 1, C = 1, P = 1$. In Figure 8 we depict the approximate frequency response of the LO (as described in the previous Section) for varying mass ratios. For comparison purposes we also depict the approximate frequency response of the uncoupled forced LO (*i.e.*, without the coupling effect to the NES). We note that there is clearly a trade-off in choosing the NES mass for the purpose of vibration reduction of the steady-state response of the LO. Moreover, we see that a relatively large NES mass reduces the frequency range of vibration reduction, without necessarily improving the amount of reduction. On the other hand, as expected, a relatively small NES mass causes the frequency response to nearly collapse to the linear response of the uncoupled LO. Therefore, the selection of the mass ratio needs to be such that the amplitude reduction is feasible and optimal. From the results of Figure 4.17 we deduce that a mass ratio of $m_1/m_2 = 30$ leads to significant amplitude reduction over a broad frequency range compared to the case of the uncoupled LO; therefore, we will employ this value of mass ratio further. We note that no stability analysis is

carried out for the steady-state plots depicted in Figure 4.17; a detailed stability study of the solutions is postponed until the final optimized system is selected.

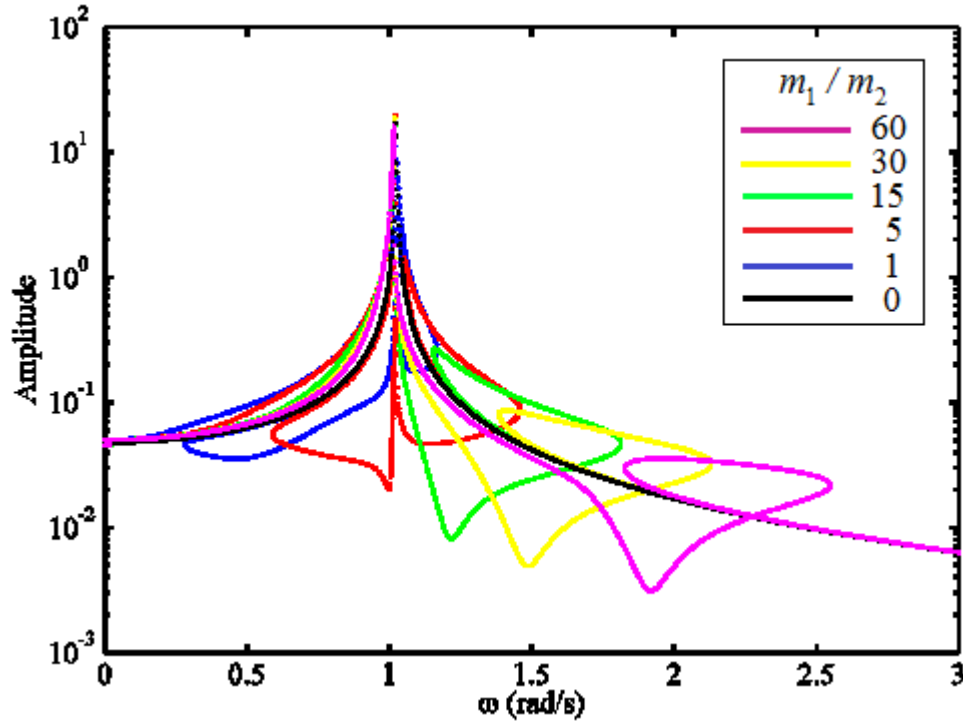


Figure 4.17 Effect of the mass ratio m_1/m_2 on the steady-state amplitude of the LO for system parameters $\lambda_1 = 0.05, \lambda_2 = 0.1, \varepsilon = 0.05, k_c = 1, C = 1, P = 1$.

Next we consider the effect of the normalized nonlinear spring coefficient C_s on the amplitude-frequency relation of the LO. In the results presented in Figure 4.18 the system parameters were fixed to $\lambda_1 = 0.05, \lambda_2 = 0.1, \varepsilon = 0.05, k_c = 1, m_1 = 30, m_2 = 1, P = 1$ and the nonlinear coefficient was varied. Depending on the value of C_s (*i.e.*, on the strength of the essential nonlinearity of the NES) some of the LO branches may vanish; these are the strongly nonlinear branches representing relatively large motions of the NES, and, as expected, in the weakly nonlinear regime (*i.e.*, for $C_s \rightarrow 0$) these motions vanish and the steady response of the system appears as a perturbation of the linear response of the LO uncoupled from the NES. For

increasing nonlinear coefficient we see that there appear frequency ranges where the steady-state branches of the LO are significantly below the corresponding response of the uncoupled LO. These branches coexist with strongly nonlinear branches of solutions corresponding to relatively large steady-state amplitudes of the NES, indicating that the reduction of the steady-state amplitude of the LO is due to irreversible vibration energy transfer from the directly excited LO to the weakly coupled NES. Moreover, a moderate increase of the nonlinear coefficient leads to a broadening of the frequency band where the reduction of the steady-state response of the LO occurs although, as discussed below, the stability of these solutions needs to be considered as well in order for the noted responses to be physically realizable. Further increase of the nonlinear coefficient, however, leads to deterioration of the vibration isolation since the nonlinear stiffness of the NES behaves as a rigid link. Then the attachment to the LO becomes nearly rigid, the nonlinear effects in the dynamics decrease, and the response becomes linearized. Taking this into account, we set the nonlinearity coefficient to $C_s = 1$, which is a good trade-off between the frequency range of effective vibration isolation and the level of vibration reduction.

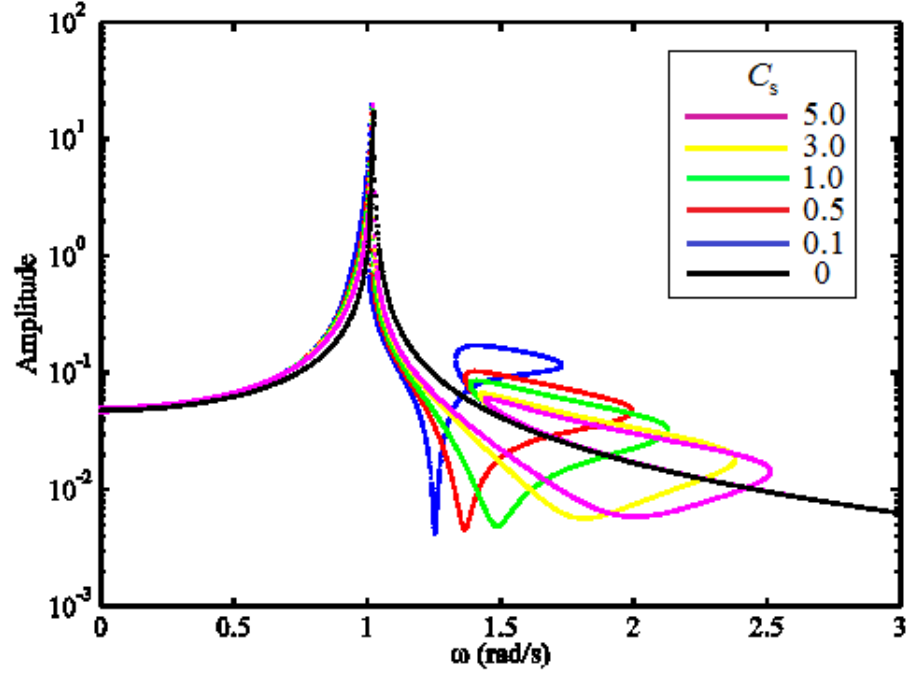


Figure 4.18 Effect of the stiffness coefficient C_s on the steady-state amplitude of the LO for system parameters $\lambda_1 = 0.05, \lambda_2 = 0.1, \varepsilon = 0.05, k_c = 1, m_1 = 30, m_2 = 1, P = 1$.

Finally, we consider the effect of the normalized NES damping parameter λ_2 on the steady-state response of the LO by fixing the system parameters $\lambda_1 = 0.05, \varepsilon = 0.05, k_c = 1, m_1 = 30, m_2 = 1, C = 1, P = 1$. In fact, a change in NES damping can result in qualitatively different dynamics; *e.g.*, stability changes of particular solutions can lead to strongly modulated responses. Therefore, although it might appear that decreasing NES damping can cause reduction of the steady-state response of the LO, as shown in Figure 4.19, for finite values of NES damping, within the vibration reduction region there appear strongly modulated responses with varying amplitudes; this is a clear indication of instability of the response of the LO. Moreover, for large values of NES damping, the attachment to the LO becomes nearly rigid, so the nonlinear effects decrease, the dynamics becomes weakly nonlinear, and the vibration isolation deteriorates. As a result, we choose the optimized NES damping coefficient to be

$\lambda_2 = 0.1$. We note again that we did not conduct a systematic study (*i.e.*, a bifurcation analysis) of the steady-state dynamics for changes of NES damping; rather, the parameter chosen should be considered a reasonable value for effective vibration suppression of the response of the LO.

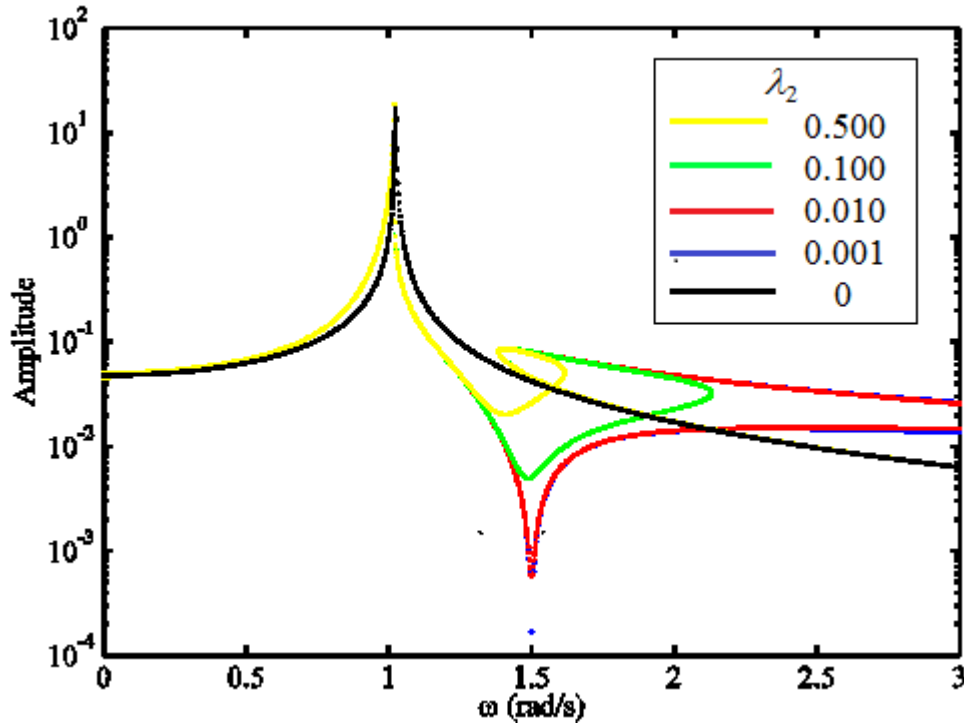


Figure 4.19 Effect of the damping coefficient λ_2 on the steady-state amplitude of the LO for system parameters $\lambda_1 = 0.05, \varepsilon = 0.05, k_c = 1, m_1 = 30, m_2 = 1, C = 1, P = 1$.

Finally, we consider the effect of the forcing amplitude P on the amplitude-frequency relation of the LO. We represent the steady-state amplitude of the LO normalized with respect to the forcing amplitude, εP in Figure 4.20, where the other system parameters were fixed to $\lambda_1 = 0.05, \lambda_2 = 0.1, C = 1, \varepsilon = 0.05, k_c = 1, m_1 = 30, m_2 = 1$ and the forcing amplitude was varied. Forcing amplitude has a very similar effect as with the nonlinear coefficient: A moderate increase of the forcing amplitude leads to a broadening of the frequency band where the reduction of the steady-state response of the LO occurs; however, further increase of the forcing amplitude results

in deterioration of the vibration isolation since the nonlinear stiffness of the NES behaves as a rigid link for high forcing levels.

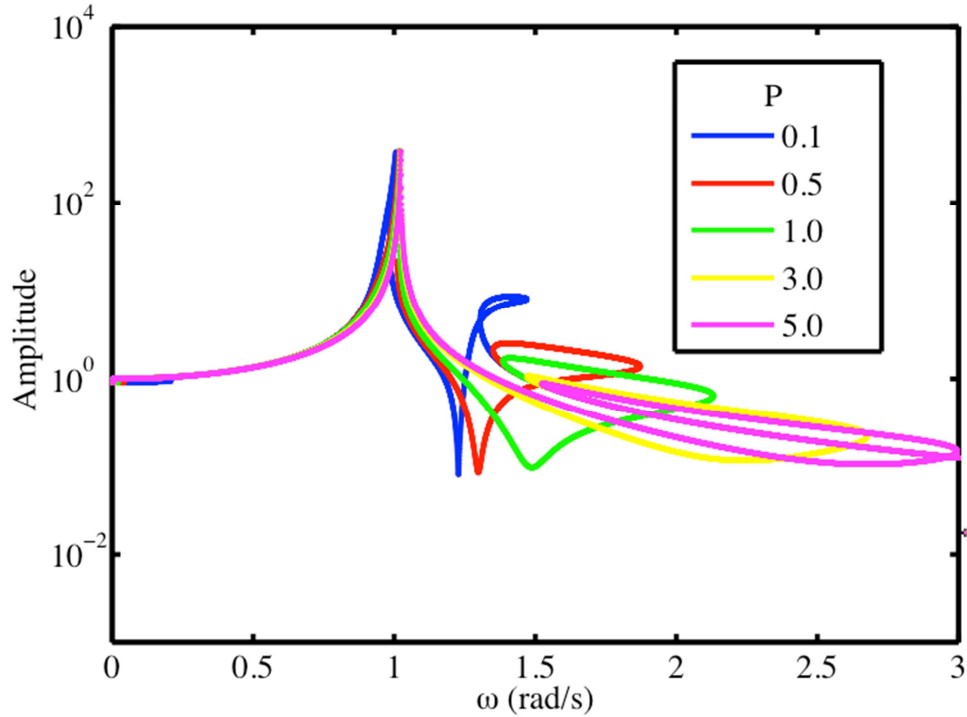


Figure 4.20 Effect of the forcing amplitude P on the steady-state amplitude of the LO for system parameters. $\lambda_1 = 0.05, \lambda_2 = 0.1, C = 1, \varepsilon = 0.05, k_c = 1, m_1 = 30, m_2 = 1$.

As a result of the studies carried out in this subsection, we selected the system parameters to be $\lambda_1 = 0.05, \lambda_2 = 0.1, \varepsilon = 0.05, k_c = 1, m_1 = 30, m_2 = 1, C = 1, P = 1$, leading to the steady-state responses for the LO and NES depicted in Figure 4.21. We emphasize yet again that these parameters are not “globally optimal” values but rather parameters which help us understand the sensitivity of the steady-state dynamics of the system to parameter changes. Indeed, a full optimization analysis, including the bifurcation of stable solutions by changing these parameters, is necessary to achieve a “globally optimal” set of parameters, but this is not performed in this work

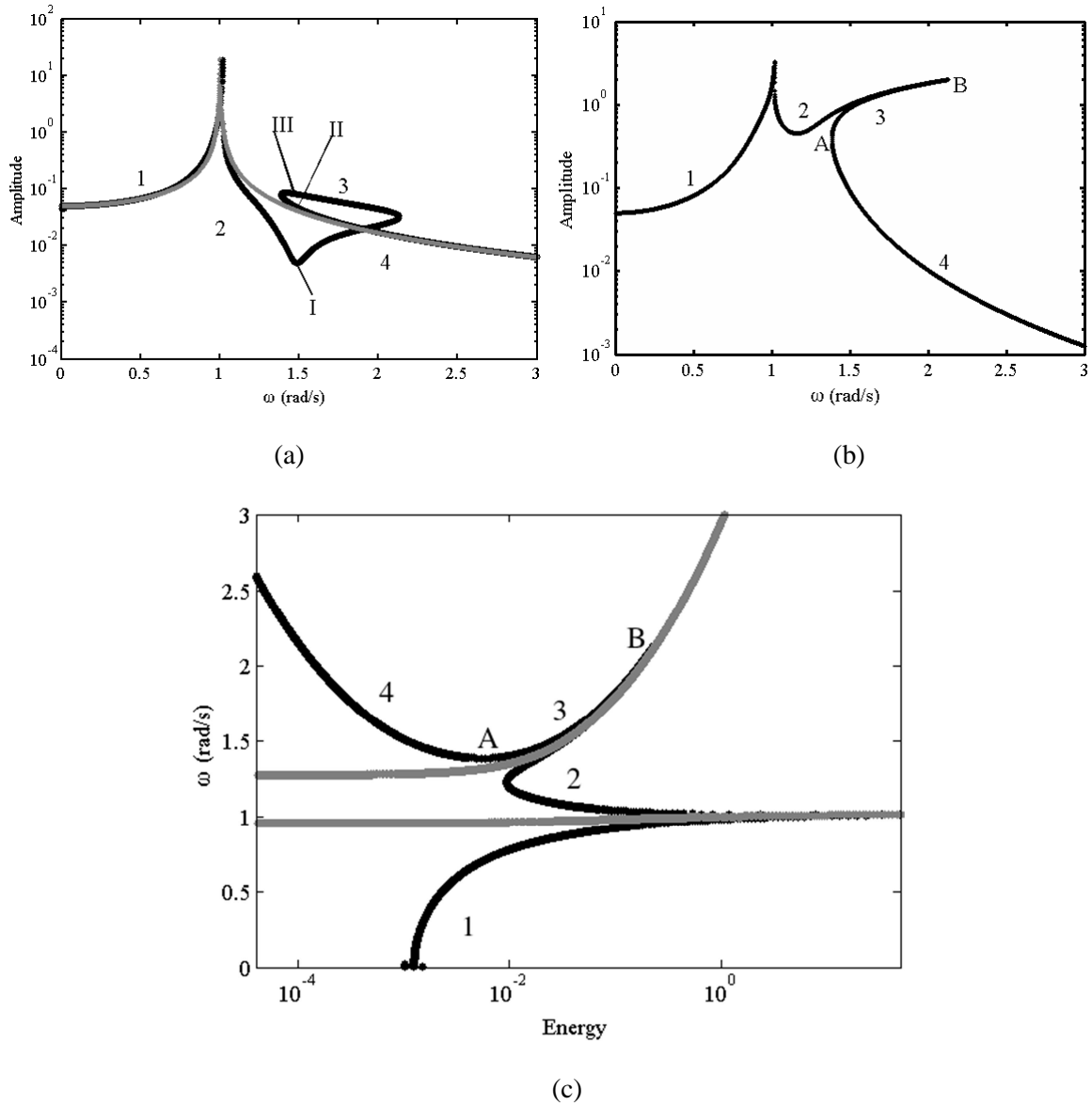
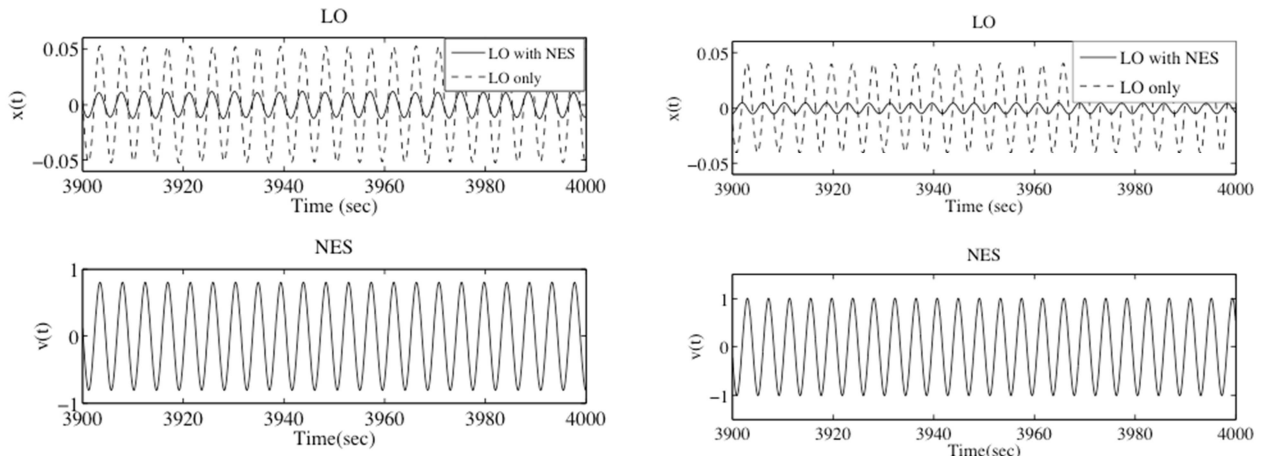
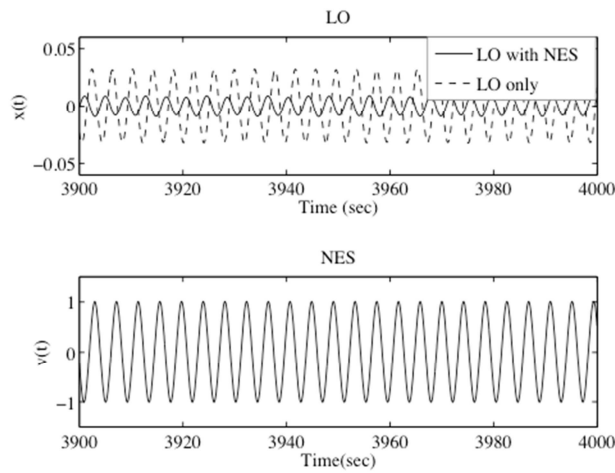


Figure 4.21. Steady state dynamics of the optimized solution: (a) Response of LO without the attached NES and of LO with the attached NES; (b) response of NES, (c) damped FEP where gray solid lines depict the NNMs of the underlying Hamiltonian system (the comparisons of the steady state responses with and without NES attached are shown to assess the effectiveness of vibration suppression).



(a)

(b)



(c)

Figure 4.22. Time simulations carried out for selected steady-state solutions of the plots of Figure 12 for the LO without attached NES, the LO with attached NES, and the NES; initial conditions are taken on the steady-state branch 2 at frequency (a) 1.4 rad/s, (b) 1.5 rad/s, (c) 1.6 rad/s.

We note that, consistent with our previous observations, branches 1, 2 and 4 are stable, whereas branch 3 is unstable. As we see in Figure 12a, we appear to have a reasonable region of vibration reduction around 1.5 rad/s, when compared with the LO without the NES. Indeed, to validate such a conclusion, we first must test the stability of these solutions. Taking ICs from the

lower branch of the curve in Figure 4.21, we see that this lower branch is completely stable until the coalescence point near 1.8 rad/s. This conclusion can be reached by looking at the time responses in steady-state of each IC corresponding to this lower branch curve. An almost maximum suppression, which corresponds to a 1-to-5 ratio, can be reached around 1.5 rad/s. We depict the time responses of both the LO and NES at frequencies 1.4, 1.5 and 1.6 rad/s with the initial conditions starting from branch 2 in Figure 4.22 to prove the stability of these responses in steady-state. In comparison to the case of the LO without the attached NES, we appear to obtain excellent vibration isolation.

Since we have two competing stable branches between approximately 1.3 and 1.8 rad/s, it might be interesting to consider the domains of attraction of these solutions. Note that the domain of attraction of the original problem is in fact 5 dimensional, consisting of two amplitudes, two phases and time; however, we will consider the projection of this domain of attraction onto a 2D plane, where we vary only the amplitude initial conditions as in (18) with x_1 corresponding to the LO, and x_2 corresponding to the NES, giving

$$\begin{aligned}
 x_{1,2}(0) &= X_{1,2} \cos(\theta_{1,2}) \\
 \dot{x}_{1,2}(0) &= \omega X_{1,2} \sin(\theta_{1,2}) \\
 \omega &= 1.5 \text{ rad/s}, \theta_{1,2} \approx \frac{\pi}{2}
 \end{aligned} \tag{4.18}$$

while fixing the frequency to $\omega=1.5$ rad/s and the phase angles to $\theta_{1,2} = \pi / 2$. In Figure 4.23, we depict the corresponding domains of attraction of the two stable steady-states denoted by I and II in Figure 4.22 (with the unstable steady-state denoted by III); these were computed by numerically integrating the original equations of motion (1) subject to the initial conditions (18) and the aforementioned optimal values of the system parameters. Initial conditions corresponding

to solutions that converge to the non-localized steady-state solution are denoted by crosses (x), whereas initial conditions generating solutions that converge to the localized solution by gray dots (•). We note that for sufficiently small initial conditions (including zero initial conditions) there appears to be an elliptical region where the solutions converge to the nonlocalized stable state II on branch 4. However, we also note a large region of attraction of the localized steady-state solution I on branch 2, indicating robustness of this solution within that domain of attraction.

To demonstrate this, we consider four simulations in Figure 4.24, with the points chosen from Figure 4.23. We observe in Figure 15a,b that a small deviation in the ICs in some regions of the domain, such as Points A and B of Figure 14, can result in undesired and desired solutions, respectively. This is due to the effect of the underlying nonlinear dynamics at large amplitudes. In Figure 4.24c, we see that ICs corresponding to point C of Figure 4.23, where the IC for the LO is quite large and the IC condition for NES is very small, we seem to obtain the desired solution, which has practical importance.

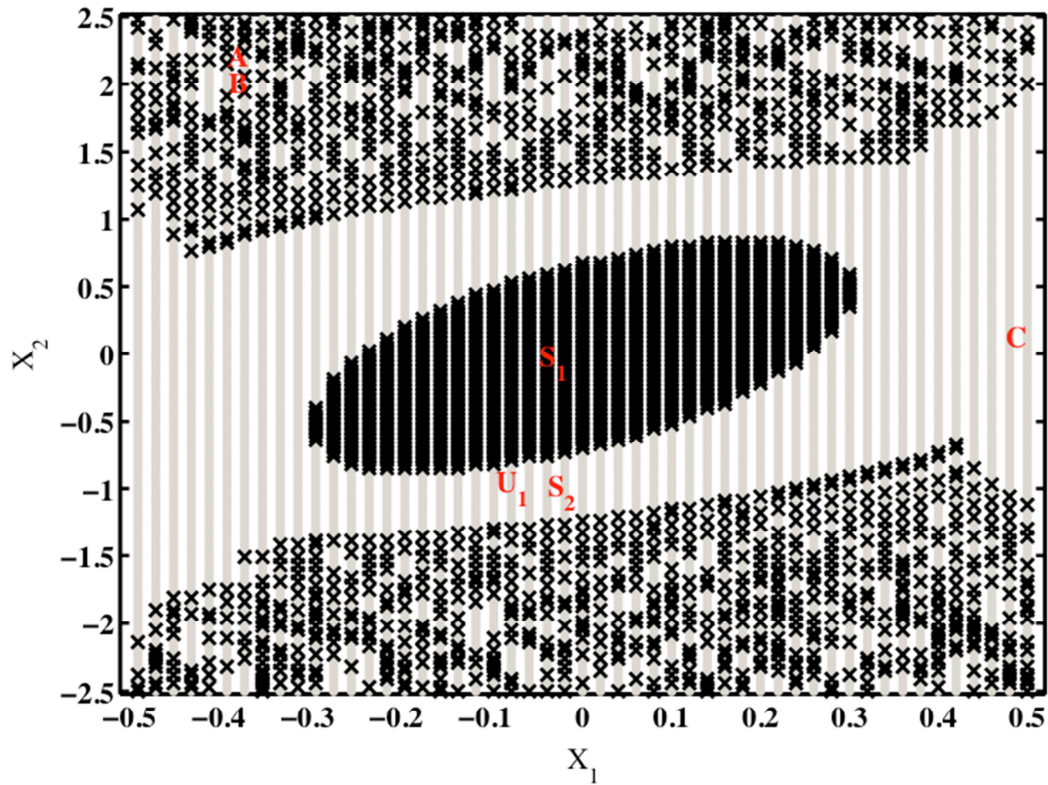
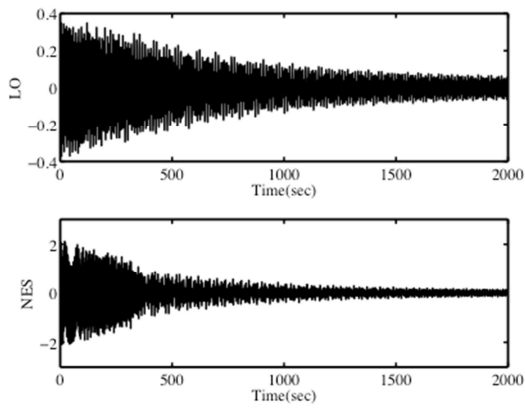
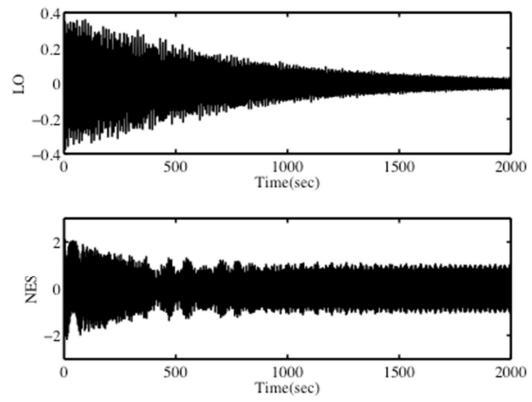


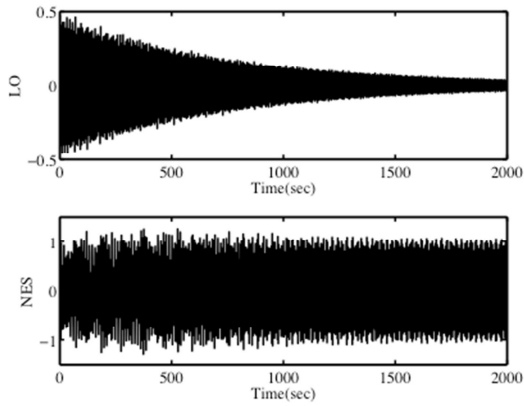
Figure 4.23 Projection of the domains of attraction of the competing stable steady state solutions I and II of Figure 12: Gray dots (*) depict the initial conditions corresponding to solutions that converge to the optimized localized steady state I, whereas black crosses (x) depict the initial conditions corresponding to solutions converge to the competing stable solution II; points S1 and S2 denote the initial conditions of the stable steady states I and II, respectively, whereas U1 the initial conditions for the unstable solution III.



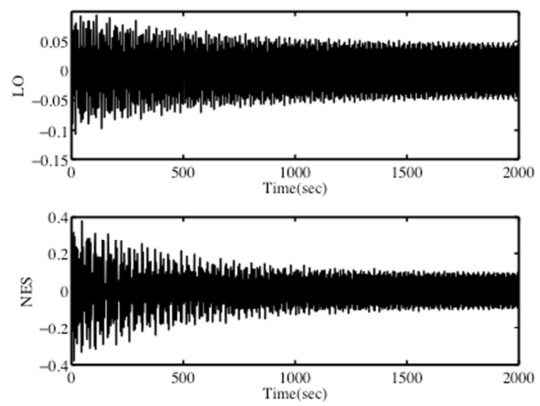
(a)



(b)



(c)



(d)

Figure 4.24 Time simulations for initial conditions depicted in Figure 14: (a) Point A corresponding to $X_1=-0.36$, $X_2=2.06$, (b) point B corresponding to $X_1=-0.36$, $X_2=2.03$, (c) Point C corresponding to $X_1=0.48$, $X_2=-0.05$, (d) zero initial conditions.

4.3.1.4 Concluding Remarks

In this section, we considered a two-DOF system, consisting of a linear oscillator weakly coupled to a nonlinear energy sink (NES) through a linear spring. The system is examined through 3 cases: Hamiltonian, forced, and forced and damped. We were interested in the amplitude-frequency dependence of the NES and the LO, and therefore depicted the NNMs of the system, calculated through approximate slow flow analysis and shown in FEPs. We observed that there are mainly 4 branches in the forced and forced and damped cases, which correspond to forced (linear) and nonlinear responses, respectively. In the last section, we examined some practical implications of this approach, basically showing that the NES in the given configuration can be utilized as a good vibration absorber within predefined frequency ranges.

4.3.2 Application to 1:3 Resonance in a Two-Degree-of-Freedom Oscillator (Kurt, Slavkin, et al. 2014)

4.3.2.1 Introduction and System Description

As shown in previous works, two-dimensional FEPs provide a synoptic global description of the frequency and energy dependencies of periodic orbits of Hamiltonian n –degree-of-freedom (DOF) dynamical systems, and can be used to interpret complex dynamical transitions of weakly damped systems possessing even strong, non-smooth nonlinearities (Lee, Nucera, et al. 2009). This is achieved by superimposing wavelet spectra of the damped responses onto the Hamiltonian FEPs, thus identifying the underlying Hamiltonian dynamics that influence the damped transitions (Vakakis 2008). In a recent study, these FEPs were extended to forced and damped systems as well, which make them a practical tool for analyzing strongly nonlinear systems (Kurt, Eriten, et al. 2014b).

In strongly nonlinear systems, interesting dynamical phenomena such as internal resonances and mode-mixing may occur. Unlike in linear systems, in nonlinear systems modes can interact with each other not only in 1:1 resonance but also in any rationally related ratios. *Internal resonance* denotes a strongly nonlinear energy transfer phenomenon, whereby two structural modes (even widely spaced in the frequency domain) become coupled by the system nonlinearity and start exchanging energy between them, giving rise to *nonlinear beat phenomena* (Manevich and Manevitch 2005; Kurt, Eriten, et al. 2014a). In this study, our main aim is to investigate a grounded nonlinear oscillator coupled with a light linear attachment which has two linearized eigenfrequencies with ratio 3:1. The main concentration will be on studying the 1:3 internal resonance branch around the first linearized frequency region for both forced and

unforced cases.

In this study we consider a two-DOF system, a grounded nonlinear oscillator coupled with a light linear attachment (whose mass is denoted by the small parameter ε , with $|\varepsilon| \ll 1$). The stiffness nonlinearity is characterized as *essential* since its characteristic is purely cubic (with coefficient k_{nl}) and lacking a linear part, hence making the nonlinearity *non-linearizable*, and a 1:3 resonance exists in the system as explained below. The grounded nonlinear oscillator is excited by a harmonic force with amplitude F and frequency ω . The configuration of the system is depicted in Figure 4.25. We are mainly interested in the amplitude-frequency dependence of the steady-state responses of the nonlinear oscillator and the light attachment. The main concentration will be placed on studying responses that are affected by 1:3 resonance in the neighborhood of the first linearized frequency region both for forced and unforced cases.

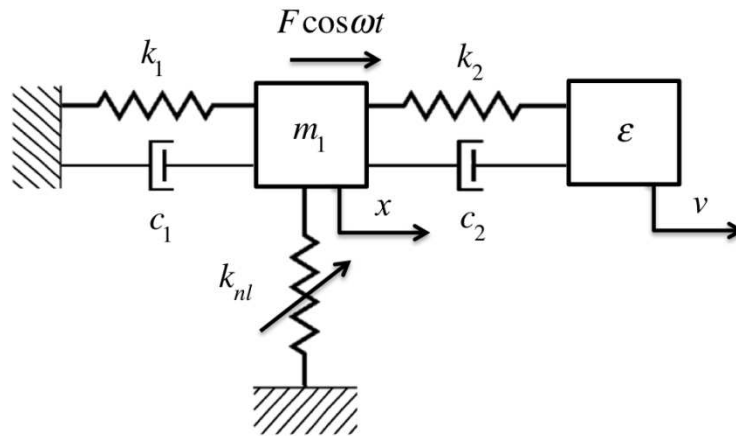


Figure 4.25. Grounded nonlinear oscillator and light linear attachment under harmonic forcing.

We will study the steady-state dynamics of the system depicted in Figure 1 both analytically and numerically. This system has practical interest due to its specially tuned system

parameters, which give the system two basic eigenfrequencies in the ratio 3:1. We start with the assumption that both steady state responses $x(t)$ and $v(t)$ possess two harmonics at frequencies ω and 3ω respectively. We apply the complexification-averaging (CX-A) method and slow/fast partition of the steady-state dynamics to analytically construct forced perturbations of the FEP of the underlying Hamiltonian system (which corresponds to no damping nor forcing). We note that this analytical approach is applicable even for such a strongly nonlinear case, when traditional asymptotic methods for nonlinear dynamics, based on the assumption of weak nonlinearity and linear generating solutions, are not valid (since the current problem is non-linearizable). Then, we will compare the analytical and numerical results for the steady-state dynamics and examine by direct numerical simulation of the equations of motion interesting dynamical phenomena of practical interest.

4.3.2.2 Study of the Frequency-Energy Plots (FEPs) of the system

We start by expressing the equations of motion of the undamped system of Figure 4.25 as,

$$\begin{aligned} m_1 \ddot{x} + c_1 \dot{x} + k_1 x + k_2(x-v) + k_n x^3 &= F \cos \omega t \\ \varepsilon \ddot{v} + c_2(\dot{v} - \dot{x}) + k_2(v-x) &= 0 \end{aligned} \tag{4.19}$$

where the parameters are taken as $k_1 = 1.05$, $k_2 = 0.378$, $k_n = 1$, $m_1 = 1$, $\varepsilon = 0.044$, $c_1 = c_2 = 0$. These parameters are chosen to make the linear frequencies of the system equal to 1 and 3. Using these parameters the linearized modal frequencies are given by $\omega_1 \approx 1$ rad/s and $\omega_2 \approx 3$ rad/s. In order to study the steady-state dynamics of system (4.19), we apply CX-A. This method was first introduced by (Manevitch 1999) and then applied extensively in further studies of nonlinear

targeted energy transfer (e.g.,(Vakakis 2008; Kurt, Eriten, et al. 2014b)). To this end, we complexify the normalized equations of motion (4.19) with new complex variables of the form

$$\begin{aligned}\psi_1(t) = \dot{x}_1(t) + j\omega x_1(t) &\equiv \underbrace{\varphi_1(t)}_{\text{'Slow' part}} \underbrace{e^{j\omega t}}_{\text{'Fast' part}}, & \psi_3(t) = \dot{x}_2(t) + 3j\omega x_2(t) &\equiv \underbrace{\varphi_3(t)}_{\text{'Slow' part}} \underbrace{e^{3j\omega t}}_{\text{'Fast' part}} \\ \psi_2(t) = \dot{v}_1(t) + j\omega v_1(t) &\equiv \underbrace{\varphi_2(t)}_{\text{'Slow' part}} \underbrace{e^{j\omega t}}_{\text{'Fast' part}}, & \psi_4(t) = \dot{v}_2(t) + 3j\omega v_2(t) &\equiv \underbrace{\varphi_4(t)}_{\text{'Slow' part}} \underbrace{e^{3j\omega t}}_{\text{'Fast' part}}\end{aligned}\quad (4.20)$$

In (4.20) a slow/fast decomposition was additionally imposed, whereby the new complex variables $\psi_i(t)$ were expressed in terms of slowly varying envelopes $\varphi_i(t)$ that modulate fast harmonic oscillations at frequencies ω and 3ω . Moreover, (4.20) indicates that the desired solutions possess dominant harmonic components at the frequency and at three times the frequency of the harmonic excitation, so both 1:3 *resonances* of the system (4.19) will be examined. Then, we express the original variable x in terms of the new complex variables as,

$$\begin{aligned}x &= \frac{\varphi_1 e^{j\omega t} - \varphi_1^* e^{-j\omega t}}{2j\omega} + \frac{\varphi_3 e^{3j\omega t} - \varphi_3^* e^{-3j\omega t}}{6j\omega}, & x &= \frac{\varphi_1 e^{j\omega t} + \varphi_1^* e^{-j\omega t}}{2} + \frac{\varphi_3 e^{3j\omega t} + \varphi_3^* e^{-3j\omega t}}{2}, \\ \ddot{x} &= \dot{\varphi}_1 e^{j\omega t} + j\omega \frac{\varphi_1 e^{j\omega t} - \varphi_1^* e^{-j\omega t}}{2} + \dot{\varphi}_3 e^{3j\omega t} + 3j\omega \frac{\varphi_3 e^{3j\omega t} - \varphi_3^* e^{-3j\omega t}}{2}\end{aligned}\quad (4.21)$$

We note that similar expressions to (4.21) hold for the displacement v , as well. Substituting expressions (4.20) and (4.21) into the equations of motion (4.19) and averaging over the fast frequencies ω and 3ω separately, we derive the following *approximate set of modulation equations* governing 1:3 resonance in system (4.19):

$$\begin{aligned}
\dot{\phi}_1 - \frac{1}{2}j\omega\phi_1 - \frac{j(k_1+k_2)}{2\omega}\phi_1 + \frac{jk_2}{2\omega}\phi_2 - \frac{j|\phi_3|^2\phi_1}{12\omega^3} + \frac{j\phi_1^*\phi_3}{8\omega^3} - \frac{3j|\phi_1|^2\phi_1}{8\omega^3} &= \frac{P}{2} \\
\varepsilon\dot{\phi}_2 + \frac{1}{2}\varepsilon j\omega\phi_2 - \frac{jk_2}{2\omega}\phi_2 + \frac{jk_2}{2\omega}\phi_1 &= 0 \\
\dot{\phi}_3 + \frac{3}{2}j\omega\phi_3 - \frac{j(k_1+k_2)}{6\omega}\phi_3 + \frac{jk_2}{6\omega}\phi_4 + \frac{j\phi_1^3}{8\omega^3} - \frac{j|\phi_3|^2\phi_3}{72\omega^3} - \frac{j|\phi_1|^2\phi_3}{4\omega^3} + \frac{j\phi_1^3}{8\omega^3} &= 0 \\
\varepsilon\dot{\phi}_4 + \frac{3}{2}\varepsilon j\omega\phi_4 - \frac{jk_2}{6\omega}\phi_4 + \frac{jk_2}{6\omega}\phi_3 &= 0
\end{aligned} \tag{4.22}$$

This is also referred to as the *slow flow*. Note that the first and second equations in (4.22) refer to the slowly varying complex equations governing the important (slow) dynamics of the 1:3 resonance of system (4.19) after the unimportant (fast) dynamics at frequency ω has been averaged out. Similarly, the third and fourth equations in (4.22) refer to the slowly varying complex equations after the fast dynamics at frequency 3ω has been averaged out. We note that the approximation in (4.22) takes both ω and 3ω harmonic components into account, since, as it will be shown below, both harmonics are needed to accurately analyze the steady state dynamics in the energy and frequency regions of interest.

Since the slow flow (4.22) is complex, we need to transform the analysis back to the real domain. To this end, we note that if we express the complex variables in (4.22) in polar form, $\phi_i = \phi_i e^{j\theta_i}$, where ϕ_i and θ_i are real amplitudes and phases, and setting separately equal to zero the real and imaginary parts, expresses the slow flow system in terms of real variables. The stationary points of this system yield the periodic steady-state solutions for 1:3 resonance. Hence, we set $\dot{\phi}_k = 0$, $\dot{\theta}_k = 0$ to derive the following system of real nonlinear algebraic equations:

$$\begin{aligned}
& -12F\omega^3 \cos 2\theta_1 + 12k_1\omega^2\phi_1 \sin 3\theta_1 + 12k_2\omega^2\phi_1 \sin 3\theta_1 - \\
& 12\omega^4\phi_1 \sin 3\theta_1 + 9\phi_1^3 \sin 3\theta_1 + 2\phi_1\phi_3^2 \sin 3\theta_1 - \\
& 12k_2\omega^2\phi_2 \sin(2\theta_1 + \theta_2) - 3\phi_1^2\phi_3 \sin \theta_3 = 0 \\
& -9\phi_1^3 \cos 3\theta_1 - 2\phi_1(6\omega^2(k_1 + k_2 - \omega^2) + \phi_3^2) \cos 3\theta_1 + 3\phi_1^2\phi_3 \cos 3\theta_1 \\
& + 12\omega^2(k_2\phi_2 \cos(2\theta_1 + \theta_2) - F\omega \sin 2\theta_1) = 0 \\
& k_2\phi_1 \sin \theta_1 - (k_2 - \varepsilon\omega^2)\phi_2 \sin \theta_2 = 0 \\
& k_2\phi_1 \cos \theta_1 - (k_2 - \varepsilon\omega^2)\phi_2 \cos \theta_2 = 0 \\
& 9\phi_1^3 \cos 3\theta_1 - \phi_3(18\phi_1^2 + \phi_3^2) \cos 3\theta_1 - \\
& 12\omega^2((k_1 + k_2 - 9\omega^2) \cos \theta_3 - k_2\phi_4 \cos \theta_4) = 0 \\
& 9\phi_1^3 \sin 3\theta_1 - \phi_3(18\phi_1^2 + \phi_3^2) \sin 3\theta_1 - \\
& 12\omega^2((k_1 + k_2 - 9\omega^2) \sin \theta_3 - k_2\phi_4 \sin \theta_4) = 0 \\
& k_2\phi_3 \sin \theta_3 - (k_2 - 9\varepsilon\omega^2)\phi_4 \sin \theta_4 = 0 \\
& k_2\phi_3 \cos \theta_3 - (k_2 - 9\varepsilon\omega^2)\phi_4 \cos \theta_4 = 0
\end{aligned} \tag{4.23}$$

Once the solutions of (4.23) are derived, the steady state responses in terms of physical coordinates are expressed as:

$$\begin{aligned}
x &= X_1 \sin(\omega t + \theta_1) + X_2 \sin(3\omega t + \theta_3) = \frac{\phi_1}{\omega} \sin(\omega t + \theta_1) + \frac{\phi_3}{3\omega} \sin(3\omega t + \theta_3) \\
v &= V_1 \sin(\omega t + \theta_2) + V_2 \sin(3\omega t + \theta_4) = \frac{\phi_2}{\omega} \sin(\omega t + \theta_2) + \frac{\phi_4}{3\omega} \sin(3\omega t + \theta_4)
\end{aligned} \tag{4.24}$$

Returning to system (4.23), since there is no damping in the system the second, fourth, fifth and eighth equations can be solved trivially by setting $\theta_1 = \theta_2 = \theta_3 = \theta_4 = \pi/2$, which results in the

simplified system (4.25). This set of equations is valid for both the Hamiltonian and forced systems:

$$\begin{aligned}
12\omega^2(F\omega - k_1\phi_1 - k_2\phi_1 + \omega^2\phi_1 + k_2\phi_2) - 9\phi_1^3 - 2\phi_1\phi_3^2 - 3\phi_1^2\phi_3 &= 0 \\
k_2\phi_1 - (k_2 - \varepsilon\omega^2)\phi_2 &= 0 \\
-9\phi_1^3 + \phi_3(18\phi_1^2 + \phi_3^2) - 12\omega^2((k_1 + k_2 - 9\omega^2) - k_2\phi_4) &= 0 \\
k_2\phi_3 - (k_2 - 9\varepsilon\omega^2)\phi_4 &= 0
\end{aligned} \tag{4.25}$$

In the next section we consider the Hamiltonian system corresponding to $F = 0$. Then system (4.25) provides the nonlinear normal modes (NNMs) of the system in the frequency-energy domain, which can then be used as basis for examining the forced and damped dynamics of system (4.19).

4.3.2.3 Time-Periodic Solutions of the Hamiltonian System

Setting $F = 0$ in (4.25) these equations take the form:

$$\begin{aligned}
12\omega^2(-k_1\phi_1 - k_2\phi_1 + \omega^2\phi_1 + k_2\phi_2) - 9\phi_1^3 - 2\phi_1\phi_3^2 - 3\phi_1^2\phi_3 &= 0 \\
k_2\phi_1 - (k_2 - \varepsilon\omega^2)\phi_2 &= 0 \\
-9\phi_1^3 + \phi_3(18\phi_1^2 + \phi_3^2) - 12\omega^2((k_1 + k_2 - 9\omega^2) - k_2\phi_4) &= 0 \\
k_2\phi_3 - (k_2 - 9\varepsilon\omega^2)\phi_4 &= 0
\end{aligned} \tag{4.26}$$

We solve the system of equations (4.26) and analytically relate the ω and 3ω steady- state amplitudes of both displacements as,

$$\frac{\phi_2}{\phi_1} = \frac{V_1}{X_1} = \frac{k_2}{k_2 - \varepsilon\omega^2}, \quad \frac{\phi_4}{\phi_2} = \frac{V_2}{X_2} = \frac{k_2}{k_2 - 9\varepsilon\omega^2}$$

$$\frac{\phi_2}{\phi_1} = \frac{V_1}{X_1} = \frac{k_2}{k_2 - \varepsilon\omega^2}, \quad \frac{\phi_4}{\phi_2} = \frac{V_2}{X_2} = \frac{k_2}{k_2 - 9\varepsilon\omega^2}, \quad \frac{\phi_2}{\phi_1} = \frac{V_1}{X_1} = \frac{k_2}{k_2 - \varepsilon\omega^2}, \quad \frac{\phi_4}{\phi_2} = \frac{V_2}{X_2} = \frac{k_2}{k_2 - 9\varepsilon\omega^2}$$
(4.27)

These steady-state periodic solutions of the Hamiltonian system are also referred to as nonlinear normal modes (NNMs) (Rosenberg 1966). Then, we find the conserved energy E of the Hamiltonian system, by calculating the maximum potential energy stored in the stiffness elements:

$$E = k_1 \frac{(X_1 + X_2)^2}{2} + k_2 \frac{((X_1 + X_2) - (V_1 + V_2))^2}{2} + \frac{(X_1 + X_2)^4}{4}$$
(4.28)

Before we use the analytical formulas given above to investigate the steady-state dynamics of system (4.19), we first determine the frequency range where the phenomena of practical interest occur. In Figure 2 we depict the Hamiltonian frequency – energy plot (FEP) of system (4.19), calculated numerically utilizing a shooting method to compute NNMs as introduced by (Peeters et al. 2009). Specifically, at a specific energy level we formulate the problem of computing the periodic solutions of (4.19) (with no damping or forcing) as a nonlinear boundary value problem which we solve numerically with the period of the oscillation playing the role of nonlinear eigenvalue. Then, by varying the energy level we produce the branches of periodic solutions presented in Figures 4.26 and 4.27.

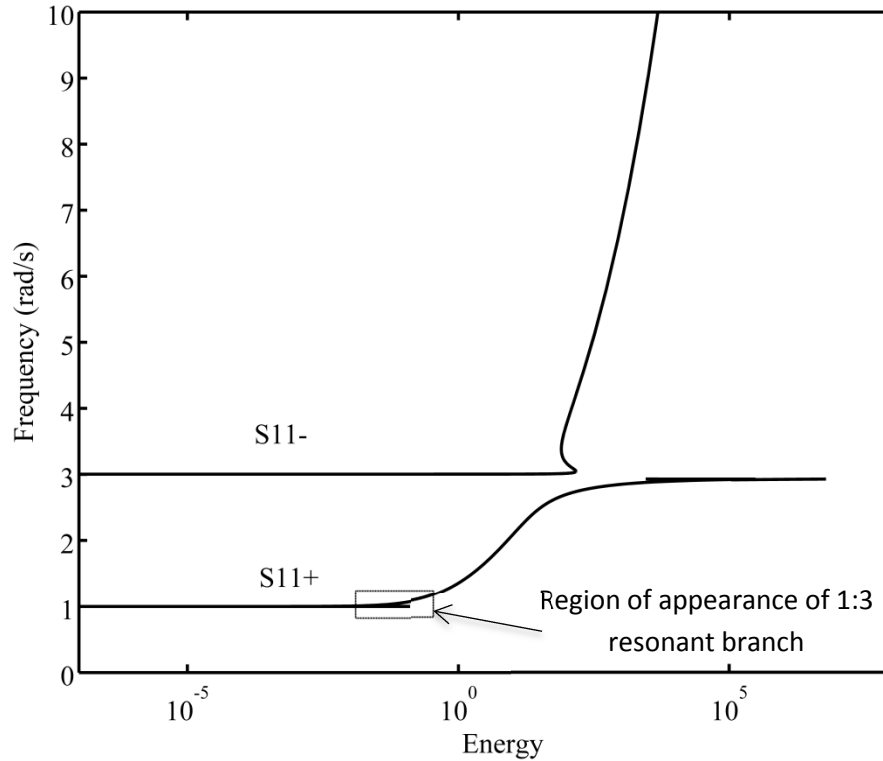


Figure 4.26. Frequency-energy plot (FEP) of the unforced and undamped (Hamiltonian) system; the box indicates the branch produced by 1:3 resonance which is depicted in detail in Figure 4.27.

Here, we depict the topological structure in the frequency – energy plane of the periodic orbits of the underlying Hamiltonian system derived by eliminating the damping and forcing terms from (4.19). The lower and upper branches in the FEP correspond to the in-phase ($S11+$) and out-of-phase ($S11-$) backbone branches for 1:1 resonance, respectively; that is, each point on these branches represents free periodic oscillations (or a nonlinear normal mode – NNM (Vakakis 2008)) where the two masses of the system oscillate with identical frequencies, either in-phase or out-of-phase. The notation $S_{mn} \pm$ denotes a time-periodic motion of system (4.19) with n being the number of half-waves in x , and m the number of half-waves in v in a half-period of the response, and (\pm) denotes the in-phase or out-of-phase character of the oscillations. However, due to the presence of 1:3 resonance in this system, two additional 1:3 internal

resonance branches appear in the neighborhood of the lowest linearized natural frequency of system (14.19) at 1 rad/s, as highlighted in Figure 4.26. This is the region of practical interest for our study, since this internal resonance branch governs the nonlinear targeted energy transfer due to the 1:3 internal resonance and covers a relatively broad energy regime.

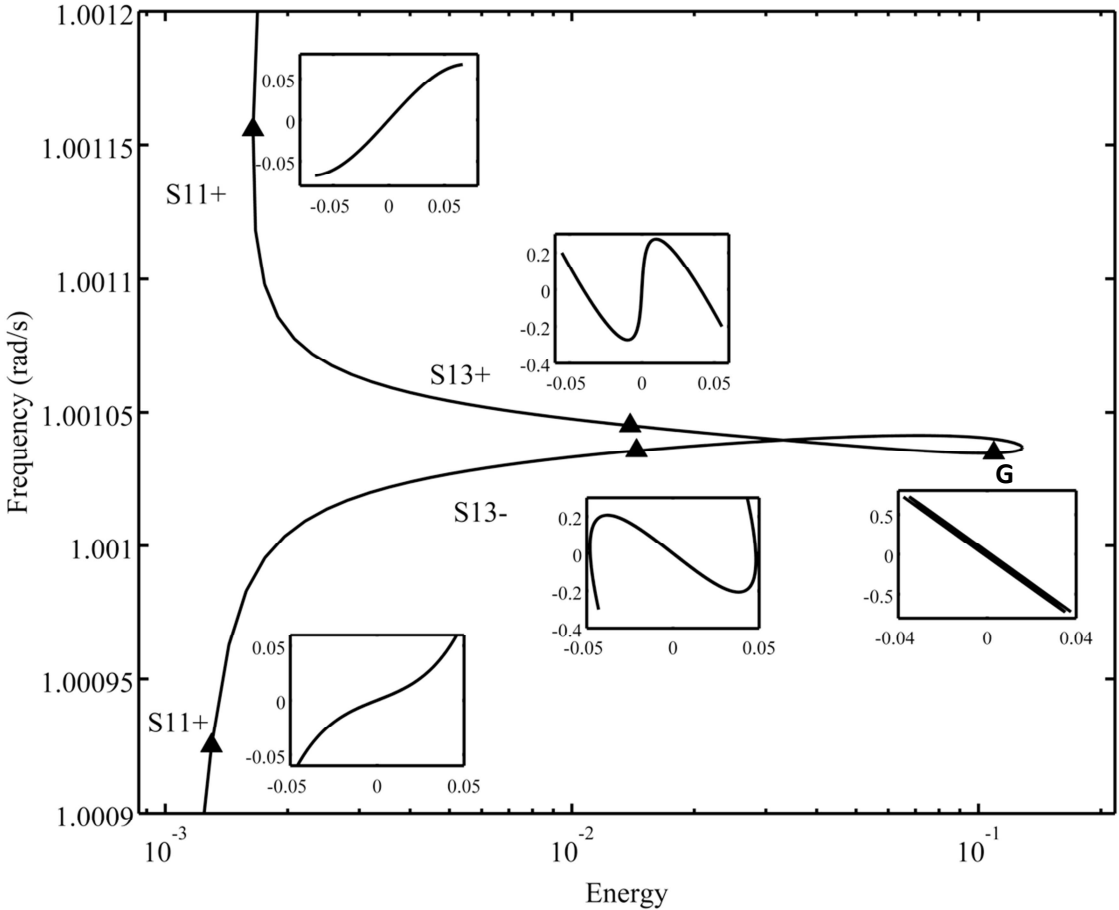


Figure 4.27. $S_{13\pm}$ branches due to 1:3 resonance; — FEP of the Hamiltonian system, ▲ points for which the configuration plots are depicted.

In Figure 4.27, we depict the general view of the two branches produced by 1:3 resonance, namely, $S_{13} \pm$. Each point on these branches corresponds to time-periodic motions (or NNMs) where both masses undergo oscillations with two frequency components 1 rad/s and 3 rad/s. Whereas, such ‘resonance tongues’ appear also in coupled oscillators with no internal resonances (Vakakis 2008) the energy ranges where they are realized are small. On the contrary, the 1:3 resonance imposed in the present system extends the energy range where these branches are realized, a feature which is important for the practical implementation of this dynamics. In Figure 4.27 we depict some representative plots in the configuration plane of the system, computed numerically. The horizontal axis of each configuration plot corresponds to the response of the grounded nonlinear oscillator and the vertical axis to the response of the light linear attachment.

Considering the two branches $S_{13} \pm$ of 1:3 resonant time-periodic solutions depicted in Figure 4.27, we note that with increasing energy the third-harmonic components in the oscillations become stronger until point G where both branches coalesce with branch $S_{33} -$. We note that branches $S_{nn} -$ are, in essence, identical to the branch $S_{11} -$, since they are identified over the domain of their common minimal period (the $S_{nn} -$ branches are branches $S_{11} -$ ‘repeated n times’). This can be clearly deduced by observing the depictions of selected NNMs in Figure 4.27, where close to point G the mode shape becomes close to the anti-phase NNM $S_{11} -$. With increasing energy the in-phase 1:3 resonant branch $S_{13} +$ makes a smooth transition to the in-phase branch $S_{11} +$, whereas for decreasing frequency the out-of-phase 1:3 resonant branch $S_{13} -$ makes a similar smooth transition to the same branch. Again, this is clearly deduced by considering the plots of the selected NNMs in Figure 4.27. Finally, we note that due to the tuned linear frequencies of system (4.19) in the ratio 1:3, this internal resonance tongue

spans a relatively large energy range, however the corresponding frequency range is confined in a narrow range.

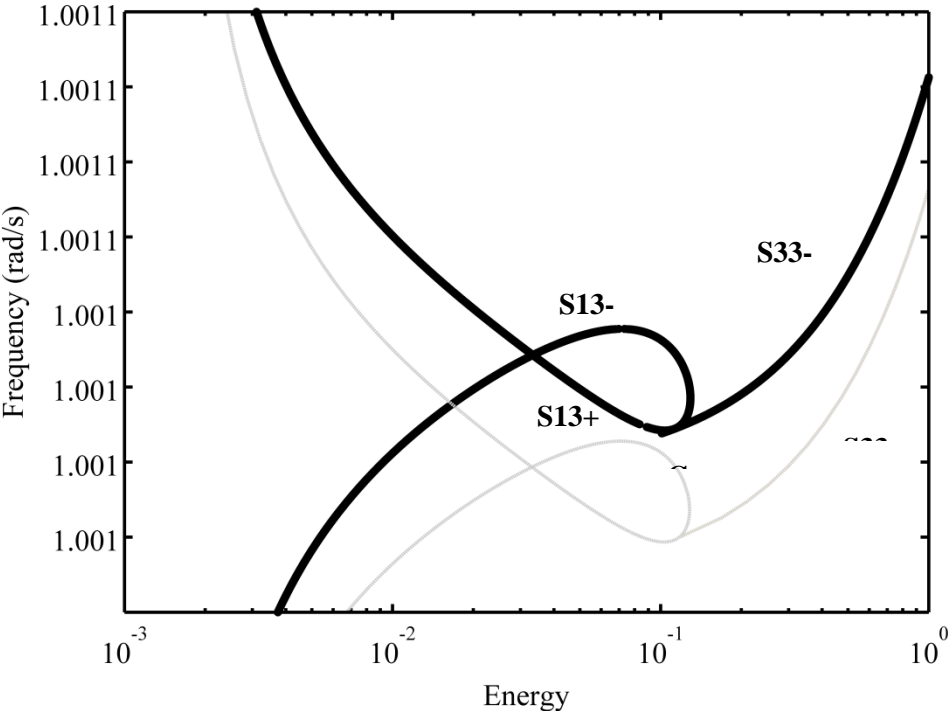


Figure 4.28. Comparisons of $S13_{\pm}$ and $S33-$ branches for the underlying Hamiltonian system: **————** Analytical results obtained by solving equations (8), **————** results from direct numerical integrations of system (1) with no damping or forcing.

At this point, having determined the frequency range of interest for 1:3 resonance, we wish to test the predictive capacity of the analytical model (4.26) to reconstruct the numerical solutions of Figure 3. Solving numerically the system of equations (4.26) in the neighborhood of the first linearized natural frequency at 1 rad/s and at the energy range of interest, we compare the resulting branches with the numerically computed $S13_{\pm}$ branches depicted in Figure 3. We note that the numerical treatment of system (4.26) is quite challenging in the very narrow frequency range where the 1:3 resonant branches are realized; therefore, the computation requires great

numerical precision and significant effort in order to reconstruct the full topology of the two branches $S_{13 \pm}$.

In Figure 4.28, we depict the $S_{13 \pm}$ branches computed by solving the system of equations (4.26) for the Hamiltonian case over a very small frequency range around the first linearized frequency and compare it with the numerically computed Hamiltonian $S_{13 \pm}$ branches (previously depicted in Figure 4.27). We note that the numerically and analytically computed $S_{13 \pm}$ branches agree quite well and any mismatch, extremely small both in the frequency and energy scales, is due to the difference in numerical precision and number of harmonics assumed in each method. Also, although the $S_{33 -}$ branch in Figure 4.28 extends to lower energy levels as well, we present just the portions of this branch that are of interest to us, which start from the triple coalescence point G of Figure 4.27.

4.3.2.4 Steady-State Dynamics of the Forced and Undamped System

We now reconsider the system of equations (4.25) with zero damping but nonzero forcing in order to investigate the effect of the forcing parameters (magnitude and frequency) on the interesting nonlinear dynamical phenomena that result due to 1:3 resonance. To this end, we wish to study the perturbations of the Hamiltonian branches $S_{13 \pm}$ (studied in subsection 4.3.2.3) when harmonic excitation is applied to the undamped system. To start with, we take the forcing amplitude as $F = 5N$ and again focus on the steady state response of the system in the neighborhood of the first linear frequency, 1 rad/s, since in that frequency range the most interesting dynamics induced by 1:3 resonance were detected in the Hamiltonian system.

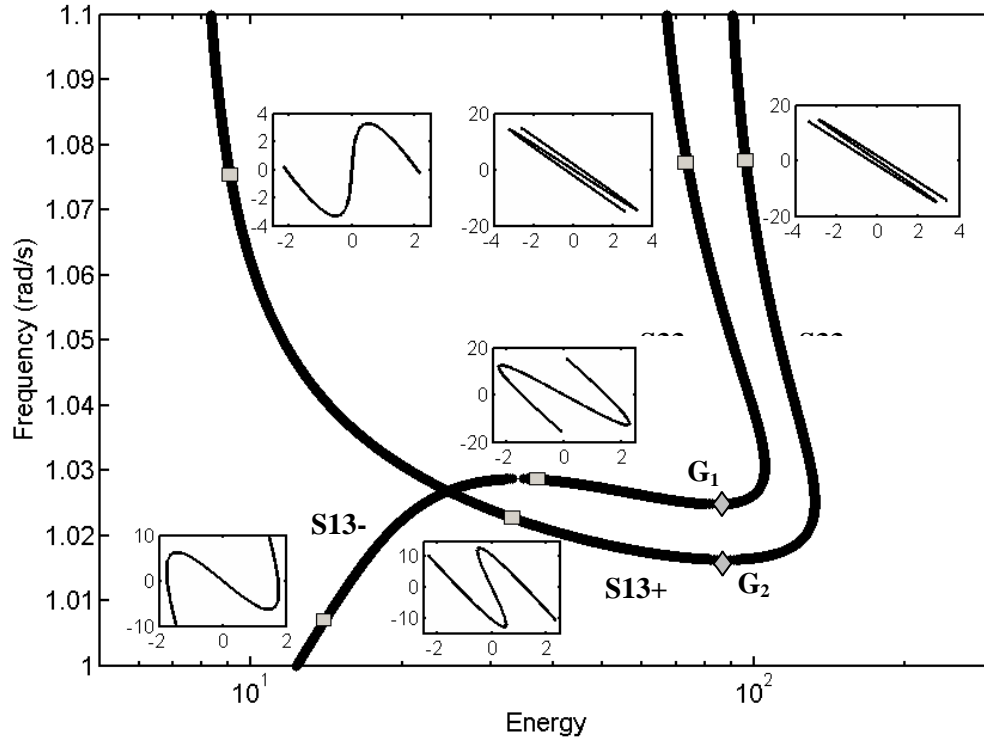


Figure 4.29. Perturbations of the Hamiltonian branches $S13 \pm$ and $S33 -$ for applied harmonic forcing of constant magnitude $F = 5 N$ and no damping in system (1): — Branches of time-periodic steady state solutions; ■ selected points corresponding to the shown plots of the responses in the configuration plane; ◆ coalescence points between branches $S13 \pm$ and $S33 -$.

In Figure 4.29, we depict the computed perturbations of the Hamiltonian branches $S13 \pm$ at the frequency range close to the first linearized natural frequency. These computations were performed by solving the slow-flow equations (4.25) for varying frequency. In the same plot we also depict the configuration-plane plots at selected points on these branches (again in each plot the horizontal axis corresponds to the response of the grounded nonlinear oscillator and the vertical axis to that of the light linear attachment). The computed branches show very interesting properties, which are somewhat similar to their Hamiltonian counterparts shown in Figures 4.27 and 28. The first thing to notice in Figure 4.29 is the extended frequency range where for effects of 1:3 resonance occur in the forced but undamped system. In other words, the transitions from

$S_{11} +$ to $S_{13} -$ and, likewise, from $S_{13} -$ to $S_{11} +$ occur over a broader frequency scale, indicating the 1:3 resonance has stronger significance in the forced dynamics. Moreover, the effect of the applied harmonic excitation is to ‘split’ the coalescence point G of the Hamiltonian plots of Figures 4.27 and 28 ‘splits’ into two distinct coalescence points. Indeed, as shown in Figure 4.29 with increasing frequency the out-of-phase resonance branch $S_{13} -$ coalesces with branch $S_{33} -$ at point G_1 , whereas the in-phase resonance branch $S_{13} +$ coalesces with branch $S_{33} -$ at point G_2 . The reason behind this ‘splitting’ is that, due to the forcing of the system, there are now two branches $S_{33} -$, which are forced in-phase and out-of-phase perturbations of the Hamiltonian branches $S_{33} -$ (in fact, it is well known that in forced nonlinear systems backbone curves representing NNMs – or free nonlinear oscillations – ‘split’ into in-phase or out-of-phase forced analogs); since we did not consider damping in this computation, these perturbed branches extend to arbitrary large frequencies. Similar observations were reported in the study by Kurt et al. (2014b), where nonlinear localization and targeted energy transfer were implemented in vibration isolation designs.

Having studied the forced perturbations of branches $S_{13} \pm$ in the neighborhood of the first linearized natural frequency, we now wish to examine the global topological structure of the FEP of the forced and undamped system when both ω and 3ω harmonics are taken into account. In Figure 6, we depict the FEP of the forced system with both ω and 3ω harmonic components shown. This plot was computed by numerically solving the system of equations (4.25) for $F = 5$ N, and compared to the numerical Hamiltonian FEP studied in subsection 4.2.2.3. Referring to the plot of Figure 4.30, we observe that branch 1 is the forced perturbation of the in-phase NNM, below the first linearized natural frequency 1 rad/s. We also note that, for low

frequencies, branch 2 is the forced perturbation of the branch of in-phase free periodic motions (in-phase NNMs), whereas at higher frequencies it represents a perturbation of the strongly nonlinear, high frequency and out-of-phase NNM, which is strongly localized to the nonlinear oscillator.

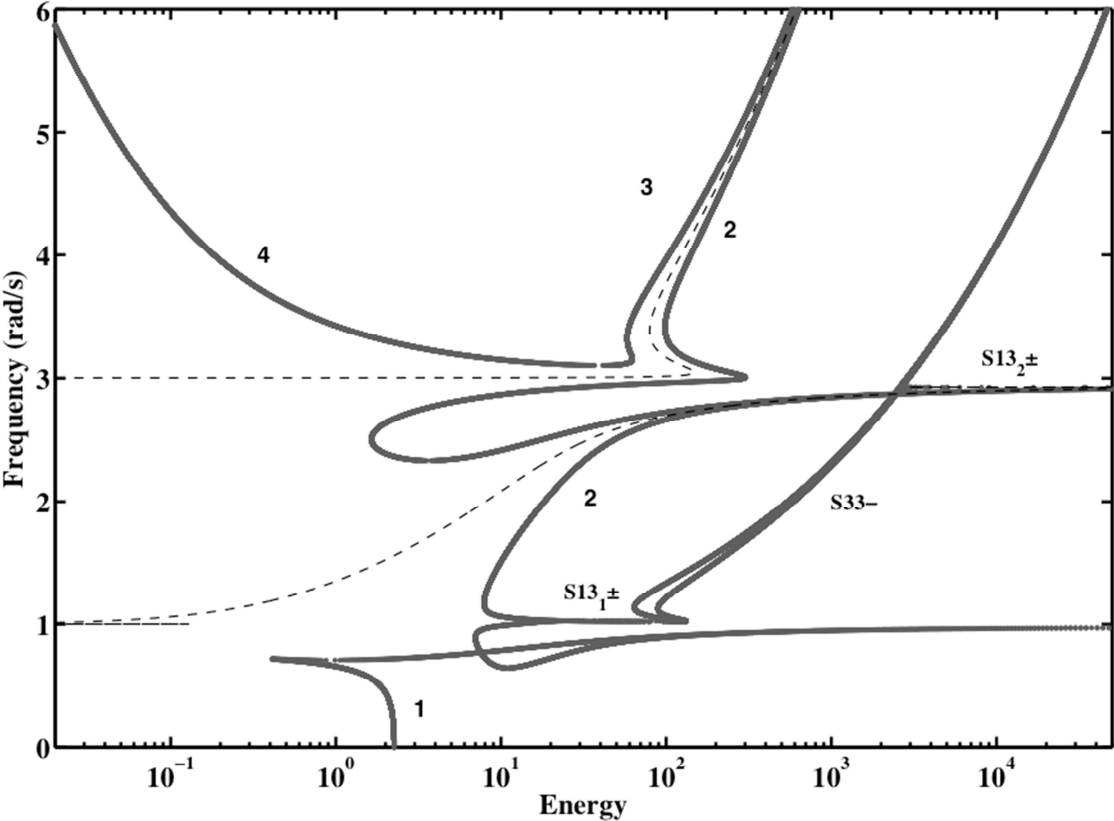


Figure 4.30. FEP of the forced and undamped system computed by solving (7) for $F = 5 N$, and with both ω and 3ω harmonic components shown (—); underlying numerical Hamiltonian FEP for the undamped and unforced system (-----).

In addition, branch 3 represents the forced perturbation of the high-frequency out-of-phase strongly nonlinear branch of NNMs, so it consists of strongly nonlinear out-of-phase resonances localized to the nonlinear oscillator. This branch meets the weakly nonlinear out-of-phase branch

4 since this branch is located at lower energies. Branch 2 undergoes an interesting dynamical transition with increasing frequency. In particular, at lower frequencies and in the neighborhood of the first linearized natural frequency of the system, this branch exhibits the strong effects of 1:3 resonance as it connects to the forced perturbations of branches $S13_{\pm}$ (presented in Figure 4.29 and depicted as $S13_1 \pm$ in Figure 4.30); whereas at higher frequencies becomes strongly nonlinear and the system undergoes out-of-phase oscillations that are strongly localized to the nonlinear oscillator. This branch also exhibits the strong effects of 1:3 resonance at high energy levels, on the branches depicted as $S13_2 \pm$, which connect to the $S33 -$ branches in Figure 6. This 1:3 resonance basically occurs between the forced perturbations of out-of-phase mode and in phase modes at high energy levels. Similar $S13 \pm$ branches can be observed at high energies in the in-phase mode of the Hamiltonian system as well, as shown in Figure 4.26. Note that since this phenomenon occurs at very high energy levels, it has less practical meaning for our study.

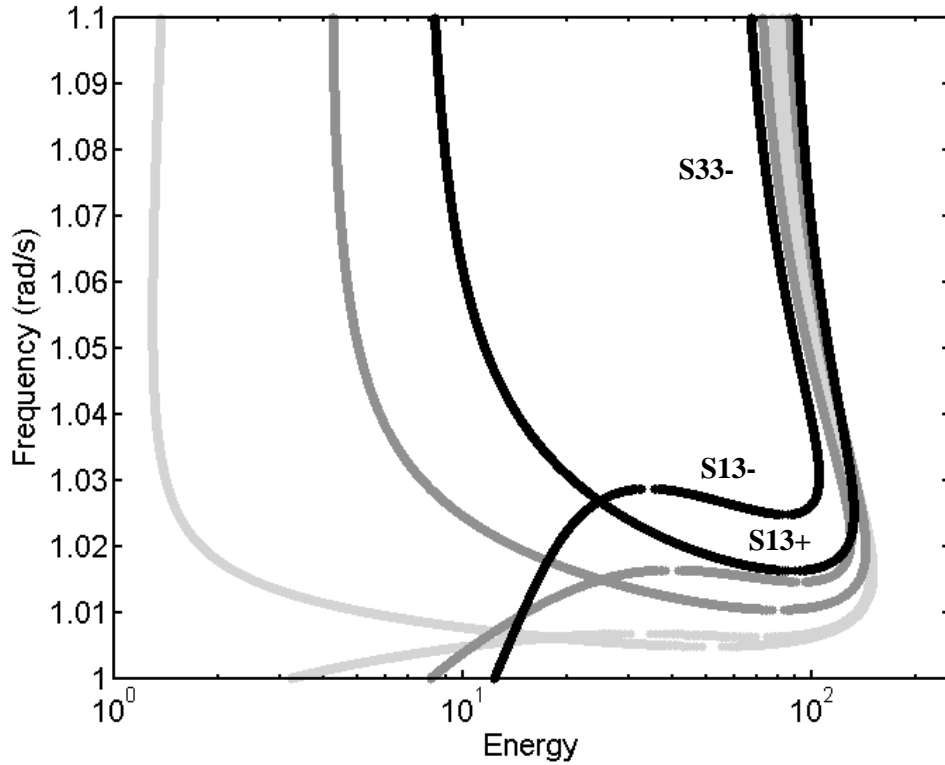
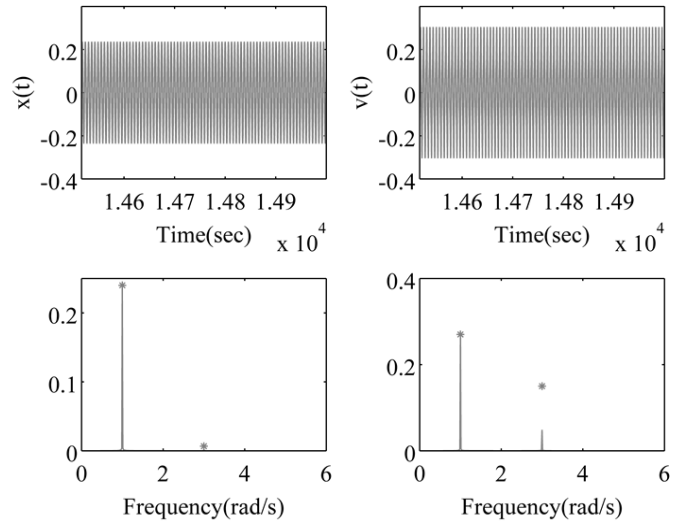


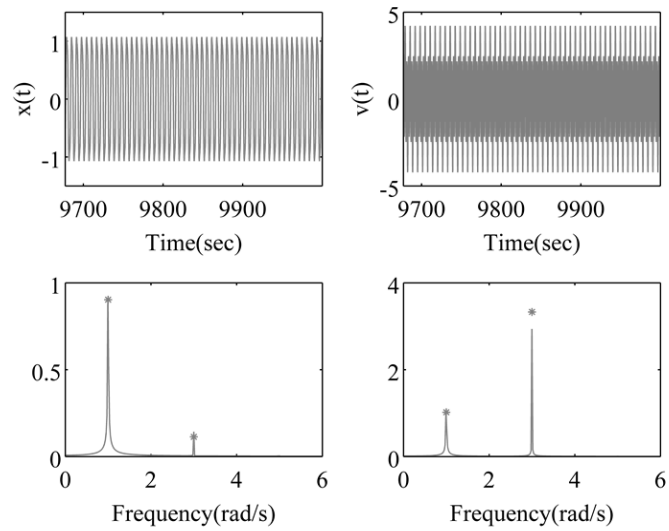
Figure 4.31: Effect of varying the magnitude of the applied excitation on the branches $S13 \pm$ of the forced and undamped system for: $\text{---} F = 1 N$, $\text{---} F = 3 N$, $\text{---} F = 5 N$.

4.3.2.5 Effect of Varying the Magnitude of the Harmonic Excitation on the Steady-State Dynamics

At this point, we investigate the effect of varying the magnitude of the applied force, F , on the topological features of the branches $S13 \pm$, which as discussed in previous sections they are the primary manifestations of the dynamical effects of 1:3 resonance. In Figure 4.31, we depict the topologies of these branches for the forced and undamped system for three distinct forcing levels, namely, $F = 1, 3$ and $5 N$. We observe that a larger force magnitude results in an expanded internal resonance region in the frequency domain; moreover, the internal resonance effects occur at larger energy values.

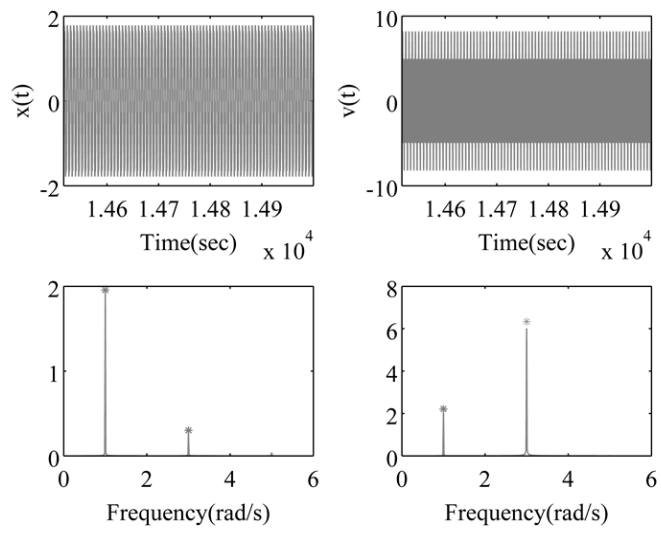


(a)

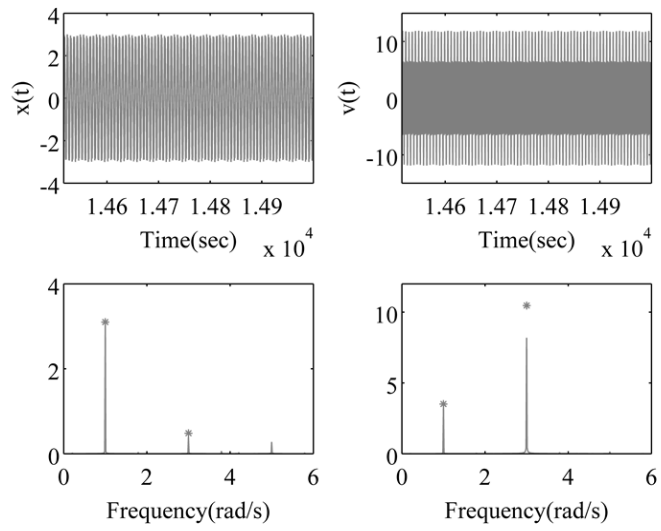


(b)

Figure 4.32. Direct numerical simulation results (with small damping $c_1 = c_2 = 0.001 Ns/m$) showing the steady state responses of system (1) and their Fourier spectra with the excitation frequency $\omega = 1 \text{ rad/s}$, and, (a) $F = 0.01 N$, (b) $F = 1 N$, (c) $F = 5 N$, (d) $F = 20 N$; for comparison we depict the analytical predictions (\bullet) for the harmonic content from the slow-flow equations (4.25).



(c)



(d)

Figure 4.32 (cont.)

These results are of practical significance, since they increase the frequency and energy ranges in which the dynamical effects of 1:3 resonance can be practically realized and implemented in design. In addition, it is interesting to note that a larger force magnitude makes the two branches $S_{13 \pm}$ more robust in the frequency domain, which means that the dynamical effects of 1:3 resonance extends over a larger frequency span, as shown in Figure 4.32.

As a next step, we seek to confirm our general observations regarding the results of Figure 4.31 by directly integrating the nonlinear equations of motion (4.19); in the simulations small damping was added to system (4.18) in order to dampen out the initial transient and obtain the steady-state responses. The results of the simulations are depicted in Figure 4.32. Considering the result of Figure 8a corresponding to small forcing magnitude, we note that the responses of both masses of the system possess dominant frequency components at the excitation frequency, and these are predicted well by the analytical results obtained by the slow flow system (4.25) as explained later. However, the dynamics changes drastically when the forcing magnitude is increased. As seen from the results of Figures 4.32b,c,d corresponding to larger forcing magnitudes, the ω –component dominates the response of the grounded nonlinear oscillator but the 3ω –component dominates the response of the light linear attachment, which is a clear indication of 1:3 resonance in the system. This occurs since, at higher excitation magnitudes the third harmonic component in the response of the grounded nonlinear oscillator is excited, which, in turn, resonates with the second linearized natural frequency of the system (which is at exactly three times the first linearized frequency). This leads to a relatively strong third harmonic of the light linear attachment. Of course, the disadvantage of applying a stronger harmonic excitation is that in that case both the ω –harmonic component of the response of the light attachment and the 3ω –harmonic component of the response of the grounded nonlinear oscillator also increase,

thereby causing a mixed-mode response of both masses. However, for practical applications, it is much more useful to use a forcing level which leads to a clear separation of the different harmonic components in the responses of different masses. In Figure 4.32, we also assess the theoretical predictions derived by solving the system of slow-flow equations (4.25) by comparing them with the corresponding Fourier transform spectra of the direct numerical solutions of the exact governing equations of motion (4.19). In general, satisfactory agreement between the analytical predictions and the numerical simulations is deduced. Wherever mismatches occur (see Figures 4.32a,d) the reason is that, for very low and very high forcing amplitudes, the third harmonic component of the response of the light attachment is very sensitive to damping, which we did not take into account in the slow-flow equations (4.25). Also, at higher forcing levels, higher harmonics are generated in the responses, which, again, are not taken into account when deriving the slow-flow system (4.25). However, we clearly observe that, in the responses depicted in Figures 4.32b,c, all steady-state amplitudes of both masses are predicted with good accuracy by the analytical results.

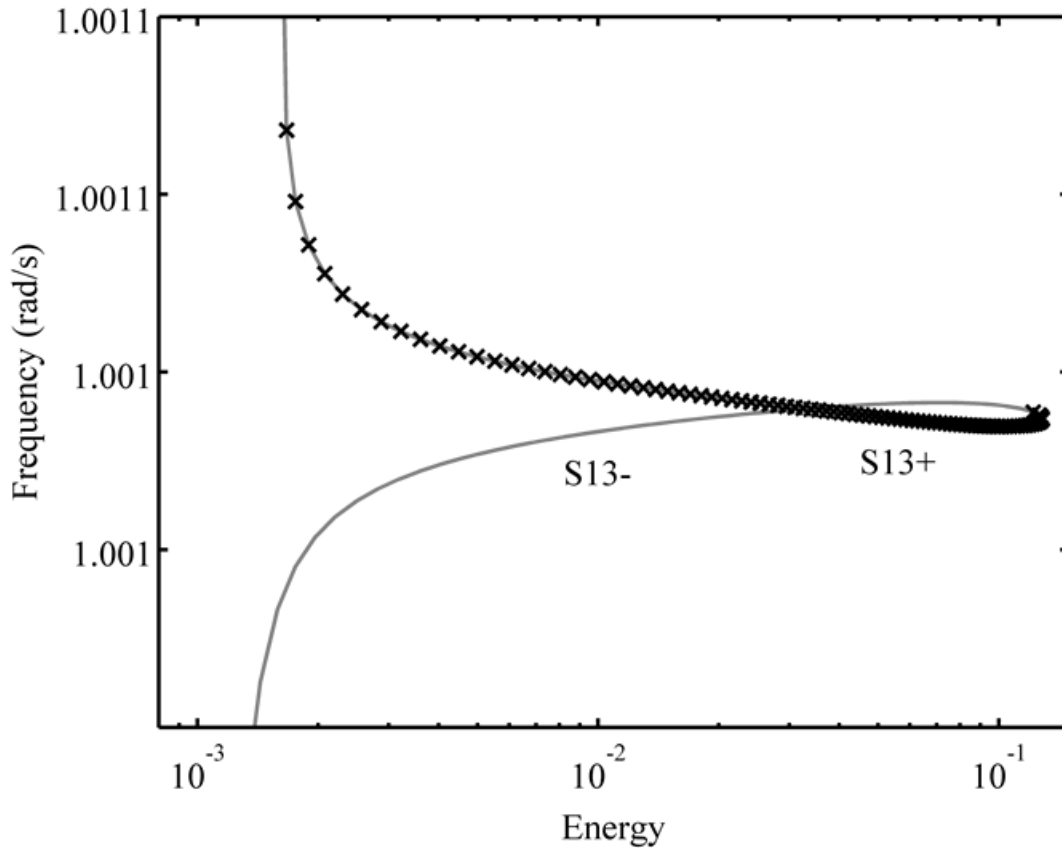


Figure 4.33. Stability analysis of the numerical branches $S13 \pm$ for the underlying Hamiltonian system by studying Floquet multipliers of the steady state responses; unstable NNMs are denoted by (\times).

Finally, we proceed with the stability analysis of the branches $S13 \pm$ of the Hamiltonian system and their perturbations for the forced and undamped system. In Figure 4.33 we depict the stability results for the numerically computed branches $S13 \pm$ for the Hamiltonian system. The stability analysis is carried out by calculating the Floquet multipliers of the responses of the Hamiltonian system (Kerschen et al. 2009). We observe that branch $S13 -$ is stable, whereas, starting from the triple coalescence point branch $S13 +$ is unstable. After a smooth yet unstable transition from $S13 +$ to $S11 +$, the NNMs become stable again with increasing frequency.

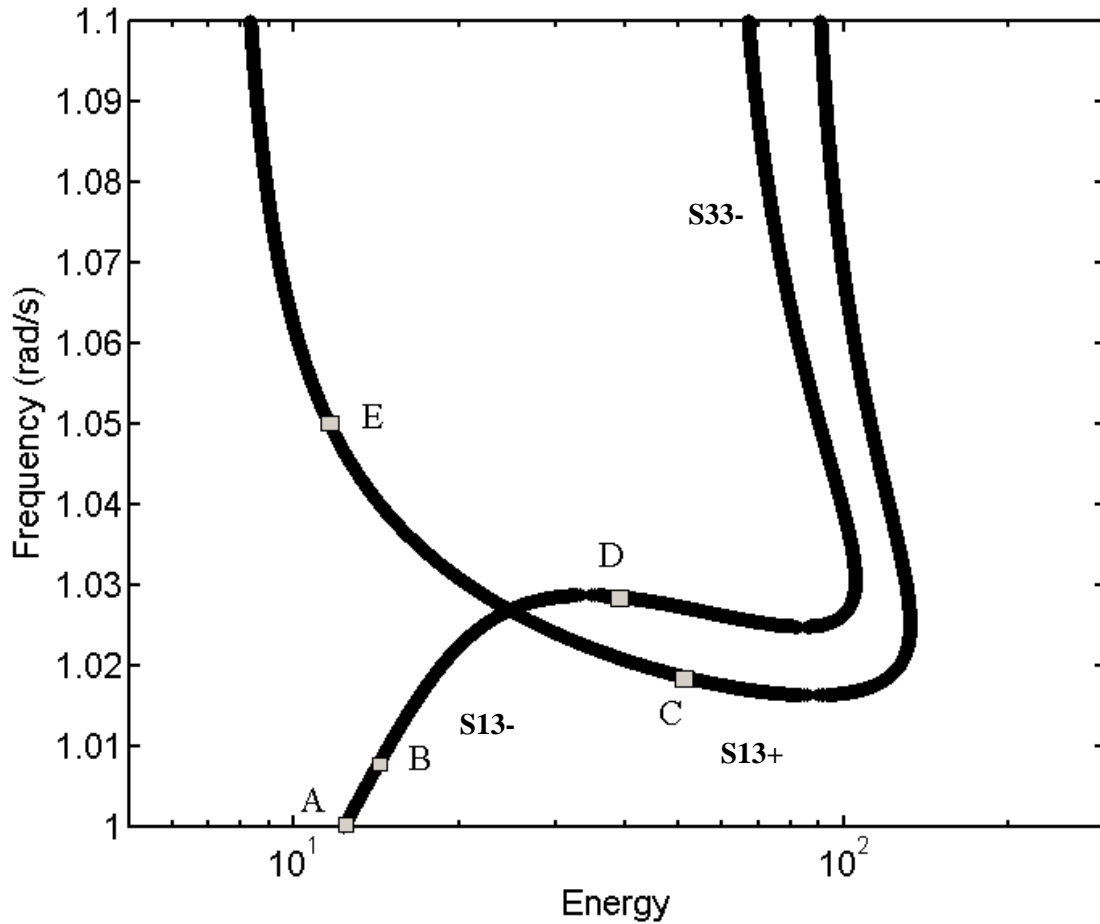
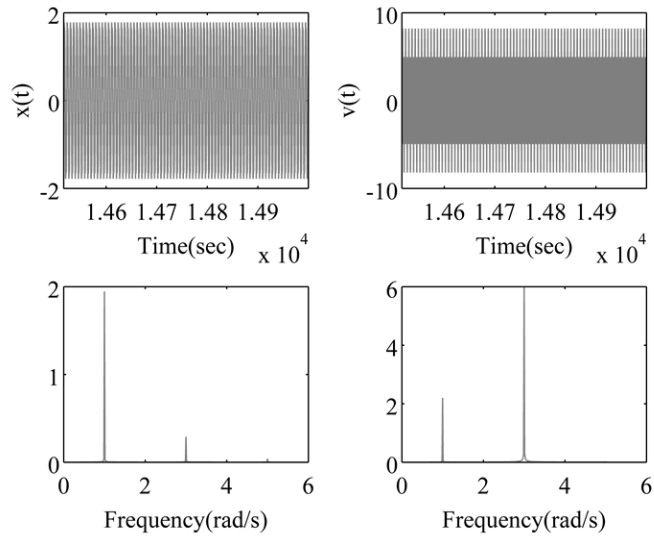
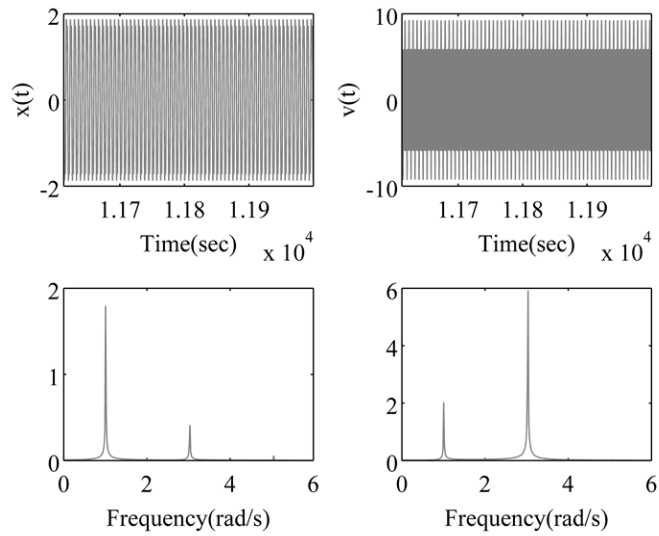


Figure 4.34. Steady-state periodic solutions computed by system (4.25) for the forced and undamped system with $F = 5 N$, with points where the stability is investigated denoted by (■); letters refer to the numerical simulations of Figure 4.35.

Stability analysis of the forced system is more challenging since, for varying forcing amplitude and damping values, the system can exhibit strongly nonlinear, quasiperiodic or even chaotic dynamical behavior. Note that, due to the extremely narrow frequency range where the effects of 1:3 resonance are realized, the most straightforward way to study the stability of the steady-state solutions at these frequencies is through direct numerical simulations of the equations of motion (4.19) for the analytically predicted initial conditions (on the solution branches shown in Figure 4.34).

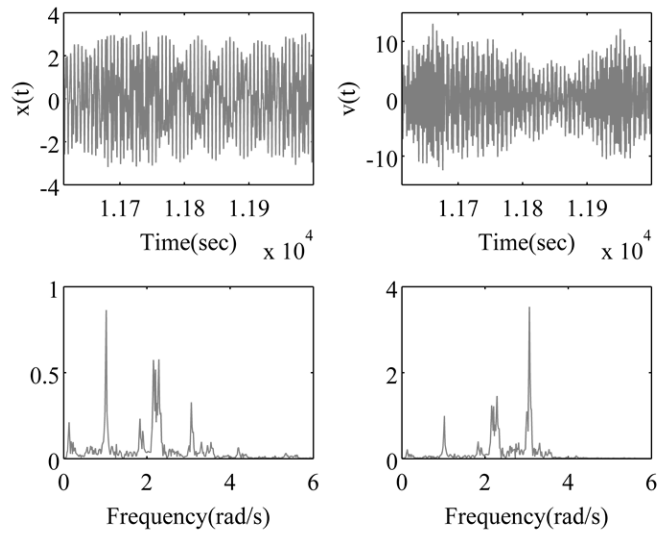


(a)

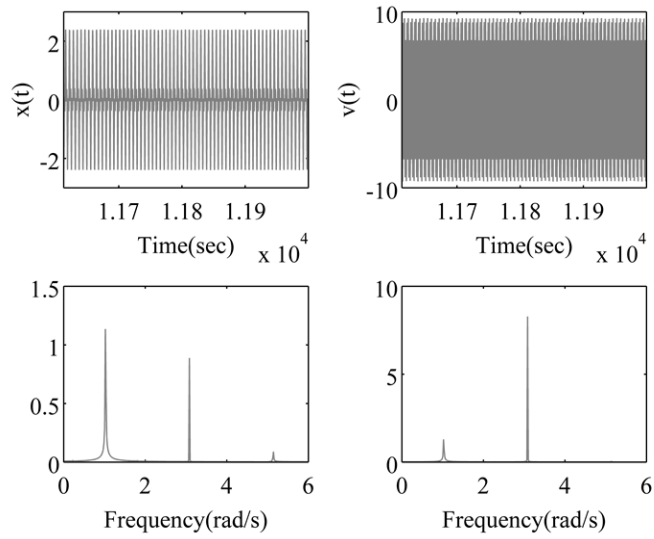


(b)

Figure 4.35. Direct numerical simulation results showing the steady state responses of system (1) and their Fourier spectra for $F = 5 N$ with initial conditions and the excitation frequency taken from (a) Point A, (b) Point B (c) Point C (d) Point D (e) Point E in the plot of Figure 4.34; weak damping values, $c_1 = c_2 = 0.001 Ns / m$, were used for the simulations.

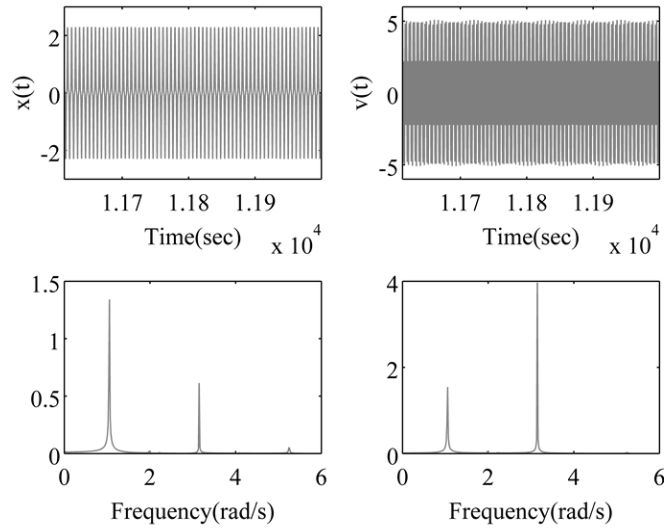


(c)



(d)

Figure 4.35 (cont.)



(e)

Figure 4.35 (cont.)

Therefore, we focus on the fixed forcing magnitude $F = 5 N$ and weak damping values $c_1 = c_2 = 0.001 Ns / m$.

We note that an extended study of the stability and domains of attraction of the solutions are beyond the scope of this work. In Figure 4.35, we depict the numerical simulation results by using the initial conditions and the excitation frequencies from points A-E indicated on Figure 4.34. We see that, similar to the Hamiltonian stability analysis in Figure 4.33, steady-state solutions on the forced perturbation of S13-, which are A, B, and D, appear to be stable, whereas the response on point C, which is on the forced perturbation of S13+ branch, is unstable. The branches regain their stability after the transition from the forced S13+ to the forced S11+ as the frequency increases. This is verified by looking at the stability of the response on point E, which is found to be stable

in Figure 4.35. Also interesting is that point D, which is on the forced S13- branch, experiences a larger 3ω component although the excitation frequency is only varied from 1 to 1.028 rad/s. This is because, as shown in Figure 4.31, as the forcing level increases the 1:3 resonance occurs over a broader frequency range, and a change in the excitation frequency may cause a large qualitative change in the responses. This result can be used to achieve an even greater separation of harmonic components between the grounded nonlinear oscillator and the light attachment; however, a detailed and careful stability analysis is needed to complete the assessment.

4.3.2.6 Concluding Remarks

In this section, we studied the interesting and complicated dynamics of a 2-DOF system consisting of a grounded nonlinear oscillator under harmonic forcing coupled to a light linear attachment, under condition of 1:3 resonance. We examined the periodic steady-state solutions of the Hamiltonian and the forced configurations of the system and compared them in the frequency-energy domain by computing forced frequency-energy plots (FEPs). The dynamics of the system was drastically affected by the 1:3 resonance. Indeed, we observed localization of the ω – and 3ω – harmonic components to the grounded nonlinear oscillator and the light linear attachment, respectively, when the system is operating near its first linearized frequency. Varying the forcing amplitude revealed that the phenomena of interest can be enhanced greatly when optimal forcing levels and excitation frequencies are applied.

We also note that this type of localization in the dynamics of the system may have practical implications. An example of such an application could entail utilizing the

variation of the forcing amplitude to introduce essential and controllable changes in the frequency spectrum of a nonlinear structure with a lightweight attachment. This, in turn, could be used to design a new type of atomic force microscope (AFM) probe, in the form of a nonlinear cantilever beam with an internal lightweight linear paddle, with their linearized frequencies being in the ratio 1:3. The resulting 1:3 resonance can be utilized to magnify the third harmonic of the paddle response which can then be measured for high-frequency AFM. Moreover, the sensitivity of this design to produce enhanced high-frequency response could be increased greatly by a simple variation of the excitation amplitude, as predicted by the present study.

Chapter 5

NONLINEAR MODEL UPDATING

5.1 Introduction and Background Information

In this chapter, we propose a new nonlinear model updating strategy based on the global/local nonlinear system identification procedure discussed previously. The approach relies on analyzing the system in the frequency-energy domain by constructing Hamiltonian or forced and damped frequency- energy plots (FEPs). The system parameters are characterized and updated by matching the backbone branches of the FEPs with the frequency-energy dependence of the given system by using experimental or computational data. The main advantage of this method is that no type of nonlinearity model is assumed *a priori*, and the system model is updated solely based on simulation and/or experimental results. By matching the frequency-energy dependence of a dynamical system with that of its reduced order model, we show that we are able to retrieve the global dynamics and characterize the nonlinear properties of the system. We believe that this methodology represents a first step toward a widely applicable a nonlinear model updating methodology.

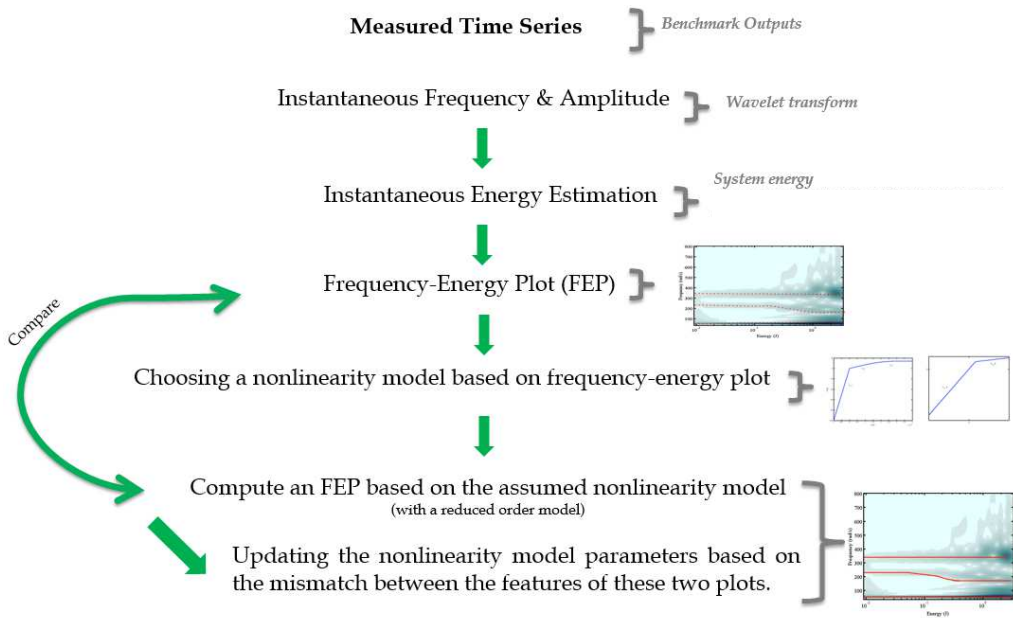


Figure 5.1 Summary of the proposed nonlinear model updating approach

In Figure 5.1, the general outline of the proposed nonlinear model updating approach is presented. As in the case of local and global applications of NSI, the proposed nonlinear model updating strategy starts with the measured time series. In order to find the global frequency-energy behavior of a system, we measure time series from a number of sensors throughout the system under transient excitation. Afterwards, we estimate the instantaneous frequency, amplitude and the energy of the transient data by making use of the WT and its superposition onto a “reference” FEP. A very useful feature of the FEP for system identification purposes is its relation to the transient dynamics of the corresponding weakly damped system. This is due to the fact that *the effect on the dynamics of weak damping is parasitic*: Instead of introducing “new” dynamics, it just causes transitions of the dynamics between branches of normal modes leading to multi-frequency nonlinear dynamical transitions. It has been shown that the superposition of a frequency-energy plot (FEP) depicting the periodic orbits of the underlying Hamiltonian

system and the wavelet transform (WT) spectra of the corresponding weakly damped responses represents a suitable tool for analyzing energy exchanges and transfers taking place in the damped system (Kerschen et al. 2007; Andersen et al. 2012; Remick et al. 2013). Therefore, by utilizing this (empirical) frequency-energy dependence obtained from the superposition of the WT spectra onto the FEP, we arrive at a nonlinearity model, since we can infer the properties of the nonlinearities in the frequency-energy domain, provided that the transient data has sufficient energy and frequency range. The parameters of the nonlinearity model are then optimized by comparing the numerical frequency-energy dependence from the simulations to the Hamiltonian FEPs computed by NNMcont (Peeters et al. 2009).

5.2 System with Hardening/Softening Behavior

5.2.1 Introduction and System Description

One of the main characteristics of nonlinear oscillations is their frequency dependence on vibration amplitude, which can be of hardening or softening type (Nayfeh and Mook 2008). If the frequency increases with the amplitude of oscillations, the system is said to have a *hardening* behavior; whereas in the opposite case, it is said to be *softening*.

In order to apply the nonlinear model updating strategy proposed in Section 5.1 and summarized in Figure 5.1, we consider the dynamics of a system consisting of two facing steel cantilever beams connected with a membrane-like element, depicted in Figure 5.2.

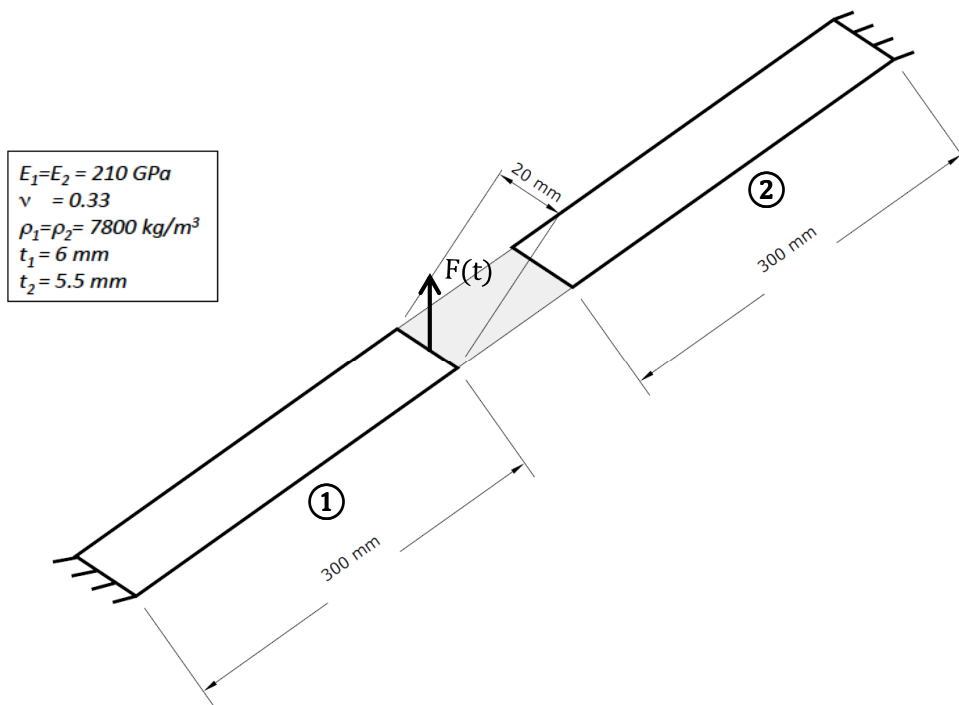


Figure 5.2 Overview of the examined system with the physical properties and dimensions. The two clamped beams are connected by a non-linear element whose force-displacement curve is given in Figure 5.3.

The general scheme and physical properties of the system are given in Figure 5.2. The two facing cantilever beams are identical except for their thickness values, which are 6 and 5.5 mm, respectively, for beams 1 and 2. The goal will be to characterize and identify the nonlinear properties, if any, of the element connecting the two cantilever beams in Figure 5.2. Note that, for the sake of testing our “model updating” ideas, we, in fact, will treat the connecting element as “non-identified” in the upcoming sections. In Figure 5.3 (and 5.1), we present the empirical force-displacement curve of the “unknown” element for the load shown in Figure 5.2.

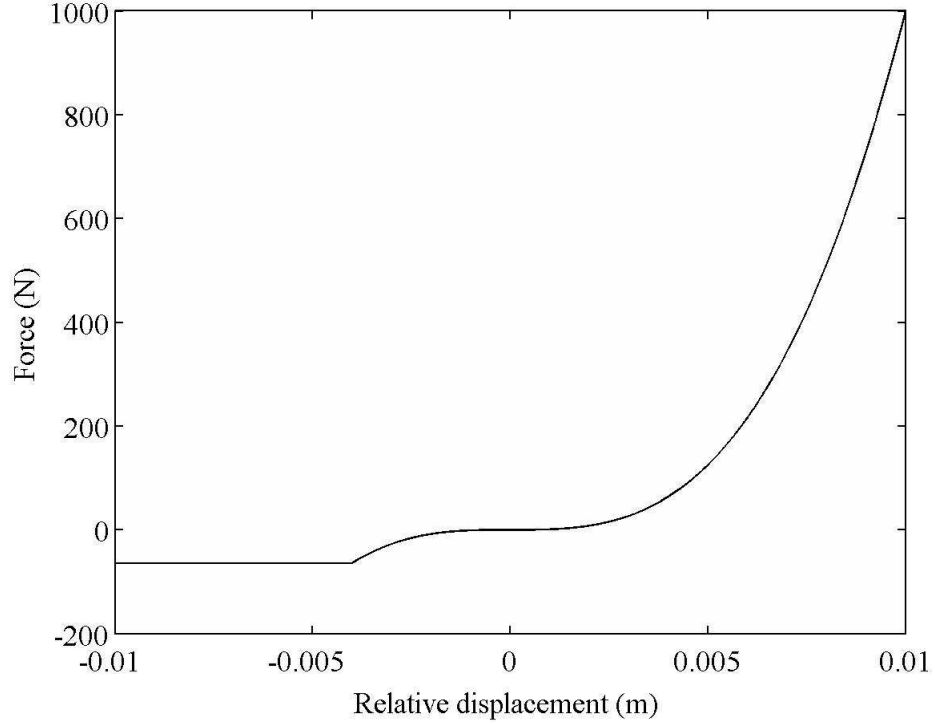


Figure 5.3 The force-displacement relationship of the nonlinear connection in Figure 5.2.

$$F(\Delta x) = \begin{cases} 1 \times 10^9 \Delta x^3 \text{ N} & \Delta x \geq -4 \times 10^{-3} \text{ m} \triangleq x_b \\ 1 \times 10^9 \text{ N/m}^3 (-4 \times 10^{-3} \text{ m})^3 = 64 \text{ N} & \Delta x < -4 \times 10^{-3} \text{ m} \triangleq x_b \end{cases} \quad (5.1)$$

As seen in Figure 5.3 and (5.1), the force-displacement curve of the connection has two parts: For relative displacements larger than x_b , defined as the “breaking point” of the force-displacement curve with a value of -4 mm, there is a cubic relationship (essentially [non-linearizable] nonlinear stiffness) between the relative displacement of the end points of the connection and the force exerted on the connection. Beyond the breaking point x_b (*i.e.*, for relative displacement values smaller than -4 mm), the curve reaches zero stiffness and has a constant value of 64 N afterwards. Such hardening/softening behavior resembles the buckling of membranes and shell-type structures: Until the breaking point

x_b , the connection possesses geometric nonlinearities, and thus, exhibits a cubic order nonlinearity; however, once the relative displacement of the end points is smaller than -4 mm, the connection “buckles” and reaches (almost) zero stiffness. Similar hardening/softening behavior of beams, shells and membranes have been studied extensively in the literature for nonlinear vibration problems (Lacarbonara 1997; Tiso, Jansen, and Abdalla 2006; Iu and Chia 1988; Cho et al. 2012).

The properties of the linking member make this problem challenging and particularly interesting for model updating purposes. Due to the strong nonlinear properties of the connection, the system responses will possess strongly nonlinear characteristics, which cannot be analyzed with linear methods. Furthermore, since the force-displacement curve of the connection is asymmetric, the system will behave differently depending on the direction and the amplitude of the excitation force. Finally, the type of nonlinear behavior will depend on the instantaneous energy level of the response, since the connection switches between softening/hardening behaviors, depending on the relative displacement value of the two clamped beams at any instant.

5.2.2 Numerical Simulations

5.2.2.1 Numerical Simulation with the FE model

As noted in Section 5.1, transient dynamics is at the center of our nonlinear model updating strategy, since it reveals the nonlinear dynamical transitions which, in turn, helps us obtain the approximate frequency-energy relationship of the dynamical system. Therefore, in this section, we carry out multiple impulse tests for the system under

consideration in order to obtain transient data, which will be incorporated into the model updating process later on.

In order to simulate the system given in Figure 5.2, we construct FE models of the two beams, both consisting of 15 elements. We use a half-sine pulse with duration of 0.1 ms for the excitation force, as depicted in Figure 5.4. The direction and the location of the force is also shown in Figure 5.2; *i.e.*, the force is applied to the tip of beam 1, in the positive direction. The system is simulated with varying magnitudes of F_{\max} , in order to obtain transient data both in the linear, weakly and strongly nonlinear regimes.

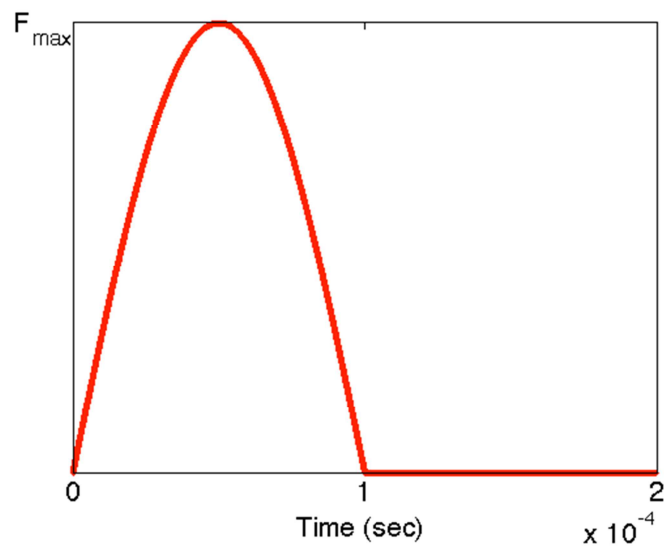


Figure 5.4 Impulse force used for the numerical simulations of the system depicted in Figure 5.2, which is applied to the tip of the beam 1.

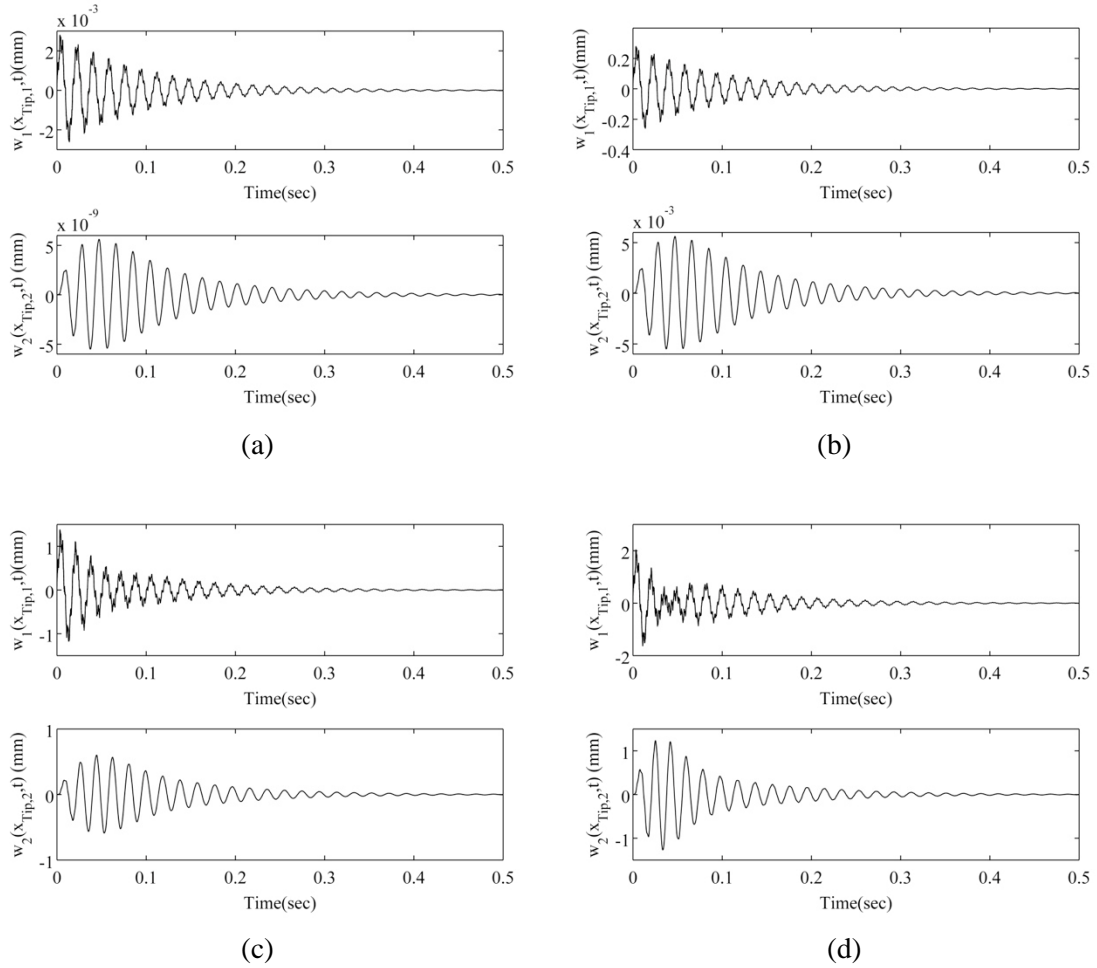


Figure 5.5 Impulse responses of the tips of the two beams $w_1(x_{Tip,1}, t)$ and $w_2(x_{Tip,2}, t)$ for (a) $F_{max} = 1$ N (b) $F_{max} = 100$ N (c) $F_{max} = 500$ N (d) $F_{max} = 750$ N

In Figures 5.5 and 5.6, we present the numerical simulation results for the displacements of the tips of the two beams, depicted as $w_1(x_{Tip,1}, t)$ and $w_2(x_{Tip,2}, t)$, respectively, for varying F_{max} values. In Figure 5.5a,b, where $F_{max} = 1$ N and 100 N, respectively, we observe that the oscillation amplitudes of $w_2(x_{Tip,2}, t)$ are much smaller when compared with those of $w_1(x_{Tip,1}, t)$. That is because, as seen in Figure 5.3 and formulated in (5.1), for small relative displacements (*i.e.* $\Delta x \triangleq w_1(x_{Tip,1}, t) - w_2(x_{Tip,2}, t) \approx 0$), there is a cubic

force-displacement relationship, which results in a very weak coupling between the two beams. It is also interesting to note that, a nonlinear beating starts to appear in $w_1(x_{Tip,1}, t)$ around $F_{max} = 750$ N, which is an indication that, above this forcing level, the effects of the hardening term in (5.1) begin to appear, increasing the coupling between the two beams and initiating the phenomenon called *mode-mixing* (between the first bending modes of the two beams) in the signals.

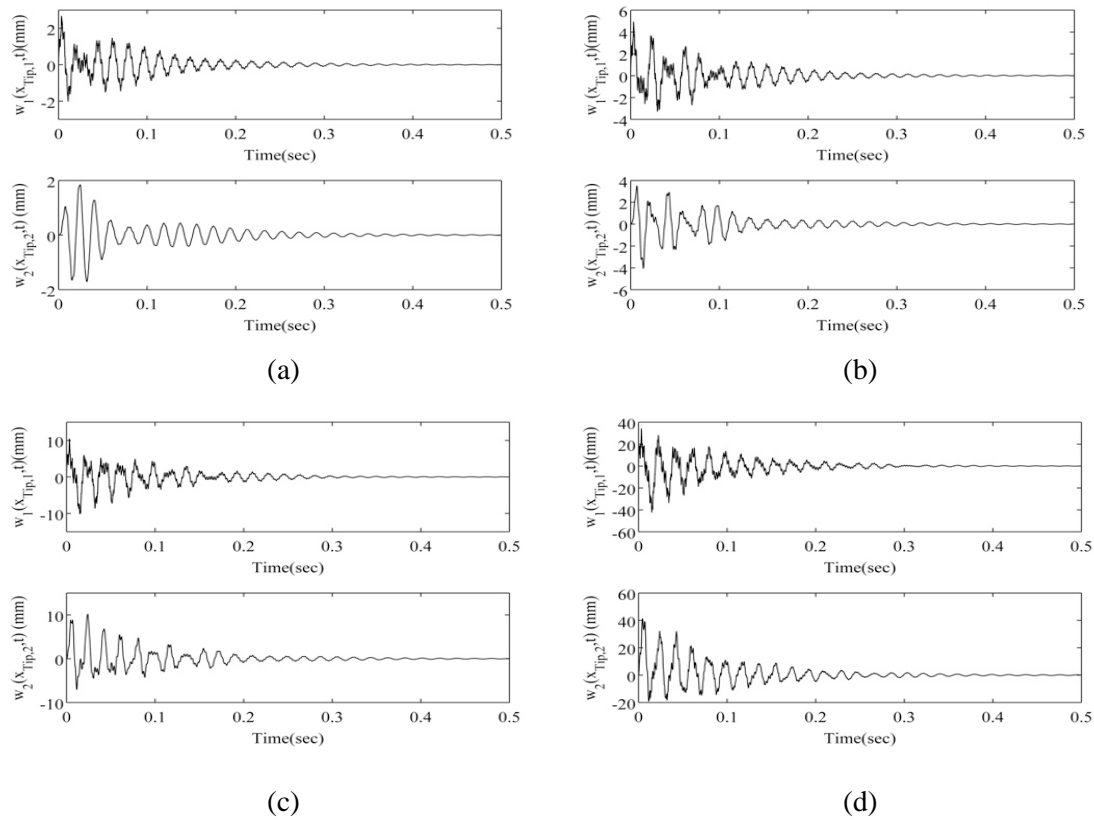
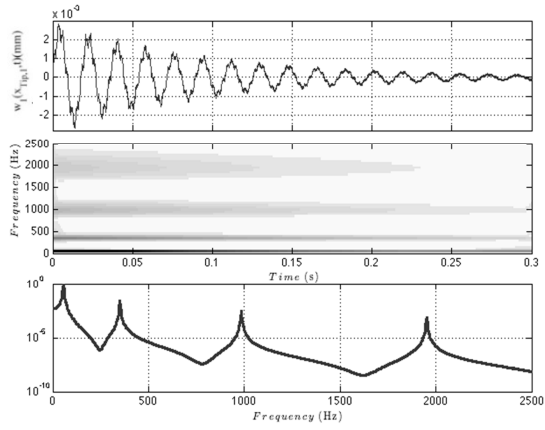


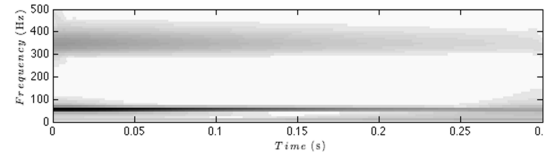
Figure 5.6 Impulse responses of the tips of the two beams $w_1(x_{Tip,1}, t)$ and $w_2(x_{Tip,2}, t)$ for (a) $F_{max} = 1000$ N (b) $F_{max} = 2500$ N (c) $F_{max} = 5000$ N (d) $F_{max} = 20000$ N.

In Figure 5.6a, where $F_{\max} = 1000$ N, we observe that the effect of the hardening term in (5.1) causes asymmetric oscillations and mode mixing in both of the beams. In Figure 5.6b,c, Δx , the relative displacement between the tips of the two beams, surpasses the breaking point x_b , and breaks the symmetry of the oscillations since after the breaking point, the connection has zero stiffness and its nonlinear properties depicted in Figure 5.3 are no longer symmetric around zero relative displacement. When the forcing level is increased dramatically, as in the case of Figure 5.6d, where $F_{\max} = 20000$ N, the hardening effect of the nonlinear connection overcomes the softening effect and the two beams become strongly coupled, thus resulting in similar $w_1(x_{Tip,1}, t)$ and $w_2(x_{Tip,2}, t)$.

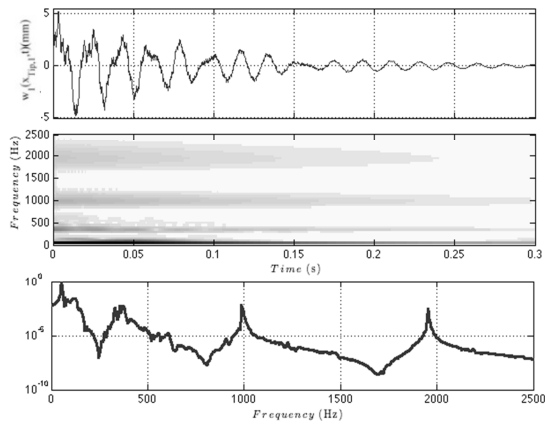
In Figure 5.7, wavelet and Fourier transforms of the tip deflection for the first beam, $w_1(x_{Tip,1}, t)$ for varying F_{\max} values are depicted. For $F_{\max} = 100$ N, in Figure 5.7a,b, the response is linear due to the low forcing level, as is evident in both the WT and FT of the signal. In Figure 5.7c,d, the frequency of the second mode clearly starts to increase, since, as shown in Figure 5.6a,b, the effect of the hardening term starts to dominate around this forcing level. In Figure 5.7e,f, the second mode of the system undergoes an interesting transition. The frequency of this mode increases (*i.e.*, hardening effect) with energy until the relative displacement between the tips of the two beams is -4 mm, after which the connection softens and the frequency of the second mode in Figure 5.7e,f decreases.



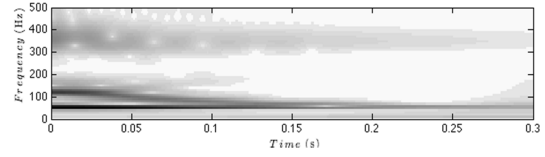
(a)



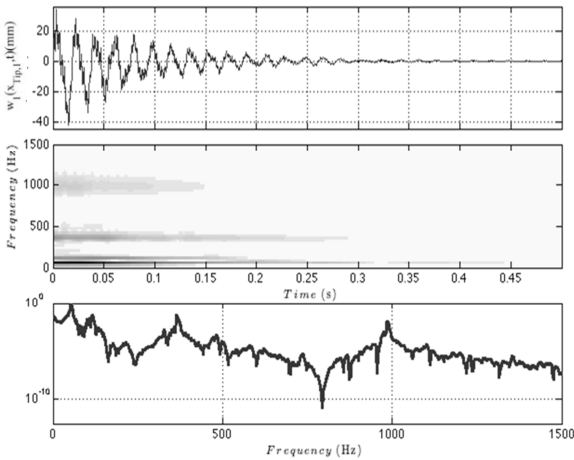
(b)



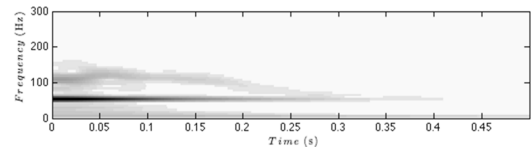
(c)



(d)



(e)



(f)

Figure 5.7 Wavelet and Fourier transforms of the tip deflection for the first beam, $w_1(x_{Tip,1}, t)$ for (a) $F_{\max} = 100$ N, (c) $F_{\max} = 2500$ N, (e) $F_{\max} = 10000$ N. (b), (d) and (f) are the close-ups of the WTs of the time signals depicted in (a), (c) and (e), respectively.

5.2.2.2 Numerical Simulations of the Reduced Order Model

In the previous subsection, we discussed the dynamics of the system depicted in Figure 5.2 consisting of two cantilever beams coupled through a membrane-like member whose force-displacement characteristics are given in Figure 5.3. As was shown in Figure 5.7e,f, the frequency of the second mode undergoes an interesting transition, which increases (*i.e.*, hardening effect) with energy until the relative displacement between the tips of the two beams is -4 mm, after which the connection buckles and the frequency of the second mode in Figure 5.7e,f decreases.

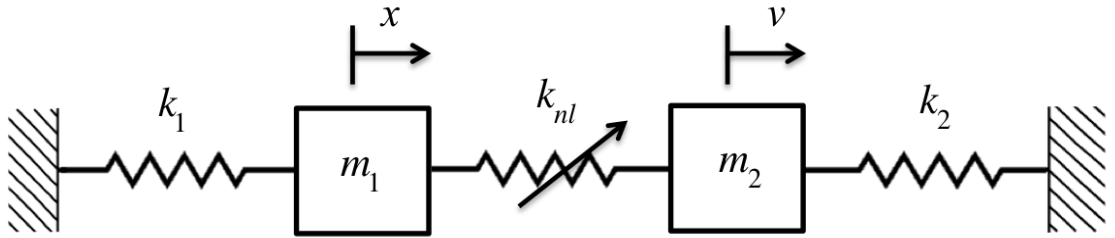


Figure 5.8 Reduced-order model of the system depicted in Figure 5.2 with parameters

As explained in Section 5.1, obtaining the empirical frequency-energy relationship from the transient data is crucial in our nonlinear model updating strategy. However, strongly nonlinear modal interactions make this a hard task to complete in the FE model, since it is not trivial to distinguish the modal interactions from the actual backbone tracking. Therefore, in this section, we model the system depicted in Figure 5.2 with a 2-DOF reduced-order model shown in Figure 5.8. The parameters of Figure 5.8 are calculated by finding the linear spring constants and effective masses of the two beams, given in (5.2).

$$\begin{aligned}
m_1 \ddot{x} + k_1 x + \tilde{F}(x-v) &= F(t) \\
m_2 \ddot{v} + k_2 v - \tilde{F}(x-v) &= 0
\end{aligned}
\tag{5.2}$$

$$\begin{aligned}
k_1 &= \frac{3EI_1}{L^3} = 8400 \text{ N/m}, \quad k_2 = \frac{3EI_2}{L^3} = 6470 \text{ N/m} \\
m_1 &= \frac{33}{140} L w \hat{t}_1 = 0.066 \text{ kg}, \quad m_2 = \frac{33}{140} L w \hat{t}_2 = 0.060 \text{ kg}
\end{aligned}$$

where, for the time being, $\tilde{F}(x-v)$ has the same form as (5.1). In Figures 5.9 and 5.10, we present the numerical simulation results for the displacements of the tips of the two beams, depicted as $w_1(x_{Tip,1}, t)$ and $w_2(x_{Tip,2}, t)$, respectively and their counterparts in the ROM (*cf.* Figure 5.8), $x(t)$ and $v(t)$ for varying F_{\max} values. The ROM is excited with the same forcing depicted in Figure 5.4, which is applied to the first DOF in Figure 5.8. In Figure 5.9a,b,c, we see that the ROM captures the general trend of the corresponding responses from the FE model, since near the linear region, the first 2 modes are dominant (*cf.* Figure 5.7a). Note that there seems to be a small phase difference, which is due to the fact that the frequency values for the first 2 modes between the ROM and FEM model, although very close, are not identical. In Figures 5.8d and 5.9a-c, we see that the important dynamical transitions have been captured by the ROM. Note that these are strongly nonlinear cases, where the nonlinear connection undergoes both hardening and softening depending on the relative tip displacement between the two beams. Indeed, as the forcing level increases, the discrepancies between the responses increase, as the contributions of the higher modes to each beam's response become more significant.

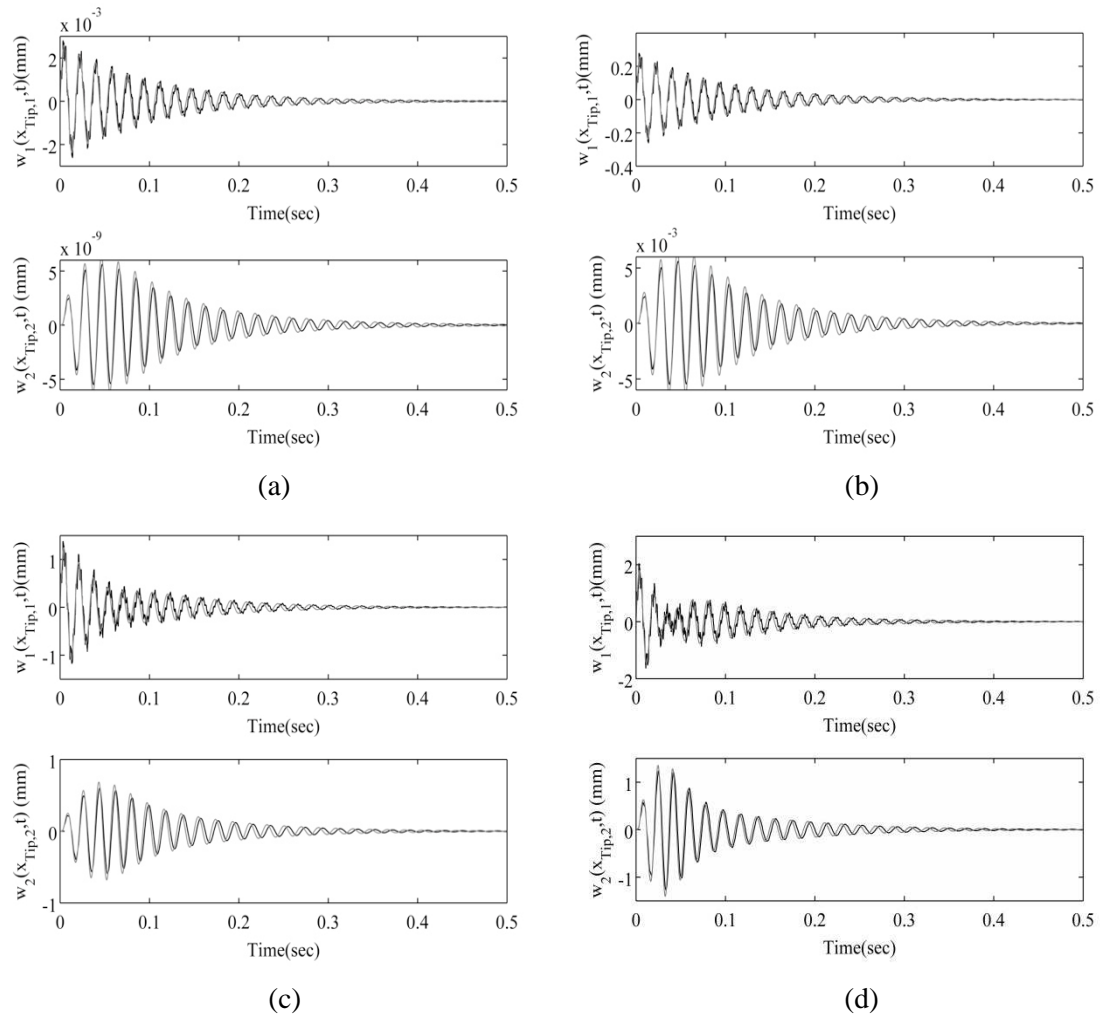




Figure 5.9 Comparison of impulse responses of the tips of the two beams $w_1(x_{Tip,1}, t)$ and $w_2(x_{Tip,2}, t)$ between  Reduced order model,  FEM model for (a) $F_{max} = 1$ N (b) $F_{max} = 100$ N (c) $F_{max} = 500$ N (d) $F_{max} = 750$ N.

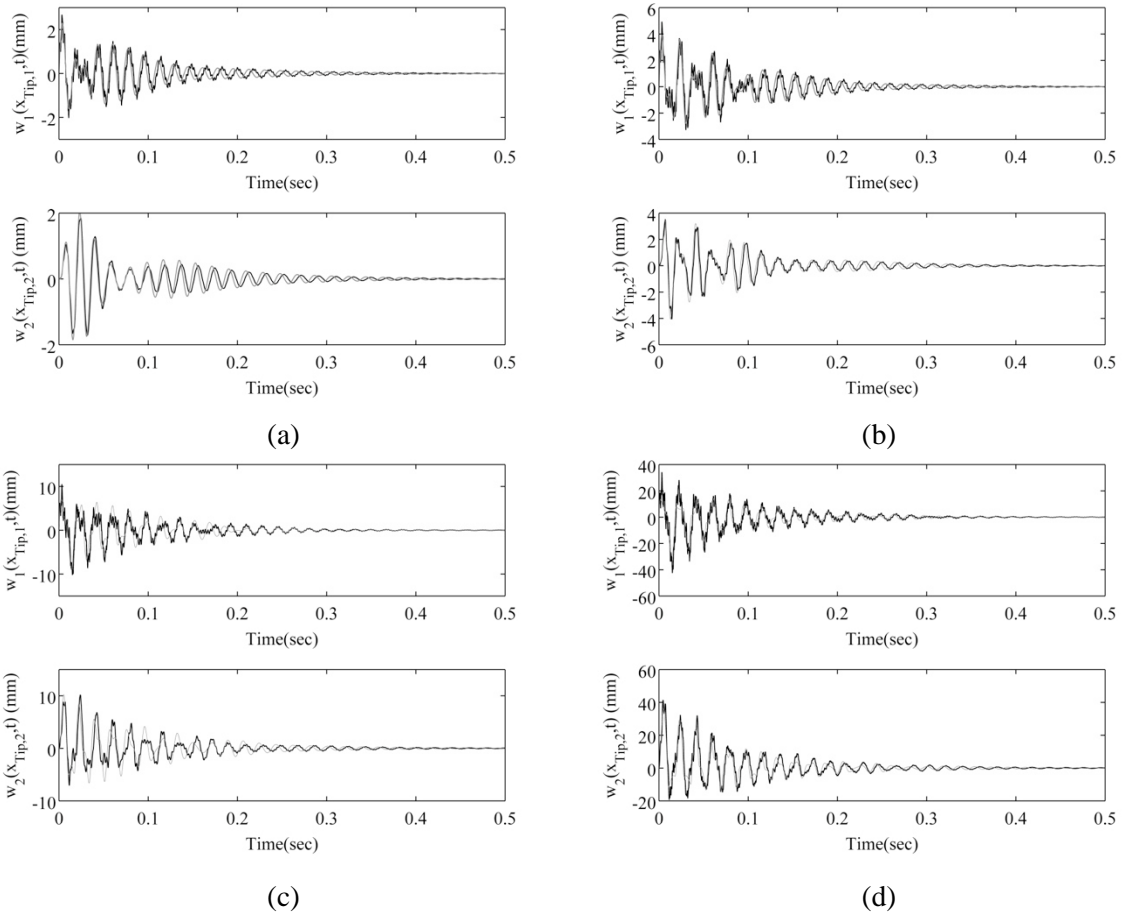




Figure 5.10. Comparison of Impulse responses of the tips of the two beams $w_1(x_{Tip,1}, t)$ and $w_2(x_{Tip,2}, t)$ between  Reduced order model,  FEM model for for (a) $F_{max}=1000$ N (b) $F_{max}=2500$ N (c) $F_{max}=5000$ N (d) $F_{max}=20000$ N.

5.2.3 Frequency-Energy Plots of the System

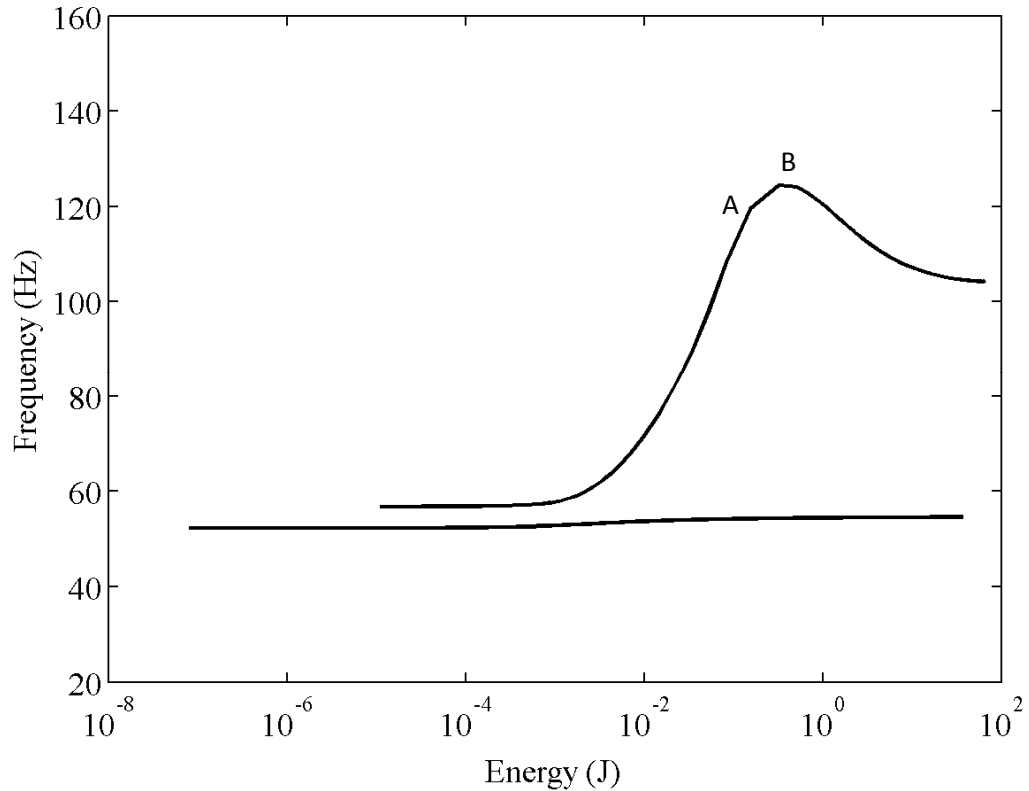


Figure 5.11 Frequency-Energy Plot of the ROM depicted in Figure 5.8, with the nonlinear connection given in Figure 5.3.

In Figure 5.11, the frequency-energy plot (FEP) of the reduced order model is computed by NNMcont (Peeters et al. 2009) and depicted. The FEP consists of two backbone branches, depicting the in-phase and out-of-phase NNMs, respectively. It is interesting to note that the frequency of the in-phase NNMs changes insignificantly over the energy. This is expected, since the nonlinear connection is located between the two masses and “activated” only during the out-of-phase motion.

The out-of-phase backbone branch in Figure 5.11 follows an interesting transition. For low energies, the branch behaves like a linear mode; and as the energy level increases, due to the hardening behavior of the nonlinear connection (*cf.* Figure 5.3), the

frequency of the out-of-phase NNMs increases. After a critical point, depicted as A in Figure 5.11, which can be viewed as the energy level which corresponds to the breaking point x_b (cf. Figure 5.3), the slope of the second backbone branch starts to decrease until it finally reaches zero at point B. Afterwards, the softening part of (5.1) dominates the hardening, and the frequency of the out-of-phase NNMs starts to decrease, until the softening and hardening effects balance again.

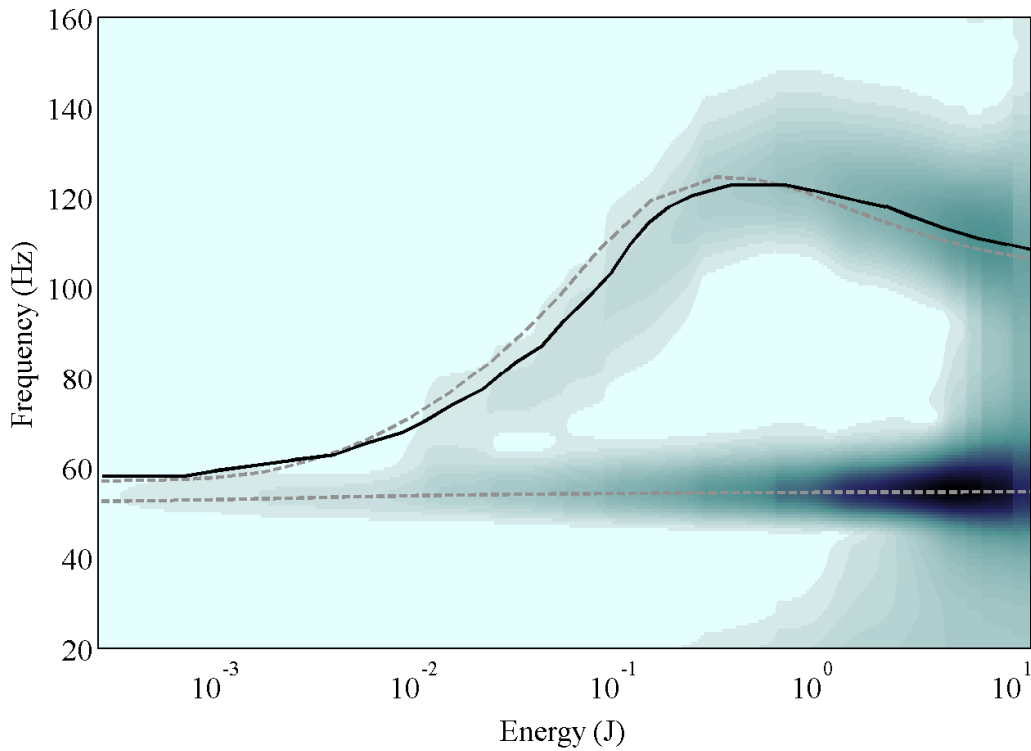


Figure 5.12 Superposition of WT of the 2nd DOF responses (Figures 5.9 and 5.10) of the ROM onto: — Adjusted frequency-energy transition of the 2nd mode, obtained from the numerical simulations - - - Backbone branches computed by NNMcont (Peeters et al. 2009).

In Figure 5.12, the wavelet transform corresponding to the impulse responses of the 2nd DOF in the reduced order model is superimposed onto the computed Hamiltonian backbone branches (depicted with gray dashed lines). Afterward, by calculating the maximum amplitude of the wavelet at each energy level, a numerical backbone curve corresponding to the out-of-phase mode is calculated, which is depicted with a black solid line in Figure 5.12. Note that, we only consider the second mode for our nonlinear model updating strategy, since the change in the frequency of the first mode is insignificant.

We immediately observe that the Hamiltonian branch computed numerically and the backbone branch computed from the WTs of direct numerical simulations are very close to each other. The major difference appears during the hardening behavior, due to the low damping in the numerical simulations, which shifts the backbone branch toward the right in the frequency-energy domain.

5.2.4 Modeling the Nonlinear Connection

In this section, by interpreting the dynamical transitions shown in Figure 5.12, we will determine a model for the nonlinear connection in Figure 5.8. Note that we aim to treat the nonlinear connection (5.1) as “unknown” and construct a model solely based on the frequency-energy features of the numerical data, shown in Figure 5.12. Looking at the frequency transition of the second mode in Figure 5.12, we can deduce the following: First, there must be a hardening component in the nonlinear connection, since the frequency of the out-of-phase mode seems to increase until a critical energy level. Second, after this critical energy level the frequency starts to decrease, we can infer that

there must be a softening part in the connection, which appears after a critical energy level; *i.e.*, a critical relative displacement value.

In the light of this discussion, we arrive at the nonlinearity model shown in Figure 5.13, for the connecting element. We assume linear softening behavior with slope k_b after the breaking point x_b . Although, for simplicity, only one breaking point is assumed, this can be modified. For the hardening part of the connection, we assume a single nonlinear term, although more terms can be added. Another assumption we make is *symmetric* hardening nonlinearity about the origin, which makes $a_1 \equiv b_1$ and $n \equiv m$ in Figure 5.13.

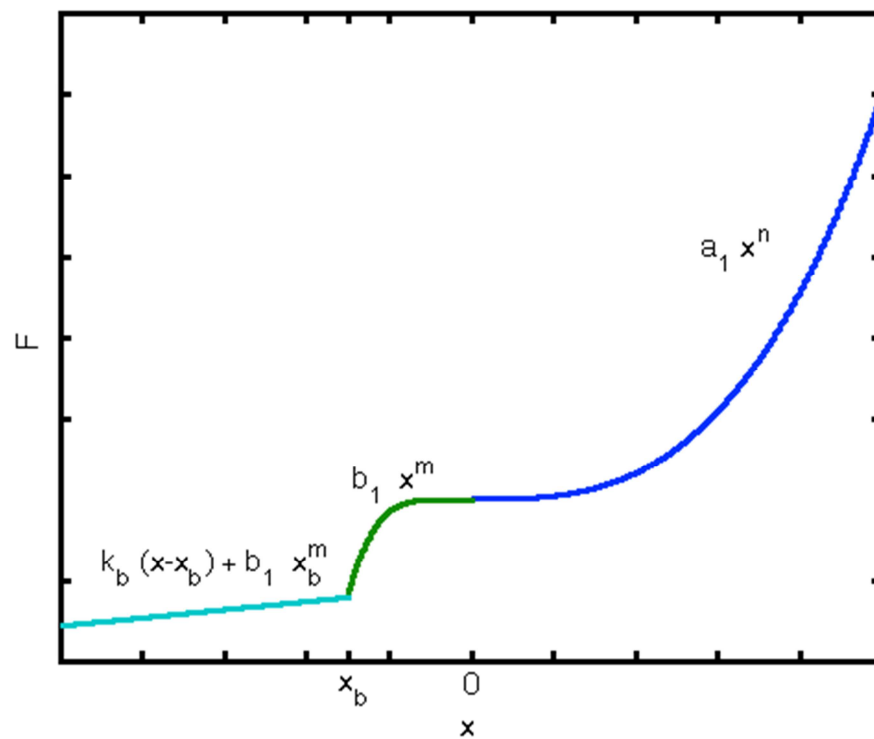


Figure 5.13 The general form of the assumed nonlinearity, based on the findings of Figure 5.12.

Having determined the type of nonlinearity that will be used, it remains to develop the nonlinear model updating and optimization strategies in order to match the frequency-energy relationships of the reduced order model and the original system. This process involves optimizing the parameters of the nonlinearity model depicted in Figure 5.13. The free parameters are the power and coefficient of the hardening nonlinearity, n and a_1 , respectively; the breaking point x_b beyond which the connection undergoes softening behavior; and the slope of the softening increment, k_b . A simultaneous multi-variable optimization, although possible, would be quite challenging in this case due to the complexity of the problem. Therefore, we will address each of these parameters individually and attempt to optimize them one-by-one based on the sensitivity of the difference to each. For each parameter, we iteratively compute the 2nd backbone branches with NNMcont and compare against the backbone branch obtained from the numerical simulations in Figure 5.12. We justify this simplistic approach by noting that the primary objective of this study is to develop a nonlinear model updating strategy; therefore we leave the improved optimization procedure to define the nonlinearity model to future work.

The first parameter of the nonlinear connection that we will attempt to optimize is the order of the hardening nonlinearity. For simplicity, only a single nonlinearity of integer order is selected, and optimization of the exponent is trivial and almost immediate.

$$\begin{aligned}
 n_{i+1} &= n_i - \mu_n \Delta \frac{\partial \omega}{\partial E}(\omega_a) \\
 \mu_n &> 0
 \end{aligned}
 \tag{5.3}$$

As formulated in (5.3), in order to optimize the value of the hardening nonlinearity exponent, one should consider the slope of the backbone branch around a pre-chosen frequency value ω_a , such that the effect of the hardening is dominant. The convergence is almost immediate and the exponent is found to be $n=3$.

The effect of the hardening nonlinearity coefficient a_1 (*cf.* Figure 5.13), other parameters held fixed, is a shift in the energy level in the frequency-energy domain. Since the effect of the hardening nonlinearity will be reflected in the smooth part of the 2nd backbone branch and since we already know the exponent ($n=3$); we optimize a_1 by matching the smooth parts of the reference backbone branch (black solid line in Figure 5.12) and the branches computed with NNMcont using the following iteration scheme

$$\begin{aligned} a_{1,i+1} &= a_{1,i} + \mu_s \Delta E_{av} \\ \mu_s &> 0 \end{aligned} \tag{5.4}$$

where ΔE_{av} is the average error between the backbone branches at each iteration step and μ_s is an arbitrary positive number. We stop the iteration when the error between the reference and the computed backbone branches falls below a certain pre-defined tolerance.

The result of the computation (5.4) for optimizing a_1 is presented in Figure 5.14. As observed, the smooth parts of the reference and the optimized branches match quite well, and the optimized value of a_1 , which is found to be $0.92 \times 10^9 \text{ N/m}^3$ is reasonably close to the original hardening nonlinearity coefficient in (5.1), which is $1 \times 10^9 \text{ N/m}^3$.

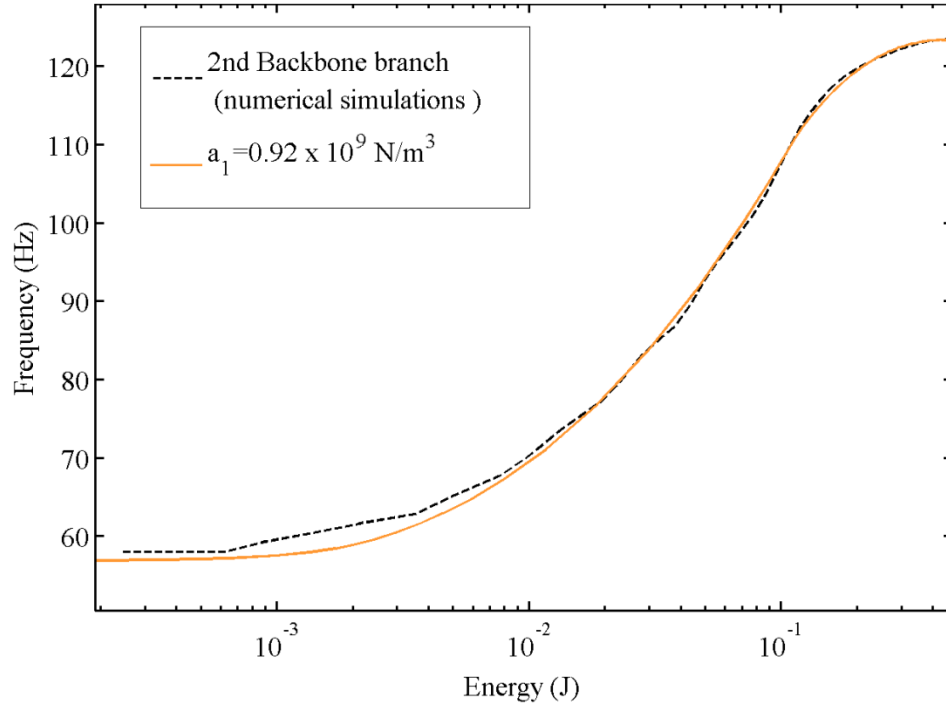


Figure 5.14 Optimization result for the smooth part of the 2nd backbone branch to find the coefficient of the hardening nonlinearity, a_1 .

The next variable to optimize is x_b , which is the breaking point of the model shown in Figure 5.13, after which the connection has a linear force-displacement relationship. Since the smooth part of the 2nd backbone branch is already optimized (*cf.* Figure 5.14), the parameter x_b will reflect itself in the peak-zero frequency of the backbone branch. For instance, a larger x_b value would result in a larger peak zero frequency value as well.

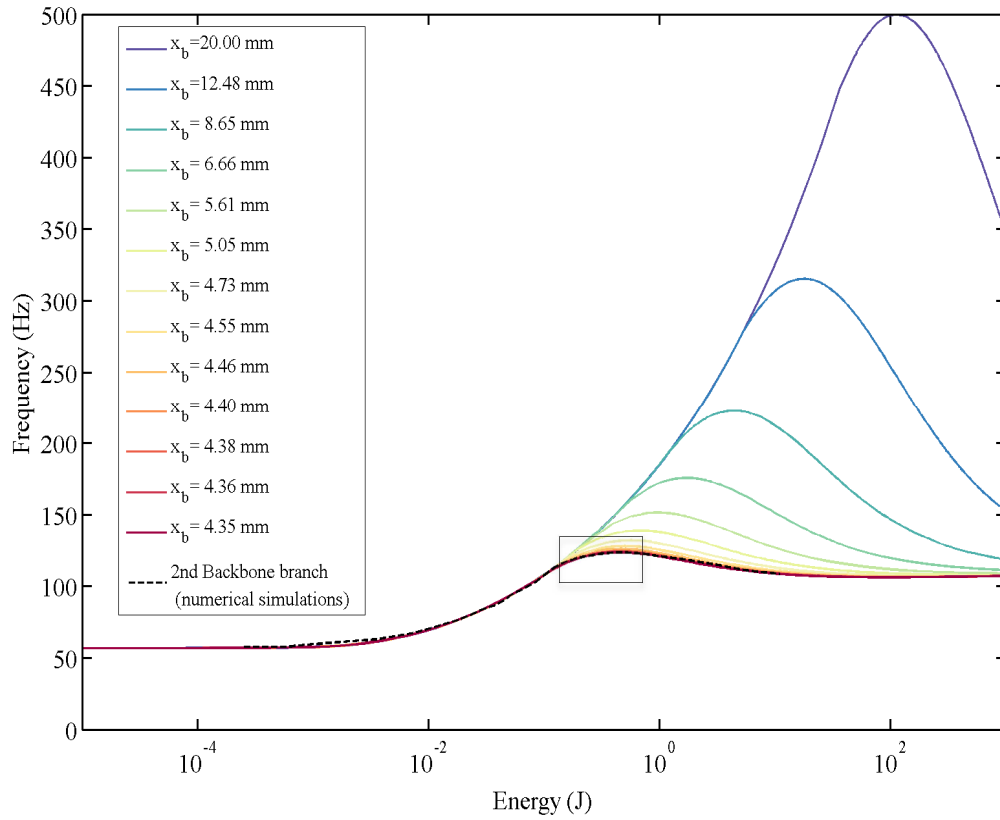
Thus, the iteration scheme is given as

$$\begin{aligned} x_{b,i+1} &= x_{b,i} + \mu_x \Delta \omega_p \\ \mu_x &> 0 \end{aligned} \tag{5.5}$$

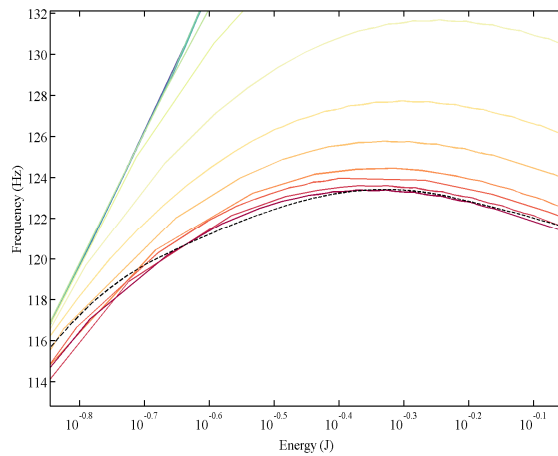
where $\Delta \omega_p$ is the difference between peak zero frequencies of the reference and

computed backbone branches at each iteration step, and μ_x is an arbitrary positive number (chosen as 0.02 for the iterations depicted in Figure 5.15).

In Figure 5.15, we show the iteration process to optimize the breaking point of our nonlinearity model, x_b . Using (5.5), we iterate on x_b by computing the second backbone branches with NNMcont, until the peak frequencies of the backbone branches match within our tolerance, which we have chosen to be 0.1 in this case. We clearly observe in Figure 5.15 that, for $x_b = -4.35$ mm, the peak frequencies of the optimized and numerical backbone branches match almost perfectly, which concludes our iteration. Note that, in the iteration process, we used only the information about the peak frequencies, not the energy values at those points. This is due to the fact that we already optimized the smooth part of this backbone branch, so the contribution of the energy level of the peak frequency would not be significant in our iteration scheme.



(a)



(b)

Figure 5.15 (a) Iterations showing the optimization process for x_b for the nonlinearity model assumed in Figure 5.13, (b) Close-up of (a) within the rectangle region.

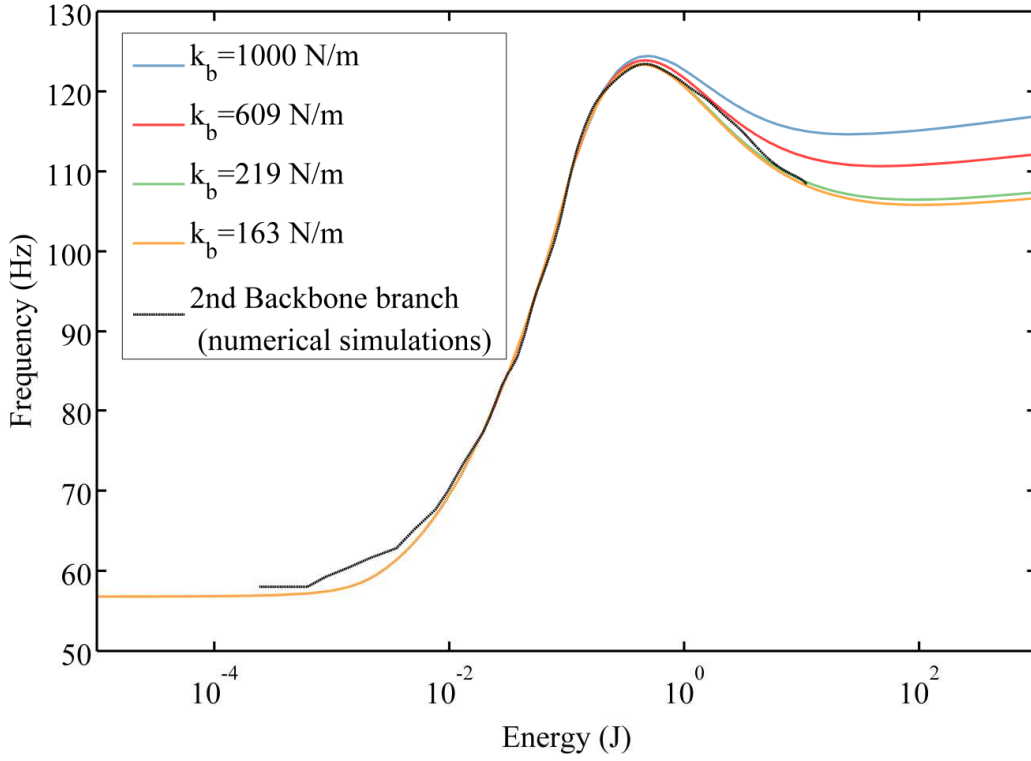


Figure 5.16 Iterations showing the optimization process for k_b for the nonlinearity model assumed in Figure 5.13.

The final parameter that needs to be optimized is the slope of the softening part, k_b . To find k_b , we use the iteration scheme

$$\begin{aligned} k_{b,i+1} &= k_{b,i} + \mu_{ns} \Delta E_{av} \\ \mu_{ns} &> 0 \end{aligned} \quad (5.6)$$

Where μ_{ns} is an arbitrary positive number and ΔE_{av} is the average error between the backbone branches at each iteration step. Note that a bigger k_b will imply a smaller decrease in the frequencies of the out-of-phase NNMs. In Figure 5.16, several iterations carried out on the parameter k_b is shown. As observed, for $k_b=163$ N/m, the reference and optimized backbone branches agree quite well, thus finalizing the form and parameters of our nonlinearity model as follows

$$\tilde{F}(\Delta x) = \begin{cases} 0.92 \times 10^9 \Delta x^3 \text{ N} & \Delta x \geq -4.35 \times 10^{-3} \text{ m} \triangleq x_b \\ 0.92 \times 10^9 \text{ N/m}^3 (-4.35 \times 10^{-3} \text{ m})^3 + 163(\Delta x + 4.35 \times 10^{-3} \text{ m}) & \Delta x < -4.35 \times 10^{-3} \text{ m} \triangleq x_b \end{cases} \quad (5.7)$$

Comparing (5.7) with (5.1) and also examining Figure 5.17, we see that the optimized nonlinearity model is in close agreement with the original nonlinearity, which we treated as “non-identified” during the model updating process.

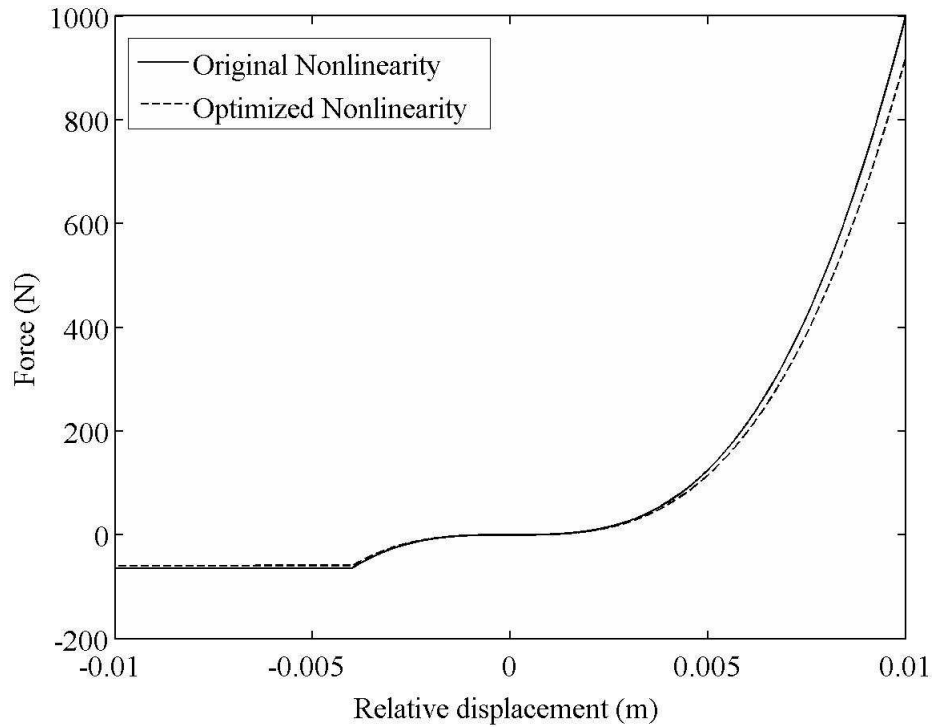
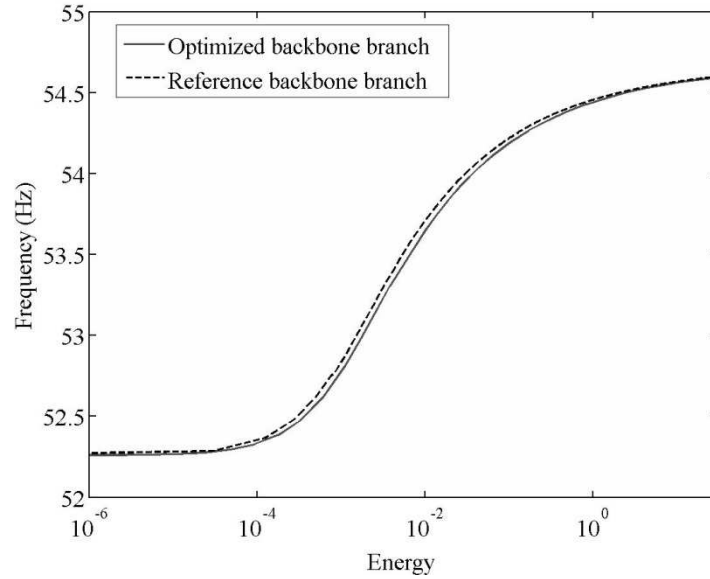


Figure 5.17 The comparison between the optimized and original nonlinearity models

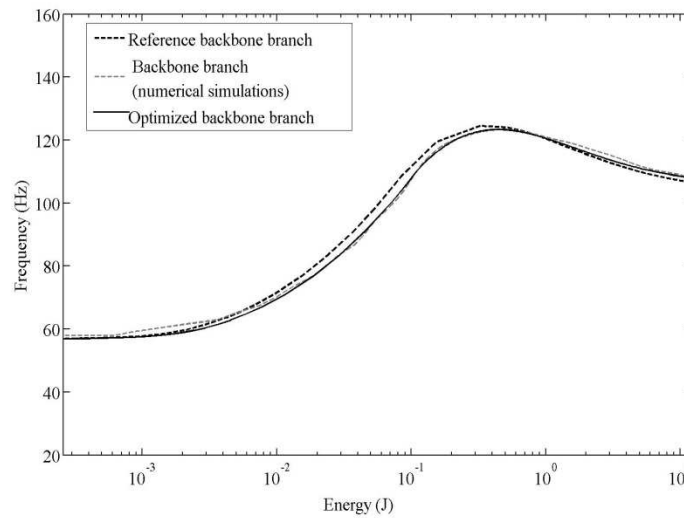
5.2.5 Comparisons between the Optimized and Original Models

In Figure 5.18, we compare the optimized 1st and 2nd backbone branches with their Hamiltonian counterparts, computed with the original membrane properties as depicted in Figure 5.3 and the backbone branch obtained from the superposition of WT of numerical simulations onto the Hamiltonian FEP. As observed, the optimized backbone branches match very closely with the reference and numerical backbone branches, which

demonstrates the accuracy of our prediction for the nonlinearity model formulated in (5.7) when compared with the original nonlinearity model in Figure 5.17.

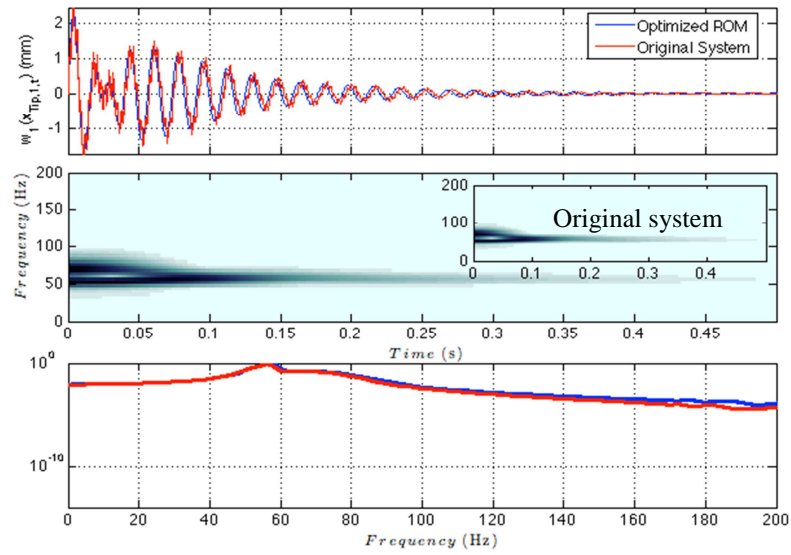


(a)

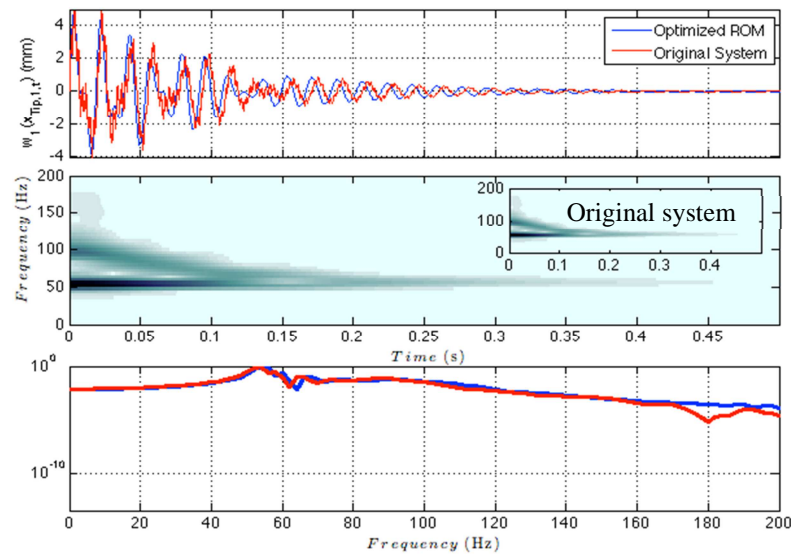


(b)

Figure 5.18 Comparison of the (a) 1st (b) 2nd backbone branches with the reference and numerical backbone branches.



(a)



(b)

Figure 5.19 Comparison of time series, wavelet and Fourier transforms for the tip deflection of the first beam, $w_1(x_{Tip,1}, t)$ for (a) $F_{max}=1000$ N, (c) $F_{max}=2500$ N between the optimized ROM and original system.

Having compared the frequency-energy relationships for the optimized and original reduced-order models, we now perform impulse tests (*cf.* Figure 5.4) with the reduced order model (*cf.* Figure 5.8) by using the optimized nonlinearity model formulated in (5.7). In Figure 5.19, we compare the responses of the optimized reduced order model, and the original system (FE) and their respective wavelet and Fourier transforms for $F_{\max} = 1000 \text{ N}$ and 2500 N . As observed, even in the case of a strongly nonlinear response (*i.e.*, Figure 5.19b), the optimized reduced order model is able to replicate the dynamics in both time and frequency domain.

One drawback of using ROMs with few DOFs, as in our case, is that it might be a challenge extending the result spatially to reproduce the dynamics at other points in the original system. There are several ways to address this issue: One is to interpolate the responses obtained from the ROM by first finding the “normalized mode shapes” from the original system response, which can be done through spatio-temporal IMOs discussed in Section 2.5. In the case of localized nonlinearities, one can attempt to use the updated nonlinear model in the original system to reproduce the dynamics. This is done in Figure 5.20: The FE model of the system (Section 5.2.1) is simulated with the optimized nonlinearity model in (5.7) and compared against the original system for an impulse excitation with $F_{\max}=1000\text{N}$. Since the optimized and the original system nonlinearities are in close agreement (*cf.* Figure 5.17); it is no surprise that the time series in Figure 5.20 match almost perfectly.

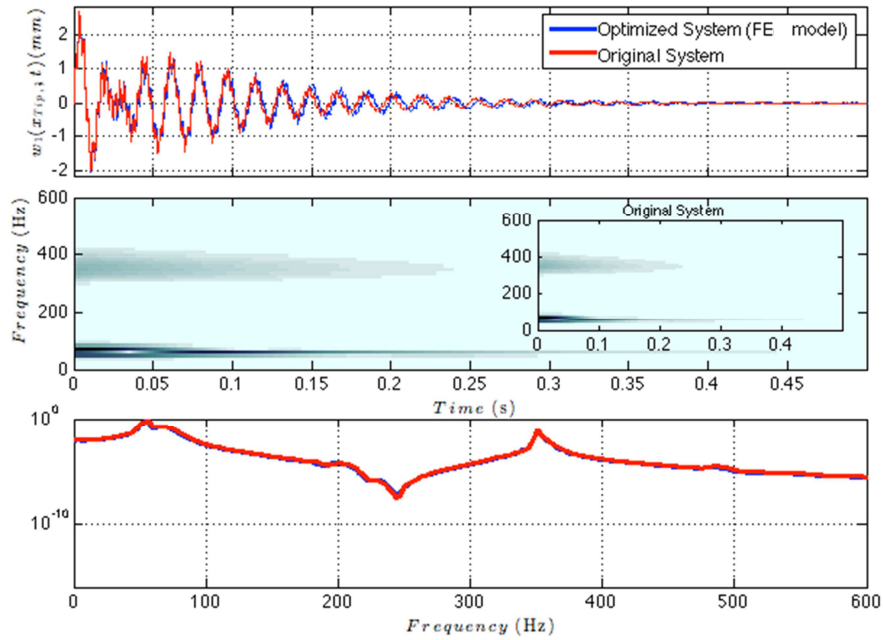


Figure 5.20 Comparison of time series, wavelet and Fourier transforms for the tip deflection of the first beam, $w_1(x_{Tip,1}, t)$ for $F_{max}=1000$ N.

5.3 Benchmark Problem

5.3.1 Introduction and System Description

In this section, a problem similar to that of Section 5.2 will be investigated as an application of the proposed nonlinear model updating strategy. This problem was posed to the system identification community prior to the IMAC XXXII held in Orlando, Florida between February 3-6, 2014, as a “Round Robin Exercise on Nonlinear System Identification”. The benchmark files used in this exercise, which is a protected code that can be simulated at 8 sensing locations depicted in Figure 5.21, and more information can be found at <http://sem.org/TDIV-Nonlin.asp>. The structure of interest consists of two facing cantilever steel beams connected by a non-identified flexible element, shown in Figure 5.21. The purpose of the exercise was to identify and model the nonlinear

characteristics of this unknown element by using only the outputs of the system, which is exactly the solid foundation of our NSI, reduced order modeling and nonlinear model updating methodologies.

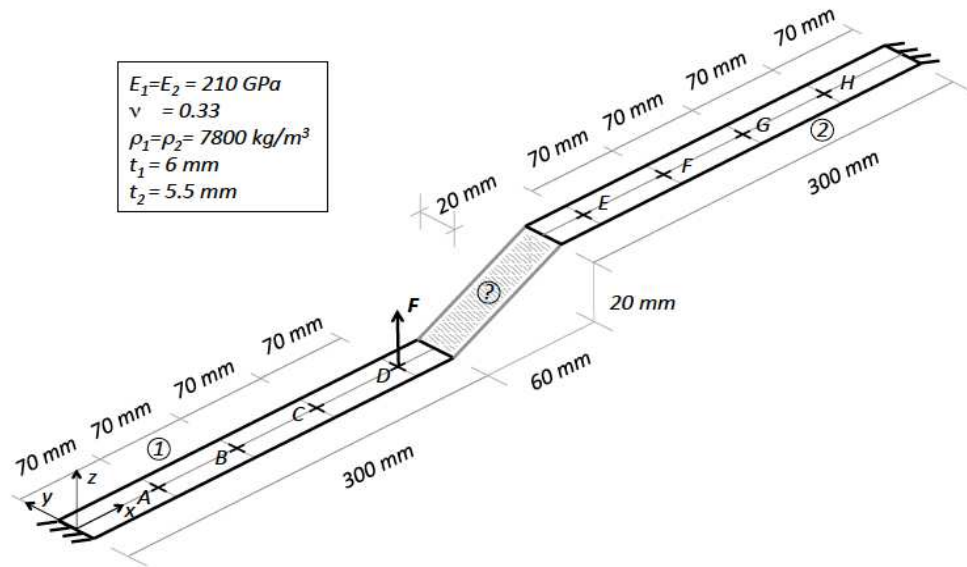


Figure 5.21 Benchmark structure. The two clamped beams are connected by a non-identified element. A force in the positive direction on sensor D is indicated.

The two beams lay on two parallel planes, so that the connecting element is inclined. The length of each beam is 300 mm, the width 20 mm, and the thicknesses of the two members are 6 mm and 5.5 mm, respectively. The linear, elastic material adopted for the beams is characterized by a Young modulus $E = 210 \text{ GPa}$, a Poisson's ratio $\nu = 0.33$, and a mass density $\rho = 7800 \text{ Kg/m}^3$. Eight sensors are placed along the beams, at the locations specified in Figure 5.21 (point A, B, C, D, E, F, G and H) from which displacements, velocities and accelerations in direction z can be measured. A time dependent force in the z direction can be applied at one sensor point at a time. The system

has an operational limit that cannot be exceeded. The limit is set at 40 mm; if the displacement at any point of the structure exceeds this value, the time integration stops.

5.3.2 Numerical Simulations of the Benchmark Model

We perform impulse tests on the given system in order to obtain transient responses that will be useful in obtaining the frequency-energy relationship for the system, The applied force, shown in Figure 5.4, is a half-sine signal with a duration of 0.1 ms , acting close to the tip of the first beam, point D in Figure 5.21. We depict the tip responses of the two beams as $w_1(x_D, t)$ and $w_2(x_E, t)$, respectively.

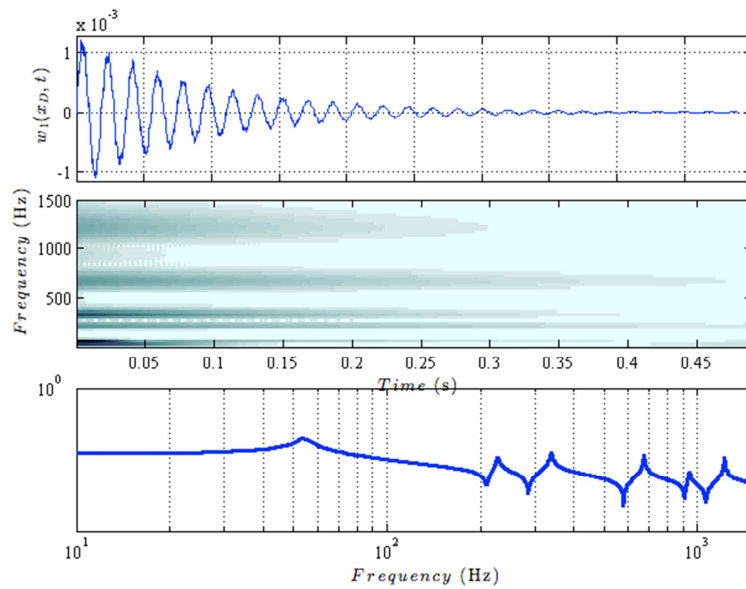


Figure 5.22 Time series, wavelet and Fourier transforms for the tip deflection of the first beam, $w_1(x_D, t)$ for $F_{\max}=1\text{N}$.

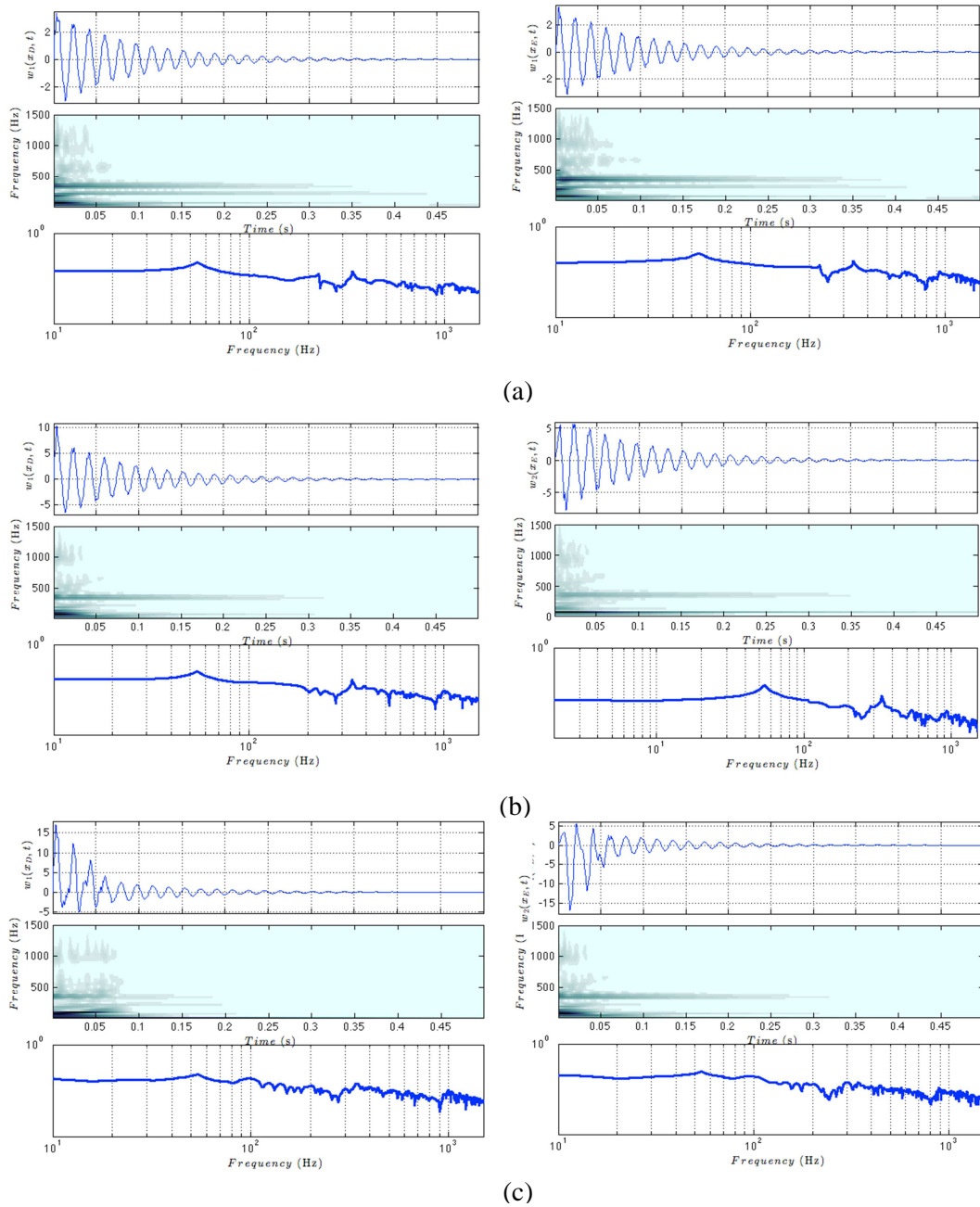


Figure 5.23 Time series, wavelet and Fourier transforms for the tip deflections of the first and second beam, $w_1(x_D, t)$ and $w_2(x_E, t)$ for (a) $F_{\max}=2500$ N (b) $F_{\max}=5000$ N (c) $F_{\max}=7500$ N.

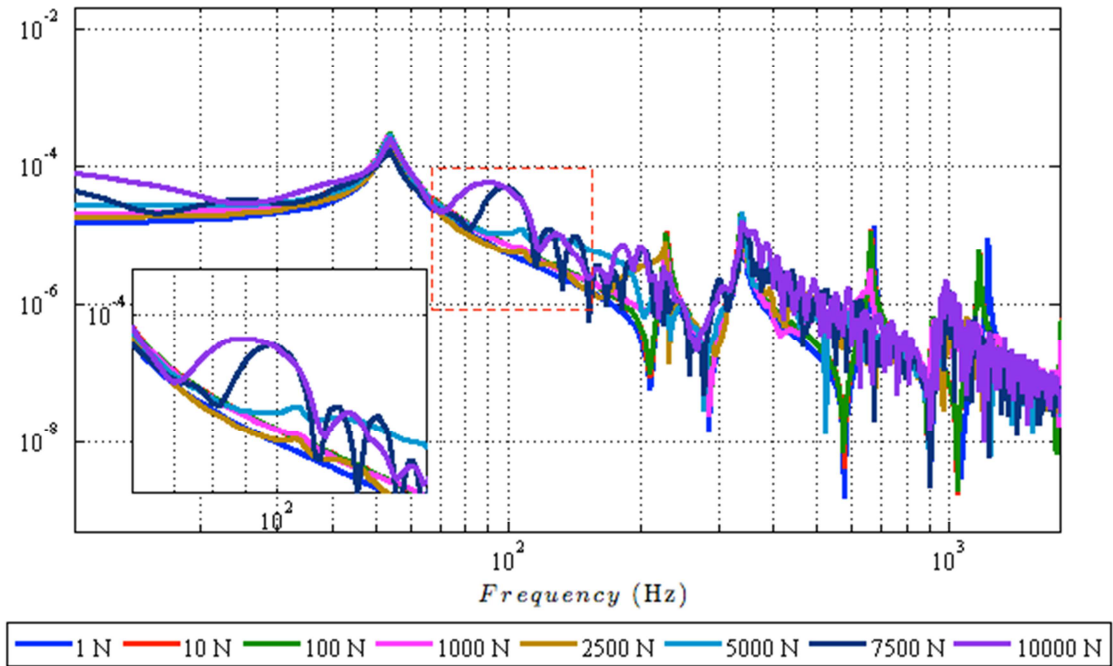


Figure 5.24 Superpositions of FFTs resulting from the impulse test with varying F_{\max} values ,for the tip point deflection of the first beam , $w_1(x_D, t)$.

In Figure 5.22, we depict the time series for $w_1(x_D, t)$ with $F_{\max}=1\text{N}$ applied at point D, to show the modes of the beam in the linear regime. Indeed, as we increase F_{\max} , as is done in Figures 5.23 and 24, we start observing strongly nonlinear phenomena in the frequency domain for $w_1(x_D, t)$ and $w_2(x_E, t)$. As is evident in Figure 5.23b,c and 5.24, an interesting damped transition occurs around the second bending mode: The frequency of the second mode seems to be decreasing after a critical energy level, which is achieved when F_{\max} is equal to or larger than 2500 N. Also interesting to notice is that, in Figure 5.23b,c , and the oscillations in $w_1(x_D, t)$ and $w_2(x_E, t)$ lose their symmetry, which implies the fact that the nonlinear relation for the connecting link in Figure 5.21 is asymmetric about the origin.

5.3.3 Modeling the Nonlinear Properties of the Connection

With the transient data from the impulse tests in hand, we plot the WT spectra of the transient data by estimating instantaneous energy to derive an empirical relationship for the frequency-energy relationship of the system. Note that, while estimating the instantaneous energy, the energy stored in the connecting link has been neglected.

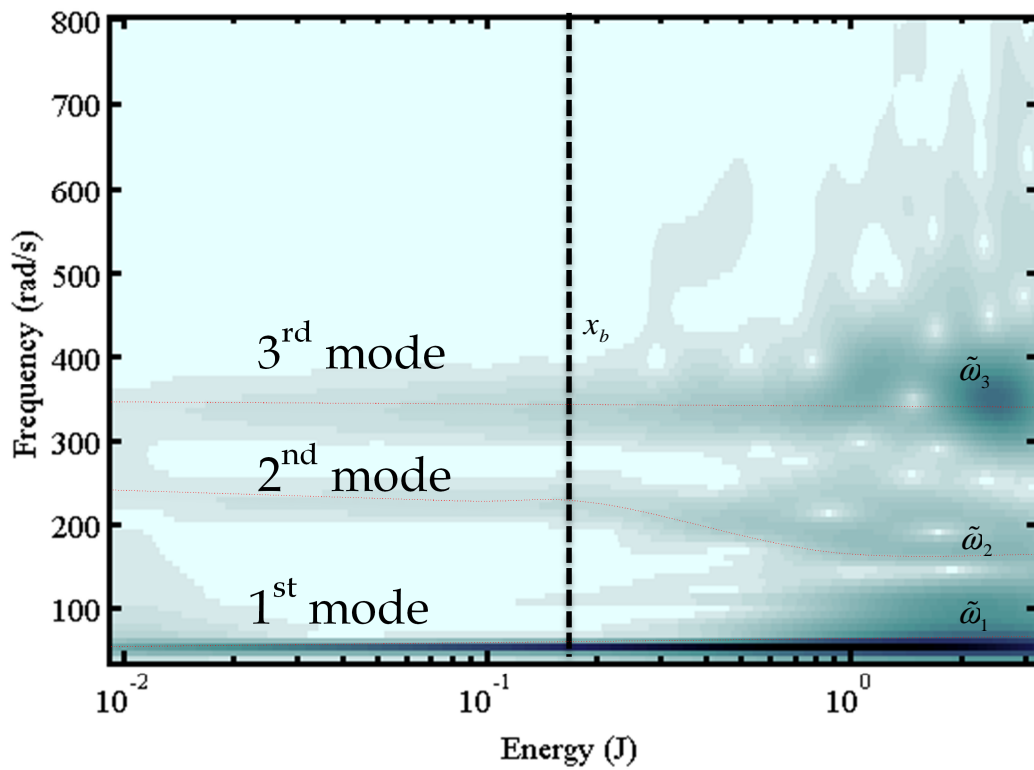


Figure 5.25 Superposition of the WT spectra onto the frequency-energy domain. The transient data used are the impulse test results from the previous section for $w_1(x_D, t)$.

In Figure 5.25, we depict the empirical frequency-energy relationship of the system obtained from the impulse tests with F_{\max} varying from 1 N to 10000 N. For the superposition of the WT spectra, we used the transient data from the tip of the first beam, which is denoted as $w_1(x_D, t)$. The frequency-energy relationship of the system reveals interesting yet very complex damped frequency transitions: Although the frequencies of the first and third modes do not appear to change significantly with increasing force and energy level, the second mode, after some critical energy level (*i.e.*, after some critical relative displacement of the tips of the two beams, x_b), seems to undergo a softening effect and reaches a new asymptote at the high energy extremes.

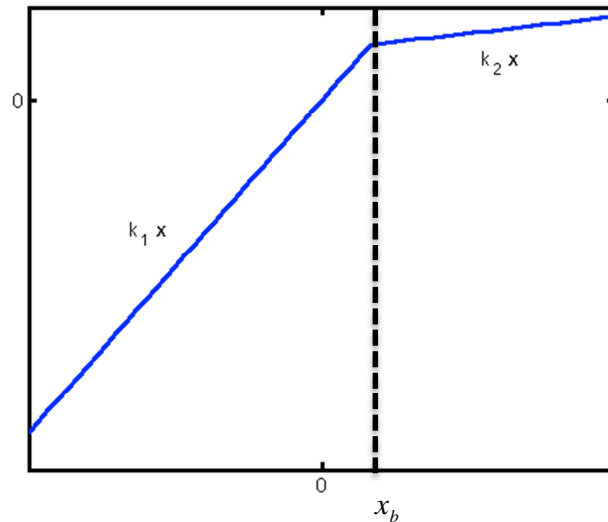


Figure 5.26 Modeling of the nonlinear properties for the “non-identified” connection in Figure 5.2

We then model the nonlinear connection based on the frequency-energy relationship obtained from the impulse tests in Figure 5.25. Examining the frequency-energy relationship on the numerical FEP, we recognize the need for a member that softens in one bending direction beyond some energy level (*i.e.*, beyond some critical displacement value, x_b), which is similar to buckling-type behavior. Thus, the nonlinear connection, after interpreting the frequency-energy relationship on the numerical FEP, is initially depicted in Figure 5.26. It is basically a member which softens in one bending direction beyond some critical point x_b and buckles. Since we observed linear behavior in our impulse tests for small forcing values (*cf.* Figure 5.22), we can assume symmetric linear behavior close to zero relative displacement, thus further simplify our model as shown.

The optimization procedure involves using the nonlinearity model shown in Figure 5.26 and computing the nonlinear normal modes (NNMs) of the system with varying parameters k_1, k_2 and x_b such that the features shown in the numerical FEP are captured, such as linear frequencies, asymptotic frequencies and the energy level at which softening begins. Due to limitations in number of measurement points, loading types and duration of the time integration, we undertake a two-fold optimization which seeks to match the backbone branches at each iteration step meanwhile significantly monitoring the agreement between the time series. Note that this is a more time-consuming optimization process when compared with the previous section. To calculate the backbone branches during the iterations, we use a 15 element linear FE model for each beam.

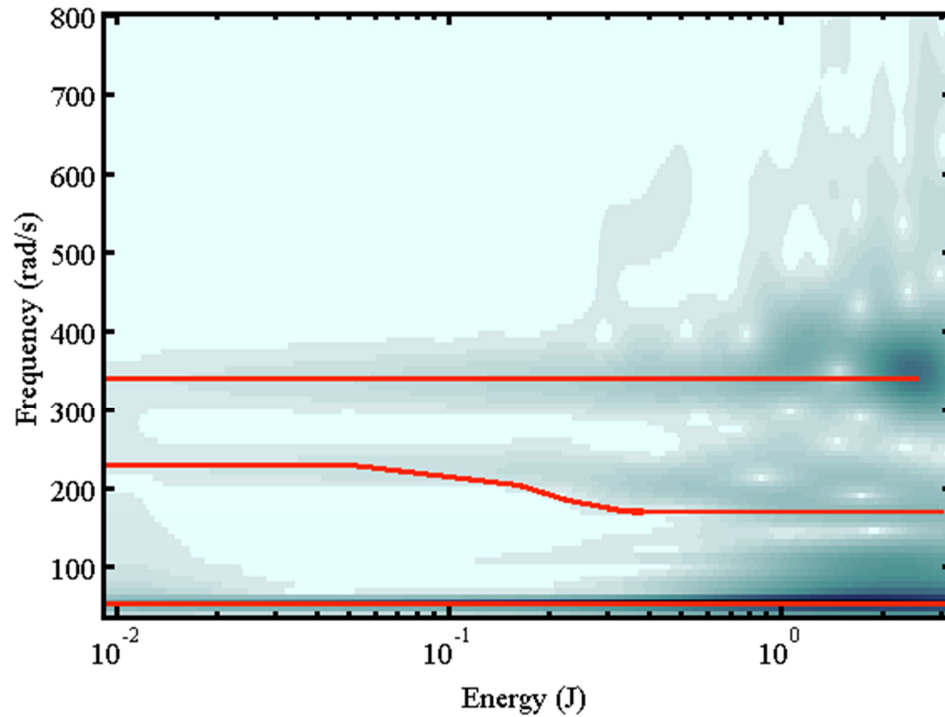


Figure 5.27 Optimized backbone branches with $k_1 = 6 \times 10^5$ N/m, $k_2 = 5 \times 10^2$ N/m, $x_b = 0.02$ mm.

Based on this complex, time-demanding yet fruitful optimization strategy, the optimized parameters for the nonlinearity model depicted in Figure 5.26 become $k_1 = 6 \times 10^5$ N/m, $k_2 = 5 \times 10^2$ N/m, $x_b = 0.02$ mm. In Figure 5.27, we see the backbone branches computed with NNMcont using these parameters superimposed onto the empirical frequency-energy relationship of the original benchmark model. As observed, they are in very close agreement with the backbone branches obtained from the direct numerical simulations.

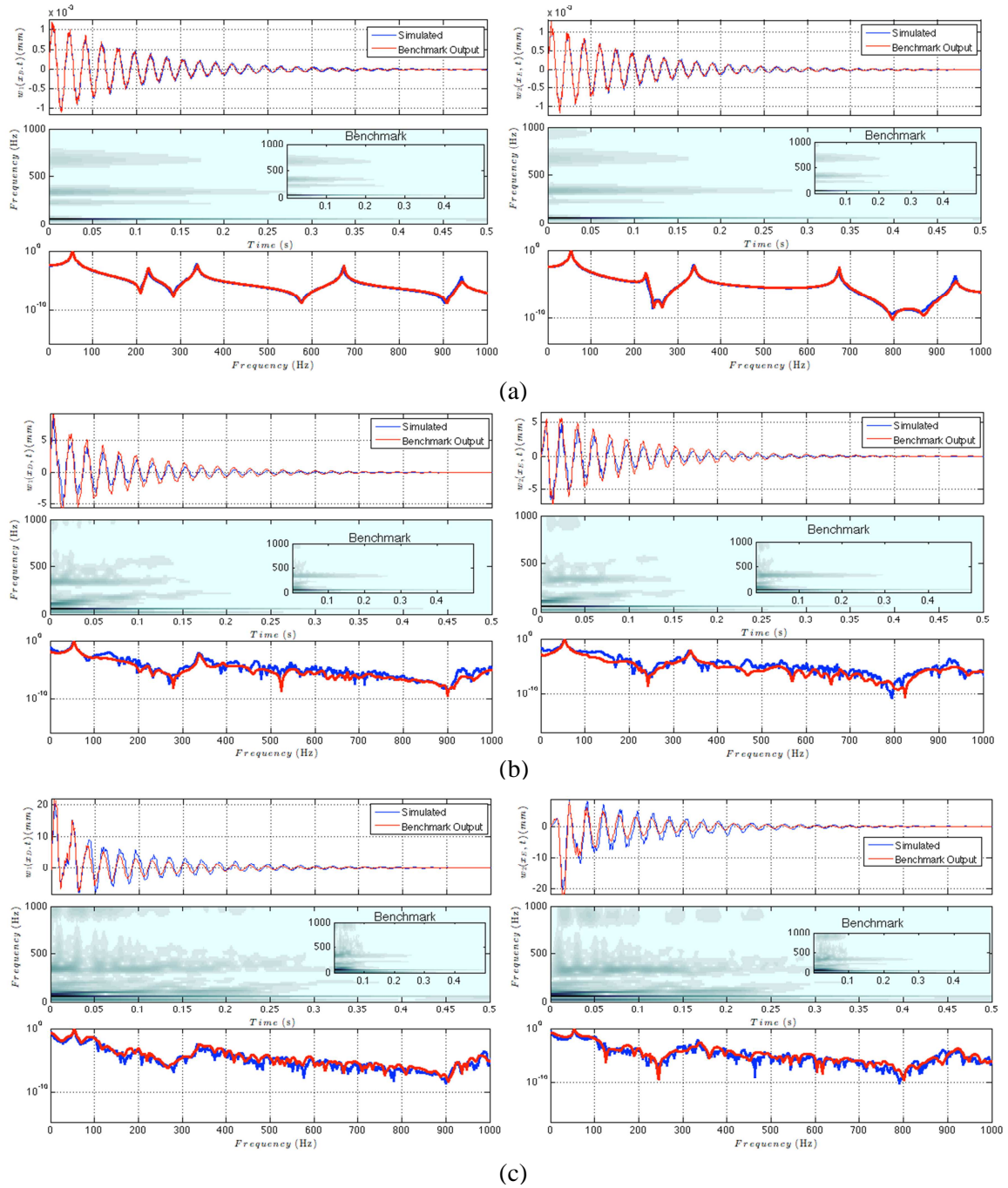


Figure 5.28 Comparisons of the time series, wavelet and Fourier transforms for the tip deflections of the first and second beam, $w_1(x_D, t)$ and $w_2(x_E, t)$ for (a) $F_{\max}=1$ N (b) $F_{\max}=5000$ N (c) $F_{\max}=10000$ N.

Having found the optimized nonlinearity model for the connection in Figure 5.21, we now simulate the system with our optimized nonlinear connection by using a 15-element FE model for each beam and compare the results with those from the benchmark model. In Figure 5.28, we see this comparison for F_{\max} values 1 N, 5000 N and 10000 N. Looking at the comparisons of time series, wavelet and Fourier transforms, we see a very good agreement between our prediction and the benchmark model, which was really nothing more than a “black-box”. This result is quite remarkable and demonstrates the power of our nonlinear model updating strategy, which used only the transient time series from the system to infer the strongly nonlinear properties within the system. Furthermore, we were able to model the actual nonlinearity and reproduce the dynamics for both linear and strongly nonlinear regimes, as shown in Figure 5.28.

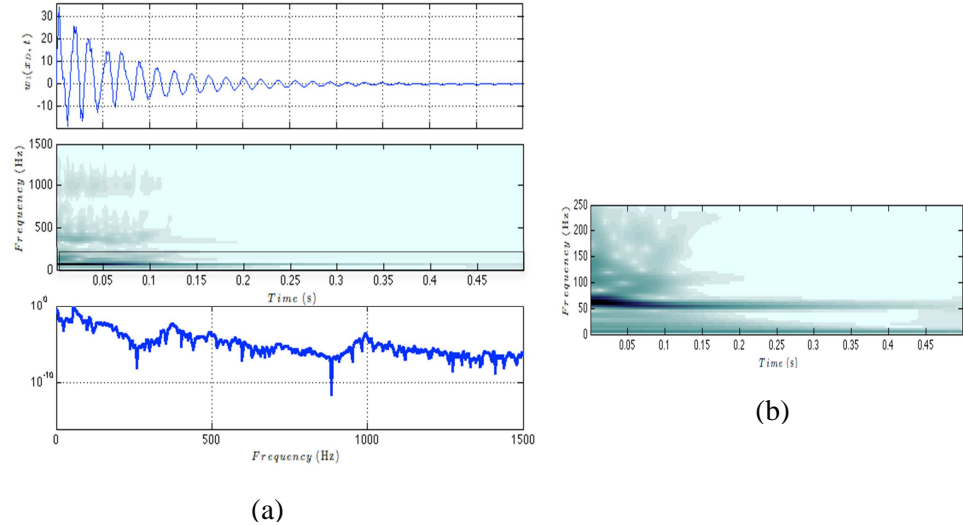


Figure 5.29 (a) Impulse response of the tip of the first beam, $w_1(x_D, t)$ with $F_{\max}=20000$ N (b) Close-up of its WT.

In Figure 5.29, we show the response of the tip of the first beam to the forcing depicted in Figure 5.4, with $F_{\max}=20000$ N. Looking at Figure 5.29b, we observe an interesting phenomenon: Starting from this forcing level, the first mode seems to undergo hardening behavior, which is unexpected since we do not expect the in-phase mode to be affected in the frequency domain by the position of the nonlinearity in Figure 5.21. This has an interesting implication: For very large forcing values (*i.e.*, at very high energies), not only the behavior of the linking member depicted in Figure 5.26, but also the effective system configuration changes. Indeed, as observed in Figure 5.30, when F_{\max} is larger than 17500 N, the shapes of the two beams undergo a dramatic change.

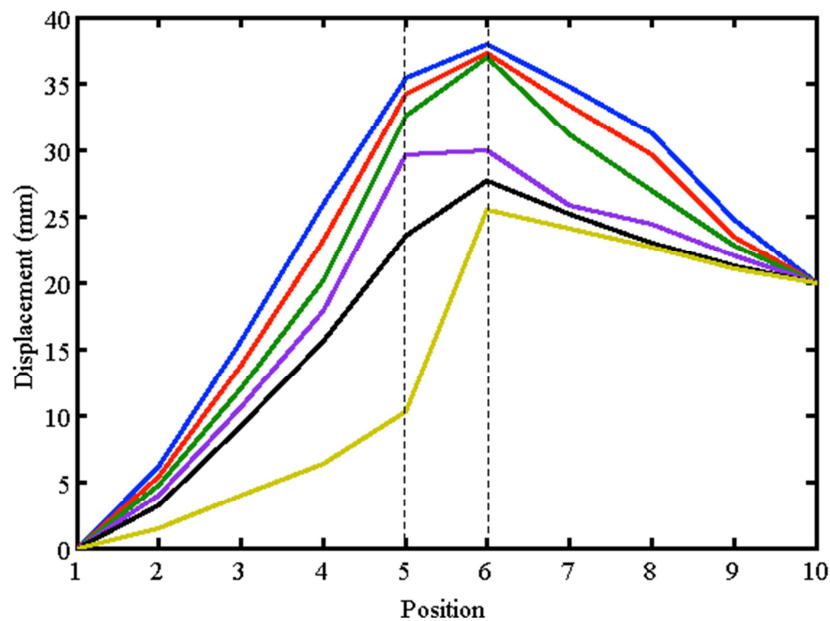


Figure 5.30 The maximum displacement configurations of the two beams for $F_{\max}= 17500$, 20000, 21000, 22000, 23000, 24000 N, respectively, in the increasing amplitude direction.

Clearly, to model the hardening behavior of the first mode, depicted in Figure 5.29a,b , we must change the system configuration. In order to reproduce the results, we consider the system configuration depicted in Figure 5.8, where k_1, k_2, m_1, m_2 are unknown but the nonlinear connection is the optimized model obtained in this section. The general idea will be as follows: Since it was shown in Figure 5.30 that, when the relative tip displacement between the two beams is 20 mm, the configurations of the beams undergo a dramatic change. The unknown system parameters of Figure 5.8 will be represented by an arbitrary asymptotic shape for the two beams at high energy levels, and the effective stiffness and mass values at that configuration are computed. Since the benchmark code only allows displacement values up to 40 mm, we use the beam shape (in blue) corresponding to the impulse input of 24000 N amplitude. Then, by using these beam shapes as our new configuration, we find the effective stiffness and mass values as $m_1 = 0.0792$ kg, $m_2 = 0.072$ kg, $k_1 = 18480$ N/m and $k_2 = 14234$ N/m .

We then simulate the 2-DOF system in Figure 5.8 as follows: When the relative displacement of the masses exceeds 20 mm, we switch to the asymptotic configuration thus changing the stiffness and mass values; and when the relative displacement between the masses at any instant during the time integration drops to 20 mm, we go back to the effective stiffness and mass values that are found in Section 5.2 for the cantilever beams in Figures 5.2 and 5.21. Although this seems like a non-physical and counter-intuitive process, our main aim is to indeed prove that strongly nonlinear effects can cause changes in system configuration. If we compare the simulation with the switching mechanism for $F_{\max} = 20000$ N to the benchmark output as done in Figure 5.31 for

$w_1(x_D, t)$, we see that we can indeed capture the hardening behavior of the first mode and obtain close agreement between the two time series.

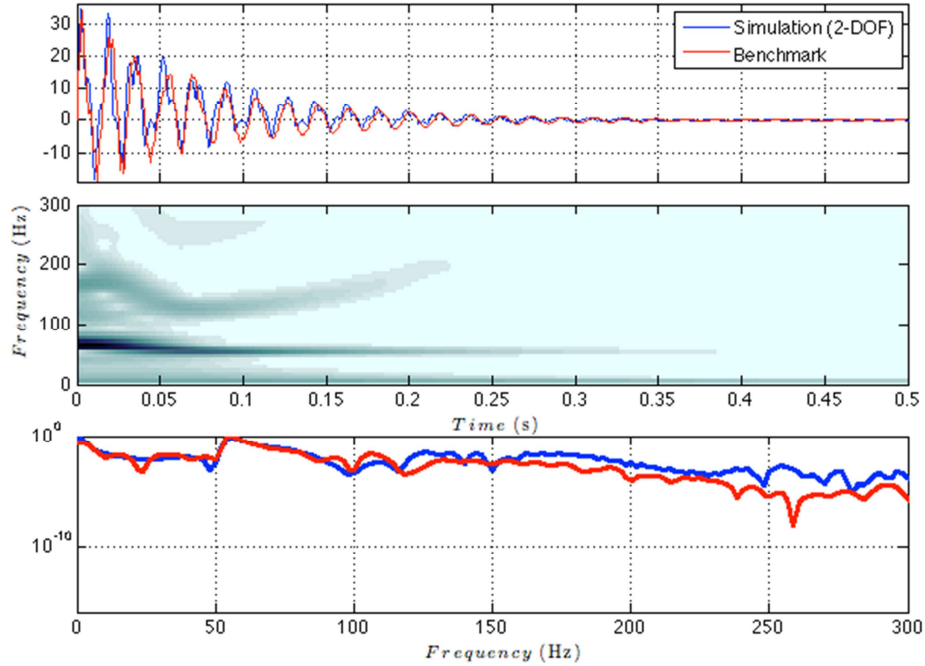


Figure 5.31 Comparison of the simulation result by using the 2-DOF system of Figure 5.8 with the proposed configuration switching mechanism to the benchmark output for $F_{\max} = 20000$ N at the tip of the first beam, $w_1(x_D, t)$.

5.4 Concluding Remarks

In this section, a nonlinear model updating strategy based on global/local nonlinear system identification of a broad class of nonlinear systems was proposed. The approach relied on analyzing the system in the frequency-energy domain by constructing Hamiltonian or forced and damped frequency – energy plots (FEPs) and comparing against the frequency-energy relationship implied by the data obtained from transient dynamics. The first application was a system consisting of two facing steel cantilever beams connected by a membrane-like element which had hardening/softening properties.

It was shown that by constructing a ROM of the original system and modeling the nonlinear connection, it was possible to reproduce the transient dynamics. The second application was a benchmark problem with a system again consisting of two facing, but offset, steel cantilever beams coupled by an “unknown” nonlinear element, whose parameters were optimized and the underlying dynamics successfully reproduced.

CHAPTER 6

CONCLUDING REMARKS AND FUTURE WORK

6.1 Summary

This dissertation presented a novel nonlinear system identification (NSI) and nonlinear model updating methodology that utilizes the close correspondence between analytical (CX-A) and empirical (EMD) slow-flow dynamics and the frequency-energy relationship of nonlinear systems. The proposed NSI methodology, which has the promise of broad applicability to a wide range of dynamical systems, is based on the direct analysis of measured time series, requiring no *a priori* system information (*i.e.*, it is purely an output-based approach). Global / local issues of NSI were discussed: Global aspects can be examined by “probing” the transient dynamics in a frequency-energy plot (nonparametric), whereas local aspects can be modeled by a set of intrinsic modal oscillators (parametric). A novel nonlinear model updating strategy based on global/local nonlinear system identification of a broad class of nonlinear systems was introduced, which relied on analyzing the system in the frequency-energy domain by constructing Hamiltonian or forced and damped frequency – energy plots (FEPs).

Now, we will briefly summarize the scope and the main results of each chapter. In Chapter 2, we reviewed the basic elements of the global/local nonlinear system identification, reduced order modeling and nonlinear model updating methodology considered in this dissertation. With these issues addressed, in Chapter 3, three main

applications of the local NSI methodology were investigated. As the first application, in Section 3.2, we studied the dynamics of a cantilever beam with two symmetric rigid stops with prescribed clearances by performing nonlinear system identification (NSI) based on the correspondence between analytical and empirical slow-flow dynamics. Performing empirical mode decomposition (EMD) analysis on the numerically-computed acceleration responses at ten, nearly evenly-spaced, spanwise positions along the beam, we constructed sets of the intrinsic modal oscillators at different time scales of the dynamics. Afterwards, we established nonlinear interaction models (NIMs) for the respective intrinsic mode oscillations. By comparing the spatio-temporal variations of the nonlinear modal interactions for the vibro-impact beam and the underlying linear beam model, we demonstrated that vibro-impacts significantly influence the lower intrinsic mode functions involving strongly nonlinear modal interactions, whereas the higher modes tend to retain their linear dynamics between impacts. The second application of the local NSI methodology was the analysis and modeling of the nonlinear damping effects induced by a frictional interface on the dynamics of a beam with a bolted joint connection, studied throughout Section 3.3. The analysis was performed by decomposing measured time series using empirical mode decomposition (EMD), and modeling the resulting dominant intrinsic modal functions (IMFs) in terms of sets of intrinsic modal oscillators (IMOs) that capture the multi-scale dynamics in the measured time series. It was shown that by studying the temporal decays of the logarithms of the moduli of the complex amplitudes of the forcing functions of the IMOs we can deduce the nonlinear damping effects in the dynamics. As a final application of the local NSI methodology, in Section 3.4 the nonlinear system identification of a cantilever beam with

an essentially (non-linearizable) nonlinear stiffness at its free end was considered. We observed strongly nonlinear beat phenomena in the transient dynamics of the cantilever beam, which upon further analysis we discovered was due to nonlinear modal interactions arising through internal resonances between cantilever modes. We demonstrated the relation between nonlinear beat phenomena and internal resonances by constructing a reduced order model of the full finite-element dynamic model using Guyan reduction and studying the dynamics of the reduced-order system in the frequency-energy plane. Finally, we extended our nonlinear system identification approach developed for nearly mono-frequency (mono-chromatic) signals, to the identification of the multi-frequency signals, which possess strongly nonlinear beating phenomena.

In Chapter 4, the global aspects of the NSI methodology were discussed and more advanced global NSI tools were developed, which extended its range of application to a broader class of dynamical systems. In Section 4.2, we demonstrated the practical use of FEPs in global NSI. It was shown that by studying the FEPs, a great deal of information can be retrieved about a dynamical system, such as the nonlinear characteristics (*e.g.*, position of the nonlinearity, nonlinear exponent and coefficient) and the configuration of the underlying system. The main assumption we made in using FEPs for system identification was that we can reconstruct/track the backbone branches of the system by using empirical (experimental or numerical) data. This was demonstrated in an experimental study in 4.2.2, where the frequency-energy dependence of a 2-DOF system consisting of a linear oscillator attached to a nonlinear energy sink was compared against numerical predictions. Since FEPs are at the heart of our NSI methodology and are usually computed for Hamiltonian systems so far, in Section 4.3, they were extended to

include forced and damped FEPs, as well. They were then applied to study some practical implications, such as the performance of an NES as a vibration absorber within predefined frequency ranges (Section 4.3.1.3) and studying the interesting and complicated dynamics of a 2-DOF system consisting of a grounded nonlinear oscillator under harmonic forcing coupled to a light linear attachment, under condition of 1:3 resonance (Section 4.3.2).

Finally, in Chapter 5, we proposed a nonlinear model updating strategy based on global/local nonlinear system identification of a broad class of nonlinear systems. The approach relied on analyzing the system in the frequency-energy domain by constructing Hamiltonian or forced and damped frequency – energy plots (FEPs) and comparing against the frequency-energy relationship of the data obtained directly from transient dynamics. Two applications were considered: The first application was a system consisting of two facing steel cantilever beams connected with a membrane-like element, that had hardening/softening properties. It was shown that by constructing a ROM of the original system and modeling the nonlinear connection, it was possible to reproduce the transient dynamics. The second application was a benchmark problem with a system again consisting of two facing though offset, steel cantilever beams coupled with an “unknown” nonlinear element whose parameters were optimized using a similar approach.

6.2 Future Work and Improvements

Extensions of this work would require further improvements and refinements in the proposed NSI methodology. One crucial improvement would be to automate the

system identification procedure and decrease the “user-dependence” of the process. The automation of this technique is a new challenge since it requires simultaneous consideration of both the global and local aspects of the proposed methodology. This should almost completely remove the “user-dependence” of the developed NSI methodology and make it an important practical tool for both academia and industry, much as experimental modal analysis is to the linear system identification community.

However, automating the NSI methodology brings its own set of important challenges: Recalling that EMD is applied in an *ad hoc* manner, thus having certain deficiencies related to issues such as uniqueness of the EMD results, and lack of orthogonality between the computed IMFs; a “step-by-step” EMD method was proposed in Section 2 in order to obtain well-decomposed, nearly mono-chromatic and orthogonal sets of IMFs. Although throughout Chapters 3-5, it was shown that the step-by-step EMD approach worked quite well to obtain almost-orthogonal sets of IMFs, this approach is manual and can be time-demanding for complex signals (*i.e.*, responses from strongly nonlinear systems and/or time signals with many closely spaced modes).

Another challenge that needs to be tackled in making the NSI methodology automated and more robust is related to obtaining the frequency-energy relationship of nonlinear systems using transient dynamics. Computing FEPs for systems with a large number of DOFs can be time consuming, thus slowing the model updating process. Furthermore, more work needs to be done on obtaining the instantaneous frequency-amplitude relationship of the transient data by using WTs and eliminating the spurious data.

Although the proposed NSI and nonlinear model updating methodologies have only been applied to nonlinear mechanical systems in this dissertation, it would be particularly interesting to explore applications in different disciplines, where nonlinear phenomena play a great role, such as in biology, cognitive sciences, economics and meteorology. Since the proposed NSI methodology has an “output-based” approach and uses the frequency-energy domain for global identification, it has the promise of broad applicability. One potential application might be to apply the methodology to medical applications. For instance, the NSI methodology can be used to study the heart rate variability (HRV), which is a sensitive indicator of a healthy heart. Changes in HRV can be identified, and the relevant nonlinear dynamical model can be updated to make better predictions regarding the patient’s condition. Another example is to study traumatic brain injury (TBI) as an application of nonlinear system identification and model updating. Occurrence of TBI is a highly nonlinear and complex process, which is often associated with impacts to the head and head acceleration during an incident. Therefore, modeling the highly nonlinear motion of the head, neck and brain during impacts and identifying the nonlinear effects that might be useful in the development preventive mechanisms will be crucial in addressing this medical condition.

Since the proposed approach is “time-series driven”, especially in the case of experimental analysis, a question that needs to be addressed is how the uncertainties such as process noise (*e.g.*, the mismatch between the actual process and the predictions from model equations) and measurement noise (*e.g.*, uncertainties from sensors) can be incorporated or accounted for in the system identification and model updating processes. For a robust modeling and identification process, we need to be able to distinguish

nonlinearity from uncertainty when analyzing the dynamics of uncertain nonlinear systems.

References

- Allemang, R.J., and D. L. Brown. 1998. "A Unified Matrix Polynomial Approach to Modal Identification." *Journal of Sound and Vibration* 211 (3): 301–22.
- Allemang, R.J., and A. W. Phillips. 2004. "The Unified Matrix Polynomial Approach to Understanding Modal Parameter Estimation: An Update." In *Proceedings of ISMA International Conference on Noise and Vibration Engineering, Katholieke Universiteit Leuven, Belgium*. http://www.sdrl.uc.edu/sdrl-info/doc/Papers/ISMA2004_UMPA.pdf.
- Allison, Timothy C., A. Keith Miller, and Daniel J. Inman. 2008. "A Deconvolution-Based Approach to Structural Dynamics System Identification and Response Prediction." *Journal of Vibration and Acoustics* 130 (3): 031010–031010. doi:10.1115/1.2890387.
- Andersen, David, Yuli Starosvetsky, Alexander Vakakis, and Lawrence Bergman. 2012. "Dynamic Instabilities in Coupled Oscillators Induced by Geometrically Nonlinear Damping." *Nonlinear Dynamics* 67 (1): 807–27. doi:10.1007/s11071-011-0028-0.
- Apiwattanalungarn, Polarith, Steven W. Shaw, and Christophe Pierre. 2005. "Component Mode Synthesis Using Nonlinear Normal Modes." *Nonlinear Dynamics* 41 (1-3): 17–46. doi:10.1007/s11071-005-2791-2.
- Arnold, Vladimir I. 1988. *Encyclopaedia of Mathematical Sciences: Dynamical Systems III*. Springer-Verlag.
- Azeez, M. F. A., and A.F. Vakakis. 2001. "Proper Orthogonal Decomposition (POD) of a Class of Vibroimpact Oscillations." *Journal of Sound and Vibration* 240 (5): 859–89. doi:10.1006/jsvi.2000.3264.
- Bai, Zhaojun. 2002. "Krylov Subspace Techniques for Reduced-Order Modeling of Large-Scale Dynamical Systems." *Applied Numerical Mathematics* 43 (1): 9–44.
- Bellizzi, Sergio, and Rubens Sampaio. 2006. "POMs Analysis of Randomly Vibrating Systems Obtained from Karhunen–Loève Expansion." *Journal of Sound and Vibration* 297 (3–5): 774–93. doi:10.1016/j.jsv.2006.04.023.
- Benfield, W.A., and R.F. Hrudá. 1971. "Vibration Analysis of Structures by Component Mode Substitution." *AIAA Journal* 9 (7): 1255–61. doi:10.2514/3.49936.
- Blevins, Robert D. 2001. *Formulas for Natural Frequency and Mode Shape*. Malabar, Fla.: Krieger Pub Co.
- Brandon, J. A. 1998. "Some Insights into the Dynamics of Defective Structures." *Proceedings of the Institution of Mechanical Engineers, Part C: Journal of Mechanical Engineering Science* 212 (6): 441–54.
- Brownjohn, J. M. W., Pin-Qi Xia, Hong Hao, and Yong Xia. 2001. "Civil Structure Condition Assessment by FE Model Updating: Methodology and Case Studies." *Finite Elements in Analysis and Design* 37 (10): 761–75. doi:10.1016/S0168-874X(00)00071-8.
- Chati, M., R. Rand, and S. Mukherjee. 1997. "MODAL ANALYSIS OF A CRACKED BEAM." *Journal of Sound and Vibration* 207 (2): 249–70. doi:10.1006/jsvi.1997.1099.
- Chelidze, David, and Wenliang Zhou. 2006. "Smooth Orthogonal Decomposition-Based Vibration Mode Identification." *Journal of Sound and Vibration* 292 (3): 461–73.

- Chen, H. G., Y. J. Yan, and J. S. Jiang. 2007. "Vibration-Based Damage Detection in Composite Wingbox Structures by HHT." *Mechanical Systems and Signal Processing* 21 (1): 307–21. doi:10.1016/j.ymsp.2006.03.013.
- Chen, Heng, Mehmet Kurt, Young S. Lee, D. Michael McFarland, Lawrence A. Bergman, and Alexander F. Vakakis. 2014. "Experimental System Identification of the Dynamics of a Vibro-Impact Beam with a View towards Structural Health Monitoring and Damage Detection." *Mechanical Systems and Signal Processing* 46 (1): 91–113. doi:10.1016/j.ymsp.2013.12.014.
- Cho, Hanna, Bongwon Jeong, Min-Feng Yu, Alexander F. Vakakis, D. Michael McFarland, and Lawrence A. Bergman. 2012. "Nonlinear Hardening and Softening Resonances in Micromechanical Cantilever-Nanotube Systems Originated from Nanoscale Geometric Nonlinearities." *International Journal of Solids and Structures* 49 (15–16): 2059–65. doi:10.1016/j.ijsolstr.2012.04.016.
- Clement, Simon, Sergio Bellizzi, Bruno Cochelin, and Guillaume Ricciardi. 2014. "Sliding Window Proper Orthogonal Decomposition: Application to Linear and Nonlinear Modal Identification." *Journal of Sound and Vibration*. <http://www.sciencedirect.com/science/article/pii/S0022460X14004441>.
- Crawley, E. F., and A. C. Aubert. 1986. "Identification of Nonlinear Structural Elements by Force-State Mapping." *AIAA Journal* 24 (1): 155–62. doi:10.2514/3.9236.
- Cusumano, J. P., and B. -Y. Bai. 1993. "Period-Infinity Periodic Motions, Chaos, and Spatial Coherence in a 10 Degree of Freedom Impact Oscillator." *Chaos, Solitons & Fractals* 3 (5): 515–35. doi:10.1016/0960-0779(93)90003-J.
- Cusumano, J. P., M. T. Sharkady, and B. W. Kimble. 1994. "Experimental Measurements of Dimensionality and Spatial Coherence in the Dynamics of a Flexible-Beam Impact Oscillator." *Philosophical Transactions of the Royal Society of London. Series A: Physical and Engineering Sciences* 347 (1683): 421–38. doi:10.1098/rsta.1994.0052.
- Datta, Biswa Nath. 2002. "Finite-Element Model Updating, Eigenstructure Assignment and Eigenvalue Embedding Techniques for Vibrating Systems." *Mechanical Systems and Signal Processing* 16 (1): 83–96.
- Dawes, Jonathan. 2010. "The Emergence of a Coherent Structure for Coherent Structures: Localized States in Nonlinear Systems." *Philosophical Transactions of the Royal Society A: Mathematical, Physical and Engineering Sciences* 368 (1924): 3519–34. doi:10.1098/rsta.2010.0057.
- Deering, R., and J.F. Kaiser. 2005. "The Use of a Masking Signal to Improve Empirical Mode Decomposition." In *IEEE International Conference on Acoustics, Speech, and Signal Processing, 2005. Proceedings. (ICASSP '05)*, 4:iv/485–iv/488 Vol. 4. doi:10.1109/ICASSP.2005.1416051.
- Deléchelle, Eric, Jacques Lemoine, and Oumar Niang. 2005. "Empirical Mode Decomposition: An Analytical Approach for Sifting Process." *IEEE Signal Processing Letters*, 764–67.
- Derkevorkian, Armen, Miguel Hernandez-Garcia, Hae-Bum Yun, Sami F. Masri, and Peizhen Li. 2014. "Nonlinear Data-Driven Computational Models for Response Prediction and Change Detection." *Structural Control and Health Monitoring*, May, n/a–n/a. doi:10.1002/stc.1673.

- Detroux, T., L. Renson, G. Kerschen, and Gaetan Kerschen. 2014. "The Harmonic Balance Method for Advanced Analysis and Design of Nonlinear Mechanical Systems." *Nonlinear Dynamics, Volume 2*, Conference Proceedings of the Society for Experimental Mechanics Series, , January, 19–34.
- Eriten, Melih, Mehmet Kurt, Guanyang Luo, D. Michael McFarland, Lawrence A. Bergman, and Alexander F. Vakakis. 2013. "Nonlinear System Identification of Frictional Effects in a Beam with a Bolted Joint Connection." *Mechanical Systems and Signal Processing* 39 (1–2): 245–64. doi:10.1016/j.ymsp.2013.03.003.
- Ewins, D. J. "Modal Testing: Theory, Practice and Application, 2000." *Research Studies Press LTD., Baldock, Hertfordshire, England* 171: 415–37.
- Ewins, D.J. 1984. *Modal Testing: Theory and Practice*. Vol. 79. Research studies press Letchworth. http://catalogue.escorts.co.in:8000/escort_images/books/E000949.pdf.
- Feeny, B. F., and R. Kappagantu. 1998. "On the Physical Interpretation of Proper Orthogonal Modes in Vibrations." *Journal of Sound and Vibration* 211 (4): 607–16.
- Feldman, Michael. 1994. "Non-Linear System Vibration Analysis Using Hilbert transform–II. Forced Vibration Analysis method'Forcevib'." *Mechanical Systems and Signal Processing* 8 (3): 309–18.
- . 2006. "Time-Varying Vibration Decomposition and Analysis Based on the Hilbert Transform." *Journal of Sound and Vibration* 295 (3–5): 518–30. doi:10.1016/j.jsv.2005.12.058.
- Freund, Roland W. 2003. "Model Reduction Methods Based on Krylov Subspaces." *Acta Numerica* 12: 267–319.
- Friswell, Michael, and John E. Mottershead. 1995. *Finite Element Model Updating in Structural Dynamics*. Vol. 38. Springer.
- Galvanetto, U., C. Surace, and A. Tassotti. 2008. "Structural Damage Detection Based on Proper Orthogonal Decomposition: Experimental Verification." *AIAA Journal* 46 (7): 1624–30. doi:10.2514/1.30191.
- Gendelman, O. V., and Yu. Starosvetsky. 2006. "Quasi-Periodic Response Regimes of Linear Oscillator Coupled to Nonlinear Energy Sink Under Periodic Forcing." *Journal of Applied Mechanics* 74 (2): 325–31. doi:10.1115/1.2198546.
- Gendelman, O.V, A. F. Vakakis, R. M'Closkey, and L. I. Manevitch. 2001. "Energy Pumping in Nonlinear Mechanical Oscillators: Part I—Dynamics of the Underlying Hamiltonian Systems." *Journal of Applied Mechanics* 68 (1): 34–41.
- Georgiou, Ioannis. 2005. "Advanced Proper Orthogonal Decomposition Tools: Using Reduced Order Models to Identify Normal Modes of Vibration and Slow Invariant Manifolds in the Dynamics of Planar Nonlinear Rods." *Nonlinear Dynamics* 41 (1-3): 69–110. doi:10.1007/s11071-005-2793-0.
- Gourdon, E., N. A. Alexander, C. A. Taylor, C. H. Lamarque, and S. Pernot. 2007. "Nonlinear Energy Pumping under Transient Forcing with Strongly Nonlinear Coupling: Theoretical and Experimental Results." *Journal of Sound and Vibration* 300 (3–5): 522–51. doi:10.1016/j.jsv.2006.06.074.
- Gourdon, E., C. H. Lamarque, and S. Pernot. 2007. "Contribution to Efficiency of Irreversible Passive Energy Pumping with a Strong Nonlinear Attachment." *Nonlinear Dynamics* 50 (4): 793–808. doi:10.1007/s11071-007-9229-y.

- Gugercin, Serkan, and Athanasios C. Antoulas. 2004. "A Survey of Model Reduction by Balanced Truncation and Some New Results." *International Journal of Control* 77 (8): 748–66. doi:10.1080/00207170410001713448.
- Guyan, Robert J. 1965. "Reduction of Stiffness and Mass Matrices." *AIAA Journal* 3 (2): 380–380.
- Hemez, François M., and Scott W. Doebling. 2001. "Review and Assessment of Model Updating for Non-Linear, Transient Dynamics." *Mechanical Systems and Signal Processing* 15 (1): 45–74.
- Huang, Norden E., Zheng Shen, Steven R. Long, Manli C. Wu, Hsing H. Shih, Quanan Zheng, Nai-Chyuan Yen, Chi Chao Tung, and Henry H. Liu. 1998. "The Empirical Mode Decomposition and the Hilbert Spectrum for Nonlinear and Non-Stationary Time Series Analysis." *Proceedings of the Royal Society of London. Series A: Mathematical, Physical and Engineering Sciences* 454 (1971): 903–95. doi:10.1098/rspa.1998.0193.
- Hurty, W. C. 1965. "Dynamic Analysis of Structural Systems Using Component Modes." *AIAA Journal* 3 (4): 678–85. doi:10.2514/3.2947.
- Ibrahim, Samir Rochoy. 1973. "A Time Domain Vibration Test Technique." <http://dspace.ucalgary.ca/handle/1880/13163>.
- Iu, V. P., and C. Y. Chia. 1988. "Non-Linear Vibration and Postbuckling of Unsymmetric Cross-Ply Circular Cylindrical Shells." *International Journal of Solids and Structures* 24 (2): 195–210.
- Jaishi, B., and W. Ren. 2005. "Structural Finite Element Model Updating Using Ambient Vibration Test Results." *Journal of Structural Engineering* 131 (4): 617–28. doi:10.1061/(ASCE)0733-9445(2005)131:4(617).
- Jalali, Hassan, Hamid Ahmadian, and John E. Mottershead. 2007. "Identification of Nonlinear Bolted Lap-Joint Parameters by Force-State Mapping." *International Journal of Solids and Structures* 44 (25–26): 8087–8105. doi:10.1016/j.ijsolstr.2007.06.003.
- Jensen, H. A., E. Millas, D. Kusanovic, and C. Papadimitriou. 2014. "Model-Reduction Techniques for Bayesian Finite Element Model Updating Using Dynamic Response Data." *Computer Methods in Applied Mechanics and Engineering*. <http://www.sciencedirect.com/science/article/pii/S0045782514002187>.
- Jiang, Xiaoi, D. Michael McFarland, Lawrence A. Bergman, and Alexander F. Vakakis. 2003. "Steady State Passive Nonlinear Energy Pumping in Coupled Oscillators: Theoretical and Experimental Results." *Nonlinear Dynamics* 33 (1): 87–102. doi:10.1023/A:1025599211712.
- Kalaycıoğlu, Taner, and H. Nevzat Özgüven. 2014. "Nonlinear Structural Modification and Nonlinear Coupling." *Mechanical Systems and Signal Processing* 46 (2): 289–306.
- Kerschen, G., Oleg Gendelman, Alexander F. Vakakis, Lawrence A. Bergman, and D. Michael McFarland. 2008. "Impulsive Periodic and Quasi-Periodic Orbits of Coupled Oscillators with Essential Stiffness Nonlinearity." *Communications in Nonlinear Science and Numerical Simulation* 13 (5): 959–78. doi:10.1016/j.cnsns.2006.08.001.
- Kerschen, G., and J. C. Golinval. 2004. "A Model Updating Strategy of Non-Linear Vibrating Structures." *International Journal for Numerical Methods in Engineering* 60 (13): 2147–64. doi:10.1002/nme.1040.

- Kerschen, G., and Jean-Claude Golinval. 2002. "Physical Interpretation of the Proper Orthogonal Modes Using the Singular Value Decomposition." *Journal of Sound and Vibration* 249 (5): 849–65.
- Kerschen, G., Jean-claude Golinval, Alexander F. Vakakis, and Lawrence A. Bergman. 2005. "The Method of Proper Orthogonal Decomposition for Dynamical Characterization and Order Reduction of Mechanical Systems: An Overview." *Nonlinear Dynamics* 41 (1-3): 147–69. doi:10.1007/s11071-005-2803-2.
- Kerschen, G., D. Michael McFarland, Jeffrey J. Kowtko, Young S. Lee, Lawrence A. Bergman, and Alexander F. Vakakis. 2007. "Experimental Demonstration of Transient Resonance Capture in a System of Two Coupled Oscillators with Essential Stiffness Nonlinearity." *Journal of Sound and Vibration* 299 (4–5): 822–38. doi:10.1016/j.jsv.2006.07.029.
- Kerschen, G., M. Peeters, J. C. Golinval, and A. F. Vakakis. 2009. "Nonlinear Normal Modes, Part I: A Useful Framework for the Structural Dynamicist." *Mechanical Systems and Signal Processing*, Special Issue: Non-linear Structural Dynamics, 23 (1): 170–94. doi:10.1016/j.ymsp.2008.04.002.
- Kerschen, G., Keith Worden, Alexander F. Vakakis, and Jean-Claude Golinval. 2006. "Past, Present and Future of Nonlinear System Identification in Structural Dynamics." *Mechanical Systems and Signal Processing* 20 (3): 505–92. doi:10.1016/j.ymsp.2005.04.008.
- Kisa, M., J Brandon, and M Topcu. 1998. "Free Vibration Analysis of Cracked Beams by a Combination of Finite Elements and Component Mode Synthesis Methods." *Computers & Structures* 67 (4): 215–23. doi:10.1016/S0045-7949(98)00056-X.
- Klerk, D. de, D. J. Rixen, and S. N. Voormeeren. 2008. "General Framework for Dynamic Substructuring: History, Review and Classification of Techniques." *AIAA Journal* 46 (5): 1169–81.
- Krysl, P., S. Lall, and J. E. Marsden. 2001. "Dimensional Model Reduction in Non-Linear Finite Element Dynamics of Solids and Structures." *International Journal for Numerical Methods in Engineering* 51 (4): 479–504.
- Kurt, Mehmet, Heng Chen, Young S. Lee, D. Michael McFarland, Lawrence A. Bergman, and Alexander F. Vakakis. 2012. "Nonlinear System Identification of the Dynamics of a Vibro-Impact Beam: Numerical Results." *Archive of Applied Mechanics* 82 (10-11): 1461–79. doi:10.1007/s00419-012-0678-5.
- Kurt, Mehmet, Melih Eriten, D. Michael McFarland, Lawrence A. Bergman, and Alexander F. Vakakis. 2014a. "Strongly Nonlinear Beats in the Dynamics of an Elastic System with a Strong Local Stiffness Nonlinearity: Analysis and Identification." *Journal of Sound and Vibration* 333 (7): 2054–72. doi:10.1016/j.jsv.2013.11.021.
- . 2014b. "Frequency-Energy Plots of Steady-State Solutions for Forced and Damped Systems, and Vibration Isolation by Nonlinear Mode Localization." *Communications in Nonlinear Science and Numerical Simulations* 19 (August): 2905–17. doi:10.1016/j.cnsns.2013.12.018.

- Kurt, Mehmet, Ilya Slavkin, Melih Eriten, D. Michael McFarland, Oleg V. Gendelman, Lawrence A. Bergman, and Alexander F. Vakakis. 2014. "Effect of 1:3 Resonance on the Steady-State Dynamics of a Forced Strongly Nonlinear Oscillator with a Linear Light Attachment." *Archive of Applied Mechanics*, June, 1–15. doi:10.1007/s00419-014-0877-3.
- Lacarbonara, Walter. 1997. "A Theoretical and Experimental Investigation of Nonlinear Vibrations of Buckled Beams". Virginia Polytechnic Institute and State University. <http://scholar.lib.vt.edu/theses/public/etd-441520272974850/wlacarbo.pdf>.
- Lee, Y. S., Stylianos Tsakirtzis, Alexander F. Vakakis, Lawrence A. Bergman, and D. Michael McFarland. 2011. "A Time-Domain Nonlinear System Identification Method Based on Multiscale Dynamic Partitions." *Meccanica* 46 (4): 625–49. doi:10.1007/s11012-010-9327-7.
- Lee, Y. S., A. F. Vakakis, D. M. McFarland, and L. A. Bergman. 2010a. "A Global–local Approach to Nonlinear System Identification: A Review." *Structural Control and Health Monitoring* 17 (7): 742–60. doi:10.1002/stc.414.
- Lee, Y. S., Alexander F. Vakakis, L. A. Bergman, D. M. McFarland, Gaëtan Kerschen, F. Nucera, S. Tsakirtzis, and P. N. Panagopoulos. 2008. "Passive Non-Linear Targeted Energy Transfer and Its Applications to Vibration Absorption: A Review." *Proceedings of the Institution of Mechanical Engineers, Part K: Journal of Multi-Body Dynamics* 222 (2): 77–134.
- Lee, Y.S., Heng Chen, Alexander F. Vakakis, D. Michael McFarland, and Lawrence A. Bergman. 2011. "Nonlinear System Identification of Vibro-Impact Nonsmooth Dynamical Systems." *52nd AIAA/ASME/ASCE/AHS/ASC Structures, Structural Dynamics and Materials Conference*. <http://arc.aiaa.org/doi/pdf/10.2514/6.2011-2067>.
- Lee, Y.S., Francesco Nucera, Alexander F. Vakakis, D. Michael McFarland, and Lawrence A. Bergman. 2009. "Periodic Orbits, Damped Transitions and Targeted Energy Transfers in Oscillators with Vibro-Impact Attachments." *Physica D: Nonlinear Phenomena* 238 (18): 1868–96. doi:10.1016/j.physd.2009.06.013.
- Lee, Y.S., Stylianos Tsakirtzis, Alexander F. Vakakis, Lawrence A. Bergman, and D. Michael McFarland. 2009. "Physics-Based Foundation for Empirical Mode Decomposition." *AIAA Journal* 47 (12): 2938–63. doi:10.2514/1.43207.
- Lee, Y.S., A.F. Vakakis, D.M. McFarland, and L.A. Bergman. 2010b. "Non-Linear System Identification of the Dynamics of Aeroelastic Instability Suppression Based on Targeted Energy Transfers." *Aeronautical Journal* 114 (1152): 61–62.
- Leontaritis, I. J., and Stephen A. Billings. 1985. "Input-Output Parametric Models for Non-Linear Systems Part I: Deterministic Non-Linear Systems." *International Journal of Control* 41 (2): 303–28.
- Li, L. M., and S. A. Billings. 2011. "Analysis of Nonlinear Oscillators Using Volterra Series in the Frequency Domain." *Journal of Sound and Vibration* 330 (2): 337–55. doi:10.1016/j.jsv.2010.08.016.
- Liang, Y. C., D. P. Feng, and J. E. Cooper. 2001. "Identification of Restoring Forces in Non-Linear Vibration Systems Using Fuzzy Adaptive Neural Networks." *Journal of Sound and Vibration* 242 (1): 47–58.

- Link, Michael, Rolf G. Rohrmann, and Stanislaw Pietrzko. 1996. "Experience with Automated Procedures for Adjusting the Finite Element Model of a Complex Highway Bridge to Experimental Modal Data." In *Proceedings-Spie The International Society For Optical Engineering*, 218–25. Spie International Society For Optical.
- Ljung, Lennart. 1987. "System Identification: Theory for the User." *Information and System Sciences Series. Prentice-Hall, Englewood Cliffs, New Jersey* 7632.
- Lochak, P., C. Meunier, and H. S. Dumas. 2013. *Multiphase Averaging for Classical Systems: With Applications to Adiabatic Theorems*. Softcover reprint of the original 1st ed. 1988 edition. New York: Springer.
- Ma, X., M. F. A. Azeez, and A.F. Vakakis. 2000. "Non-Linear Normal Modes And Non-Parametric System Identification Of Non-Linear Oscillators." *Mechanical Systems and Signal Processing* 14 (1): 37–48. doi:10.1006/mssp.1999.1267.
- Ma, X., L. Bergman, and A. Vakakis. 2001. "Identification of Bolted Joints through Laser Vibrometry." *Journal of Sound and Vibration* 246 (3): 441–60. doi:10.1006/jsvi.2001.3573.
- Malatkar, Pramod, and Ali H. Nayfeh. 2007. "Steady-State Dynamics of a Linear Structure Weakly Coupled to an Essentially Nonlinear Oscillator." *Nonlinear Dynamics* 47 (1-3): 167–79. doi:10.1007/s11071-006-9066-4.
- Mane, Mercedes. 2010. "Experiments in Vibro-Impact Beam Dynamics and a System Exhibiting a Landau-Zener Quantum Effect." <http://hdl.handle.net/2142/18326>.
- Manevich, Arkadiy I., and Leonid I. Manevitch. 2005. *The Mechanics of Nonlinear Systems with Internal Resonances*. London : Singapore ; Hackensack, NJ: Imperial College Press.
- Manevitch, Leonid I. 1999. "Complex Representation of Dynamics of Coupled Nonlinear Oscillators." In *Mathematical Models of Non-Linear Excitations, Transfer, Dynamics, and Control in Condensed Systems and Other Media*, edited by Ludmila A. Uvarova, Arkadii E. Arinstein, and Anatolii V. Latyshev, 269–300. Springer US. http://link.springer.com/chapter/10.1007/978-1-4615-4799-0_24.
- Mariani, Stefano, and Aldo Ghisi. 2007. "Unscented Kalman Filtering for Nonlinear Structural Dynamics." *Nonlinear Dynamics* 49 (1-2): 131–50. doi:10.1007/s11071-006-9118-9.
- Masri, S. F., and T. K. Caughey. 1979. "A Nonparametric Identification Technique for Nonlinear Dynamic Problems." *Journal of Applied Mechanics* 46 (2): 433–47. doi:10.1115/1.3424568.
- Masri, S. F., A. W. Smyth, A. G. Chassiakos, T. K. Caughey, and N. F. Hunter. 2000. "Application of Neural Networks for Detection of Changes in Nonlinear Systems." *Journal of Engineering Mechanics* 126 (7): 666–76.
- Mohammadali, M., and H. Ahmadian. 2014. "Efficient Model Order Reduction of Structural Dynamic Systems with Local Nonlinearities under Periodic Motion." *Shock and Vibration* 2014 (June): e152145. doi:10.1155/2014/152145.
- Mottershead, J. E., and M. I. Friswell. 1993. "Model Updating in Structural Dynamics: A Survey." *Journal of Sound and Vibration* 167 (2): 347–75.
- Nataraj, C1, and H. D. Nelson. 1989. "Periodic Solutions in Rotor Dynamic Systems with Nonlinear Supports: A General Approach." *Journal of Vibration and Acoustics* 111 (2): 187–93.

- Nayfeh, Ali H., and Dean T. Mook. 2008. *Nonlinear Oscillations*. John Wiley & Sons. <http://books.google.com/books?hl=en&lr=&id=sj3ebg7jRaoC&oi=fnd&pg=PR1&dq=%22Nonlinear+oscillations%22+Nayfeh&ots=46IXtEMZXN&sig=4Hbt5yKU4jEKQWmU2FKcq2f3i9E>.
- Noël, Jean-Philippe, and Gaëtan Kerschen. 2013. "Frequency-Domain Subspace Identification for Nonlinear Mechanical Systems." *Mechanical Systems and Signal Processing* 40 (2): 701–17.
- Nordmark, A. B. 2001. "Existence of Periodic Orbits in Grazing Bifurcations of Impacting Mechanical Oscillators". Text. <http://ilurbana.library.ingentaconnect.com/content/iop/non/2001/00000014/00000006/art00306>.
- Peeters, M., R. Vigié, G. Sérandour, G. Kerschen, and J. -C. Golinval. 2009. "Nonlinear Normal Modes, Part II: Toward a Practical Computation Using Numerical Continuation Techniques." *Mechanical Systems and Signal Processing*, Special Issue: Non-linear Structural Dynamics, 23 (1): 195–216. doi:10.1016/j.ymsp.2008.04.003.
- Pokale, Bharat, and Sayan Gupta. 2014. "Damage Estimation in Vibrating Beams from Time Domain Experimental Measurements." *Archive of Applied Mechanics*, July, 1–23. doi:10.1007/s00419-014-0878-2.
- Remick, Kevin, Alexander Vakakis, Lawrence Bergman, D. Michael McFarland, D. Dane Quinn, and Themistoklis P. Sapsis. 2013. "Sustained High-Frequency Dynamic Instability of a Nonlinear System of Coupled Oscillators Forced by Single or Repeated Impulses: Theoretical and Experimental Results." *Journal of Vibration and Acoustics* 136 (1): 011013–011013. doi:10.1115/1.4025605.
- Richardson, Mark H., and David L. Formenti. 1982. "Parameter Estimation from Frequency Response Measurements Using Rational Fraction Polynomials." In *Proceedings of the 1st International Modal Analysis Conference*, 1:167–86. <http://systemplus.co.jp/support/data/techpaper/mescope/tech/07.pdf>.
- Ritto, T. G., F. S. Buezas, and Rubens Sampaio. 2011. "A New Measure of Efficiency for Model Reduction: Application to a Vibroimpact System." *Journal of Sound and Vibration* 330 (9): 1977–84. doi:10.1016/j.jsv.2010.11.004.
- Rosenberg, R. M. 1960. "Normal Modes of Nonlinear Dual-Mode Systems." *Journal of Applied Mechanics* 27 (2): 263–68. doi:10.1115/1.3643948.
- . 1962. "The Normal Modes of Nonlinear N-Degree-of-Freedom Systems." *Journal of Applied Mechanics* 29 (1): 7–14. doi:10.1115/1.3636501.
- . 1966. "On Nonlinear Vibrations of Systems with Many Degrees of Freedom." *Advances in Applied Mechanics* 9: 155.
- Roy Craig, Jr. 2014. "Coupling of Substructures for Dynamic Analyses - An Overview." In *41st Structures, Structural Dynamics, and Materials Conference and Exhibit*. American Institute of Aeronautics and Astronautics. Accessed July 12. <http://arc.aiaa.org/doi/abs/10.2514/6.2000-1573>.
- Saito, Akira, and Bogdan I. Epureanu. 2011. "Bilinear Modal Representations for Reduced-Order Modeling of Localized Piecewise-Linear Oscillators." *Journal of Sound and Vibration* 330 (14): 3442–57. doi:10.1016/j.jsv.2011.02.018.

- Segalman, Daniel J. 2007. "Model Reduction of Systems With Localized Nonlinearities." *Journal of Computational and Nonlinear Dynamics* 2 (3): 249–66. doi:10.1115/1.2727495.
- Senroy, N., and S. Suryanarayanan. 2007. "Two Techniques to Enhance Empirical Mode Decomposition for Power Quality Applications." In *IEEE Power Engineering Society General Meeting, 2007*, 1–6. doi:10.1109/PES.2007.386016.
- Soderstrom, T., and P. Stoica. 1989. "System Identification." *Prencite Hall Lntemational*.
- Starosvetsky, Y., and O. V. Gendelman. 2008a. "Strongly Modulated Response in Forced 2DOF Oscillatory System with Essential Mass and Potential Asymmetry." *Physica D: Nonlinear Phenomena* 237 (13): 1719–33.
- . 2008b. "Dynamics of a Strongly Nonlinear Vibration Absorber Coupled to a Harmonically Excited Two-Degree-of-Freedom System." *Journal of Sound and Vibration* 312 (1–2): 234–56. doi:10.1016/j.jsv.2007.10.035.
- Teughels, Anne, Johan Maeck, and Guido De Roeck. 2002. "Damage Assessment by FE Model Updating Using Damage Functions." *Computers & Structures* 80 (25): 1869–79. doi:10.1016/S0045-7949(02)00217-1.
- Thothadri, M., R. A. Casas, F. C. Moon, R. D'Andrea, and C. R. Johnson Jr. 2003. "Nonlinear System Identification of Multi-Degree-of-Freedom Systems." *Nonlinear Dynamics* 32 (3): 307–22. doi:10.1023/A:1024489210804.
- Tiboaca, D., P. L. Green, R. J. Barthorpe, and K. Worden. 2014. "Bayesian System Identification of Dynamical Systems Using Reversible Jump Markov Chain Monte Carlo." In *Topics in Modal Analysis II, Volume 8*, 277–84. Springer. http://link.springer.com/chapter/10.1007/978-3-319-04774-4_27.
- Tiso, Paolo, Eelco Jansen, and Mostafa Abdalla. 2006. "A Reduction Method for Finite Element Nonlinear Dynamic Analysis of Shells." In *Proceedings of the 47th AIAA/ASME/ASCE/AHS/ASC Structures, Structural Dynamics, and Materials Conference*. <http://arc.aiaa.org/doi/pdf/10.2514/6.2006-1746>.
- Tsakirtzis, S., Y. S. Lee, A. F. Vakakis, L. A. Bergman, and D. M. McFarland. 2010. "Modelling of Nonlinear Modal Interactions in the Transient Dynamics of an Elastic Rod with an Essentially Nonlinear Attachment." *Communications in Nonlinear Science and Numerical Simulation* 15 (9): 2617–33. doi:10.1016/j.cnsns.2009.10.014.
- Vakakis, A.F. 2002. *Normal Modes and Localization in Nonlinear Systems*. 2001 edition. Dordrecht ; Boston: Springer.
- . 2008. *Nonlinear Targeted Energy Transfer in Mechanical and Structural Systems*. Vol. 156. Springer.
- Vakakis, A.F., L. A. Bergman, D. M. McFarland, Y. S. Lee, and M. Kurt. 2011. "Current Efforts towards a Non-Linear System Identification Methodology of Broad Applicability." *Proceedings of the Institution of Mechanical Engineers, Part C: Journal of Mechanical Engineering Science* 225 (11): 2497–2515. doi:10.1177/0954406211417217.
- Vakakis, A.F., and O.V Gendelman. 2001. "Energy Pumping in Nonlinear Mechanical Oscillators: Part II—resonance Capture." *Journal of Applied Mechanics* 68 (1): 42–48.

- Vakakis, A.F., D. Michael McFarland, Lawrence Bergman, Leonid I. Manevitch, and Oleg Gendelman. 2004. "Isolated Resonance Captures and Resonance Capture Cascades Leading to Single- or Multi-Mode Passive Energy Pumping in Damped Coupled Oscillators." *Journal of Vibration and Acoustics* 126 (2): 235–44. doi:10.1115/1.1687397.
- Worden, K., and J. J. Hensman. 2012. "Parameter Estimation and Model Selection for a Class of Hysteretic Systems Using Bayesian Inference." *Mechanical Systems and Signal Processing* 32: 153–69.
- Worden, K., and G. Manson. 2012. "On the Identification of Hysteretic Systems. Part I: Fitness Landscapes and Evolutionary Identification." *Mechanical Systems and Signal Processing* 29: 201–12.
- Worden, Keith, and Will Becker. 2011. "On the Identification of Hysteretic Systems, Part II: Bayesian Sensitivity Analysis." In *Nonlinear Modeling and Applications, Volume 2*, 77–91. Springer. http://link.springer.com/chapter/10.1007/978-1-4419-9719-7_8.
- Worden, Keith, and Geoffrey R. Tomlinson. 2010. *Nonlinearity in Structural Dynamics: Detection, Identification and Modelling*. CRC Press. <http://books.google.com/books?hl=en&lr=&id=QHoj8MlxFV0C&oi=fnd&pg=PR15&dq=model+updating+structural+dynamics+nonlinear&ots=6XuQa9H-lp&sig=B2N3erZ7bD2l6dp0xYIHHIO06sM>.
- Y. Ren, T. M. Lim. 1998. "Identification of Properties of Nonlinear Joints Using Dynamic Test Data." *Journal of Vibration and Acoustics* 120 (2). doi:10.1115/1.2893834.
- Yang, J. N., Y. Lei, S. Lin, and N. Huang. 2004. "Hilbert-Huang Based Approach for Structural Damage Detection." *Journal of Engineering Mechanics* 130 (1): 85–95. doi:10.1061/(ASCE)0733-9399(2004)130:1(85).
- Yang, J. N., Ying Lei, Shuwen Pan, and Norden Huang. 2003a. "System Identification of Linear Structures Based on Hilbert–Huang Spectral Analysis. Part 1: Normal Modes." *Earthquake Engineering & Structural Dynamics* 32 (9): 1443–67. doi:10.1002/eqe.287.
- . 2003b. "System Identification of Linear Structures Based on Hilbert–Huang Spectral Analysis. Part 2: Complex Modes." *Earthquake Engineering & Structural Dynamics* 32 (10): 1533–54. doi:10.1002/eqe.288.
- Zucca, S., and B. I. Epureanu. 2014. "Bi-Linear Reduced-Order Models of Structures with Friction Intermittent Contacts." *Nonlinear Dynamics*, April, 1–13. doi:10.1007/s11071-014-1363-8.